Advances in Polymer Technology

Polymer-Based Hybrid Materials for Theranostic Applications

Lead Guest Editor: Mingqiang Li
Guest Editors: Jianxun Ding, Yu Tao, Dan Shao, and Liyuan Zhang

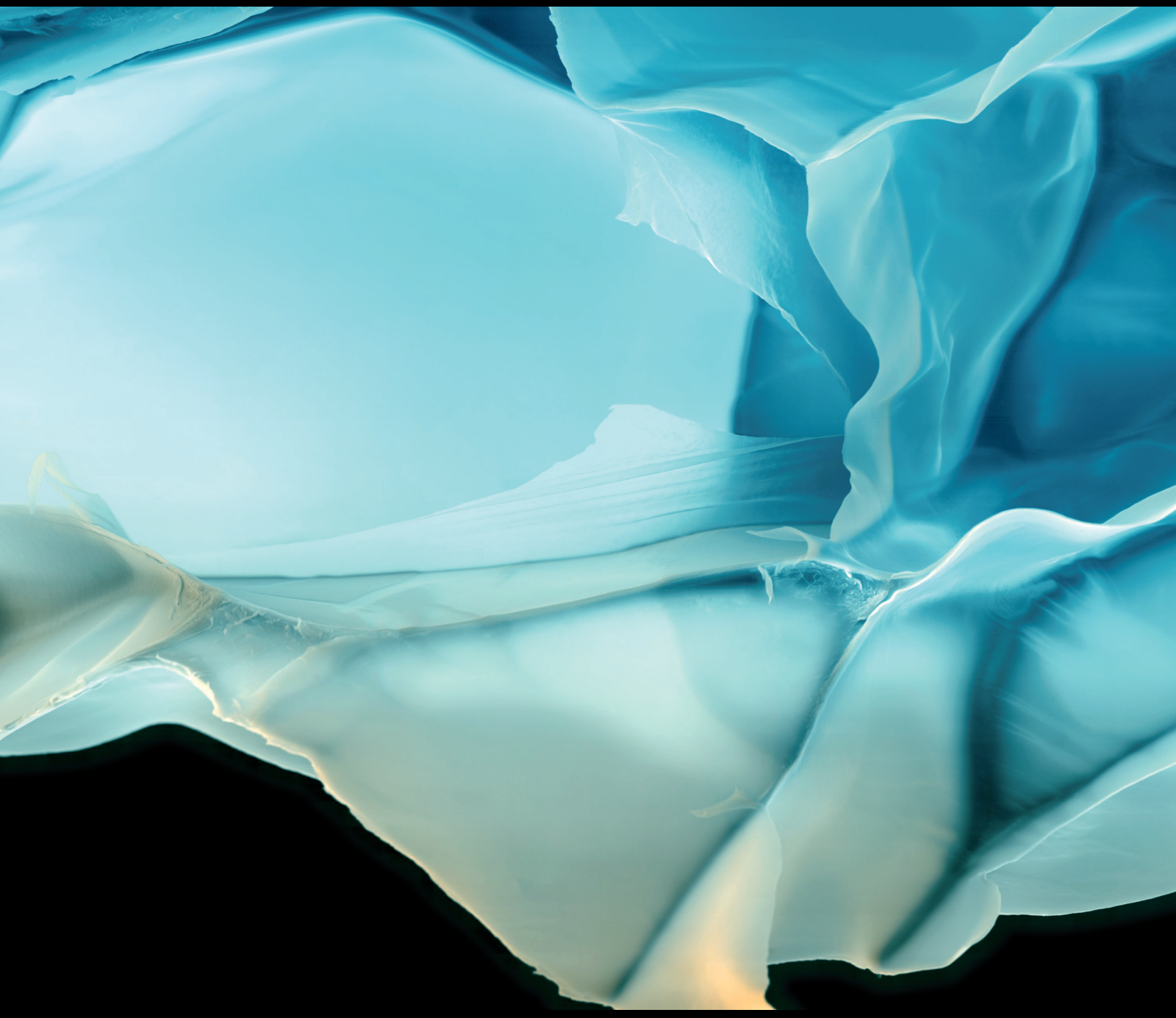

Polymer-Based Hybrid Materials for Theranostic Applications

Advances in Polymer Technology

Polymer-Based Hybrid Materials for Theranostic Applications

Lead Guest Editor: Mingqiang Li
Guest Editors: Jianxun Ding, Yu Tao, Dan Shao, and Liyuan Zhang

Contents

Hindawi
Advances in Polymer Technology
Volume 2020, Article ID 2709536, 8 pages
https://doi.org/10.1155/2020/2709536

Review Article

Purification, Preliminary Structural Characterization, and *In Vitro* Inhibitory Effect on Digestive Enzymes by β-Glucan from Qingke (Tibetan Hulless Barley)

Jialiang Hu,[1] Yue Wu,[2] Huifang Xie,[3] Wanyin Shi,[2] Zhiyuan Chen,[4] Dan Jiang,[4] Hui Hu,[5] Xiangwei Zheng,[1] Jian Xu,[2] Yuejun Yang,[2] and Yuancai Liu[2]

[1]*Shanghai University of Traditional Chinese Medicine Engineering Research Center of Modern Preparation Technology of TCM, Ministry of Education, China*
[2]*Hubei Provincial Key Laboratory for Quality and Safety of Traditional Chinese Medicine Health Food, Jing Brand Research Institute, Jing Brand Co. Ltd., China*
[3]*Biotechnology Research & Innovation Department, Shanghai Huangdian Investment Co., Ltd, China*
[4]*Jing Brand Chizhengtang Pharmaceutical Co., Ltd., China*
[5]*Hubei Provincial Traditional Chinese Medicine Formula Granule Engineering Technology Research Center, Huangshi, China*

Correspondence should be addressed to Xiangwei Zheng; zhengxwsh@hotmail.com, Jian Xu; xujian@jingpai.com, Yuejun Yang; yyj@jingpai.com, and Yuancai Liu; lyc@jingpai.com

Jialiang Hu, Yue Wu, and Huifang Xie contributed equally to this work.

Received 11 January 2020; Revised 31 March 2020; Accepted 22 April 2020; Published 19 May 2020

Guest Editor: Yu Tao

Background and Objective. Qingke (Tibetan hulless barley, *Hordeum vulgare L.*) contains a high content of β-glucan among all the cereal varieties. Although β-glucan has multiple physiological functions, the physiological function of qingke β-glucan was few studied. In this study, the β-glucan was isolated, purified, determined the structural characterization, and measured the inhibitory activity to enzymes correlating blood sugar and lipid. *Methods*. β-Glucan was isolated from enzymatic aqueous extract of qingke by using deproteinization, decolorization, DEAE-52 column chromatography, and sepharose CL-4B agarose gel column chromatography. The structure of the β-glucan was determined using FT-IR and ^{13}C-NMR spectra analysis, and molecular mass by use of HPSEC-dRI-LS. The kinematic viscosity was measured. The inhibitory effects of this β-glucan on four enzymes were investigated. *Results*. This β-glucan had a uniform molecular weight of 201,000 Da with β-(1⟶4) as the main chain and β-(1⟶3) as a side chain. The β-glucan presented a relatively strong inhibitory activity on α-glucosidase, moderate inhibition on invertase, and a weak inhibition on α-amylase, whereas it did not inhibit lipase. *Conclusion*. The study indicates that the enzymatic β-glucan from qingke has the potential as natural auxiliary hypoglycemic additives in functional medicine or foods.

1. Introduction

Hull-less barley is a kind of cultivated barley variety widely spreading over highland areas throughout the world. As the husk covering the palea and lemma is fell off during the harvest, it is also known as naked barley. Hull-less barley is the main grain source for the local population in cold regions such as countries in the Himalayas and North Africa [1]. Qingke (Tibetan hulless barley, *Hordeum vulgare L.*) is one of the hull-less barleys that distributes in the highland areas of China (Qinghai-Tibet plateau, Yunnan and Sichuan province). Over the past decade, it is gradually becoming to notice that qingke is healthy and can be used as a functional food.

It is prominent that qingke has a high content of β-glucan in cereal crops [2, 3]. β-Glucan of qingke is an unbranched polysaccharides consisting of β-D-

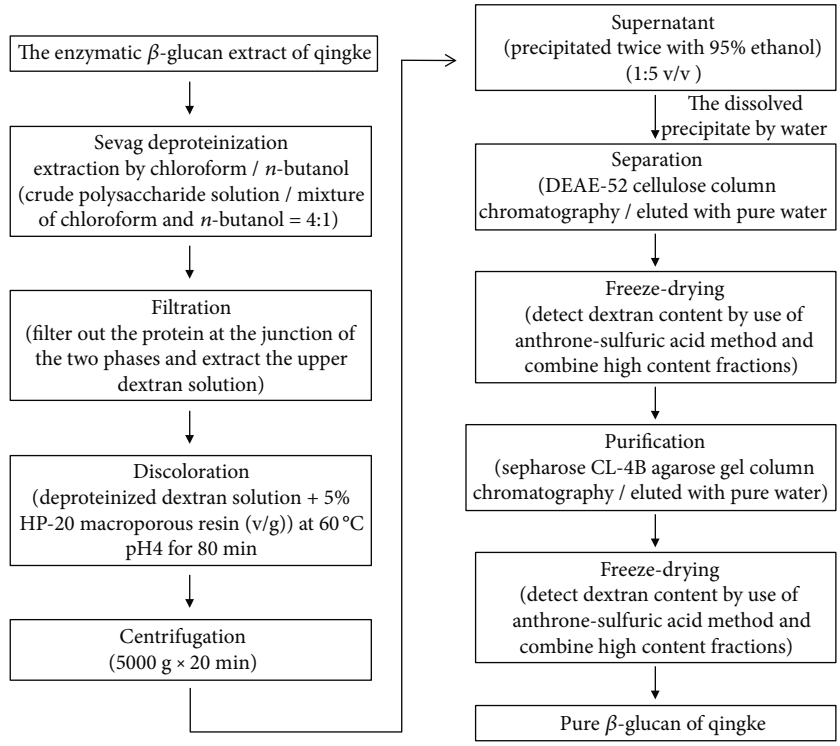

Figure 1: Extraction–purification scheme of β-glucan prepared from qingke (Tibetan Hulless Barley).

glucopyranose units linked through (1⟶4, 1⟶3) glycosidic bonds. The cereal β-glucan is a kind of dietary fiber that supports plant cell wall and possesses a number of functionalities, which include lowering blood cholesterol level, decreasing insulin level, and attenuating postprandial blood sugar [4, 5]. The β-glucan of qingke has been studied to show some activities *in vivo* and *in vitro*. The β-glucan extract from qingke showed obviously prebiotic characteristics [6]. It could effectively reduce the risk of arterial sclerosis *via* decreasing the serum glucose, serum lipid, and insulin resistance [7]. The enzymatic β-glucan extract of qingke has auxiliary hypoglycemic function on mice [8]. The chemical modification of purified β-glucan is helpful for improving the inhibition of the lipase *in vitro*, as published by Guo et al. [9–11]. However, up to now, no systematic study has been done on the activities of the purified β-glucan from qingke on the direct inhibitory activity against glycosidases relating to serum glucose. The glycosidases, such as α-glucosidase, α-amylase, and invertase, can hydrolyze polysaccharides to increase the blood sugar [12]. The inhibition to the digestive enzymes (glycosidases and lipase) might contribute to the health caring and therapy for hyperglycemia and hyperlipidemia. In our previous studies, qingke β-glucan was enzymatically extracted with the aim of broadening its application [8]. And the biological activity of the enzymatic β-glucan was not investigated. In this study, we set out to separate and purify the enzymatic β-glucan from qingke, then to explore the structural characterization and bio-activities, of the purified β-glucan, on digestive enzymes accounting for increasing glucose and lipid. It may be helpful to expand the application of qingke β-glucan.

2. Materials and Methods

2.1. Materials and Reagents. The enzymatic β-glucan crude extract of qingke was obtained from Jing Brand Chizhengtang Pharmaceutical Co., Ltd. All the chemical reagents were analytical grade and purchased from Sinopharm Group Co. Ltd (China). α-Amylase (EC number 3.2.1.1), invertase (EC number 3.2.1.26), and α-glucosidase (EC number 3.2.1.20) were purchased from Sigma (USA) with the catalog number of A3176, I4504, and G5003, respectively. The lipase (CAS number 9001-62-1) was purchased from Sinopharm Group Co. Ltd. with a catalog number of 64005761. The positive compound of acarbose was purchased from the BAYER (Germany). The compound of orlistat (catalog number O4139), *p*-nitrophenyl glucopyranoside (catalog number 877250), and *p*-nitrophenol (catalog number N2752) were purchased from Sigma. The soluble starch (catalog number 10021318), sucrose (catalog number 10021487), and 3,5-dinitrosalicylic acid (catalog number 30073424) were purchased from Sinopharm Group Co. Ltd.

2.2. Isolation and Purification of β-Glucan from Qingke. The enzymatic β-glucan crude extract of qingke was prepared as described previously [8]. The subsequent separation and purification process referred literature method [13, 14] and included four main steps: deproteinization, decolorization, DEAE-52 column chromatography, and sepharose CL-4B agarose gel column chromatography (Figure 1). Chloroform and *n*-butanol were mixed with a volume ratio of 4 : 1. Then the mixture was added into the enzymatic β-glucan solution with a volume ratio of 1 : 4, followed with shaking vigorously

for 20 min and centrifugation. The denatured protein layer at the junction of the aqueous phase and the organic phase was removed by filtration. The upper aqueous solution was mixed with HP-20 macroporous resin in the ratio of 20 : 1 (v/g), followed with stirring evenly, pH adjustment to 4.0, and then standing for 80 min at 60°C. The mixture was centrifuged to collect the supernatant for 20 min at 5000 r/min to obtain the decolored β-glucan solution. The supernatant was added with 5 times volume of 95% ethanol for precipitation overnight and then was centrifuged for 20 min at 9000 r/min to collect the precipitate. The precipitation and centrifugation were repeated twice. The dissolved precipitated by water was eluted using DEAE-52 cellulose column chromatography with pure water. Throughout the elution, the UV detector (SPD-10A, Shimadzu, Japan) connecting with the fraction collector was used to detect the protein profile of the eluent at 280 nm wavelength. The sugar concentrations of the eluent in each tube were measured by the anthrone-sulfuric acid method at 620 nm wavelength [15]. The main sugar-containing fractions of the eluent were harvested, combined, and lyophilized by freeze-drying. The redissolved sugar-containing fraction was then purified by sepharose CL-4B agarose gel column chromatography and eluted with pure water. The eluents were measured by the anthrone-sulfuric acid method at 620 nm wavelength to track the sugar concentrations. Then, the sugar-containing fractions were also harvested, combined, and lyophilized by freeze-drying to obtain the purified enzymatic β-glucan from qingke (EGQK).

2.3. Viscosity. EGQK solution was prepared by dispersing the EGQK in deionized water at a concentration of 0.1%. Then, the Ubbelohde capillary viscosimeter was used to determine the kinematic viscosity (v) based on a previously reported method [16]. Time of suspension flow was taken from 5 measurements as average, and the kinematic viscosity was calculated from the equation:

$$\begin{aligned}\text{Kinematic viscosity}\left(\text{mm}^2\cdot\text{sec}^{-1}\right) &= \text{capillary constant}\left(\text{mm}^2\cdot\text{sec}^{-2}\right)\\ &\times \text{average flow time(sec)}\end{aligned} \quad (1)$$

2.4. Molecular Mass Analysis of EGQK. The molecular weight distribution of EGQK was obtained on high-performance size-exclusion chromatography (HPSEC) using the column (Shodex SB-803 HQ, Showa Denko K.K., Japan) [17]. Samples were filtered through a syringe filter (0.45 μm pore), and 20 μl filtrate was injected into the HPSEC column. The column was eluted with 0.15 M $NaNO_3$ with a flow rate of 0.6 ml/min, with a laser scattering detector (Wyatt dawn heleos-II, Wyatt DAWN Technology, USA) (LS) and refractive index detector (Optilab T-rEX, Wyatt DAWN Technology, USA) (dRI).

2.5. Fourier-Transform Infrared Spectroscopy (FT-IR) Spectrum of EGQK Analysis. The FT-IR spectrum of EGQK was recorded on a Bruker Vector 22 spectrometer (Bruker Optik GmbH, Germany) using KBr pellets.

2.6. ^{13}C-NMR Spectrum Analysis of the Monosaccharide Composition of EGQK. The sample of EGQK (30 mg) was dissolved in 1.0 ml D_2O (99.9 at% D) for NMR analysis. The ^{13}C NMR spectrum was obtained at 298 K on a Bruker DRX-600 NMR spectrometer (Bruker BioSpin GmbH, Germany) with TMS as an internal standard. MestReNova software (6.1.1.2.2.4) was used to count the data.

2.7. In Vitro Enzyme Inhibition Assays

2.7.1. Inhibition to α-Amylase and Invertase. The activity inhibition assays to α-amylase and invertase were measured by 3,5-dinitrosalicylic acid (DNS) [18]. The EGQK sample or positive control compound (acarbose) was added to the enzyme solution and then incubated for 10 min at 37°C or 55°C in α-amylase and invertase assay, respectively. The substrate solution was added to each tube, and then the reaction was carried out at 37°C for 20 min. Each tube was added with 800 μl and 600 μl DNS solution for α-amylase and invertase assay, respectively. And then, the tube was heated at 100°C for 5 min. 800 μl solution in each tube was transferred to the well of the 24-well plate, and the OD value was read at 540 nm.

2.7.2. Inhibition to α-Glucosidase Assay. The assay of activity inhibition to α-glucosidase was measured by p-nitrophenyl glucopyranoside (pNPG) [19]. In 96-well plate, the EGQK sample or acarbose was added to the enzyme solution and then incubated for 5 min at 37°C. Each well was added with 20 μl of 2.5 mM pNPG solution, and then heated at 37°C for 30 min. Each well was added with 80 μl of 0.2 M Na_2CO_3 stop solution, and then the OD value was read at 405 nm.

2.7.3. Inhibition to Lipase Assay. The activity inhibition to lipase was measured by p-nitrophenol (p-NPP) [20]. The EGQK sample or orlistat was added to the lipase solution and then incubated for 10 min at 37°C. Each tube was added with 0.3 mg/ml p-NPP solution and then incubated at 37°C for 30 min. Each tube was added with 300 μl of 10% trichloroacetic acid (TCA), followed with 300 μl of 10% Na_2CO_3 stop solution. 1500 μl solution in each tube was transferred to the well of the 24-well plate, and the OD value was read at 405 nm. The parameters of the indicating enzyme inhibition assay were shown in Table 1. The enzymatic inhibitory activity was exhibited as inhibition % and was calculated as follows:

$$\text{Inhibition}(\%) = \frac{\text{ODsample} - \text{ODnegtive control}}{\text{ODpositive control} - \text{ODnegtive control}} \times 100\% \quad (2)$$

3. Results

3.1. The Preparation Result of EGQK. The elution curve of crude β-glucan by DEAE-52 cellulose column chromatography was shown in Figure 2. The elution peaks appeared in the 16-48 tubes, 64-78 tubes, and 96-106 tubes. The content of protein impurity was less, only appearing in the 66-84 tubes

Table 1: The enzyme assay parameters.

Enzyme assay	Sample	Substrate		Enzyme		Buffer (pH)
	Vol. (μl)	Final Conc.	Vol. (μl)	Final Conc.	Vol. (μl)	
α-Amylase	200	1.5%	400	0.1 μg/ml	200	Tris-HCl (pH 7.0)
Invertase	200	50 mM	200	1 μg/ml	200	Tris-HCl (pH 4.5)
α-Glucosidase	20	1.25 mM	20	0.01 unit	40	PBS (pH 6.8)
Lipase	300	0.15 mg/ml	600	1 mg/ml	300	Tris-HCl (pH 8.0)

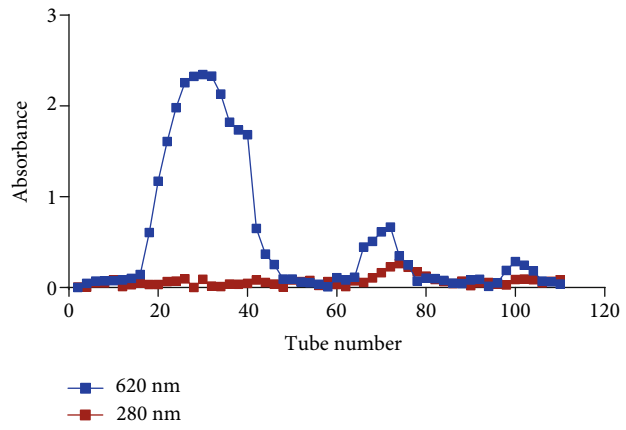

Figure 2: The elution curve of crude β-glucan by DEAE-52 cellulose column chromatography.

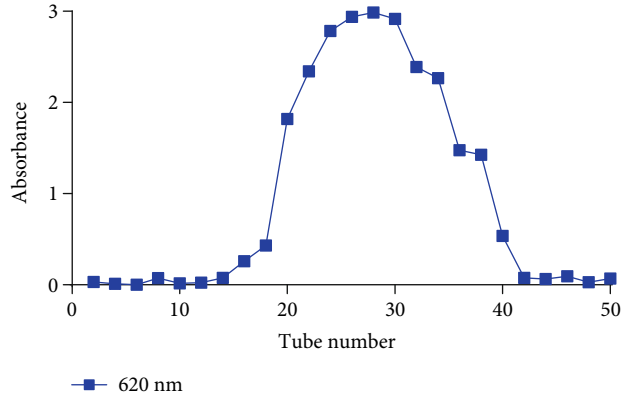

Figure 3: The elution curve of β-glucan by sepharose CL-4B agarose gel column chromatography.

with a weak absorbance and elution peak. The main sugar-containing fractions presenting in 16-48 tubes were combined and further purified to obtain EGQK. Figure 3 showed the elution curve of EGQK by sepharose CL-4B agarose gel column chromatography, suggesting that EGQK had a uniform molecular weight. As the β-glucan was extracted and purified using this procedure, 22.8-gram β-glucan could be prepared from 1-kilogram qingke dry powder.

3.2. The Appearance and Viscosity of EGQK. EGQK showed the appearance of a light yellow powder (Figure 4). The kinematic viscosity of 0.1% solution of EGQK was 1.87 $mm^2 \cdot sec^{-1}$.

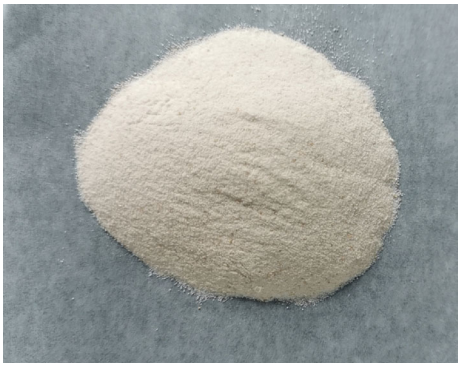

Figure 4: The appearance of purified enzymatic β-glucan from qingke (EGQK).

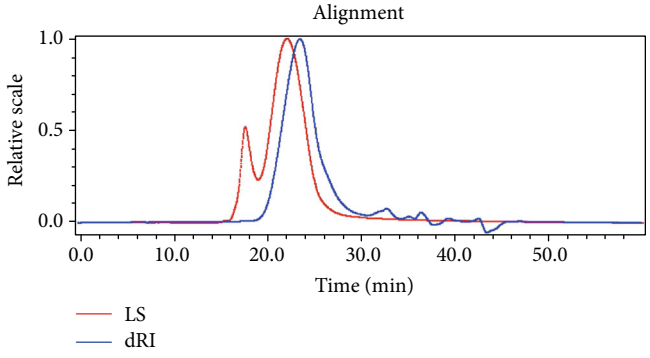

Figure 5: HPSEC-dRI-LS profile of the purified enzymatic β-glucan from qingke (EGQK).

3.3. Molecular Mass of EGQK. As shown in Figure 5, the HPSEC profile of EGQK was a single peak, indicating a uniform molecular weight. The molecular mass of EGQK was further analyzed and calculated by Astra software. It showed that the distribution range of the EGQK molecular weight was 201,000 Da (±1.323%), and the dispersion coefficient (Mw/Mn) was 1.525 (±2.107%).

3.4. FT-IR Characterization of EGQK. The FT-IR of EGQK (Figure 6) was assigned according to a previous report [21, 22]. Its spectral analysis revealed a wide band at 3500~3200 cm^{-1} representing hydroxyl stretching vibration absorption, whereas a band at 1655 cm^{-1} representing its bending vibration absorption peak. Weak absorptions at 2800~2950 cm^{-1} and 1350~1300 cm^{-1} indicated the bend and stretching vibration of a C-H. The deformation absorption

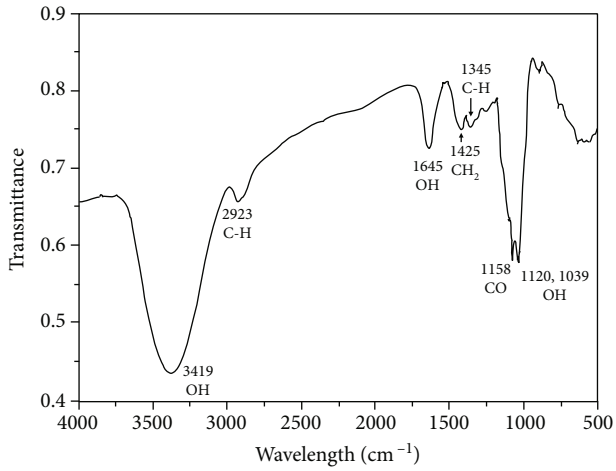

Figure 6: Fourier-transform infrared spectroscopy (FT-IR) spectrum of the purified enzymatic β-glucan from qingke (EGQK).

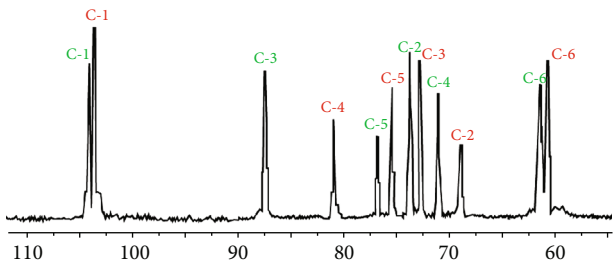

Figure 7: ^{13}C nuclear magnetic resonance (NMR) spectrum analysis of the purified enzymatic β-glucan from qingke (EGQK). β-(1⟶4) is labeled red, β-(1⟶3) is labeled green.

at 1425 cm^{-1} might indicate the presence of stretching vibrations of terminal methylene (glucose). The absorption peak at 1158 cm^{-1} was assigned mainly to C-O stretching vibration on rings. The angular vibrations of alcohol hydroxyl were at both 1120 cm^{-1} and 1039 cm^{-1} with double absorption peaks.

3.5. ^{13}C NMR Analysis. ^{13}C NMR spectrum of EGQK (Figure 7) was assigned according to the previous report [23, 24]. The resonance peaks at 104.04 ppm and 103.40 ppm were the anomeric carbon C-1 of β-(1⟶3)-D-glc, as well as β-(1⟶4)-D-glc [25, 26]. The peak at 87.75 ppm was analyzed as the C-3 carbon of the β-(1⟶3)-D-Glc. The peaks at 73.40, 71.06, 76.73, and 61.28 ppm were the C-2, C-4, C-5, and C-6 of the β-(1⟶3)-D-glc residues, respectively [24]. There were the resonances at 68.74, 72.66, 80.77, 75.38, and 60.71 ppm, assigned to C-2, C-3, C-4, C-5, and C-6 carbons of the β-(1⟶4)-D-glc residue, respectively. The assignments were presented in Table 2. The ratio of β-(1⟶4)-linkages and β-(1⟶3)-linkages in EGQK was approximately 3 : 1 according to the proportion of the resonance peaks of anomeric carbon (C-1) in ^{13}C NMR spectrum. As a result, we speculated that the EGQK was β-glucan. And EGQK contained some β-(1⟶3) linked glucose residues among the predominant β-(1⟶4) linked linear glucan chains.

3.6. The Enzymatic Inhibition. It was shown that in Figure 8, EGQK had certain inhibitory effects on the activities of glycosidases (α-glucosidase, α-amylase, and invertase), but all of the inhibitory effects were lower than that of acarbose. All the effects exhibited a dose-dependent manner of increasing inhibition % with the increasing EGQK concentration. EGQK presented a relatively strong inhibitory activity on α-glucosidase. The inhibition of α-glucosidase reached a plateau of 77% at the concentrations of 5 mg/ml and 10 mg/ml. The inhibition activity of EGQK on invertase was moderate, which was similar to that of acarbose. The highest inhibition rate was around 50% at the concentrations of 6.66 mg/ml EGQK. EGQK showed a weak inhibitory effect on α-amylase, which also had a dose-dependent manner. The inhibition rate was 25.6% by 10 mg/ml EGQK. However, EGQK did not show an inhibitory effect on lipase (data not shown). The detected inhibition % was very low and did not present dose-dependent manner in lipase inhibition assay by EGQK, whereas the orlistat showed good dose-dependent inhibition. The results suggested that EGQK has a mechanism as a hypoglycemic additive due to the inhibitory effect on glycosidases.

Table 2: ^{13}C-NMR assigments for the purified enzymatic β-glucan from qingke (EGQK).

β-Glucan residue	^{13}C-NMR chemical shifts (ppm)					
	C-1	C-2	C-3	C-4	C-5	C-6
β-(1⟶3)	104.04	73.40	87.75	71.06	76.73	61.28
β-(1⟶4)	103.40	68.74	72.66	80.77	75.38	60.71

4. Discussion

β-Glucan exists in barley, oat, and wheat. It is edible and defined as a dietary fiber. There are few reports about β-glucan purification although the content of β-glucan in qingke is relatively high in cereal crops [27]. In this present study, the yield of purified and enzymatic β-glucan was 2.28%. Moreover, the waste residue in the extraction and purification process generally does not contain toxic and harmful substances, thus can be reused. The physicochemical properties of the purified β-glucan were also investigated for the possible interest in food and beverage applications.

Cereal β-glucan is a type of linear glucose polymers containing oligosaccharides which are formed by the linkage of β-D-glucopyranosyl units. It is mainly linked by β-(1⟶4) and separated by β-(1⟶3) [28]. In this study, by using ^{13}C NMR spectrum, it showed that EGQK possessed β-D-glucan mainly with β-(1⟶4)-linkages and occasionally with β-(1⟶3)-linkages. The molecular weight of β-glucan is related to its viscosity. The kinematic viscosity of EGQK is relatively moderate compared to the high viscosity of the high-molecular β-glucan previously reported [16]. The viscous property expands the application into beverages.

Hull-less barley (qingke) contains a high content of β-glucan among all the cereal varieties [29, 30], with an average content of 5.25% and the normal content range from 4% to 8% [31]. And the content ranges of β-glucan in other barleys and oats are 2%-10% and 2.5%-6.6%, respectively, which are overall lower than qingke β-glucan [32]. A new variety

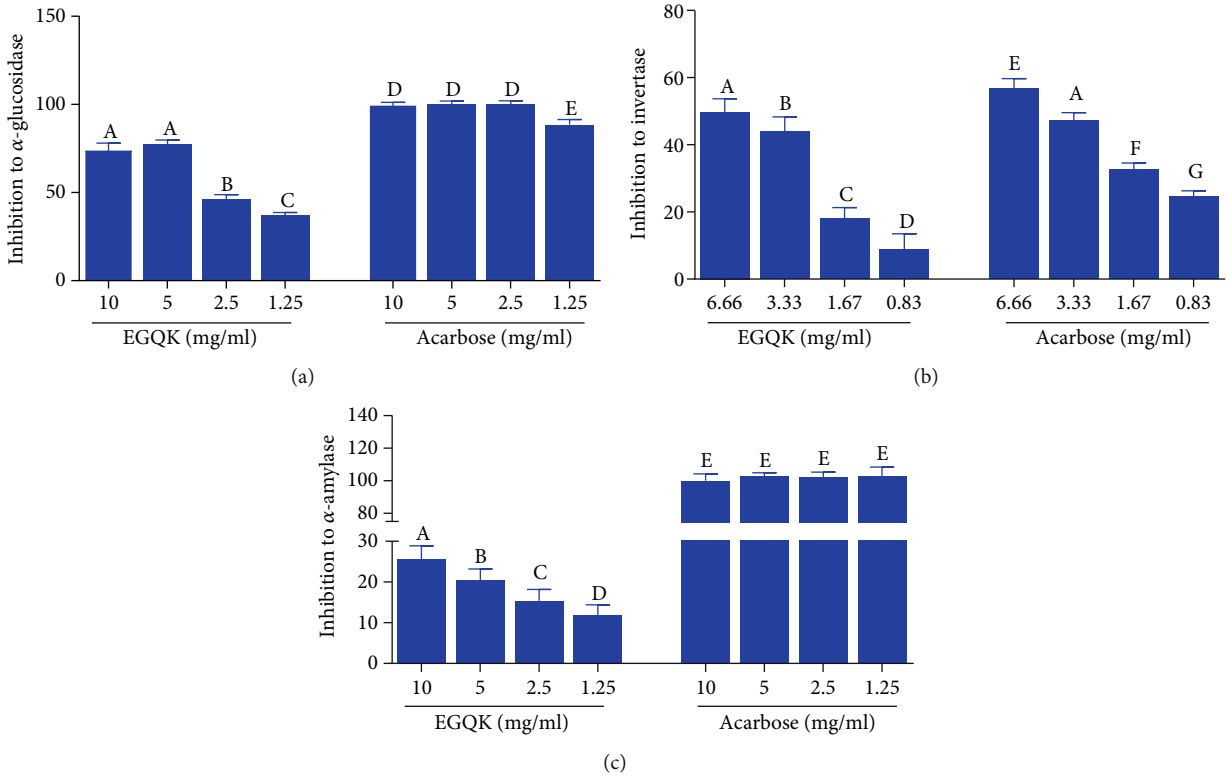

FIGURE 8: The enzymatic inhibition of the purified enzymatic β-glucan from qingke (EGQK). (a) α-Glucosidase. (b) Invertase. (c) α-Amylase. Bars (mean value ± SD) with different lower case letters indicate significant differences ($p < 0.05$).

named "Zang Qing No. 25" contains 8.62% of β-glucan [33, 34]. Moreover, the bran and shorts of qingke contain more β-glucan contents (over 7%) than reduction flours (2~3%) and breaks (0.8~3%) [35]. This suggests that β-glucan could be processed and utilized as functional food additives from the by-product of bran, which indicates the comprehensive usage of qingke. However, there is not much in-depth study on the characteristics of β-glucan enriching in qingke. β-glucan has multiple physiological functions [36, 37] including anticancer [38], clearing bowel [39, 40], regulating blood sugar [41], lowering cholesterol [42], healing wounds [43], and improving immunity [44]. As the main physiological active component of qingke, the research for β-glucan was only focused on the studies of reducing cholesterol [42] and blood sugar [41] currently. In this present study, it is the first time to explore the direct inhibitory effects of qingke β-glucan on digestive enzymes. The inhibitory effects of β-glucan on α-glucosidase, α-amylase, invertase, and lipase were investigated.

In Asia, the bulk of the diet is mainly starch, which metabolism involves the enzymatic hydrolysis by α-glucosidase [45] and α-amylase [46]. The inhibition of these two enzymes [47] is beneficial to reducing the blood sugar content [48, 49], preventing and treating the postprandial hyperglycemia [50, 51], and relieving the hyperinsulinemia [52, 53]. Invertase is a kind of disaccharidase hydrolyzing sucrose as a substrate. By inhibiting the absorption of sucrose *in vivo*, the intervention has the function of reducing blood sugar and cannot stimulate the insulin secretion by the pancreas. The results of our study showed that EGQK had a mild inhibitory effect on these enzymes, especially on α-glucosidase. Moreover, the inhibitory effect of EGQK on invertase was similar to that by acarbose. Although the inhibitory effect of EGQK on α-amylase was much weak, it also presented the dose-dependent manner. These results could partly support the auxiliary hypoglycemic function of qingke β-glucan *in vivo*.

Qingke β-glucan can reduce the blood cholesterol content of experimental animals, which study is reported by Tong et al. in 2015 [42]. It confirmed that qingke β-glucan had the hypocholesterolemic effects on cholesterol metabolism in hamsters fed with hypercholesterolemic diet. And qingke β-glucan presented more inhibitory activity to 3-hydroxy-3-methyl glutaryl-coenzyme A (HMG-CoA) reductase compared with oat β-glucan. Thus, the inhibitory effect of EGQK on lipase was detected *in vitro* in this study. However, it showed that EGQK did not inhibit lipase activity and dose-dependent manner. It speculated that the loss of lipase inhibition might be due to the enzymolysis and the reduced viscosity. But the viscosity of EGQK might perhaps be involved in the intervention on the absorption of lipid, cholesterol, and fat in digestive tract in vivo [54].

In this study, the β-glucan from qingke was isolated through cellulose column chromatography to obtain three fractions. After collecting the main fraction by agarose gel column chromatography, the EGQK has a molecular weight of 201 kDa. NMR spectroscopy indicated the preliminary structural characterization with β-(1⟶4) main chain and β-(1⟶3) side chain. Meanwhile, EGQK exhibited a certain inhibitory activity on α-glucosidase, α-amylase, and invertase and has no direct inhibitory activity on lipase. The

preliminary study indicates that the EGQK purified from enzymatic β-glucan has the potential as natural auxiliary hypoglycemic additives in functional medicine or foods.

Conflicts of Interest

The authors declare no conflict of interest.

Authors' Contributions

Jialiang Hu, Yue Wu and Huifang Xie contributed equally to this work.

Acknowledgments

The study was financially supported by the Jing Brand Chizhengtang Pharmaceutical Co., Ltd., for the study of "Hypoglycemic function of hull-less barley β-glucan".

References

[1] B. K. Baik and S. E. Ullrich, "Barley for food: Characteristics, improvement, and renewed interest," *Journal of Cereal Science*, vol. 48, no. 2, pp. 233–242, 2008.

[2] G. Zhang, W. Junmei, and C. Jinxin, "Analysis of β-glucan content in barley cultivars from different locations of China," *Food Chemistry*, vol. 79, no. 2, pp. 251–254, 2002.

[3] R. S. Bhatty, "The Potential of Hull-less Barley," *Cereal Chemistry*, vol. 76, no. 5, pp. 589–599, 1999.

[4] A. Lazaridou and C. G. Biliaderis, "Molecular aspects of cereal β-glucan functionality: Physical properties, technological applications and physiological effects," *Journal of Cereal Science*, vol. 46, no. 2, pp. 101–118, 2007.

[5] P. J. Wood, "Cereal β-glucans in diet and health," *Journal of Cereal Science*, vol. 46, no. 3, pp. 230–238, 2007.

[6] Y. Ren, H. Xie, L. Liu, D. Jia, K. Yao, and Y. Chi, "Processing and Prebiotics Characteristics of β-Glucan Extract from Highland Barley," *Applied Sciences*, vol. 8, no. 9, p. 1481, 2018.

[7] M. J. Tian, J. N. Song, P. P. Liu, L. H. Su, C. H. Sun, and Y. Li, "Effects of beta glucan in highland barley on blood glucose and serum lipid in high fat-induced C57 mouse," *Chin J Prev Med.*, vol. 47, no. 1, pp. 55–58, 2013.

[8] H. Hu, P. Liu, P. P. Cheng, W. Wang, and Y. C. Liu, "Study on the auxiliary hypoglycemic function of small molecule β-glucan from Hull-less barley," *Food Research and Development*, vol. 39, no. 21, pp. 33–37, 2018, 99.

[9] H. Guo, S. Lin, M. Lu et al., "Characterization, in vitro binding properties, and inhibitory activity on pancreatic lipase of β-glucans from different Qingke (Tibetan hulless barley) cultivars," *International Journal of Biological Macromolecules*, vol. 120, pp. 2517–2522, 2018.

[10] H. Guo, K. L. Feng, J. Zhou et al., "Carboxymethylation of Qingke β-glucans and their physicochemical properties and biological activities," *International Journal of Biological Macromolecules*, vol. 147, pp. 200–208, 2020.

[11] H. Guo, H. Y. Li, L. Liu et al., "Effects of sulfated modification on the physicochemical properties and biological activities of β-glucans from Qingke (Tibetan hulless barley)," *International Journal of Biological Macromolecules*, vol. 141, pp. 41–50, 2019.

[12] H. B. I. S. C. H. O. F. F. B. AG, "Pharmacology of α-glucosidase inhibition," *European Journal of Clinical Investigation*, vol. 24, no. S3, pp. 3–10.

[13] H. Chen, Q. Nie, M. Xie et al., "Protective effects of β-glucan isolated from highland barley on ethanol- induced gastric damage in rats and its benefits to mice gut conditions," *Food Research International*, vol. 122, pp. 157–166, 2019.

[14] G. Maheshwari, S. Sowrirajan, and B. Joseph, "Extraction and Isolation of β-Glucan from Grain Sources-A Review," *Journal of Food Science*, vol. 82, no. 7, pp. 1535–1545, 2017.

[15] Z. Dische, "General color reactions," *Methods Carbohydr Chem*, vol. 1, pp. 478–492, 1962.

[16] J. Harasym, D. Suchecka, and J. Gromadzka-Ostrowska, "Effect of size reduction by freeze-milling on processing properties of beta- glucan oat bran," *Journal of Cereal Science*, vol. 61, pp. 119–125, 2015.

[17] W. Cui, P. J. Wood, B. Blackwell, and J. Nikiforuk, "Physicochemical properties and structural characterization by two-dimensional NMR spectroscopy of wheat β-D-glucan—comparison with other cereal β-D-glucans," *Carbohydrate Polymers*, vol. 41, no. 3, pp. 249–258, 2000.

[18] G. L. Miller, "Use of dinitrosalicylic acid reagent for determination of reducing sugar," *Analytical Chemistry*, vol. 31, no. 3, pp. 426–428, 1959.

[19] T. Satoh, A. Inoue, and T. Ojima, "Characterization of an α-glucosidase, HdAgl, from the digestive fluid of Haliotis discus hannai," *Comparative Biochemistry and Physiology. Part B, Biochemistry & Molecular Biology*, vol. 166, no. 1, pp. 15–22, 2013.

[20] S. Bendicho, M. C. Trigueros, T. Hernández, and O. Martin, "Validation and comparison of analytical methods based on the release of p-nitrophenol to determine lipase activity in milk," *Journal of Dairy Science*, vol. 84, no. 7, pp. 1590–1596, 2001.

[21] C. H. Xia, Q. Dai, W. Fang, and H. S. Chen, "Research on the IR Spectrscopy of Kinds of Polysaccharide," *Journal Wuhan University Technology*, vol. 29, no. 1, pp. 45–47, 2007.

[22] C. J. Edge, T. W. Rademacher, M. R. Wormald et al., "Fast sequencing of oligosaccharides: the reagent-array analysis method," *Proceedings of the National Academy of Sciences of the United States of America*, vol. 89, no. 14, pp. 6338–6342, 1992.

[23] L. Johansson, L. Virkki, S. Maunu, M. Lehto, P. Ekholm, and P. Varo, "Structural characterization of water soluble β-glucan of oat bran," *Carbohydrate Polymers*, vol. 42, no. 2, pp. 143–148, 2000.

[24] B. C. Lehtovaara and F. X. Gu, "Pharmacological, structural, and drug delivery properties and applications of 1, 3-beta-glucans," *Journal of Agricultural and Food Chemistry*, vol. 59, no. 13, pp. 6813–6828, 2011.

[25] A. Idström, S. Schantz, J. Sundberg, B. F. Chmelka, P. Gatenholm, and L. Nordstierna, "13C NMR assignments of regenerated cellulose from solid-state 2D NMR spectroscopy," *Carbohydrate Polymers*, vol. 151, pp. 480–487, 2016.

[26] Y. Rong, N. Xu, B. Xie et al., "Sequencing analysis of β-glucan from highland barley with high performance anion exchange chromatography coupled to quadrupole time – Of – Flight mass spectrometry," *Food Hydrocolloids*, vol. 73, pp. 235–242, 2017.

[27] B. Du, F. M. Zhu, and B. J. Xu, "β-Glucan extraction from bran of hull-less barley by accelerated solvent extraction combined

with response surface methodology," *Journal of Cereal Science*, vol. 59, no. 1, pp. 95–100, 2014.

[28] A. Cavallero, S. Empilli, F. Brighenti, and A. M. Stanca, "High (1⟶3,1⟶4)-β-Glucan Barley Fractions in Bread Making and their Effects on Human Glycemic Respons," *Journal of Cereal Science*, vol. 36, no. 1, pp. 59–66, 2002.

[29] I. Wiege, M. Sluková, K. Vaculová, B. Panciková, and B. Wiege, "Characterization of milling fractions from new sources of barley for use in food industry," *Stärke*, vol. 68, no. 3-4, pp. 321–328, 2016.

[30] X. L. Zheng, L. M. Li, and Q. Wang, "Distribution and molecular characterization of β-glucans from hull-less barley bran, shorts and flour," *International Journal of Molecular Sciences*, vol. 12, no. 3, pp. 1563–1574, 2011.

[31] M. S. Izydorczyk, M. Jacobs, and J. E. Dexter, "Distribution and structural variation of nonstarch polysaccharides in milling fractions of hull-less barley with variable amylose content," *Cereal Chemistry*, vol. 80, no. 6, pp. 645–653, 2003.

[32] R. S. Bhatty, "β-Glucan and flour yield of hull-less barley," *Cereal Chemistry*, vol. 76, no. 2, pp. 314-315, 1999.

[33] S. F. Ma, Z. M. Diao, and B. F. Wu, "Production and Development Prospect of Qinghai *Hordeum Vulgare* L," *Journal of Anhui Agricultural Sciences*, vol. 34, no. 12, pp. 2661-2662, 2006.

[34] C. R. Dun and Y. H. Zhang, "The Scientific Practicality Technology~ of Using the Pesticides on Standardization Production with High Quality & Health Care Highland Barley-"Zang Qing No. 25"," *Tibetan J. Agri.Sci*, vol. 4, pp. 20–24, 2009.

[35] G. Šimić, D. Horvat, A. Lalić, D. Koceva Komlenić, I. Abičić, and Z. Zdunić, "Distribution of β-Glucan, Phenolic Acids, and Proteins as Functional Phytonutrients of Hull-Less Barley Grain," *Foods*, vol. 8, no. 12, p. 680, 2019.

[36] F. Zhu, B. Du, and B. J. Xu, "A critical review on production and industrial applications of beta-glucans," *Food Hydrocolloids*, vol. 52, pp. 275–288, 2016.

[37] H. Yuan, P. Lan, Y. He, C. Li, and X. Ma, "Effect of the Modifications on the Physicochemical and Biological Properties of β-Glucan—A Critical Review," *Molecules*, vol. 25, no. 1, p. 57.

[38] L. Mo, Y. Chen, W. Li et al., "Anti-tumor effects of (1⟶3)-β-d-glucan from Saccharomyces cerevisiae in S180 tumor-bearing mice," *International Journal of Biological Macromolecules*, vol. 95, pp. 385–392, 2017.

[39] J. M. Fouhse, J. Gao, T. Vasanthan, M. Izydorczyk, A. D. Beattie, and R. T. Zijlstra, "Whole-Grain Fiber Composition Influences Site of Nutrient Digestion, Standardized Ileal Digestibility of Amino Acids, and Whole-Body Energy Utilization in Grower Pigs," *The Journal of Nutrition*, vol. 147, no. 1, pp. 29–36, 2017.

[40] J. M. Fouhse, M. G. Gänzle, A. D. Beattie, T. Vasanthan, and R. T. Zijlstra, "Whole-Grain Starch and Fiber Composition Modifies Ileal Flow of Nutrients and Nutrient Availability in the Hindgut, Shifting Fecal Microbial Profiles in Pigs," *The Journal of Nutrition*, vol. 147, no. 11, pp. 2031–2040, 2017.

[41] M. Kinner, S. Nitschko, J. Sommeregger et al., "Naked barley—Optimized recipe for pure barley bread with sufficient beta- glucan according to the EFSA health claims," *Journal of Cereal Science*, vol. 53, no. 2, pp. 225–230, 2011.

[42] L. T. Tong, K. Zhong, L. Liu, X. Zhou, J. Qiu, and S. Zhou, "Effects of dietary hull-less barley β-glucan on the cholesterol metabolism of hypercholesterolemic hamsters," *Food Chemistry*, vol. 169, pp. 344–349, 2015.

[43] N. P. Fusté, M. Guasch, P. Guillen et al., "Barley β-glucan accelerates wound healing by favoring migration versus proliferation of human dermal fibroblasts," *Carbohydrate Polymers*, vol. 210, pp. 389–398, 2019.

[44] Y. Ning, D. Xu, X. Zhang et al., "β-glucan restores tumor-educated dendritic cell maturation to enhance antitumor immune responses," *International Journal of Cancer*, vol. 138, no. 11, pp. 2713–2723, 2016.

[45] Z. Yang, X. Xu, R. Singh et al., "Effect of amyloglucosidase hydrolysis on the multi-scale supramolecular structure of corn starch," *Carbohydrate Polymers*, vol. 212, pp. 40–50, 2019.

[46] X. Cao, C. Zhang, Y. Dong, P. Geng, F. Bai, and G. Bai, "Modeling of cooked starch digestion process using recombinant human pancreatic α-amylase and maltase-glucoamylase for in vitro evaluation of α-glucosidase inhibitors," *Carbohydrate Research*, vol. 414, pp. 15–21, 2015.

[47] J. L. Ríos, F. Francini, and G. R. Schinella, "Natural Products for the Treatment of Type 2 Diabetes Mellitus," *Planta Medica*, vol. 81, no. 12/13, pp. 975–994, 2015.

[48] H. Wen, B. Tang, A. J. Stewart et al., "Erythritol Attenuates Postprandial Blood Glucose by Inhibiting α-Glucosidase," *Journal of Agricultural and Food Chemistry*, vol. 66, no. 6, pp. 1401–1407, 2018.

[49] Y. Zhang, L. Luo, Z. Li, H. Li, X. Yao, and R. Luo, "Anti-Lipid Peroxidation,α-Glucosidase andα-Amylase Inhibitory Effects of the Extract of Capitula ofCoreopsis tinctoriaNutt. and Protection Effects on High-Fat/High-Sugar and Streptozotocin-Induced Type 2 Diabetes in Mice," *Chemistry & Biodiversity*, vol. 16, no. 12, p. e1900514, 2019.

[50] C. Serra-Barcellona, N. C. Habib, S. M. Honoré, S. S. Sánchez, and S. B. Genta, "Enhydrin Regulates Postprandial Hyperglycemia in Diabetic Rats by inhibition of α-Glucosidase Activity," *Plant Foods for Human Nutrition*, vol. 72, no. 2, pp. 156–160, 2017.

[51] K. Rehman, T. A. Chohan, I. Waheed, Z. Gilani, and M. S. H. Akash, "Taxifolin prevents postprandial hyperglycemia by regulating the activity of α-amylase: Evidence from an in vivo and in silico studies," *Journal of Cellular Biochemistry*, vol. 120, no. 1, pp. 425–438, 2019.

[52] K. Wang, L. Bao, K. Ma et al., "A novel class of α-glucosidase and HMG-CoA reductase inhibitors from Ganoderma leucocontextum and the anti-diabetic properties of ganomycin I in KK-A y mice," *European Journal of Medicinal Chemistry*, vol. 127, pp. 1035–1046, 2017.

[53] C. P. Gachons and P. Breslin, "Salivary Amylase: Digestion and Metabolic Syndrome," *Current Diabetes Reports*, vol. 16, no. 10, p. 102, 2016.

[54] S. Leuzinger, A. Steingötter, and L. Nyström, "Viscosity of Cereal β-Glucan in the Gastrointestinal Tract," *CHIMIA International Journal for Chemistry*, vol. 72, no. 10, pp. 733–735, 2018.

Hindawi
Advances in Polymer Technology
Volume 2020, Article ID 4789475, 9 pages
https://doi.org/10.1155/2020/4789475

Research Article

Melatonin-Loaded Nanoparticles for Enhanced Antidepressant Effects and HPA Hormone Modulation

Min Si,[1] Qianshu Sun,[1] Hongcheng Ding,[1] Chengcheng Cao,[2] Mingwei Huang,[1] Qian Wang,[1] Hua Yang,[3] and Yi Yao[1]

[1]*Department of Endocrine, Renmin Hospital, Hubei University of Medicine, Shiyan, Hubei 442000, China*
[2]*Department of Internal Medicine, Guoyao Dongfeng Maojian Hospital, Shiyan, Hubei 442008, China*
[3]*Department of Urology, Renmin Hospital, Hubei University of Medicine, Shiyan, Hubei 442000, China*

Correspondence should be addressed to Yi Yao; 278764942@qq.com

Min Si and Qianshu Sun contributed equally to this work.

Received 8 January 2020; Revised 8 March 2020; Accepted 7 April 2020; Published 9 May 2020

Guest Editor: Mingqiang Li

Background. The present work aims at formulating the melatonin-loaded nanoparticles (MTNPs) exhibiting the controlled-release and pH-sensitivity to repurpose the use of melatonin in the treatment of depressive-like behaviors and hypothalamus-pituitary-adrenal (HPA) axis dysregulation. *Methods*. MTNPs were characterized for the size, drug incorporation, and *in vitro* release in the different pH environments. Its merits were *in vivo* tested on the pinealectomized rats presenting the depressive-like behaviors and the abnormal HPA axis activity by calculating the improvement on saccharin preference, swimming immobility time, and the negative feedback of HPA axis. *Results*. Results revealed that MTNPs showed nanometer size, 15.77% of drug loading, 33.82% of encapsulation efficiency, the different controlled-release profiles in different pH environments (pH 1.2, pH 6.8, and pH 7.4), more sensitivity release in simulated intestinal fluid (pH 7.4) and blood (pH 6.8), and less sensitivity release in simulated gastric fluid (pH 1.2). Furthermore, MTNPs displayed better antidepressant actions in reducing the immobility time of forced swimming test, increasing the preference for saccharin, and sensitizing the blunt negative feedback of HPA axis, when compared to the free melatonin. *Conclusions*. The controlled-release nanoparticles is shown to be an effective improvement on the dosage form for melatonin, which is worthy of futuristic and complete evaluation.

1. Introduction

The released report by the World Health Organization (WHO) in 2017 shows that depression has become the most widespread and burdensome mental illness [1]. There are currently about 350 million patients worldwide, and it is projected that depression will be the most popular disease in the developing countries by 2022 [2, 3]. Melatonin (MT) is an endogenous bioactive substance which is mainly secreted by pineal gland [4]. Melatonin has a broad range of physiological activities, including body temperature regulation [5], nervous regulation [6], endocrine regulation [7], immune regulation [8], and hormone secretion [9]. Melatonin secretion decreases during the course of depression and increases after achieving remission, suggesting that the abnormality of melatonin plays a role in the pathogenesis of depression [10, 11]. As the deep understanding of neuroendocrine therapy of depression, melatonin has been found to have a certain effect on improving depressive-like behaviors [12, 13]. Boer et al. [14] reported that melatonin may be used as a novel antidepressant in clinical treatment of a variety of depression, especially in the treatment of major depressive disorder (MDD). Clinical studies showed that the plasma level of melatonin decreases in MDD patients [15]. In the preclinical studies evaluating the antidepression efficacy of melatonin, it was found that the immobility period of mice in the forced swimming test (FST) decreased in the dose-dependent manner after the daily administration of melatonin (2.5-10 mg/kg) in 3 to 6

days [16]. The administration of melatonin by intraperitoneal (0.1-30 mg/kg) or intracerebroventricular (0.001-0.1 nmol/site) route also reduced the immobility period in the tail suspension test (TST) [17]. Unpredictable chronic exposure to stress-induced high levels of serum corticosterone in mice; however, oral administration of exogenous melatonin for 5 weeks (1 and 10 mg/kg) decreased the higher serum corticosterone levels [18]. These studies provided the direct evidences supporting the hypothesis that the melatonin acts as an antidepressant, and melatonin might have regulatory roles in the activity of hypothalamus-pituitary-adrenal (HPA) axis [19–22].

After the oral administration, the blood concentration of the melatonin increases rapidly and then decreases rapidly with a short half-life of about 60 minutes in the blood and a low bioavailability of about 15% [23]. The pharmaceutical dosage forms are useful in the precision and rationalization of drug delivery, so as to realize the sustained and stable drug release and the long-term effective blood drug concentration, to avoid the fluctuation of peak-valley concentration, and to reduce the frequency of administration [24]. In addition, the effective dosage forms can also reduce the side effects of drugs, such as the protection on gastrointestinal tract [25, 26]. By using the polymer nanometer materials and the drug-loaded nanoparticle technology, the melatonin compound is wrapped and attached to the nanoparticle, so as to slow down the dissolution rate and improve the drug absorption *in vivo* [27–29]. The design of the dosage form for melatonin has been a new strategy to improve its curative effect in various diseases [30, 31].

In this study, the gelatin, polylactic acid (PLA), and chitosan were used to prepare melatonin-loaded nanoparticles (MTNPs). Then the effects on the depressive behaviors and the hormone secretion *in vivo* in the pinealectomized rats were compared between the administration of MTNPs and free melatonin.

2. Material and Methods

2.1. Preparation of Nanoparticles Loaded with Melatonin. The absolute ethyl alcohol solution containing melatonin (0.5 mL) and the aqueous solution containing gelatin (0.5 mL) were mixed to give a clear solution under 50°C. Then the solution was dropped slowly into the dichloromethane solution containing PLA (9.0 mL) followed with 1 h stirring and 1 h ultrasonic vibration to obtain the white emulsion I. The final concentrations of melatonin, gelatin, and PLA were 0.4%, 0.1%, and 1.2%, respectively. Emulsion I was slowly dropped into the dichloromethane solution (30 mL) containing Span-80 and Tween-80, followed with 1 h stirring, subsequent heating at 39°C to evaporate 30 mL of dichloromethane, and 1 h ultrasonic vibration to obtain the yellow emulsion II (10 mL). Emulsion II was slowly dropped into the aqueous solution (50 mL) containing 0.25% chitosan and 1% acetic acid, followed with 1 h stirring and 1 h ultrasonic vibration to obtain the white emulsion III. Emulsion III was stirred to volatilize the organic solvent for 24 h at 30°C and then was centrifuged at 5000 rpm/min to obtain the precipitate. The precipitate was washed by deionized water, centrifuged for three times, and dried under vacuum decompression to obtain the product of melatonin-loaded nanoparticles (MTNPs). The procedure is schematically shown in Figure 1.

2.2. Measurement of Particle Size, PDI, and Morphology. The hydrodynamic diameter and polydispersity index (PDI) value of MTNPs were analyzed by dynamic light scattering (DLS). Five measurements were taken using the Zetasizer Nano analyzer from Malvern Instruments (Malvern, UK). Transmission electron microscopy (Philips CM12, Eindhoven, Netherlands) was applied to evaluate the morphology of MTNPs. The particle sizes of MTNPs were determined by measuring the diameters with the ImageJ measurement tool from a number of TEM images.

2.3. Determination of Drug Incorporation. One milligram per milliliter of MTNPs in dichloromethane was diluted for 100 times by 30% ethanol. Then the water phase was collected by stirring thoroughly and standing for 20 min. The absorbance of the water phase was measured by a UV spectrophotometer at 278 nm. The melatonin concentration was calculated according to the standard curve of melatonin at 278 nm. The encapsulation efficiency (EE) and drug loading (DL) of melatonin were calculated by the equations (1) and (2), respectively, as

$$\text{Encapsulation efficiency}\,(\%) = \frac{\text{Mass of melatonin in nanoparticles} \times 100\%}{\text{Mass of initial melatonin used}} \quad (1)$$

$$\text{Drug loading}\,(\%) = \frac{\text{Mass of melatonin in nanoparticles} \times 100\%}{\text{Mass of nanoparticles}} \quad (2)$$

2.4. In Vitro Release Study. The phosphate-buffered salines (PBS) of pH 7.4, pH 6.8, and pH 1.2 were prepared and used for simulating blood, intestinal fluid, and gastric fluid, respectively. 10 mL of 0.1 mg/mL MTNPs was placed into a dialysis bag. The dialysis bag was put into 50 mL PBS with different pH and then was stirred magnetically at 37°C. At the indicated interval, 1 mL of sample PBS was removed for analysis, and the new PBS (1 mL) was supplemented. The absorbance of the sample PBS was measured by a UV spectrophotometer at 278 nm to plot the cumulative release curve. All the drug release studies were performed in triplicates.

2.5. Animals and Groups. Male Wistar rats were housed in a temperature-controlled room (25°C) under the light/dark

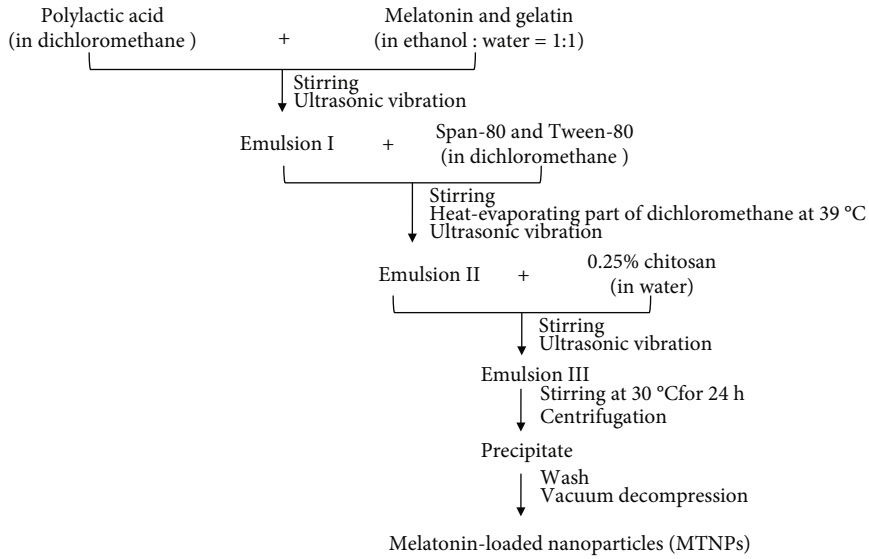

Figure 1: Schematic presentation of the preparation of melatonin-loaded nanoparticles (MTNPs).

cycle (12 : 12 h, lights on at 08:00 a.m.). Experimental procedures were approved by the Animal Ethics Committee of Hubei University of Medicine. The rats were randomly divided into four groups with 10 rats per group: the sham group, normal rats treated with vehicle; the Pin group, pinealectomized rats; the Pin-MT group, pinealectomized rats treated with free melatonin; and the Pin-MTNPs group, pinealectomized rats treated with MTNPs.

2.6. Surgery and Treatment. The surgery was performed following the method previously reported by Hoffmann and Reiter [32]. Briefly, the rats were anesthetized and adapted to a stereotactic apparatus, and then the hair on the top of the head was scraped and removed. Transverse incision was cut between two ears to expose the sagittal suture and lambdoidal suture. A piece of rectangular bone was peeled off from the dura using a pointed dental burr with the sagittal suture as the symmetry axis. After the dura was cut off, the sagittal venous sinus was ligated on two sides and was cut off at the middle, and then the pineal gland under the sagittal venous sinus was removed. After using the Gelfoam sponge to stem the bleeding, the rectangular bone was returned to its original position, and then the skin was sutured. The sham rats encountered the same procedure except that the pineal gland was removed. After 7 days of surgery, the rats could be used in the study.

Free melatonin or MTNPs, dissolved in saline containing 4% ethanol, was injected subcutaneously at 17:00 p.m. at the dose of $10\,\mathrm{mg\,kg^{-1}}$ and $60\,\mathrm{mg\,kg^{-1}}$, respectively. The doses ensured the equal amount of melatonin given to rats. The sham group and Pin group were injected the equal volume of saline subcutaneously. The administration was kept for 4 weeks.

2.7. Saccharin Preference Test. During the last four days of the administration, all rats were given two weighed bottles, one containing pure water and the other one containing 0.1% saccharin solution. After 24 h, the two bottles were weighed to calculate the consumption of drinking water using the difference before and after detection. The consumption for 4 consecutive days was recorded, and then the taste preference was calculated by the equation (3) as

$$\text{Preference for saccharin}\,(\%) = \frac{\text{Mass of saccharin solution} \times 100\%}{\text{Total mass of drinking water (saccharin + water)}} \tag{3}$$

2.8. Forced Swimming Test (FST). After 1 h of final administration, the rats in each group were put into a glass cylinder (ϕ of 20 cm, height of 40 cm) filled with 24 cm of water at 25°C. Each rat was allowed to freely swim for 6 min, and the immobility time was recorded in the last 4 min. The water was replaced before each test to avoid the interference of fecal and odor from each rat.

2.9. Hormone Assay. Before the dexamethasone (Dex) challenge, the blood of each rat was collected and the basal level of corticosterone (CORT) was detected by ELISA. Then Dex (30 mg/kg) was injected intraperitoneally to inhibit the secretion of CORT *in vivo*. After 2 h of injection, the blood sample was collected and the CORT level was measured again.

2.10. Statistical Analyses. All statistical analyses were performed using SPSS (version 12.0.1, SPSS Inc., Chicago, IL, United States). Data are expressed as the means ± SD, and $P < 0.05$ was considered statistically significant. One-way ANOVA was used followed by the post hoc test for group difference.

3. Result

3.1. Basic Characteristics of the MTNPs. The hydrodynamic particle size of MTNPs was 96.12 ± 13.53 nm, and the PDI value was 0.203 ± 0.01. The TEM image showed the morphology of MTNPs as the spherical shape (Figure 2). Histograms indicated the particle size distribution of MTNPs (Figure 3). MTNPs had the particle size distribution between 23 and 106 nm, and the average size was 54.71 ± 17.29 nm. The particle size between 39.45 and 55.90 nm accounted for 51.6% and was the relatively concentrated size range.

3.2. Encapsulation Efficiency and Drug Loading of MTNPs. The drug loading of MTNPs produced from 3 batches was 15.77 ± 1.74% in Figure 4. The encapsulation efficiency from 3 batches was 33.82 ± 0.53%.

3.3. In Vitro Release Profiles of MTNPs in Different pH Solutions. The release kinetics of melatonin was evaluated in three different *in vitro* environments (pH 1.2, simulated gastric fluid; pH 6.8, simulated intestinal fluid; and pH 7.4, simulated blood). In the simulated gastric fluid (pH 1.2), the melatonin release rate was the slowest and less than 20.3% at 8 h (Figure 5(a)). In the simulated intestinal environment (pH 6.8) and blood (pH 7.4), the degradation of PLA and chitosan was accelerated, so as that melatonin release rates increased to 81.4% (Figure 5(b)) and 96.7% (Figure 5(c)) at 8 h, respectively.

3.4. Effect of MTNPs on Saccharin Preference in the Pinealectomized Rats. The preference for saccharin is an indicator for evaluating anhedonia. As shown in Figure 6, the preference for saccharin of each group was similar before pinealectomy ($P > 0.05$). After pinealectomy, the rats of the Pin group showed statistically significantly decreased preference for saccharin ($P < 0.05$), indicating that the pinealectomized rats have the depressive-like behavior. After the various administrations, both MT and MTNPs could increase the preference for saccharin in the pinealectomized rats. As compared to the MT group, the preference for the saccharin of rats in the MTNPs group was higher, but no significant statistical significance was observed.

3.5. Effect of MTNPs in FST. As shown in Figure 7, at week 0, all groups did not present the notably difference of the immobility time ($P > 0.05$). After the pinealectomy and administration for 4 weeks, the significant difference of the immobility time between the Pin group and sham group was shown ($P < 0.001$), representing the induced depression to rats. However, both treatment groups with MT and MTNPs significantly reduced the immobility time in FST compared to the Pin group. Moreover, the FST result showed that MTNPs exhibited an improvement more significantly to MT ($P < 0.05$).

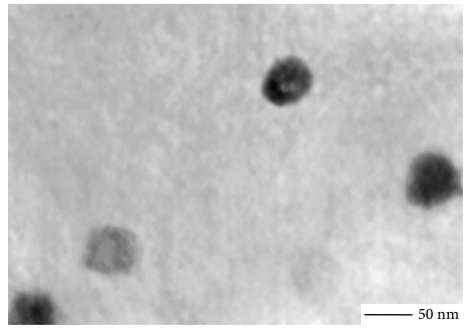

Figure 2: Transmission electron microscope image of melatonin-loaded nanoparticles (MTNPs).

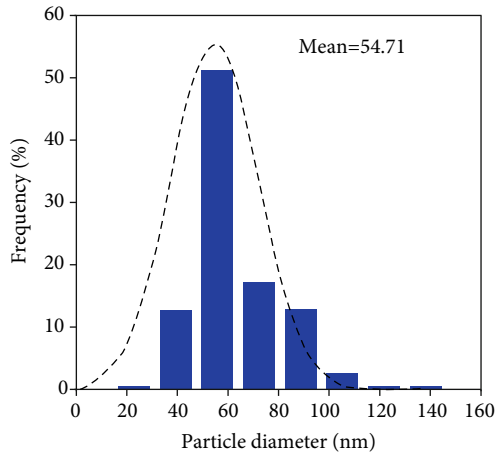

Figure 3: The particle size distribution for melatonin-loaded nanoparticles (MTNPs).

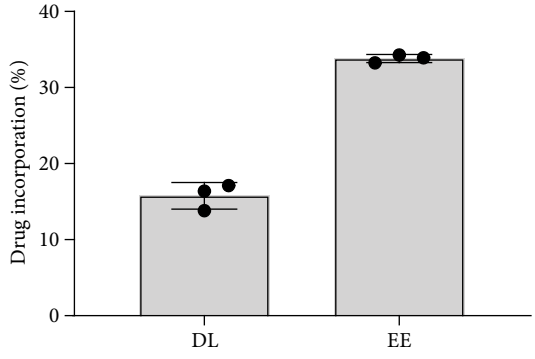

Figure 4: Drug loading and encapsulation efficiency of melatonin-loaded nanoparticles (MTNPs). DL: drug loading; EE: encapsulation efficiency.

3.6. Effect of MTNPs in HPA Axis Activity. Plasma CORT levels in basal condition (before the Dex injection) and after the Dex injection were observed (Figure 8). Before the Dex injection, the basal plasma levels of CORT of the pinealectomized rats were higher than that of sham rats, but there was no statistical difference ($P > 0.05$). After the Dex injection,

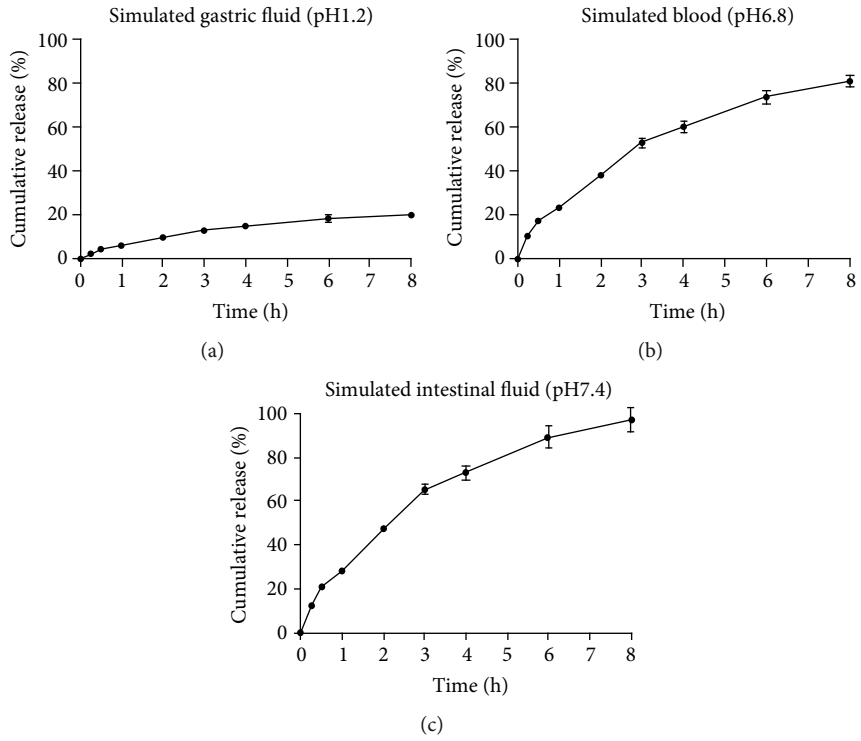

Figure 5: *In vitro* release profile of melatonin-loaded nanoparticles (MTNPs). (a) pH 1.2, simulated gastric fluid. (b) pH 6.8, simulated blood. (c) pH 7.4, simulated intestinal fluid.

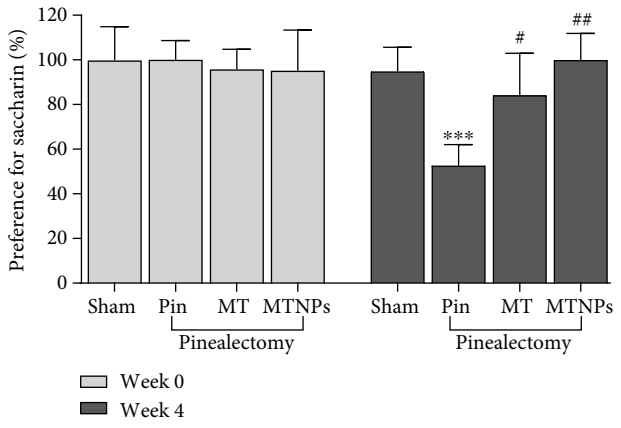

Figure 6: Effect of melatonin-loaded nanoparticles (MTNPs) on saccharin preference. $^{***}P < 0.001$ vs. the sham group; $^{\#}P < 0.05$ and $^{\#\#}P < 0.01$ vs. the Pin group. Pin: pinealectomized rats; MT: melatonin.

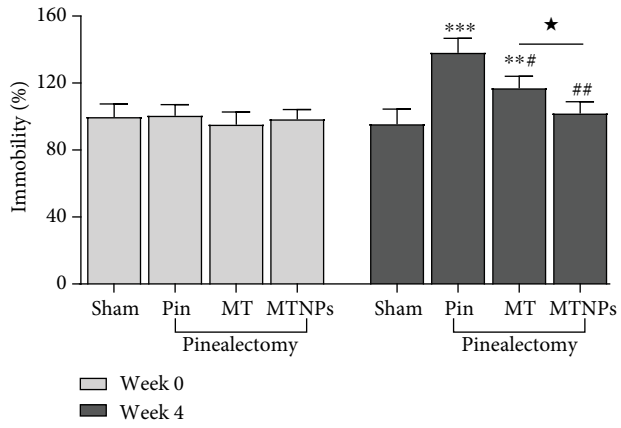

Figure 7: Effect of melatonin-loaded nanoparticles (MTNPs) on the immobility time in forced swimming test. $^{**}P < 0.01$ and $^{***}P < 0.001$ vs. the sham group; $^{\#}P < 0.05$ and $^{\#\#}P < 0.01$ vs. the Pin group; $^{\star}P < 0.05$ vs. the MT group. Pin: pinealectomized rats; MT: melatonin.

the plasma CORT levels of all rats decreased significantly ($P < 0.05$), presenting the negative feedback mechanism of the HPA axis. When analyzing the CORT levels, it was observed that the CORT level of the Pin group was significantly higher than that of the sham group ($P < 0.05$). When compared with the Pin group, the CORT level of the MT group showed a decreased tendency without statistical difference ($P > 0.05$); however, the CORT level of the MTNP group significantly decreased ($P < 0.05$). When analyzing the decreased fold of the CORT level, it was observed that the decreased fold of the Pin group was significantly lower than that of the sham group, indicating the pinealectomy impaired the negative feedback of the HPA axis. Both rats in the MT group and MTNP group showed a notable decrease in the CORT level and significant increased change fold ($P < 0.05$), indicating that MT and MTNPs could improve the impaired negative feedback. When compared with the decrease fold of CORT in the MT group, the decrease fold in the MTNP group was significantly higher ($P < 0.05$), suggesting that MTNPs improved the damaged HPA axis more than MT.

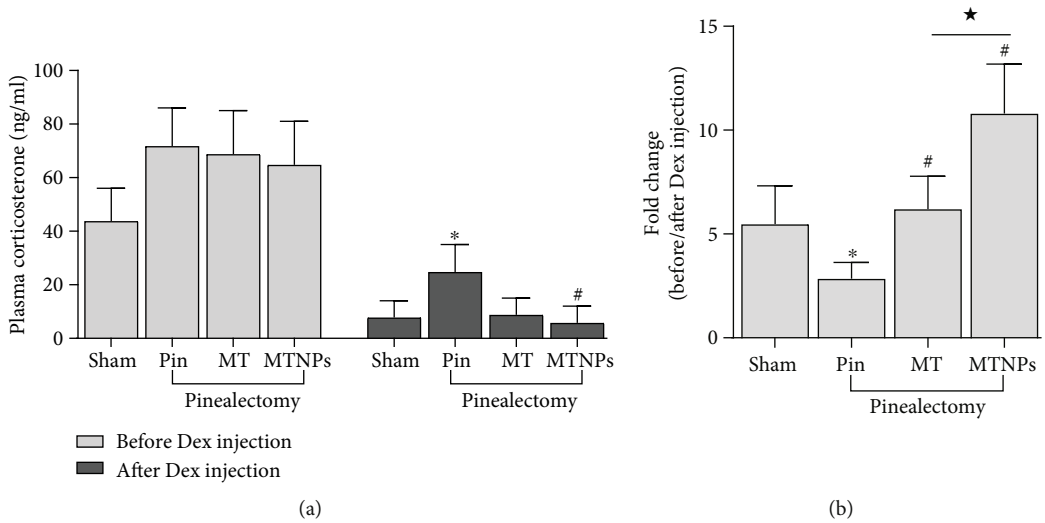

FIGURE 8: Effect of melatonin-loaded nanoparticles (MTNPs) on the plasma corticosterone level. (A) The plasma corticosterone level. (b) The decreased fold change of plasma corticosterone. $^{*}P < 0.05$ vs. the sham group; $^{\#}P < 0.05$ vs. the Pin group; $^{\bigstar}P < 0.05$ vs. the MT group. Pin: pinealectomized rats; MT: melatonin.

4. Discussion

Although melatonin is metabolized rapidly *in vivo* and has a short half-life of about 60 minutes [23], the controlled-release dosage forms can delay the elimination time of melatonin residue *in vivo,* prolong the retention time, and maintain the physiological effect of melatonin. There are various carriers used to prepare the controlled-release dosage forms of melatonin, such as silica [33], diamine polymer [33], hydroxypropyl methylcellulose phthalate [34], alginate [35], and poly(lactic-co-glycolic acid) (PLGA) [28, 36]. In the study, PLA and chitosan are used as the controlled-release carriers for melatonin, and gelatin is used as dispersant. The hydrophilic gelatin is nontoxic and nonantigenic protein and plays the role of emulsifying and stabilizing agent. PLA has good biodegradability, good biocompatibility [37, 38], and no toxicity [39]. PLA is hydrolyzed fully to lactic acid, the natural substance of human body, which in turn is converted into carbon dioxide and is expelled from the lung [40, 41]. Chitosan is a natural poly(glucosamine) with good biocompatibility, biodegradability [42], and bioactivities [43]. According to the characteristics of the polymers, the technique of emulsification-solvent evaporation is adopted to prepare the melatonin-loaded nanoparticles (MTNPs). The melatonin compound is adsorbed, embedded, and attached by PLA and chitosan, rather than chemically linked to these polymers, thus not destroying the nature of melatonin. In the process of drug production, encapsulation efficiency and particle size are the two most essential features. The purpose of the drug determines the particle size. The particle size of MTNPs is 54.71 nm, lower than 100 nm, which is favorable for the feasible purpose of penetrating the blood-brain barrier. However, the encapsulation efficiency of MTNPs is low. The improvement of encapsulation efficiency might be adjusted from the stirring speed, the polymers concentration, and the solvent evaporation temperature. The process of the controlled-release [44] of melatonin from MTNPs firstly displays as the detachment and diffusion of melatonin adsorbed on the surface of MTNPs. Secondly, PLA and chitosan which are located at the outer layer of MTNPs proceed swelling, and the swelling causes a plurality of micropores on the surface of MTNPs. These actions promote the gradual dissolution and release of melatonin through the micropores and also promote the permeation of solvent into the inside of MTNPs through the micropores and thereby accelerate again the dissolution and release of melatonin. Finally, the carrier materials of MTNPs are degraded and eroded, so that the melatonin is completely released. This process plays the role in maintaining the controlled release of melatonin.

It has been reported in literatures that melatonin has binding sites in the gastrointestinal tract of mammals, and the density of these binding sites differs in different regions of the intestines. Lee et al. demonstrated that the binding site density follows the descending order: ileum, jejunum > duodenum, colon > cecum > esophagus [45]. Poon et al. found that the binding sites of human body are mainly located in the colon, cecum, appendix, and few ileus [46]. Bubenik et al. [47] compared that the binding site density in the intestines is overall higher than that in the stomach. In the present study, according to the tissue distribution characteristics of melatonin binding sites, we prepared the MTNPs with the slow release of melatonin in the stomach and the rapid release in the intestines. The melatonin can be rapidly absorbed along with the mass release of melatonin in the intestinal tissue because of the large absorption surface area of the intestinal tissue. Thereby, this action could improve the bioavailability of melatonin. Due to the removal of the pineal gland, the *in vivo* level of melatonin is much lower. The controlled release of melatonin can maintain the retention time of melatonin *in vivo* and keep the drug effect for a long time; therefore it plays a part in simulating the physiological function of pineal gland.

Delagrange et al. [48] showed that melatonin and its receptor agonists are antidepressants. The plasma level of melatonin in the first-episode depression patients was lower than that in healthy people during the onset of depression and was also significantly lower than that in first-episode schizophrenia patients. This suggested that the decline of melatonin level is particularly closely related to the depression. Delagrange et al. also demonstrated that the plasma level of melatonin increases significantly as the depressive symptoms remission after treatment with antidepressants. In clinical trials, it is also reported that the serum level of melatonin was abnormal in MDD patients, although the level does not distinguish the severity of depression [49]. Oral administration with exogenous melatonin is useful for treating depression. Melatonin has an antidepressant effect on mouse undergoing the repeated forced swimming tests [16]. Melatonin also has the function in improving the mood of MDD patients and has good safety, good tolerance, and no adverse side effects [50]. In our study, it demonstrated that the pinealectomy produces depressive-like behaviors in rats, including significantly reducing saccharin preference in Wistar rats and prolonging the swimming immobility time. These indexes could be effectively improved by administration of exogenous melatonin [51]. Our results are consistent with the reported results. Furthermore, compared to the effects of free melatonin, MTNPs are more effective on the shortening of the immobility time and show a tendency to increase the saccharin preference, suggesting a better drug effect by MTNPs. It is speculated that this better improvement might be due to the controlled release of melatonin from MTNPs, which in turn maintains the plasma level for a long time.

Previous studies have shown that the melatonin has the inhibitory effect on the hypothalamus-pituitary-target axis activity (gonad, thyroid, and adrenal) [52, 53]. Moreover, melatonin also has an improved effect on the immune system, which causes the changes of cytokine secretion and regulates neuroendocrine. This makes the effect of melatonin more diverse and complicated on neuroendocrine, especially in many inconsistent results on the HPA axis [52]. For example, the reduction of melatonin caused by the pinealectomy has no significant effect on the CORT secretion in male rats [54], while the secretion in female rats is upregulated [55]. In the present study, the deficit of melatonin due to the pinealectomy showed a tendency to enhance the basal plasma CORT levels before Dex injection although there was no statistical difference among the four groups. However, after the Dex injection, the decrease fold of the CORT level in the Pin group was significantly less than that in the sham group, indicating that the absence of the pineal gland destroys the plastic change of the HPA axis activity. The higher CORT level in the pinealectomized rats is also consistent with their symptoms of depressive-like behaviors. The administration of the exogenous-free melatonin or MTNPs could augment the decrease folds of CORT after the Dex injection, make the plasticity of HPA axis sensitive, and improve the negative feedback of the HPA axis. Moreover, MTNPs could improve the negative feedback mechanism more than that of the free melatonin, which proves that the long-term release of melatonin might help to alleviate the overall decrease of melatonin caused by pinealectomy.

5. Conclusion

In the current work, the controlled-release nanoparticles loaded with melatonin in the treatment of pinealectomized rats were proven. These nanoparticles can effectively encapsulate melatonin and protect melatonin from degradation. The melatonin-loaded nanoparticles present both pH-sensitivity and the controlled release. It helps the rapid release and absorption in the intestinal tissue to improve melatonin bioavailability. Then the *in vivo* results prove that the nanoparticles treatment effectively improve the depression-like behaviors and the HPA axis hormone secretion in the pinealectomized rats. The study however is in its infancy, and it still requires the optimization of encapsulation efficiency and needs the complete drug efficacy evaluation using the chronic unpredictable mild stress-induced rats.

Data Availability

All raw data used and analyzed during the current study can be available from the corresponding author on reasonable request.

Conflicts of Interest

The authors have no conflicts of interest regarding the publication of this paper.

Authors' Contributions

Min Si and Qianshu Sun contributed equally to this work.

References

[1] GBD 2017 Disease and Injury Incidence and Prevalence Collaborators, "Global, regional, and national incidence, prevalence, and years lived with disability for 354 diseases and injuries for 195 countries and territories, 1990-2017: a systematic analysis for the Global Burden of Disease Study 2017," *The Lancet*, vol. 392, no. 10159, pp. 1789–1858, 2018.

[2] "Depression and Other Common Mental Disorders Global Health Estimates," 2017, https://www.who.int/mental_health/management/depression/prevalence_global_health_estimates/en/.

[3] N. Sartorius, "Depression and diabetes," *Dialogues in Clinical Neuroscience*, vol. 20, no. 1, pp. 47–52, 2018.

[4] K. Karolczak and C. Watala, "The mystery behind the pineal gland: melatonin affects the metabolism of cholesterol," *Oxidative Medicine and Cellular Longevity*, vol. 2019, Article ID 4531865, 8 pages, 2019.

[5] R. Lok, M. J. van Koningsveld, M. C. M. Gordijn, D. G. M. Beersma, and R. A. Hut, "Daytime melatonin and light independently affect human alertness and body temperature," *Journal of Pineal Research*, vol. 67, no. 1, article e12583, 2019.

[6] B. S. Alghamdi, "The neuroprotective role of melatonin in neurological disorders," *Journal of Neuroscience Research*, vol. 96, no. 7, pp. 1136–1149, 2018.

[7] I. Mishra, R. M. Knerr, A. A. Stewart, W. I. Payette, M. M. Richter, and N. T. Ashley, "Light at night disrupts diel patterns of cytokine gene expression and endocrine profiles in zebra

finch (Taeniopygia guttata)," *Scientific Reports*, vol. 9, no. 1, p. 15833, 2019.

[8] N. Ma, J. Zhang, R. J. Reiter, and X. Ma, "Melatonin mediates mucosal immune cells, microbial metabolism, and rhythm crosstalk: a therapeutic target to reduce intestinal inflammation," *Medicinal Research Reviews*, vol. 40, no. 2, pp. 606–632, 2020.

[9] E. Scarinci, A. Tropea, G. Notaristefano et al., ""Hormone of darkness" and human reproductive process: direct regulatory role of melatonin in human corpus luteum," *Journal of Endocrinological Investigation*, vol. 42, no. 10, pp. 1191–1197, 2019.

[10] M. Fava, S. D. Targum, A. A. Nierenberg et al., "An exploratory study of combination buspirone and melatonin SR in major depressive disorder (MDD): a possible role for neurogenesis in drug discovery," *Journal of Psychiatric Research*, vol. 46, no. 12, pp. 1553–1563, 2012.

[11] M. Valdés-Tovar, R. Estrada-Reyes, H. Solís-Chagoyán et al., "Circadian modulation of neuroplasticity by melatonin: a target in the treatment of depression," *British Journal of Pharmacology*, vol. 175, no. 16, pp. 3200–3208, 2018.

[12] E. H. Taniguti, Y. S. Ferreira, I. J. V. Stupp et al., "Neuroprotective effect of melatonin against lipopolysaccharide-induced depressive-like behavior in mice," *Physiology & Behavior*, vol. 188, pp. 270–275, 2018.

[13] J. Liu, S. J. Clough, and M. L. Dubocovich, "Role of the MT1and MT2melatonin receptors in mediating depressive- and anxiety-like behaviors in C3H/HeN mice," *Genes, Brain, and Behavior*, vol. 16, no. 5, pp. 546–553, 2017.

[14] J. A. den Boer, F. J. Bosker, and Y. Meesters, "Clinical efficacy of agomelatine in depression: the evidence," *International Clinical Psychopharmacology*, vol. 21, Supplement 1, pp. S21–S24, 2006.

[15] J. M. Bumb, F. Enning, J. K. Mueller et al., "Differential melatonin alterations in cerebrospinal fluid and serum of patients with major depressive disorder and bipolar disorder," *Comprehensive Psychiatry*, vol. 68, pp. 34–39, 2016.

[16] V. Raghavendra, G. Kaur, and S. K. Kulkarni, "Anti-depressant action of melatonin in chronic forced swimming-induced behavioral despair in mice, role of peripheral benzodiazepine receptor modulation," *European Neuropsychopharmacology*, vol. 10, no. 6, pp. 473–481, 2000.

[17] M. Mantovani, R. Pertile, J. B. Calixto, A. R. Santos, and A. L. Rodrigues, "Melatonin exerts an antidepressant-like effect in the tail suspension test in mice: evidence for involvement of N-methyl-D-aspartate receptors and the L-arginine-nitric oxide pathway," *Neuroscience Letters*, vol. 343, no. 1, pp. 1–4, 2003.

[18] B. C. Detanico, A. L. Piato, J. J. Freitas, F. L. Lhullier, M. P. Hidalgo, and W. Caumo, "Antidepressant-like effects of melatonin in the mouse chronic mild stress model," *European Journal of Pharmacology*, vol. 607, no. 1-3, pp. 121–125, 2009.

[19] M. Garrido, J. Espino, D. González-Gómez et al., "The consumption of a Jerte Valley cherry product in humans enhances mood, and increases 5-hydroxyindoleacetic acid but reduces cortisol levels in urine," *Experimental Gerontology*, vol. 47, no. 8, pp. 573–580, 2012.

[20] Y. H. Wu, J. N. Zhou, R. Balesar et al., "Distribution of MT1 melatonin receptor immunoreactivity in the human hypothalamus and pituitary gland: colocalization of MT1 with vasopressin, oxytocin, and corticotropin-releasing hormone," *The Journal of Comparative Neurology*, vol. 499, no. 6, pp. 897–910, 2006.

[21] A. Cagnacci, R. Soldani, and S. S. Yen, "Melatonin enhances cortisol levels in aged but not young women," *European Journal of Endocrinology*, vol. 133, no. 6, pp. 691–695, 1995.

[22] A. Turi, F. Di Prospero, O. Marasca, C. Romanini, F. Foschi, and G. Campanari, "Pineal gland hypothalamus-pituitary-adrenal axis relationships," *Acta Europaea Fertilitatis*, vol. 17, no. 3, pp. 205-206, 1986.

[23] R. L. DeMuro, A. N. Nafziger, D. E. Blask, A. M. Menhinick, and J. S. Bertino Jr., "The absolute bioavailability of oral melatonin," *Journal of Clinical Pharmacology*, vol. 40, no. 7, pp. 781–784, 2000.

[24] H. L. Gao and X. G. Jiang, "The progress of novel drug delivery systems," *Yao Xue Xue Bao*, vol. 52, no. 2, pp. 181–188, 2017.

[25] C. Andrade, "Sustained-release, extended-release, and other time-release formulations in neuropsychiatry," *The Journal of Clinical Psychiatry*, vol. 76, no. 8, pp. e995–e999, 2015.

[26] S. Talkar, S. Dhoble, A. Majumdar, and V. Patravale, "Transmucosal nanoparticles: toxicological overview," *Advances in Experimental Medicine and Biology*, vol. 1048, pp. 37–57, 2018.

[27] F. Blažević, T. Milekić, M. D. Romić et al., "Nanoparticle-mediated interplay of chitosan and melatonin for improved wound epithelialisation," *Carbohydrate Polymers*, vol. 146, pp. 445–454, 2016.

[28] D. Ç. Altındal and M. Gümüşderelioğlu, "Melatonin releasing PLGA micro/nanoparticles and their effect on osteosarcoma cells," *Journal of Microencapsulation*, vol. 33, no. 1, pp. 53–63, 2016.

[29] A. Priprem, J. R. Johns, S. Limsitthichaikoon, W. Limphirat, P. Mahakunakorn, and N. P. Johns, "Intranasal melatonin nanoniosomes: pharmacokinetic, pharmacodynamics and toxicity studies," *Therapeutic Delivery*, vol. 8, no. 6, pp. 373–390, 2017.

[30] J. Rybka, K. Kędziora-Kornatowska, D. Kupczyk, M. Muszalik, M. Kornatowski, and J. Kędziora, "Antioxidant effect of immediate- versus sustained-release melatonin in type 2 diabetes mellitus and healthy controls," *Drug Delivery*, vol. 23, no. 3, pp. 814–817, 2016.

[31] S. Hatem, M. Nasr, N. H. Moftah, M. H. Ragai, A. S. Geneidi, and S. A. Elkheshen, "Clinical cosmeceutical repurposing of melatonin in androgenic alopecia using nanostructured lipid carriers prepared with antioxidant oils," *Expert Opinion on Drug Delivery*, vol. 15, no. 10, pp. 927–935, 2018.

[32] R. A. Hoffman and R. J. Reiter, "Rapid pinealectomy in hamsters and other small rodents," *The Anatomical Record*, vol. 153, no. 1, pp. 19–21, 1965.

[33] A. M. Khattabi, W. H. Talib, and D. A. Alqdeimat, "The effect of polymer length on the *in vitro* characteristics of a drug loaded and targeted silica nanoparticles," *Saudi Pharmaceutical Journal*, vol. 26, no. 7, pp. 1022–1026, 2018.

[34] Y. Li, X. Zhao, Y. Zu et al., "Melatonin-loaded silica coated with hydroxypropyl methylcellulose phthalate for enhanced oral bioavailability: preparation, and in vitro-in vivo evaluation," *European Journal of Pharmaceutics and Biopharmaceutics*, vol. 112, pp. 58–66, 2017.

[35] E. E. Uchendu and E. R. Joachim Keller, "Melatonin-loaded alginate beads improve cryopreservation of yam (Dioscorea alata and D. cayenensis)," *Cryo Letters*, vol. 37, no. 2, pp. 77–87, 2016.

[36] L. G. Martins, N. M. Khalil, and R. M. Mainardes, "PLGA nanoparticles and Polysorbate-80-coated PLGA nanoparticles

increase the *in vitro* antioxidant activity of melatonin," *Current Drug Delivery*, vol. 15, no. 4, pp. 554–563, 2018.

[37] S. Farah, D. G. Anderson, and R. Langer, "Physical and mechanical properties of PLA, and their functions in widespread applications—a comprehensive review," *Advanced Drug Delivery Reviews*, vol. 107, pp. 367–392, 2016.

[38] K. S. Anderson, K. M. Schreck, and M. A. Hillmyer, "Toughening polylactide," *Polymer Reviews*, vol. 48, no. 1, pp. 85–108, 2008.

[39] B. Tyler, D. Gullotti, A. Mangraviti, T. Utsuki, and H. Brem, "Polylactic acid (PLA) controlled delivery carriers for biomedical applications," *Advanced Drug Delivery Reviews*, vol. 107, pp. 163–175, 2016.

[40] F. Mohamed and C. F. van der Walle, "Engineering biodegradable polyester particles with specific drug targeting and drug release properties," *Journal of Pharmaceutical Sciences*, vol. 97, no. 1, pp. 71–87, 2008.

[41] J. Liu and Y. Liu, "Preparation and application of polylactide," *Sheng Wu Yi Xue Gong Cheng Xue Za Zhi*, vol. 18, no. 2, pp. 285–7, 295, 2001, 295.

[42] B. R. Rizeq, N. N. Younes, K. Rasool, and G. K. Nasrallah, "Synthesis, bioapplications, and toxicity evaluation of chitosan-based nanoparticles," *International Journal of Molecular Sciences*, vol. 20, no. 22, p. 5776, 2019.

[43] F. Liaqat and R. Eltem, "Chitooligosaccharides and their biological activities: a comprehensive review," *Carbohydrate Polymers*, vol. 184, pp. 243–259, 2018.

[44] M. A. Mohammed, J. T. M. Syeda, K. M. Wasan, and E. K. Wasan, "An overview of chitosan nanoparticles and its application in non-parenteral drug delivery," *Pharmaceutics*, vol. 9, no. 4, p. 53, 2017.

[45] P. P. Lee and S. F. Pang, "Melatonin and its receptors in the gastrointestinal tract," *Biological Signals*, vol. 2, no. 4, pp. 181–193, 1993.

[46] A. M. Poon, P. H. Chow, A. S. Mak, and S. F. Pang, "Autoradiographic localization of 2[125I]iodomelatonin binding sites in the gastrointestinal tract of mammals including humans and birds," *Journal of Pineal Research*, vol. 23, no. 1, pp. 5–14, 1997.

[47] G. A. Bubenik, S. F. Pang, R. R. Hacker, and P. S. Smith, "Melatonin concentrations in serum and tissues of porcine gastrointestinal tract and their relationship to the intake and passage of food," *Journal of Pineal Research*, vol. 21, no. 4, pp. 251–256, 1996.

[48] P. Delagrange, J. Atkinson, and J. A. Boutin, "Therapeutic perspectives for melatonin agonists and antagonists," *Journal of Neuroendocrinology*, vol. 15, no. 4, pp. 442–448, 2003.

[49] J. Rabe-Jabłońska and A. Szymańska, "Diurnal profile of melatonin secretion in the acute phase of major depression and in remission," *Medical Science Monitor*, vol. 7, no. 5, pp. 946–952, 2001.

[50] M. A. Serfaty, D. Osborne, M. J. Buszewicz, R. Blizard, and P. W. Raven, "A randomized double-blind placebo-controlled trial of treatment as usual plus exogenous slow-release melatonin (6 mg) or placebo for sleep disturbance and depressed mood," *International Clinical Psychopharmacology*, vol. 25, no. 3, pp. 132–142, 2010.

[51] S. Moyanova, A. De Fusco, I. Santolini et al., "Abnormal hippocampal melatoninergic system: a potential link between absence epilepsy and depression-like behavior in WAG/Rij rats?," *International Journal of Molecular Sciences*, vol. 19, no. 7, p. 1973, 2018.

[52] I. Kostoglou-Athanassiou, D. F. Treacher, M. J. Wheeler, and M. L. Forsling, "Melatonin administration and pituitary hormone secretion," *Clinical Endocrinology*, vol. 48, no. 1, pp. 31–37, 1998.

[53] R. Konakchieva, Y. Mitev, O. F. Almeida, and V. K. Patchev, "Chronic melatonin treatment and the hypothalamo-pituitary-adrenal axis in the rat: attenuation of the secretory response to stress and effects on hypothalamic neuropeptide content and release," *Biology of the Cell*, vol. 89, no. 9, pp. 587–596, 1997.

[54] M. E. Diatroptov, S. M. Slesarev, and E. V. Slesareva, "Characteristics of 4-day Infradian biorhythms in mature male Wistar rats after pinealectomy," *Bulletin of Experimental Biology and Medicine*, vol. 163, no. 1, pp. 109–113, 2017.

[55] T. F. Ogle and J. I. Kitay, "Effects of pinealectomy on adrenal function *in vivo* and *in vitro* in female rats," *Endocrinology*, vol. 98, no. 1, pp. 20–24, 1976.

Hindawi
Advances in Polymer Technology
Volume 2020, Article ID 6582825, 13 pages
https://doi.org/10.1155/2020/6582825

Research Article

Nuclear-Targeting Delivery of CRISPRa System for Upregulation of β-Defensin against Virus Infection by Dexamethasone and Phenylalanine Dual-Modified Dendrimer

Mingxiang Zuo,[1] **Xiaoxia Li**,[1] **Shuang Liu**,[2] **Bin Chen**,[3] **and Du Cheng**[1]

[1]*PCFM Lab of Ministry of Education, School of Materials Science and Engineering, Sun Yat-sen University, Guangzhou 510275, China*
[2]*Zhongshan School of Medicine, Sun Yat-sen University, Guangzhou 510275, China*
[3]*Department of Orthopaedics and Traumatology, Nanfang Hospital, Southern Medical University, Guangzhou 510515, China*

Correspondence should be addressed to Bin Chen; chb@smu.edu.cn and Du Cheng; chengdu@mail.sysu.edu.cn

Received 27 January 2020; Revised 14 March 2020; Accepted 23 March 2020; Published 4 May 2020

Guest Editor: Liyuan Zhang

The dual-modified dendrimer containing dexamethasone (DET) and phenylalanine (Phe) was prepared to deliver plasmid DNA encoding dCas9 and single-guide RNA (sgRNA) for specific upregulation of β-defensin. DET and Phe moieties synergistically enhanced the transfection efficiency and reduced cytotoxicity of dendrimers. Combination of three sgRNAs targeting β-defensin gene demonstrated higher activation efficacy of β-defensin than any single sgRNA and combinations of any two sgRNAs, showing an efficient inhibition of virus infection and replication. The titer of vesicular stomatitis virus (VSV) in the cells treated with dCas9-sgRNA targeting β-defensin was reduced by about 100-fold compared to that of cells treated with dCas9-scramble sgRNA (dCas9-scr sgRNA). *In vivo* experiments demonstrated that the DET- and Phe-modified dendrimer effectively delivered plasmid DNA encoding dCas9 protein into the airway epithelium, inducing β-defensin expression. Delivery of the CRISPR activation system by a dendrimer modified with DET and Phe was a promising approach against viral disease.

1. Introduction

Identification of small molecules and vaccines for antiviral therapy is time consuming and laborious. In particular, little knowledge about emerging viruses makes it difficult to develop specific drugs or vaccines in a short time. Therefore, an alternative approach is needed against viral diseases. Except for targeting viral genome and protein, targeting host factors (i.e., innate system, adaptive immune apparatus, and other host genes) is an effective strategy to prohibit virus infection or replication. For example, maraviroc prevents cell entry of HIV and HBV virus by blocking human cellular protein CCR [1, 2]. However, only a few small molecules targeting host cellular proteins have been screened to treat viral diseases. Recently, emerging genetic manipulation technologies, including zinc-finger nucleases (ZNF), transcription activator-like effector nucleases (TALEN), and clustered regularly interspaced short palindromic repeats/Cas9 (CRISPR/Cas9) system, have provided powerful tools for inhibiting or activating host gene expression [3–5].

Among these technologies, the CRISPR/Cas9 system, a complex of Cas9 protein with single-guide RNA (sgRNA, a combination of the transactivating CRISPR RNA and spacer transcript CRISPR RNA), has attracted considerable attention because of its multiple gene regulation manners. sgRNA directs Cas9 protein to cleave its complementary double-stranded DNA. Upon cleavage by Cas9 protein, the target site is repaired *via* nonhomologous end joining (NHEJ) or homology-directed repair (HDR) mechanisms. Moreover, CRISPR activation (CRISPRa) and interference (CRISPRi) systems based on inactive Cas9 (dCas9), which specifically bind to DNA sequence without cleavage activity, were exploited to repress and induce interested gene expression [6, 7]. As for CRISPRa, transcription activator VP16 or activation domain p65 was combined with dCas9 to transactivate multiple gene transcriptions. For instance, the

CRISPRa/dCas9 approach was used to activate endogenous APOBEC3G and APOBEC3B to prevent HIV infection [8].

Defensin is one kind of key factors of the innate immunity system, being first in line against microorganism pathogens [9, 10]. The predominant expression of β-defensins was detected in the barrier epithelial cells and was considered an ideal antiviral agent. However, high cost and easy degradation of human β-defensin limit its clinical use. Fortunately, the CRISPRa system provides an alternative approach against virus by upregulating β-defensin and thereby activating innate immunity.

Plasmid DNA encoding dCas9 protein and sgRNA is unable to enter into cells by themselves. Therefore, utilization of DNA delivery vectors is of great necessity. Viral vectors (e.g., adenovirus, adeno-associated virus (AAV), and lentiviral viruses) showed high delivery efficiency, but their limited DNA packaging capacity and potential chromosome integration remain to be major hurdles [11, 12]. In contrast, nonviral vectors are readily available, cost effective, and can efficiently incorporate siRNAs or Cas9-sgRNA plasmids into one nanosystem [13, 14]. Moreover, some vectors such as dendrimers were easily modified with moieties including hydrophobic groups and nuclear localization signal molecules, which significantly enhanced transfection efficiency [15, 16]. Hydrophobic phenylalanine conjugated on the surface of dendrimer enhanced cell uptake [17]. Dexamethasone can bind to the nucleic membrane and thereby facilitate DNA transport into the nucleus [18]. Cationic polymers modified with DET remarkably increased gene expression levels [19]. However, dual-modification with Phe and DET is rarely used to enhance transfection efficiency. Moreover, there are few issues about the antivirus strategy by enhancing the β-defensin expression using nonviral delivery of the CRISPRa system.

Herein, we developed a DET and Phe dual-modified cationic dendrimer G4 (Phe)-DET for the delivery of CRISPRa plasmids targeting β-defensin. *In vitro* and *in vivo* experiments were performed to confirm antiviral effects of G4 (Phe)-DET dendrimer-based nonviral CRISPRa.

2. Materials and Method

2.1. Materials. PAMAM dendrimer G4, phenylalanine, and trifluoroacetic acid (TFA) were obtained from Sigma Aldrich (St. Louis, USA). 1-Hydroxybenzotriazole (HOBT), O-benzotriazole-N,N,N′,N′-tetramethyl-uronium-hexafluorophosphate (HBTU), dexamethasone, methanesulfonyl chloride, and 2-iminothiolane·HCl (Traut's reagent) were purchased from J&K Scientific (Beijing, China). The cells including human lung adenocarcinoma A549, human kidney 293T, human bronchial epithelial cell 16HBE cell, and mouse neuroblastoma N_2a cell were purchased from ATCC. Vesicular stomatitis virus (VSV) was from ATCC (stain; Indiana, USA). Dulbecco's modified eagle medium (DMEM), penicillin-streptomycin, fetal bovine serum (FBS), and Dulbecco's phosphate-buffered saline (PBS) were purchased from Gibco BRL (Carlsbad, USA). Biological reagents were purchased from Life Technologies. Plasmid pSP-dCas9-VPR was a gift from Prof. George Church (Addgene plasmid # 63798) and the activator was VPR, a tripartite activator composed of activation domains of VP64, p65, and Rta. Plasmid pphU6-gRNA was obtained from Prof. Charles Gersbach (Addgene plasmid # 53188). sgRNAs were prepared using T7 High Yield RNA Synthesis Kit (New England Biolabs, NEB). Primers and sgRNA sequences are shown in Table S1.

2.2. Synthesis of Dendrimer. The phenylalanine-modified generation 4.0 (G4) PAMAM dendrimer was synthesized mainly by amidation between the carboxyl group of phenylalanine and the surface amino groups of G4 PAMAM dendrimer. Briefly, G4 PAMAM dendrimer (0.5 g, 0.035 mmol) was dissolved in anhydrous DMF (5 mL) under nitrogen gas protection. Boc-phenylalanines were added at different molar ratios (carboxyl group of phenylalanine: surface amino groups of G4 PAMAM dendrimer) of 25% and 50%, followed by the addition of 1-hydroxybenzotriazole (HOBT) and O-benzotriazole-N,N,N′,N′-tetramethyl-uronium-hexafluorophosphate (HBTU) at 1.25 molar equivalents of carboxyl in Boc-phenylalanine, serving as the condensation reagent and catalyst to the reaction. After stirring at room temperature for 2 d, the reaction solution was precipitated three times in the diethyl-ether to obtain yellow solid precipitate noted as G4 (Phe-Boc). To deprotect the tert-butoxycarbonyl (Boc) groups, the G4 (Phe-Boc) dendrimer dissolved in dichloromethane was added to 5 mL trifluoroacetic acid (TFA) for 6 h with continuous magnetic stirring. After removal of TFA by rotary evaporation, the resulting crude products were again dissolved in DMF and purified by three rounds of precipitation in acetone. Finally, the yellow product G4 (Phe) was obtained by vacuum drying.

DET, a glucocorticoid, was used to modify the PAMAM dendrimer. First, the mesylate-activated DET was prepared by substituting the terminal hydroxyl group of DET for mesylate. Under nitrogen protection, DET (0.11 g, 0.269 mmol) dissolved in anhydrous pyridine (5 mL) was added to methanesulfonyl chloride at 2 molar equivalent and then incubated in an ice bath for 12 h with stirring, followed by the addition of ice deionized water to precipitate crude products. The mesylate-activated DET was purified by recrystallization from ethanol-acetic ether. Next, Traut's reagent and dexamethasone mesylate in 2.5 mL anhydrous DMSO at 0.015 mmol (8 equiv. to G4 (Phe-Boc)) were slowly added to G4 (Phe-Boc) in 2.0 mL anhydrous DMSO under nitrogen protection. The mixture was stirred for 12 h at room temperature. Excessive amounts of cold ethyl acetate were used to precipitate the reaction products. The mentioned product was dissolved in 5 mL TFA and stirred for 6 h, followed by precipitation in ethyl ether. This precipitating procedure was repeated three times to obtain pale yellow G4 (Phe)-DET. The yield of G4 (Phe)-DET was 105 mg.

2.3. Preparation of Polyplexes. To prepare polyplexes for plasmid delivery, the plasmid solution (1 μg/μL) was added to the G4 (Phe) or G4 (Phe)-DET solution at various N/P ratios. The mixture solution was pipetted approximately 50 times and then allowed to stand for 35 min.

2.4. Characterization. ^{1}H-NMR spectra were recorded on a Varian 400 MHz spectrometer using D_2O and DMSO d_6 as the solvent at room temperature. To determine macromolecular weight distributions of the polymers, gel permeation chromatography (GPC) was performed, using an acetic acid buffer system (pH 5.0) as the mobile phase at a flow rate of 1.0 mL/min. The GPC system was equipped with a Waters 515 pump, an ultrahydrogel™ 500 column, an ultrahydrogel™ 250 column, and a Waters 2410 differential refractive index detector. Samples flowed through ultrahydrogel ™ 500 column and ultrahydrogel ™ 250 column in sequence. Size of polyplexes was determined with the utilization of dynamic light scattering (DLS). The polyplex solutions were filtered through a 450 nm filter. Measurements were performed at 25°C on 90 Plus/BI-MAS equipment (Malvern Panalytical, Malvern, United Kingdom). Data were collected on an autocorrelator with a 90° detection angle of scattered light. The measurement results were recorded as the mean ± standard deviation (SD) of three independent measurements. Transmission electron microscopy (TEM) observations of the polyplexes were conducted using a Philips CM120 transmission electron microscope (Philips, Eindhoven, the Netherlands) at an accelerating voltage of 80 kV. Samples were prepared by drying a drop (10 μL) of the sample solution on a copper grid coated with amorphous carbon. For the sample staining, a small drop of uranyl acetate solution (1.5 wt% in water) was dropped on the copper grid and after 1 min blotted off with filter paper. Finally, the grid was dried overnight in a desiccator prior to TEM observation.

2.5. Gel Retardation Assay. To assess the plasmid DNA-binding ability of G4 $(Phe)_{25\%}$, G4 $(Phe)_{50\%}$, and G4 $(Phe)_{50\%}$-DET, gel electrophoresis was performed (Bio-Rad Laboratories, Inc., USA). Dendrimers were first dissolved in PBS (pH 7.4). Then, plasmids were added to the dendrimer solution to prepare polyplexes on preset N/P ratios, followed by standing for 35 min at room temperature. The polyplexes were loaded into 1% agarose gels with GoldenView (Beijing BLKW Biotechnology Co., Ltd., China). The retardation of plasmid DNA mobility was detected with UV light and imaged on DNR Bio-Imaging Systems (DNR Bio-Imaging System Ltd., Israel).

2.6. Cell Viability Assay. A549, 293T, and N_2a cells were cultured in DMEM containing 10% fetal bovine serum (FBS) in a humidified atmosphere of 5% CO_2 at 37°C. The cells were seeded into 96-well plates at a density of 1×10^3 cells/well. After incubating overnight at 37°C, cells were further incubated with Lipofectamine 2000, G4 $(Phe)_{25\%}$, G4 $(Phe)_{50\%}$, and G4 $(Phe)_{50\%}$-DET, which were combined with plasmid-GFP at various concentrations for 48 h, and cell viability was measured using MTT assay. Briefly, cell culture medium was replaced with 100 μL fresh DMEM containing 10 μL MTT solution (5 mg/mL in PBS) and then incubated for an additional 3 h at 37°C. After discarding the medium, 100 μL DMSO was added to dissolve the generated substrate for 15 min. The absorbance at 570 nm was measured using a Tecan Infinite F200 (Crailsheim, Germany). All experiments were conducted in triplicate.

2.7. Confocal Laser Scanning Microscopy (CLSM). A549, 293T, and N_2a cells were seeded in 35 mm glass-bottom dishes in 2 mL of DMEM containing 10% FBS at a density of 1×10^3 per plate. After incubation for 24 h, the medium was replaced with fresh opti-MEM containing polyplexes. The nuclei were stained with Hoechst 33342 (Beyotime Biotech, China) for 15 min. The cells were incubated at 37°C and imaged at designated times using a Zeiss LSM 710 confocal laser scanning microscope (Carl Zeiss, Oberkochen, Germany). GFP and Hoechst 33342 were excited at 488 and 352 nm and detected at 515 and 460 nm, respectively.

2.8. Quantity of Gene Expression. The expression of β-defensin in the transfected A549, 293T, and N_2a cells was evaluated at the mRNA level. Total RNA was extracted from cells using the RNeasy Micro Kit (Qiagen Inc., USA). The first-strand cDNA was synthesized using RNase H reverse transcriptase and random primers according to the manufacturer's protocol (Invitrogen, USA). cDNA (1 μg) was synthesized from the total RNA using PrimeScript™ RT reagent Kit (Takara, Japan). The mRNA expression of β-defensin was quantified with real-time PCR System using a FastStart Universal SYBR Green Master (ROX) Kit (Roche, Switzerland). The mRNA level of β-actin was also measured as an internal normalization standard. The primer and probe sequences are listed in Table S1. The real-time PCR program was run on a StepOnePlus Real-time PCR System (ABI, USA) at the thermal cycling conditions of 95°C for 10 min, followed by 40 cycles of 95°C for 30s, 58°C for 15 s, and 68°C for 15 s.

2.9. In Vitro Prevention of VSV Infection. A549 cells were seeded in 12-well plates at a density of 3×10^5 cells per well and incubated in DMEM at 37°C under a humidified atmosphere of 5% CO_2. After incubation overnight, the medium was replaced with fresh medium containing polyplexes. The amount of G4 $(Phe)_{50\%}$-DET was complexed with plasmids encoding dCas9 and sgRNA (1 μg) at N/P of 8. After incubation with polyplexes for 24 h, VSV was added to the medium at a titer of 100. The status of virus infection was detected by flow cytometry and inverted fluorescence microscopy. The culture supernatant was serially diluted 10-fold with DMEM and inoculated into the cells in 6-well plates for virus plaque assay. After 3 d of cultivation, titration of VSV was determined. All measurements were conducted three times for statistical analysis.

After being washed thrice with PBS, cells were harvested by trypsinization, centrifuged at 1,500 rpm for 5 min, and resuspended in 500 μL PBS. A Gallios flow cytometer (Beckman Coulter, California, USA) was used to evaluate the quantitative transfection efficiency by using a 488 nm laser for excitation and emission fluorescence of Alexa Fluor® 515 collected through a TRITC filter. For the evaluation of the GFP gene expression after the incubation with polyplexes, the cells were harvested according to the abovementioned method and subjected to flow cytometry. Typically,

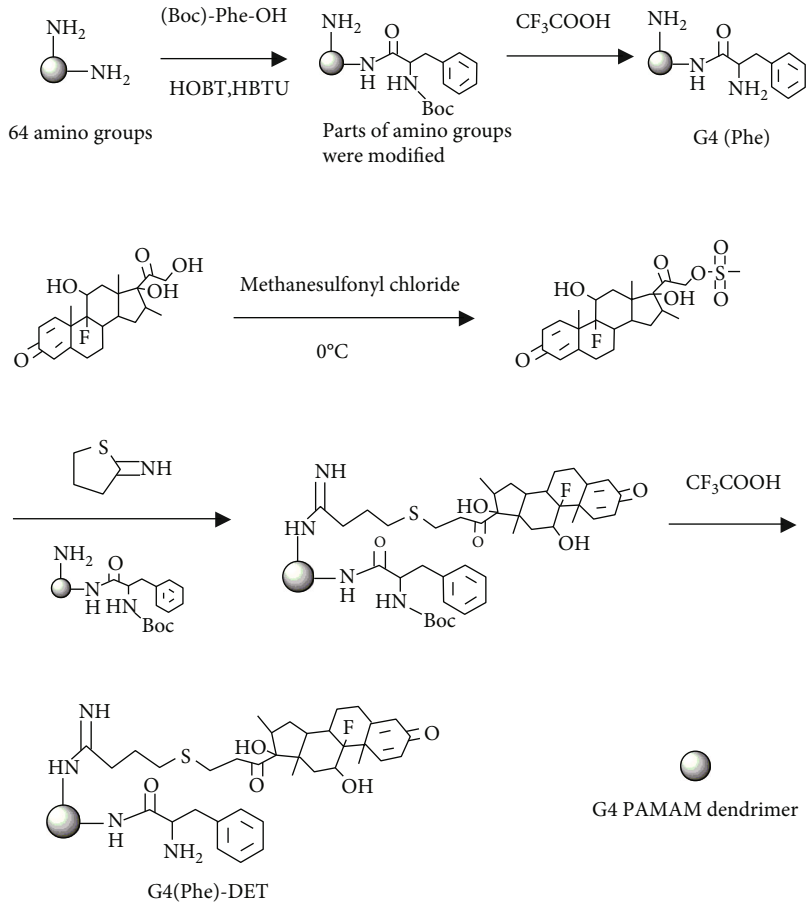

Figure 1: Synthetic route of G4 (Phe) and G4 (Phe)-DET.

cultured cells without transfection were used as controls for background calibration. Kaluza software (Version 1.2, Beckman Coulter, Inc. USA) was used to analyze the data.

2.10. In Vivo Studies. Female BALB/C mice (6–8 weeks old) were purchased from Guangdong Medical Laboratory Animal Center and kept in SPF animal center of School of Life Sciences, Sun Yat-sen University. All surgical interventions and postoperative animal care were conducted in accordance with the guidelines of the Council for the Purpose of Control and Supervision of Experiments on Animals, the Ministry of Health, and the government of China. After anesthetization via the tail vein by pentobarbital sodium at a dose of 50 mg/kg, the mice were administered polyplexes through the bronchus. The lungs were excised and subjected to detect the expression of the defensin gene. For the molecular biology assays, lung tissues were homogenized after being frozen in liquid nitrogen. Total RNA was extracted and analyzed as described in Section 2.8.

2.11. Histology and Immunohistochemistry. Mice were sacrificed, and their lungs were fixed in 4% paraformaldehyde for at least 24 h to obtain paraffin sections (2 μm) or frozen sections (5 μm). The paraffin sections were stained with H&E, and the images of the lung were assessed for the toxic effect in different treatment groups. The immunofluorescence staining for frozen sections was described briefly as follow: after blocking with 5% BSA for 0.5 h at 37°C, the frozen tissue sections were incubated with rabbit polyclonal primary antibodies for β-defensin (1 : 100 dilution in PBS/Tween; Cell Signaling Technology, Danvers, USA) and mouse monoclonal antibodies for Cas9 (Abcam, UK) overnight at 4°C. Then, AF647-labeled secondary antibody and AF488-labeled secondary antibody (Abcam, UK) were used to mark the β-defensin and dCas9 protein, respectively. After labeling the nuclei with DAPI, the tissue sections were scanned under CLSM.

2.12. Statistics. All experiments were carried out at least in triplicates. All data was indicated as mean ± standard deviation (SD). The statistical significance was determined by two-sided Student's t-test using Prism 5.0 ($^{*}p < 0.05$, $^{**}p < 0.01$, and $^{***}p < 0.001$).

3. Results

3.1. Preparation and Characterization of Dendrimer and Polyplex. DET- and Phe-modified dendrimers were prepared (Figure 1). First, Boc-protected Phe moieties were conjugated to dendrimer G4 *via* amidation between carboxyl groups of

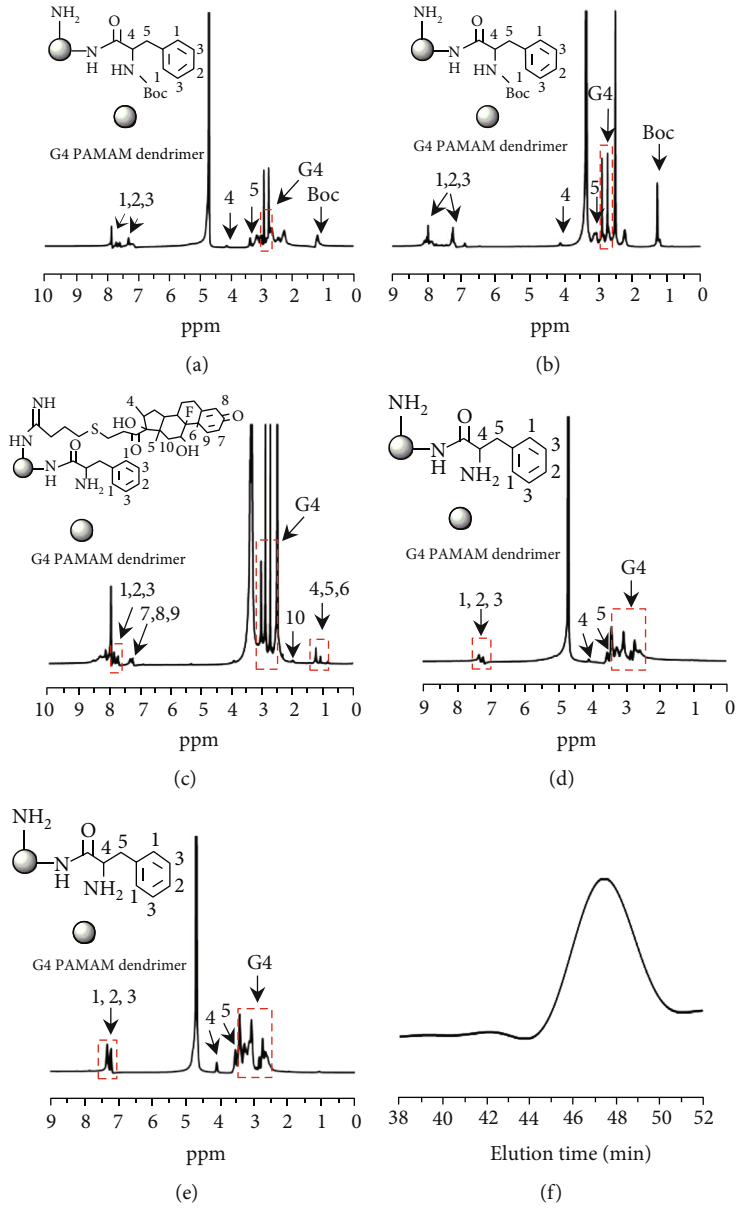

FIGURE 2: (a) ^{1}H-NMR spectra of G4 (Phe-Boc)$_{25\%}$, (b) G4 (Phe-Boc)$_{50\%}$, (c) G4 (Phe)$_{50\%}$-DET, (d) G4 (Phe)$_{25\%}$, and (e) G4 (Phe)$_{50\%}$. (f) GPC spectrum of G4 (Phe)$_{50\%}$-DET.

Boc-phenylalanine and facial amino groups of dendrimer at the molar ratios of 0.25 and 0.5, followed by deprotection of the Boc groups. The products were denoted as G4 (Phe)$_{25\%}$ and G4 (Phe)$_{50\%}$. Dexamethasone mesylate (DET-Mes) was introduced onto the surface of G4 (Phe-Boc) in the presence of Traut's reagent (2-iminothiolane hydrochloride). Finally, dendrimer G4 (Phe)-DET was obtained after removing the Boc groups, which was confirmed by the disappearance of the characteristic peak attributing to Boc at 1.2-1.4 ppm in the ^{1}H-NMR spectrum (Figure 2). DET-Mes was synthesized by conjugating a sulfonyl group with DET. The mentioned products were characterized by ^{1}H-NMR and GPC. The characteristic resonance peaks of the G4 dendrimer scaffold (C**H**$_2$ at 2.65-3.10 ppm) and phenylalanine (C**H** at 4.05-4.20 ppm, C**H**$_2$ at 3.5-3.75 ppm, and C**H** on the benzene ring of phenylalanine at 7.20-7.90 ppm) were observed, indicating successful synthesis of dendrimer G4 (Phe). Appearance of characteristic resonance peaks (0.9-1.3 ppm, CH_3, and 7.0-7.3 ppm, C**H** in dexamethasone) demonstrated that DET was conjugated with G4 (Phe). Composition of products was calculated according to the integration value of characteristic peaks attributing to G4 and Phe at 7.20-7.90 ppm, respectively. Conversion of the amino group in G4 (Phe)$_{25\%}$ and G4 (Phe)$_{50\%}$ was 22% and 47%, respectively. In the GPC chromatogram, G4 (Phe)$_{50\%}$ modified with DET (named as G4 (Phe)$_{50\%}$-DET) showed a unimodal molecular weight distribution (Figure 2(f)).

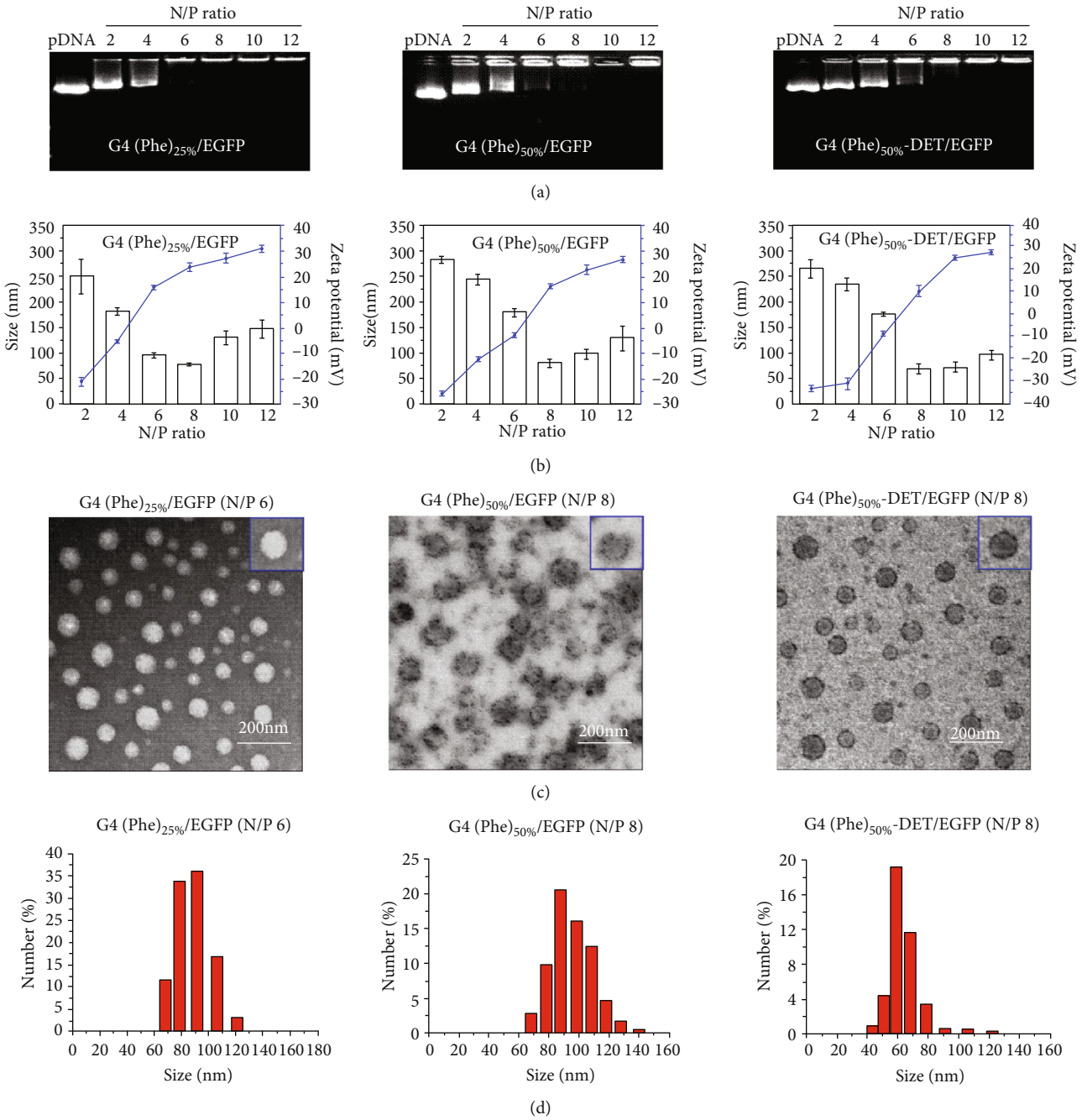

FIGURE 3: (a) Electrophoretic mobility of EGFP plasmid in agarose gel after complexing with G4 $(Phe)_{25\%}$, G4 $(Phe)_{50\%}$, and G4 $(Phe)_{50\%}$-DET at various N/P ratios. (b) Sizes and zeta potentials of G4 $(Phe)_{25\%}$/EGFP, G4 $(Phe)_{50\%}$/EGFP, and G4 $(Phe)_{50\%}$-DET/EGFP complexes at different N/P ratios. (c) Transmission electron microscopy (TEM) images and (d) DLS of G4 $(Phe)_{25\%}$/EGFP at N/P of 6, G4 $(Phe)_{50\%}$/EGFP at N/P of 8, and G4 $(Phe)_{50\%}$-DET/EGFP at N/P of 8. Results are presented as the mean ± SD ($n = 3$).

Complexation of plasmids with various dendrimers was evaluated by gel retardation assay. Disappearance of the DNA band in agarose indicates full neutralization of the negative charge of plasmid [20, 21]. As shown in Figure 3, G4 $(Phe)_{25\%}$ completely retarded DNA migration above N/P ratio of 6, but the dendrimer G4 $(Phe)_{50\%}$ achieved complete retardation above N/P ratio of 8, indicating that Phe modification reduced the DNA complexation ability of the dendrimer due to the charge shielding effect of the Phe hydrophobic benzene ring and the low surface charge density [17, 22]. The modification of DET has no significant impact on the DNA complexation ability of dendrimer G4 $(Phe)_{50\%}$-DET. Furthermore, sizes and zeta potentials of polyplexes under various N/P ratios were investigated by dynamic light scattering (DLS). As shown in Figure 3(b), zeta potentials of all dendrimers/EGFP complexes were converted to positive

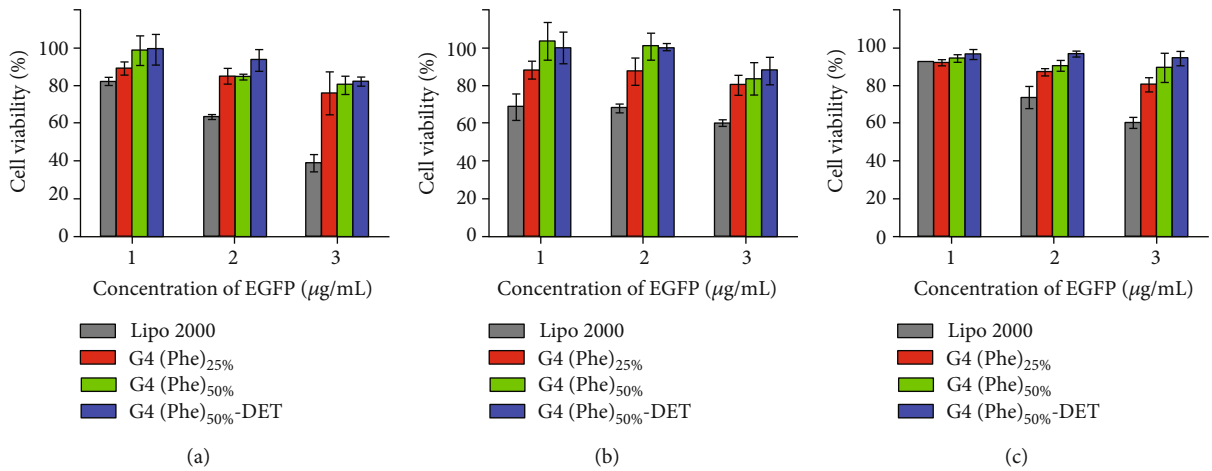

Figure 4: Cell viability of dendrimers to (a) human kidney 293T cells, (b) mouse neuroblastoma N_2a cells, (c) and human lung adenocarcinoma A549 cells. Incubation time: 48 h. Dose: 55.6 μM. Complexes were prepared at N/P of 6 for G4 $(Phe)_{25\%}$/EGFP, N/P of 8 for G4 $(Phe)_{50\%}$/EGFP, and N/P of 8 for G4 $(Phe)_{50\%}$-DET/EGFP, respectively. The concentrations of EGFP plasmid were 1, 2, and 3 μg/mL, respectively.

from negative when N/P ratio was above 6, and sizes were kept constant. At N/P ratio of 8, the zeta potentials of G4 $(Phe)_{25\%}$/EGFP complexes, G4 $(Phe)_{50\%}$/EGFP complexes, and G4 $(Phe)_{50\%}$-DET/EGFP complexes were around +23, +16, and +10 mV, respectively. At N/P ratio of 8, G4 $(Phe)_{50\%}$-DET/EGFP complexes had a smaller size than other complexes. With the excessive input of polymer (at higher N/P ratios), complexes held more positive charge and swelled maybe due to the electrostatic repelling effect between the positively charged chains. Consequently, size of G4 $(Phe)_{50\%}$-DET/EGFP complexes increased to 93.9 nm at N/P of 12. The sizes and zeta potentials of G4 $(Phe)_{50\%}$/EGFP and G4 $(Phe)_{25\%}$/EGFP complexes showed similar trends. TEM images showed that three complexes were sphere with a uniform size around 70-80 nm (Figure 3(c)), which was in line with that determined by dynamic light scattering (DLS) (Figure 3(d)).

3.2. Cytotoxicity and Cell Uptake. Although high positive surface charge is favorable for cell uptake of polyplexes, it also leads to apparent cytotoxicity to cells. Hence, it is necessary to balance these two factors. Introducing a hydrophobic moiety such as phenylalanine on the surface of dendrimer can effectively reduce its cytotoxicity and increase its affinity to cells [17]. As expected, Phe modification significantly decreased the cytotoxicity of G4 dendrimers to 293T, N_2a, and A549 cells (Figure 4). The dendrimer modified with Phe and DET slightly increased cell viability when compared with Phe-modified dendrimers. Notably, the single and dual modification with Phe and DET both enhanced transfection efficiency at various levels. In this study, the transfection efficiency of various dendrimers was evaluated in 293T, N_2a, and A549 cells using EGFP- (enhanced green fluorescence protein-) encoding plasmid as a reporter (Figure 5). The enhancement of transfection efficiency was attributed to two reasons: (1) the interaction between hydrophobic phenylalanine and the hydrophobic region of the cell membrane resulted in the destabilization of the cell membrane, thereby promoting translocation of the plasmid across the cell membrane and (2) DET guided plasmid into the nucleus [18]. The highest transfection efficiency was recorded in the cells receiving dendrimer modified with both Phe and DET, indicating that the dual modification synergistically enhanced transfection efficiency.

3.3. Antivirus Effect of CRIPSR/dCas9 by Upregulating β-Defensin. Several plasmids carrying sequences encoding sgRNA targeting the β-defensin promoter region were designed and delivered to human cells (A549, 293T, and 16HBE) and mouse cells (N_2a). The mRNA level of β-defensin was evaluated through real-time quantitative PCR, and the results are shown in Figure 6 and S1. For A549 human cells, treatment with sg5, sg7, and sg9 sgRNA complexed with G4 $(Phe)_{50\%}$-DET upregulated β-defensin by 10, 15, and 40 times in comparison with scramble sgRNA plasmid (scr sgRNA plasmid) treatment, respectively. Importantly, combination of three sgRNA plasmids (sg5+sg7+sg9) had higher mRNA copies of β-defensin than other treatments. The sgRNA (sg5+sg7+sg9) treatment enhanced gene expression by 10, 3, and 1.5 times compared with two sgRNA treatments (sg5+sg7, sg5+sg9, and sg7+sg9). Moreover, in 293T cells, the identified sgRNA treatments presented a much greater enhancing effect by around 45000 times compared to the scr sgRNA treatment (Figure 6(b)). Similar results were also confirmed in mouse N_2a cells. As shown in Figure 6(c) and S1, combination of sg2 and sg3 sgRNA (sgMBD4) increased β-defensin gene expression by about 25 times.

The antiviral effect of nonviral CRISPR/dCas9 targeting β-defensin was evaluated by plaque formation and flow cytometry assays. To monitor virus infection, A549 cells were coincubated with vesicular stomatitis virus incorporating the

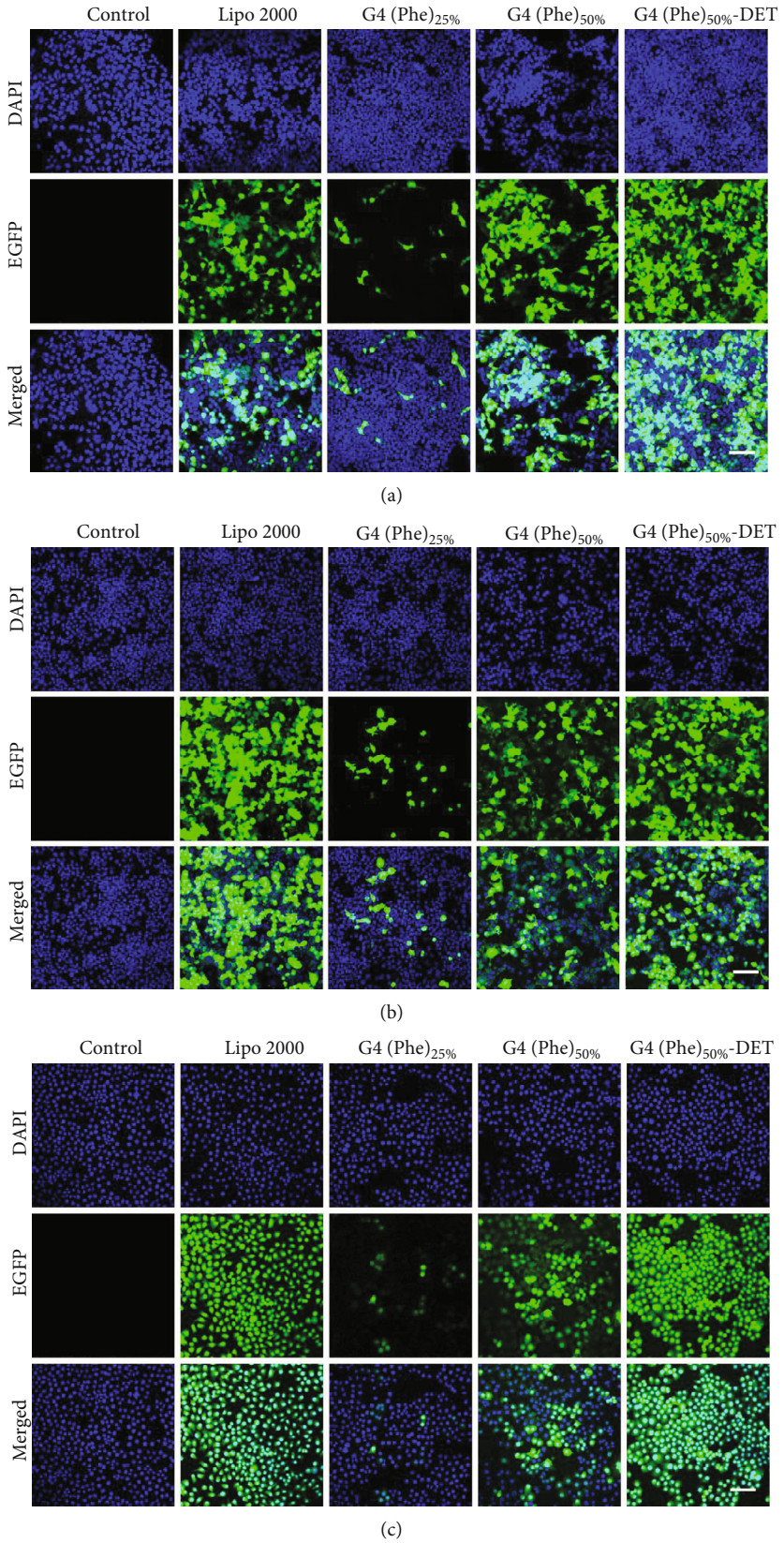

Figure 5: Confocal laser scanning microscopy (CLSM) images of human kidney 293T cells (a), mouse neuroblastoma N_2a cells (b), and human lung adenocarcinoma A549 cells (c) incubated with Lipo2000/plasmid, G4 $(Phe)_{25\%}$/plasmid, G4 $(Phe)_{50\%}$/plasmid, and G4 $(Phe)_{50\%}$-DET/plasmid. Incubation time: 48 h. Nuclei: stained blue with DAPI; green fluorescence: EGFP protein. Scale bars represent 100 μm.

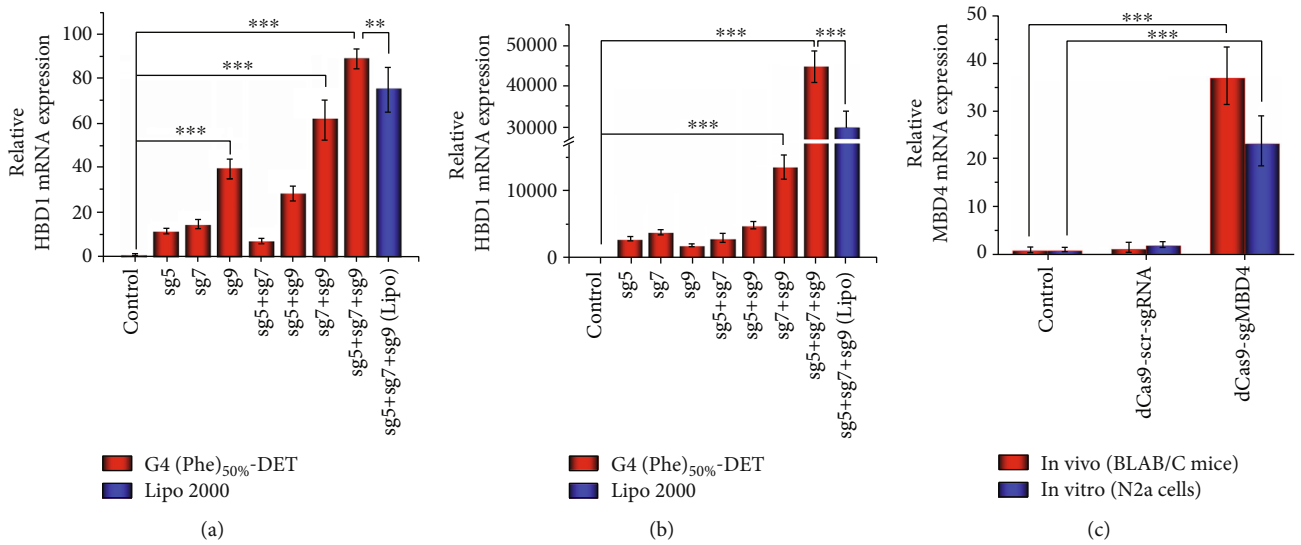

Figure 6: *In vitro* and *in vivo* relative β-defensin mRNA expression quantified by real-time PCR analysis in the human lung adenocarcinoma A549 cells (a), human kidney 293T (b), mouse neuroblastoma (*in vitro*), and BLAB/C mice (*in vivo*) (c). Dose: 1 μg/μL dCas9 plasmid and 1 μg/μL sgRNA plasmid were complexed with G4 $(Phe)_{50\%}$-DET/plasmid at N/P of 8 and Lipo2000 at N/P of 2. Inhalation dose: 5 μg/μL dCas9 plasmid and 5 μg/μL scr sgRNA or 5 μg/μL sgMBD4 in 100 μL PBS. Mouse neuroblastoma N_2a cells were used in *in vitro* experiments. BLAB/C mouse administrated with complexes was tested. MBD4 and HBD1 are abbreviations of mouse beta-defensin-4 and human beta-defensin-1, respectively. The scr sgRNA represented nonsense sgRNA and sgMBD4 represented mouse β-defensin-4 sgRNA (sg2+sg3) with the highest expression at mRNA level. Data are mean ± SD ($n = 3$). $^{**}p < 0.01$, $^{***}p < 0.001$.

GFP gene as a reporter (VSV-GFP). As shown in Figure 7, treatments with dCas9 alone and dCas9-scr sgRNA showed GFP-positive cells of 86.1% and 78.6%, respectively, indicating that dCas9 without sgRNA targeting β-defensin cannot block virus invasion. However, dCas9-sgHBD1 treatment significantly reduced the percentage of GFP-positive cells from 86.1% to 42.9%. Results of virus titer were consistent with those of flow cytometry. The titer value of cells receiving dCas9-sgHBD1 treatment decreased by about 100 times compared to that of cells receiving empty vector and dCas9-scr sgRNA treatments (Figures 7(a) and 7(b)). These results demonstrated that the delivery of dCas9-sgHBD1 with Phe- and DET-modified dendrimers remarkably prevented virus infection and replication.

3.4. In Vivo Studies. First, *in vivo* upregulation of β-defensin was evaluated after delivery of the CRISPRa system using Phe and DET dual-modified dendrimers. The nanoparticles containing 5 μg/μL dCas9 plasmids and 5 μg/μL sgRNA plasmids were prepared at N/P of 8 and intratracheally administrated into the mouse respiratory tract according to the approach [23]. Two days after inhalation administration, the lung and respiratory tract were excised and subjected to molecular biological and histological analyses [24]. Treatment with dCas9-sgMBD4 induced β-defensin gene expression by about 40-fold compared with dCas9-scr sgRNA treatment (Figure 6). As shown in Figure 8, evident dCas9 and β-defensin proteins were observed in the lung tissue sliced from mice receiving treatment with dCas9-sgMBD4. No β-defensin proteins were observed in the lung tissue from mice receiving no sgRNA or scr sgRNA treatment. In addition, the nanoparticles showed no significantly detrimental effects on the lung tissue.

4. Discussion

PAMAM dendrimers with globular structures and positively charged surfaces have been widely used as gene transfection reagents because of their ability to condense DNA and interact with cell membranes [25]. However, membrane barriers including outer cell membrane and inner nuclear membrane limited gene delivery efficiency of dendrimer carriers. Thus, several approaches have been developed to overcome these barriers by conjugating dendrimers with hydrophobic moieties and substances related to nuclear localization [15–18]. First, the hydrophobic phenylalanine was modified on the shell of the dendrimers to improve transfection activity. Interaction between phenylalanine residues and hydrophobic regions in the cell membrane destabilized the membrane and enhanced translocation of polyplexes across the cell membrane. Besides, density of phenylalanine on the surface of the dendrimer also had an impact on transfection efficiency. The dendrimer modified with high density of hydrophobic phenylalanine (50%) showed higher transfection efficiency (Figure 5), which was in line with the result that the dendrimer with 50% substitution of phenylalanine exhibited better transfection activity than other substitutions of 10% and 20% [17]. Second, several nuclear localization signal peptides and small molecules (e.g., DET) were used to translocate polyplexes into the nucleus. For example, dexamethasone-modified dendrimers or DNA enhanced their accumulation in the nucleus due to the translocation and the dilation of

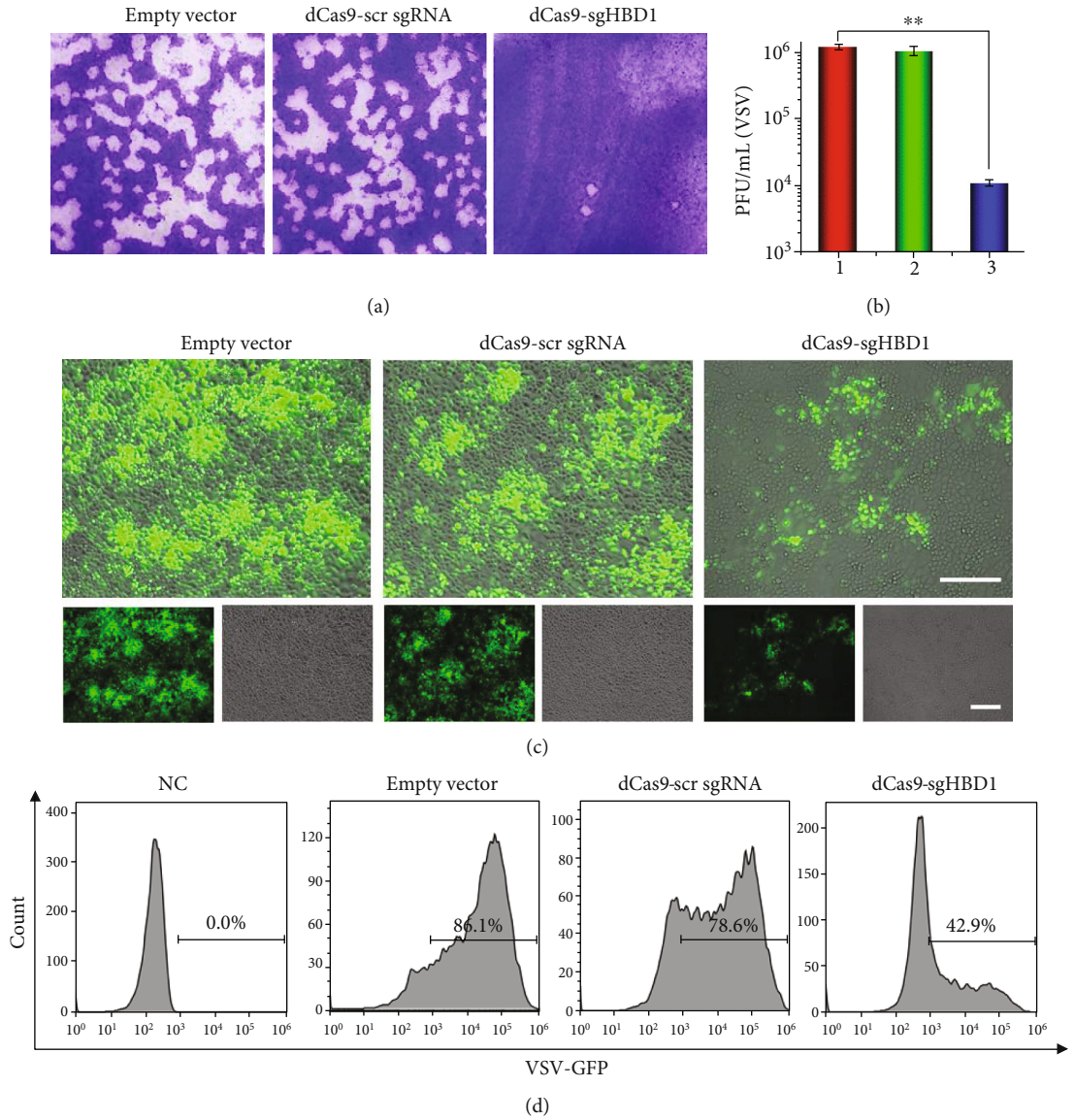

Figure 7: (a) Virus plaque images and (b) virus titer. Empty vector: G4 $(Phe)_{50\%}$-DET without plasmids; dCas9-scr sgRNA: G4 $(Phe)_{50\%}$-DET complexed with dCas9 and scr sgRNA plasmids; dCas9-sgHBD1: G4 $(Phe)_{50\%}$-DET complexed with dCas9 and HBD1 sgRNA plasmids; NC indicates mice receiving PBS treatment. Viral titers in cell culture medium were detected by plaque assay. Data were presented as mean ± SD of three independent experiments. $^{**}p < 0.01$. The "1," "2," and "3" of the X axis represent samples receiving empty vector, dCas9-scr sgRNA, and dCas9-sgHBD1 treatments, respectively. (c) Inverted fluorescence microscopy images of A549 cells receiving different treatments followed by VSV-GFP virus infection. Green fluorescence: VSV-GFP. Scale bars represent 250 μm. (d) Flow cytometry analysis of the green fluorescence- (GFP-) positive cells in samples receiving different treatments. Complexes were prepared for G4 $(Phe)_{50\%}$-DET/dCas9-sgRNA at N/P of 8. scr sgRNA represented nonsense sgRNA and sgHBD1 represented mixture of human β-defensin-1 sgRNA (sg5+sg7+sg9).

nuclear pores by the receptor of DET [18, 19]. Therefore, dual modification with Phe and DET may synergistically enhance transfection efficiency by overcoming plasma and nuclear membranes.

The limited resources of human β-defensin have hindered its clinical application. The CRISPRa technology provides a powerful and feasible approach to prohibit virus invasion by upregulating human β-defensin. The CRISPRa system was adopted to identify the host factor, beta-1,4-N-acetyl-galactosaminyltransferase 2 (B4GALNT2), which can abolish infection by inhibiting influenza virus binding to sialic acid receptors [26]. However, this strategy has rarely been explored to block virus infection *in vivo*. It is well known that a high level of β-defensin in the airway epithelium can effectively inhibit virus infection and replication [9, 10]. In this study, we utilized Phe and DET dual-modified dendrimer to deliver the CRISPRa system targeting the β-defensin gene, significantly reducing the VSV titer by

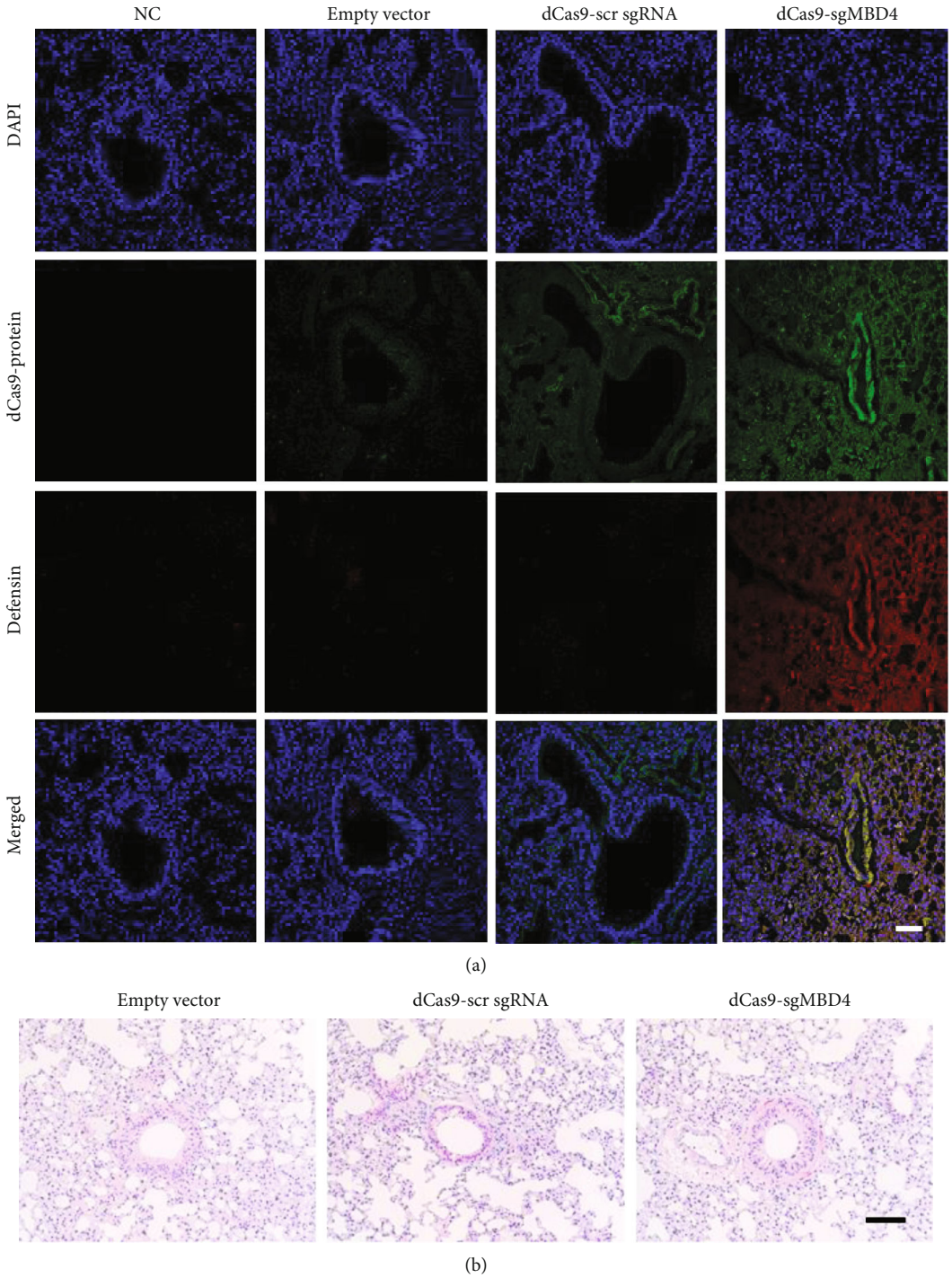

Figure 8: *Ex vivo* fluorescence immunohistochemical analyses (a) and histological characteristics (H&E stainning) (b) of lung sections from mice receiving different formulations (48 h after the inhalation). In the immunohistochemical assay, the nucleus, dCas9 protein, and β-defensin protein were stained blue, green, and red fluorescence, respectively. Inhalation dose: 5 μg/μL dCas9 plasmid and 5 μg/μL sgRNA (sgMBD4) in 100 μL PBS. Complexes were prepared at N/P value of 8. Scale bars, 100 μm in (a) and 50 μm in (b).

100-fold. CRISPR-Cas9/dCas9 causes off-target gene editing, but rationally engineered Cas9 or dCas9 can remarkably enhance specificity of gene editing [27]. Moreover, no gene disruption of dCas9-mediated CRISPRa also improved its biosafety. Except nuclear-localizing effect, dexamethasone can also improve therapeutic effects of the antivirus drug via reducing inflammation as a glucocorticoid.

5. Conclusion

The phenylalanine and dexamethasone dual-modified dendrimer was synthesized to transport the CRISPR/dCas9-sgRNA targeting β-defensin against virus infection. Phenylalanine and dexamethasone synergistically enhanced transfection efficiency, resulting in significantly antiviral activity.

Data Availability

The data used to support the findings of this study are included within the article

Conflicts of Interest

The authors declare that they have no conflicts of interest.

Authors' Contributions

Mingxiang Zuo and Xiaoxia Li contributed equally to this work.

Acknowledgments

This work was supported by the National Key R&D Program of China (2016YFE0117100), the National Natural Science Foundation of China (21875289 and U1501243), the Guangdong-Hong Kong Joint Innovation Project (2016A050503026), the Major Project on the Integration of Industry, Education and Research of Guangzhou City (201704030123), the Science and Technology Program of Guangzhou (201704020016), the Guangdong Innovative and Entrepreneurial Research Team Program (2013S086), and the Guangdong Province Science and Technology Innovation Special Fund (International Scientific Cooperation, 2018A050506035).

Supplementary Materials

The supplement file include Figure S1 and Table S1. Relative mRNA expression in cells receiving dCas9 and sgRNA plasmids delivered with Lipofectamine 2000 were reported in Figure S1; and Sequences of sgRNAs and primers were described in Table S1. *(Supplementary Materials)*

References

[1] J. Wheeler, M. McHale, V. Jackson, and M. Penny, "Assessing theoretical risk and benefit suggested by genetic association studies of CCR5: experience in a drug development programme for maraviroc," *Antiviral Therapy*, vol. 12, no. 2, pp. 233–245, 2007.

[2] L. Waters, A. Jackson, L. Else et al., "Switching safely: pharmacokinetics, efficacy and safety of switching efavirenz to maraviroc twice daily in patients on suppressive antiretroviral therapy," *Antiviral Therapy*, vol. 20, no. 2, pp. 157–163, 2015.

[3] J. C. Miller, S. Tan, G. Qiao et al., "A TALE nuclease architecture for efficient genome editing," *Nature Biotechnology*, vol. 29, no. 2, pp. 143–148, 2011.

[4] F. D. Urnov, E. J. Rebar, M. C. Holmes, H. S. Zhang, and P. D. Gregory, "Genome editing with engineered zinc finger nucleases," *Nature Reviews Genetics*, vol. 11, no. 9, pp. 636–646, 2010.

[5] W. Y. Hwang, Y. Fu, D. Reyon et al., "Efficient genome editing in zebrafish using a CRISPR-Cas system," *Nature Biotechnology*, vol. 31, no. 3, pp. 227–229, 2013.

[6] H. Zhou, J. Liu, C. Zhou et al., "*In vivo* simultaneous transcriptional activation of multiple genes in the brain using CRISPR-dCas9-activator transgenic mice," *Nature Neuroscience*, vol. 21, no. 3, pp. 440–446, 2018.

[7] M. H. Larson, L. A. Gilbert, X. Wang, W. A. Lim, J. S. Weissman, and L. S. Qi, "CRISPR interference (CRISPRi) for sequence-specific control of gene expression," *Nature Protocols*, vol. 8, no. 11, pp. 2180–2196, 2013.

[8] S. Chen, X. Yu, and D. Guo, "CRISPR-Cas targeting of host genes as an antiviral strategy," *Viruses*, vol. 10, no. 1, p. 40, 2018.

[9] W. Li, Y. Feng, Y. Kuang et al., "Construction of eukaryotic expression vector with mBD1-mBD3 fusion genes and exploring its activity against influenza a virus," *Viruses*, vol. 6, no. 3, pp. 1237–1252, 2014.

[10] T. Ganz, "Defensins: antimicrobial peptides of innate immunity," *Nature Reviews Immunology*, vol. 3, no. 9, pp. 710–720, 2003.

[11] F. A. Ran, L. Cong, W. X. Yan et al., "*In vivo* genome editing using Staphylococcus aureus Cas 9," *Nature*, vol. 520, no. 7546, pp. 186–191, 2015.

[12] H. Yin, K. J. Kauffman, and D. G. Anderson, "Delivery technologies for genome editing," *Nature Reviews Drug Discovery*, vol. 16, no. 6, pp. 387–399, 2017.

[13] G. Zhou, Y. Xu, M. Chen, D. Cheng, and X. Shuai, "Tumor-penetrating peptide modified and pH-sensitive polyplexes for tumor targeted siRNA delivery," *Polymer Chemistry*, vol. 7, no. 23, pp. 3857–3863, 2016.

[14] H. X. Wang, Z. Song, Y. H. Lao et al., "Nonviral gene editing via CRISPR/Cas 9 delivery by membrane-disruptive and endosomolytic helical polypeptide," *Proceedings of the National Academy of Sciences of the United States of America*, vol. 115, no. 19, pp. 4903–4908, 2018.

[15] C. Liu, T. Wan, H. Wang, S. Zhang, Y. Ping, and Y. Cheng, "A boronic acid-rich dendrimer with robust and unprecedented efficiency for cytosolic protein delivery and CRISPR-Cas 9 gene editing," *Science Advances*, vol. 5, no. 6, article eaaw8922, 2019.

[16] J. A. Kretzmann, D. Ho, C. W. Evans et al., "Synthetically controlling dendrimer flexibility improves delivery of large plasmid DNA," *Chemical Science*, vol. 8, no. 4, pp. 2923–2930, 2017.

[17] F. Wang, Y. Wang, H. Wang, N. Shao, Y. Chen, and Y. Cheng, "Synergistic effect of amino acids modified on dendrimer surface in gene delivery," *Biomaterials*, vol. 35, no. 33, pp. 9187–9198, 2014.

[18] Y. M. Bae, H. Choi, S. Lee et al., "Dexamethasone-conjugated low molecular weight polyethylenimine as a nucleus-targeting lipopolymer gene carrier," *Bioconjugate Chemistry*, vol. 18, no. 6, pp. 2029–2036, 2007.

[19] J. S. Choi, K. S. Ko, J. S. Park, Y. H. Kim, S. W. Kim, and M. Lee, "Dexamethasone conjugated poly (amidoamine) dendrimer as a gene carrier for efficient nuclear translocation," *International Journal of Pharmaceutics*, vol. 320, no. 1-2, pp. 171–178, 2006.

[20] J. Wu, J. Huang, S. Kuang et al., "Synergistic microRNA therapy in liver fibrotic rat using MRI-visible nanocarrier targeting hepatic stellate cells," *Advanced Science*, vol. 6, no. 5, article 1801809, 2019.

[21] J. Huang, C. Lin, J. Fang et al., "pH-sensitive nanocarrier-mediated codelivery of simvastatin and noggin siRNA for synergistic enhancement of osteogenesis," *ACS Applied Materials & Interfaces*, vol. 10, no. 34, pp. 28471–28482, 2018.

[22] K. Kono, H. Akiyama, T. Takahashi, T. Takagishi, and A. Harada, "Transfection activity of polyamidoamine dendrimers having hydrophobic amino acid residues in the periphery," *Bioconjugate Chemistry*, vol. 16, no. 1, pp. 208–214, 2005.

[23] B. J. Li, Q. Tang, D. Cheng et al., "Using siRNA in prophylactic and therapeutic regimens against SARS coronavirus in rhesus macaque," *Nature Medicine*, vol. 11, no. 9, pp. 944–951, 2005.

[24] B. J. Zheng, K. W. Chan, Y. P. Lin et al., "Delayed antiviral plus immunomodulator treatment still reduces mortality in mice infected by high inoculum of influenza A/H5N1 virus," *Proceedings of the National Academy of Sciences of the United States of America*, vol. 105, no. 23, pp. 8091–8096, 2008.

[25] S. D. Jativa, N. Thapar, D. Broyles et al., "Enhanced delivery of plasmid DNA to skeletal muscle cells using a DLC8-binding peptide and ASSLNIA-modified PAMAM dendrimer," *Molecular Pharmaceutics*, vol. 16, no. 6, pp. 2376–2384, 2019.

[26] B. E. Heaton, E. M. Kennedy, R. E. Dumm et al., "A CRISPR activation screen identifies a pan-avian influenza virus inhibitory host factor," *Cell Reports*, vol. 20, no. 7, pp. 1503–1512, 2017.

[27] I. M. Slaymaker, L. Gao, B. Zetsche, D. A. Scott, W. X. Yan, and F. Zhang, "Rationally engineered Cas9 nucleases with improved specificity," *Science*, vol. 351, no. 6268, pp. 84–88, 2015.

Hindawi
Advances in Polymer Technology
Volume 2020, Article ID 1308081, 9 pages
https://doi.org/10.1155/2020/1308081

Research Article

Tea Polysaccharide (TPS) Reduces Astrocytes Apoptosis Induced by Oxygen-Glucose Deprivation/Reoxygenation by Regulating the miR-375/SRXN1 Axis

Ying Jiang,[1] Hongmei Sun,[2] Zhiqi Yin,[3] and Jun Yan[3]

[1]*Department of Clinical Laboratory, Tianjin First Center Hospital, Tianjin 300192, China*
[2]*Department of Out-patient, Tianjin First Center Hospital, Tianjin 300192, China*
[3]*Department of Pathology, Tianjin First Center Hospital, Tianjin 300192, China*

Correspondence should be addressed to Jun Yan; yanhuang2@163.com

Received 3 February 2020; Revised 10 March 2020; Accepted 16 March 2020; Published 2 April 2020

Guest Editor: Mingqiang Li

Objective. To investigate the effect of tea polysaccharides (TPS) mediated by miR-375/SRXN1 axis on mice with cerebral ischemia-reperfusion injury and proliferation and apoptosis of astrocytes (AS) conducted with oxygen-glucose deprivation/reoxygenation (OGD/R). *Methods*. Mouse model of middle cerebral artery occlusion (MCAO) and OGD/R-induced AS injury model were established; brain obstruction volume was measured by TTC staining; dry/wet weight ratio was used for measuring brain water content; hydrogen peroxide (H_2O_2) content in brain tissue was measured by H_2O_2 assay kit; cell viability and apoptosis rate were detected by MTT assay and flow cytometry, respectively; the expression level of miR-375 in OGD/R-AS was detected using qPCR; dual-luciferase reporter assay was used to verify the targeting relationship between miR-375 and SRXN1; mRNA levels of miR-375, SRXN1, Bcl-2, Bax, and caspase-3 were measured by qPCR; the protein levels of SRXN1, Bcl-2, Bax, and caspase-3 were measured by Western blotting. *Results*. The volume of cerebral obstruction, brain water content and H_2O_2 content in mice decreased gradually with the increase of TPS concentration. TPS treatment in vitro could effectively improve OGD/R-AS viability and reduce the apoptotic rate; overexpression of miR-375 inhibited AS viability but increased the apoptotic rate; TPS treatment resulted in a decrease in the expression of miR-375 in OGD/R-AS; MiR-375 targeted SRXN1 in AS; inhibition of miR-375 expression significantly upregulated SRXN1 levels; TPS treatment with simultaneous overexpression of SRXN1 significantly increased OGD/R-AS activity and reduced apoptosis; however, TPS treatment with simultaneous overexpression of SRXN1 and miR-375 resulted in no significant difference in cell viability and apoptosis rate compared with the control group. *Conclusion*. TPS reduces astrocyte injury induced by cerebral ischemia-reperfusion in mice by regulating the miR-375/SRXN1 molecular axis.

1. Introduction

Ischemic stroke, one of the leading causes of interruption of cerebral blood flow, is also an important factor of death and disability worldwide [1]. Restoration of blood supply to the brain following ischemic stroke may lead to reperfusion injury [2]. Reperfusion stimulates the overproduction of reactive oxygen species (ROS) such as hydrogen peroxide (H2O2), which induces cell proliferation, growth arrest, and causes apoptosis and necrosis [3]. Astrocytes (AS), one of the major types of glial cells in the central nervous system (CNS), have various functions of regulating blood-brain barrier permeability, glial scar formation, and synaptic activity [4]. There is increasing evidence that apoptosis and death of nerve cells after ischemia-reperfusion are the main causes of exacerbated brain injury [5]. Therefore, it is very urgent to develop novel therapeutic strategies for cerebral ischemia-reperfusion. Sulfiredoxin-1 (SRXN1) is an endogenous antioxidant protein [6] that plays an important role in neuroprotection [7]. SRXN1 can resist cellular oxidative stress-induced ROS production [8, 9]. Zhou et al. [10] reported the antioxidant function exerted by

SRXN1 in protecting rat cortical AS from apoptosis, confirming that SRXN1 is a potential target gene for the treatment of cerebral ischemia-reperfusion injury.

Tea polysaccharides (TPS) is heteropolysaccharides extracted from leaves, flowers, and seed peels of tea trees [11] and is mainly composed of arabinose, xylose, glucose, galactose, galactoglucan, pectin, and protein. In the past few decades, significant progress has been made in the study of the chemical and biological activities of TPS and other related tea products. TPS has many health benefits. It has antioxidant, antiaging, and antitumor effects, as well as the ability to reduce cerebral ischemia-reperfusion injury after stroke [12], to improve diabetes [13], to boost body immunity [14], and to reduce hepatotoxicity [15]. However, the molecular mechanism of its role in most diseases is unknown.

MicroRNAs (miRNAs) refer to a newly discovered class of endogenous noncoding RNAs, which are involved in post-transcriptional gene regulation by binding to target sites in the $3'$-UTR of target mRNA and result in mRNA degradation or translation inhibition [16]. In an animal study, investigators analyzed miRNA profiles after cerebral ischemia-reperfusion and have found that high miR-375 expression was detected at 12 h of ischemia-reperfusion, while expressions of other up-regulated genes gradually peaked after 72 h. Therefore, miR-375 is expected to be a diagnostic and therapeutic target for cerebral ischemia-reperfusion [17]. It has been reported that miRNAs are stimulated by external factors to change their expressions, thereby specifically regulating the expressions of target genes. There have been some reports that polysaccharides exert anti-inflammatory and antioxidant effects in vitro by regulating the expression of miRNAs [18, 19]. However, there is no report that focused on the role of polysaccharides in regulating AS activity and alleviating cerebral ischemia-reperfusion injury via miRNA.

Therefore, in this study, we investigated the protective effect of TPS on AS after ischemia-reperfusion injury by establishing a MACO mouse model and an OGD/R and AS injury model and attempted to provide new insights on the role of TPS in reducing the oxidative stress-caused apoptosis. Our results showed that TPS could alleviate the brain damage caused by cerebral ischemia-reperfusion and reduce astrocyte apoptosis by regulating the miR-375/SRXN1 axis, which provided a new potential theoretical basis for the effect of polysaccharides on treating cerebral ischemia-reperfusion injury.

2. Materials and Methods

2.1. Materials

2.1.1. Animal Origin. Fifty-four male ICR mice, weighing 25-30 g, were purchased from Kay Biological Technology (Shanghai) Co., Ltd. Mice were housed in a 12 h light/12 h dark cycle in a constant temperature room, with daily feed and water provided regularly.

2.1.2. Cell Origin and Culture. Astrocytes (AS) were purchased from Shanghai Yu Bo Biological Technology Co., Ltd. (article number: HUM-YB-n012). The AS were adherently cultured in complete medium (DMEM/FBS) containing 12% bovine serum at 37°C and 5% CO_2. The cells were then cultured to the logarithmic phase for subsequent experiments.

2.1.3. Main Reagents. TPS of 99% active component (rhamnose, arabinose, xylose, glucose, galactose, galactoglucan, pectin, and protein) was purchased from Nanjing Tongying Biotechnology Co., Ltd. Fetal bovine serum, complete culture medium, and LipofectamineTM 2000 reagent were purchased from Invitrogen. Trizol and RNA extraction kits were purchased from Beijing Tianjian Biotechnology Co., Ltd. SYBR Premix Ex TaqTM II kit, PrimescripTM RT reagent kit, and miRNA PrimescripTM RT reagent kit were purchased from Takara. The primers were synthesized by Sangon Biotech (Shanghai, China). The H_2O_2 content kit was purchased from Beijing Solarbio Science & Technology Co., Ltd. The dual luciferase reporter gene kit was purchased from Beijing Baiao Laibo Co., Ltd. The protein extraction kit was purchased from NanJing KeyGen Biotech Co., Ltd. The Annexin V-PE/7-AAD apoptosis kit was purchased from Shanghai Yu Bo Biotechnology Co., Ltd.

2.2. Methods

2.2.1. MCAO Mouse Modeling and TPS Treatment. The cephalic flesh of the mice anesthetized with chloral hydrate was opened, the fascia of the skull surface was cleaned, and the probe of the laser Doppler flowmeter was fixed at a specific position on the skull. The supine skin was cut in the middle with tissues separated. The right common carotid artery, internal carotid artery, and external carotid artery were then exposed and ligated with 6-0 silk suture. The external carotid artery was separated using a microelectric coagulator, in which a small incision was made near bifurcation of the common carotid artery. A filament was inserted and tied to the incision in the external carotid artery with another silk suture. The ligated internal carotid artery was loosened, along which the filament was inserted slowly into the intracranial space to an approximate depth of 9 mm. After 60 min, the filament was pulled out, and the incision in the external carotid artery was ligated. The ligature of the common carotid artery was loosened, and the skin was sutured. The mice fully awake were then returned to their cages. The mice in sham operation group were performed the same as those in the operation group except the use of the filament. Mice in TPS treated groups were given intraperitoneal injection of TPS (0, 50, 100, 150, and 200 mg kg^{-1}) every 12 h for 72 h after reperfusion injury. The sham and model groups received an equal volume of saline per injection.

2.2.2. Detection of Cerebral Infarction Volume in Mice. The heads of mice, 72 h after cerebral ischemia and reperfusion, were removed from the body and frozen at −20° C for 30 min. The brain tissues serially sectioned at 2.0 mm were placed in 1% TTC phosphate buffer in a water bath at 37°C for 30 min. Afterwards, the sections were scanned, and the percentage of cerebral infarct volume to total brain volume was calculated by Image pro plus 5.1 software. The experiment was repeated 3 times.

Table 1: Primer sequence.

Gene	Forward primer	Reverse primer
miR-375	5′-CTTACTATCCGTTTGTTCGTTCG-3′	5′-TATGGTTGTTCTCGTCTCTGTGTC-3′
SRXN1	5′-TGCCAACCCTAGGAGGTAGA-3′	5′-CCCCAAGTTCCTGCCAGAAT-3′
Bcl-2	5′-ATCGCCCTGTGGATGACTGAG T-3′	5′-GCCAGGAGAAATCAAACAG AGGC-3′
Bax	5′-TCAGGATGCGTCCACCAAGAAG-3′	5′-TGTGTCCACGGCGGCAATCATC-3′
Caspase-3	5′-TGTGGCATTGAGACAGAC-3′	5′-CACTTGCCATACAAACTA-3′
U6	5′-CTCGCTTCGGCAGCACA-3′	5′-AACGCTTCACGAATTTGCGT-3′
GAPDH	5′-TCCTCTGACTTCAACAGCGACAC-3′	5′-CACCCTGTTGCTGTAGCCAAATTC-3′

2.2.3. Determination of Brain Water Content. The heads of mice, 72 h after cerebral ischemia and reperfusion, were removed from the body. The brains were obtained, and the wet weights were recorded. The brains were then dried to constant weight in an oven at 110–115°C to determine the dry weight. Brain water content was calculated with the following formula: water content = (wet weight − dry weight)/wet weight × 100%. Three replicates were performed.

2.2.4. H_2O_2 Assay. The H_2O_2 content in mouse brain tissue was measured at 415 nm using the H_2O_2 content kit and a microplate reader.

2.2.5. Establishment of OGD/R Model. OGD/R treatment was utilized to simulate ischemia-reperfusion injury in vitro [20]. Briefly, the original DMEM medium was replaced with glucose-free DMEM for further AS incubation. The cells were incubated for 6 h in a hypoxic environment containing 5% CO_2, 1% O_2, and 94% N_2. The AS were subsequently transferred to normal DMEM medium and incubated for another 24 h.

2.2.6. Cell Proliferation Detection. AS harvested by scraping from the medium were placed in a serum-free solution, blown into individual cells, and cultured in suspension. The cells were then seeded onto 96-well plates at a density of 5000 per well with 20 μL per well, and TPS (0, 10, 20, 40, and 60 mg/L) were added, respectively. Afterwards, a solution of 10 μL MTT dissolved in PBS was added, and the cells were incubated at 37°C in 5% CO_2 for 4-6 h. The culture solution in the wells was then removed, and 150 μL of DMSO was added. After 10 min, the absorbance value was detected at 570 nm using a microplate reader. Three replicates were performed.

2.2.7. Apoptosis Detection. The cells in different groups were treated for 48 h and centrifuged at 600 × g for 5 min, the supernatant was discarded, and the cells were washed once with PBS. The cells in each group were seeded into 6-well plates at a density of 1×10^5 and cultured for 12 h. Apoptosis under different treatments was detected using Annexin V-PE/7-AAD Apoptosis Kit and flow cytometer (BD Biosciences, USA).

2.2.8. Real-Time Fluorescence Quantitative (qPCR). Total RNA of MA was extracted using TRIzol and an RNA extraction kit. RNA quality and concentration were measured by NanoDrop and uniformly diluted to 500 ng μL^{-1}. RNA was then reverse transcribed into cDNA using PrimeScript RT and miRNA PrimeScriptTM RT kits, and primers were synthesized by Sangon Biotech (Shanghai, China). The SYBR Premix Ex TaqTM II kit was then used as a template for qPCR amplification. The LightCycler ® 96 Instrument (Roche, Switzerland) was used: initial denaturation at 95°C for 30 s, 40 cycles of denaturation at 95°C for 5 s followed by annealing/extension at 60°C for 30 s. GAPDH and U6 were used as internal references for mRNA and miRNA, and relative mRNA expression was calculated using $2^{-\Delta\Delta Ct}$ method. The sequences of the primers used for the fluorescent quantitative PCR are shown in Table 1. Three replicates were performed.

2.2.9. Western Blotting. Proteins were isolated from cells using RIPA. The protein mixture (with loading buffer) at the same concentration was boiled for 10 min at 95°C. Then, 20 μL of the mixture (containing 30–50 μg of sample) was added to a plate of 10% polyacrylamide gel and subjected to electrophoresis to separate proteins. The proteins were transferred from the gel to a PVDF membrane, blocked, and then incubated overnight at 4°C with primary antibodies. Samples were washed with TBST and incubated with secondary antibodies for 1 h at room temperature. β-Actin was used as an internal reference, and grayscale was determined with Image J. Three replicates were performed.

2.2.10. Cell Transfection. Cells in the logarithmic growth phase were taken and prepared for cell suspensions. The 1×10^5 cells were seeded in 6-well plates and incubated at 37°C and 5% CO_2 for 24 h. Lipofectamine 2000: DNA complexes were mixed gently and then allowed to stand. After incubation at room temperature for 20 min, the supernatant of cell culture medium was added, mixed, and cultured for another 24 h. Transfection efficiency of miRNA or mRNA was examined using RT-PCR and Western blotting. Three replicates were performed.

2.2.11. Dual-Luciferase Reporter Assay. Cells in logarithmic growth phase were cultured in 96-well plates, and cells with 80% confluence were obtained for transfection followed by another 48 h of culture. The 100 μL of lysate was added per well, and the solution was centrifuged at 12000 rpm for

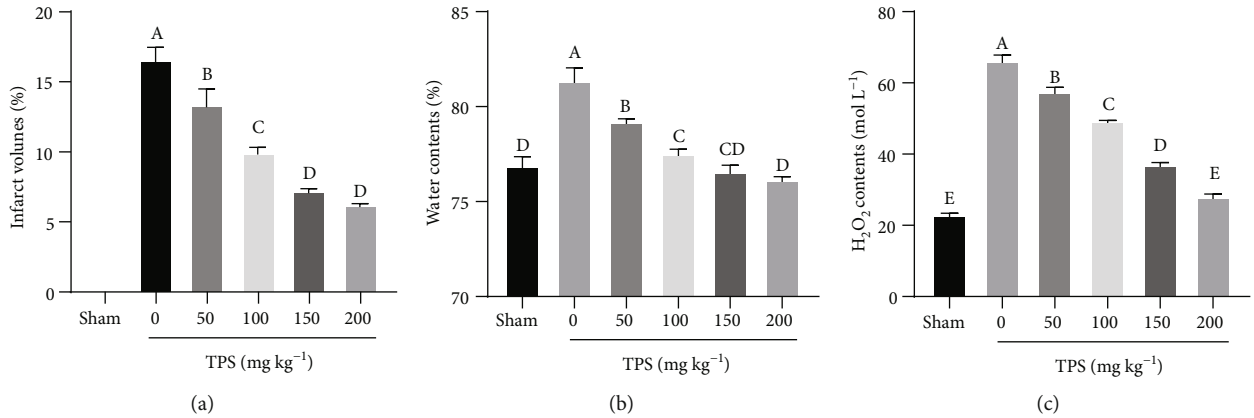

Figure 1: The effect of TPS on cerebral infarct volume, brain water content, and H2O2 content after cerebral ischemia-reperfusion injury. (a) Infarct volumes under different TPS concentration treatments. (b) Brain water contents under different TPS concentration treatments. (c) H2O2 contents under different TPS concentration treatments.

5 min. The supernatant (50 μL) was transferred into a 96-well plate, and then 40 μL of firefly luciferase assay substrate was added to each well and mixed by gentle shaking for 10 s to detect the fluorescence intensity. An additional 40 μL of Renilla luciferase assay substrate was added to the 96-well plate and mixed gently for 10 s to measure luciferase activity using a Glomax luminometer (Promega, USA). Three replicates were performed.

2.3. Statistical Analysis. Data analyses and drawing of statistical charts were performed using a GraphPad Prism 8 software. Differences in data between groups were statistically analyzed using Student's t-test and one-way ANOVA. $P < 0.05$ was considered statistically significant, $P < 0.01$ highly significant, and $P < 0.001$ extremely highly significant.

3. Results

3.1. TPS Ameliorated Cerebral Ischemia-Reperfusion Injury. The cerebral infarct area (Figure 1(a)) and brain water content (Figure 1(b)) in cerebral ischemia-reperfusion mice showed a gradual decrease with the increase of TPS concentration in the treatment groups as compared with the group without TPS administration. The H_2O_2 content in the brain tissues was measured, and it was found that the content gradually decreased as the concentration of TPS increased in the brain tissues with cerebral ischemia-reperfusion injury (Figure 1(c)).

3.2. TPS Reduced OGD/R-AS Apoptosis. The effect of TPS on AS proliferation under OGD/R treatment was examined using MTT assay, and the results revealed that AS cell viability was gradually enhanced with increasing TPS concentration, with the highest cell viability under 40 mg L^{-1} treatment (Figure 2(a)). Therefore, 0 and 40 mg L^{-1} of TPS were used in subsequent experiments. Flow cytometry to detect AS apoptosis revealed that 48 h after the TPS (40 mg L^{-1}) treatment, the level of AS apoptosis significantly declined compared with that of the control group (Figure 2(b)). Meanwhile, the results of qPCR and Western blotting assays indicated that both mRNA and protein expression levels of the apoptosis-inhibiting Bcl-2 were increased, while mRNA and protein expression levels of the apoptosis-promoting Bax and caspase-3 were inhibited (Figures 2(c) and 2(d)).

3.3. TPS Reduced OGD/R-AS Apoptosis by Inhibiting the Expression of miR-375. The expression of miR-375 in AS was examined under different concentrations of TPS treatment, and the results revealed that miR-375 expression showed a decreasing trend with increasing TPS concentration (Figure 3(a)). To further examine the role of miR-375 in OGD/R-induced AS apoptosis, miR-375 mimics vector was constructed to transfect OGD/R-treated AS. The expression of miR-375 in AS was examined using QPCR, and we found that as compared with the control group, miR-375 mimics transfection increased miR-375 expression in AS (Figure 3(b)). Cell proliferation was detected by MTT assay, and the results revealed that overexpression of miR-375 inhibited cell proliferation, while the coeffect of miR-375 overexpression and TPS treatment partially suppressed cell proliferation (Figure 3(c)). Contrary to AS proliferation, the overexpression of miR-375 increased the apoptotic rate, while miR-375 overexpression and TPS treatment could partially alleviate apoptosis (Figure 3(d)). The results of qPCR and Western blotting showed that the mRNA and protein levels of apoptosis-related Bcl-2, Bax, and caspase-3 were consistent with the cell apoptosis (Figures 3(e) and 3(f)).

3.4. MiR-375 Targeted SRXN1. The miR-375 and SRXN1 target binding sites were first predicted by bioinformatics tools (starBase) (Figure 4(a)). In addition, the interaction between miR-375 and SRXN1 was validated using a dual luciferase reporter assay, and Figure 4(b) showed that the luciferase activity was significantly lower in cells transfected with miR-375 mimics+SRXN1-WT than in miR-375 NC+SRXN1-WT transfected cells. Transfection of SRXN1-MUT had no significant effect on the luciferase activity. The results of qPCR and Western blotting showed increased mRNA and proteins expression levels of SRXN1

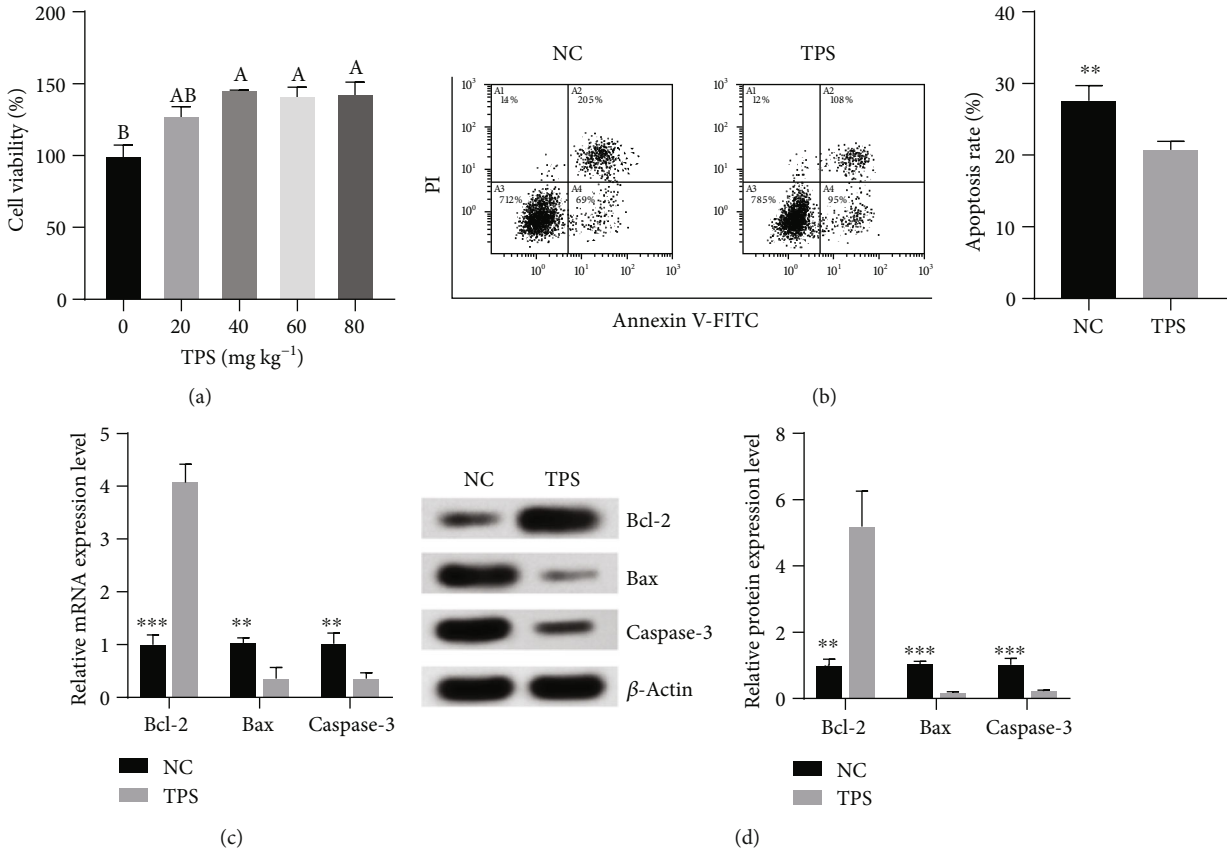

Figure 2: Effects of TPS on OGD/R-AS cell viability and apoptosis. (a) Cell viability of AS under different TPS concentration treatments. (b) Cell apoptosis rate of AS. (c) Relative mRNA expression level of apoptosis-related proteins. (d) Relative protein expression level of apoptosis-related proteins. Note: each treatment in the figure has different lowercase letters, which means that the difference between the different treatments is significant ($P < 0.05$). $^{**}P < 0.01$, $^{***}P < 0.001$ compared with NC group. NC: negative control.

in cells transfected with miR-375 inhibitor (Figures 4(c) and 4(d)).

3.5. miR-375/SRXN1 Axis Mediated TPS to Reduce OGD/R-Induced AS Injury. First, the transfection efficiency as well as the effect of overexpression of miR-375 on SRXN1 expression in AS were examined using qPCR and Western blotting. It was found that SRXN1 overexpression increased mRNA levels and protein levels of SRXN1in OGD/R-treated AS, whereas miR-375 overexpression suppressed the mRNA and protein levels of SRXN1. Furthermore, overexpression of SRXN1 and miR-375 could restore the suppressed SRXN1 expression (Figures 5(a) and 5(b)). Subsequently, the effect of miR-375/SRXN1 on cell viability and apoptosis was examined. The overexpression of SRXN1 and TPS treatment significantly increased cell viability, whereas overexpression of SRXN1 and miR-375 showed no difference in cell viability (Figure 5(c)). Compared with TPS treatment, the coeffect of overexpression of SRXN1 and TPS treatment resulted in a lower rate of apoptosis, but there was no difference in apoptosis when SRXN1 and miR-375 were cooverexpressed (Figure 5(d)). The qPCR and Western blotting results showed that SRXN1 overexpression along with TPS treatment increased the expression of Bcl-2, the inhibitor of apoptosis protein, and decreased the expression of Bax and caspase-3, the proapoptotic proteins, while simultaneous overexpression of SRXN1 and miR-375 restored the expression levels of Bcl-2, Bax, and caspase-3 to the levels when only TPS was added (Figures 5(e) and 5(f)).

4. Discussion

As food-derived polysaccharides, TPS are widely found in various teas such as black tea, green tea, and dark green tea [21] and has been proven to have many biological functions. Moreover, we confirmed in this study that TPS alleviates OGD/R-induced AS apoptosis in vitro, and verified its possible molecular mechanism.

Cerebral ischemia and reperfusion triggers a series of inflammatory reactions, oxidative stress, and apoptosis, which leads to the breakdown of the blood-brain barrier, resulting in brain edema and exacerbation of nerve injury. There is evidence that AS-derived factors play a critical role in the destruction and recovery of the blood-brain barrier following brain injury [22]. AS have been used as a major therapeutic target in brain diseases, and studies have shown that better control of AS helps reduce brain injury in various experimental animal models [4].

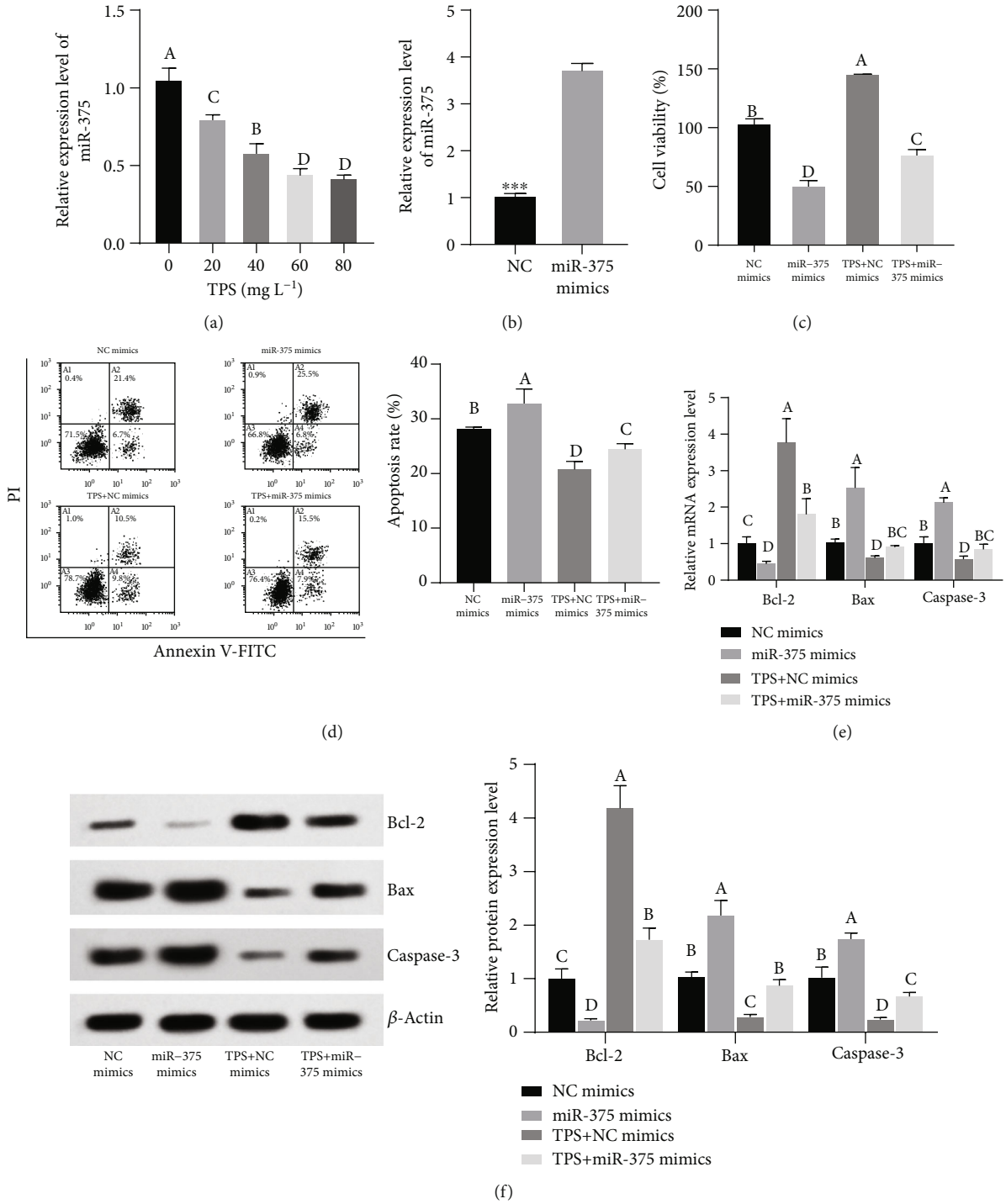

Figure 3: TPS increased cell viability and reduced apoptosis of OGD/R-AS through inhibiting the expression of miR-375. (a) Relative expression of miR-375 under different TPS concentration treatments. (b) Transfection efficiency of miR-375 mimics. (c) Cell viability of AS. (d) Cell apoptosis rate of AS. (e) Relative mRNA expression level of apoptosis-related proteins. (f) Relative protein expression level of apoptosis-related proteins. Note: each treatment in the figure has different lowercase letters, which means that the difference between the different treatments is significant ($P < 0.05$), $P < 0.001$ compared with NC group. NC: negative control.

Therefore, AS are essential for protecting the integrity of the blood-brain barrier. Our study also demonstrated that OGD/R-AS treated by TPS show significant increase in its activity.

Accumulating evidence suggests that miRNAs act as key modulators of cellular activation and inflammatory responses [23]. Guo et al. [24] reported that miR-375 induced ROS production and apoptosis in cells by

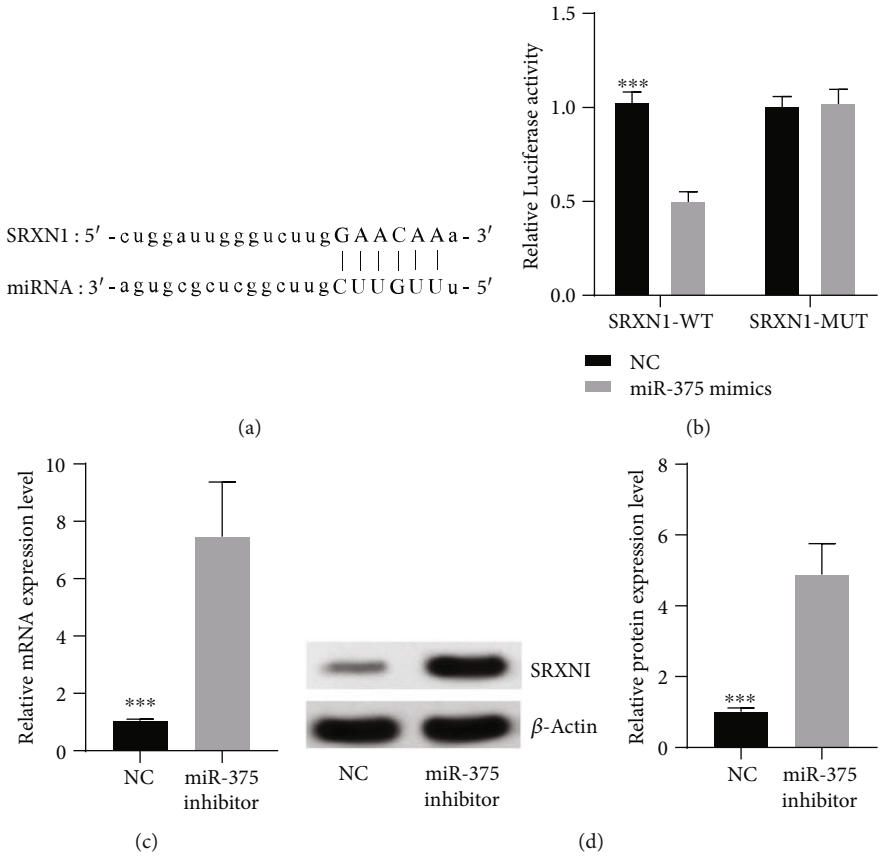

Figure 4: miR-375 directly targeted SRXN1and regulated the expression of SRXN1. (a) The binding site of miR-375 and SRXN1. (b) Dual-luciferase relative activity. (c) Relative mRNA expression level of SRXN1. (d) Relative protein expression level of SRXN1. Note: $^{***}P < 0.001$ compared with NC group. NC: negative control.

targeting HIGD1A. MiR-375 (miR-375) plays an important role in the development and progression of cervical cancer, inhibits cell proliferation, and promotes apoptosis by targeting IGF-1R [25]. In addition, upregulation of miR-375 can also inhibit HCC cell proliferation and promote apoptosis by targeting ErbB2 [26]. We found in this study that miR-375 could modulate AS activity by targeting SRXN1. The antioxidant role of SRXN1 has been widely reported, and SRXN1 protects brain tissue from damage by regulating glutathionylation/deglutathionylation in Parkinson's disease [27]. Moreover, induction of SRXN1 expression contributes to neuronal protection in response to oxygen-glucose deprivation after brief ischemic episodes in vitro and in vivo [28]. However, there are few reports on the role of SRXN1 in cerebral ischemia-reperfusion injury and apoptosis-induced injury. In our study, TPS was found to indirectly regulate SRXN1 expression through miR-375, suggesting a protective role of SRXN1 in AS apoptosis that was caused by oxidative stress. It also provided a basis for studying the molecular mechanism of SRXN1 in cerebral ischemia-reperfusion injury.

However, this study also has some limitations. The blood-brain barrier in the body can effectively filter substances entering and exiting the brain to protect the brain from external damage [29]. TPS, as a macromolecule, like other drugs in the body, may be restricted by the blood-brain barrier from entry into the brain. The results of this study showed that brain injury was significantly reduced after TPS treatment in mice, which may be due to the fact that some small pivotal components of TPS can permeate through the membrane of the intestinal epithelial barrier and blood-brain barrier. It has been reported that blood brain barrier permeability via caveolae-dependent endocytosis transports small molecules such as lipids into the brain [30]. However, it is necessary to further determine the small molecules that play a role in TPS, in order to promote the further study on protective effect of TPS on cerebral ischemia-reperfusion injury. In addition, given that the small molecules may regulate miRNAs by activating a series of complex intracellular signaling pathways to after entering the cell, studying the mechanism of miRNA regulation by polysaccharides in vivo also helps to explain how polysaccharides exert anti-inflammatory and antioxidant effect. Therefore, there is an urgent need to find a way to get the active molecules through the blood-brain barrier into the brain.

In summary, our study demonstrated that TPS alleviates AS injury induced by cerebral ischemia reperfusion both in vivo and in vitro, which is based on the inhibition of AS

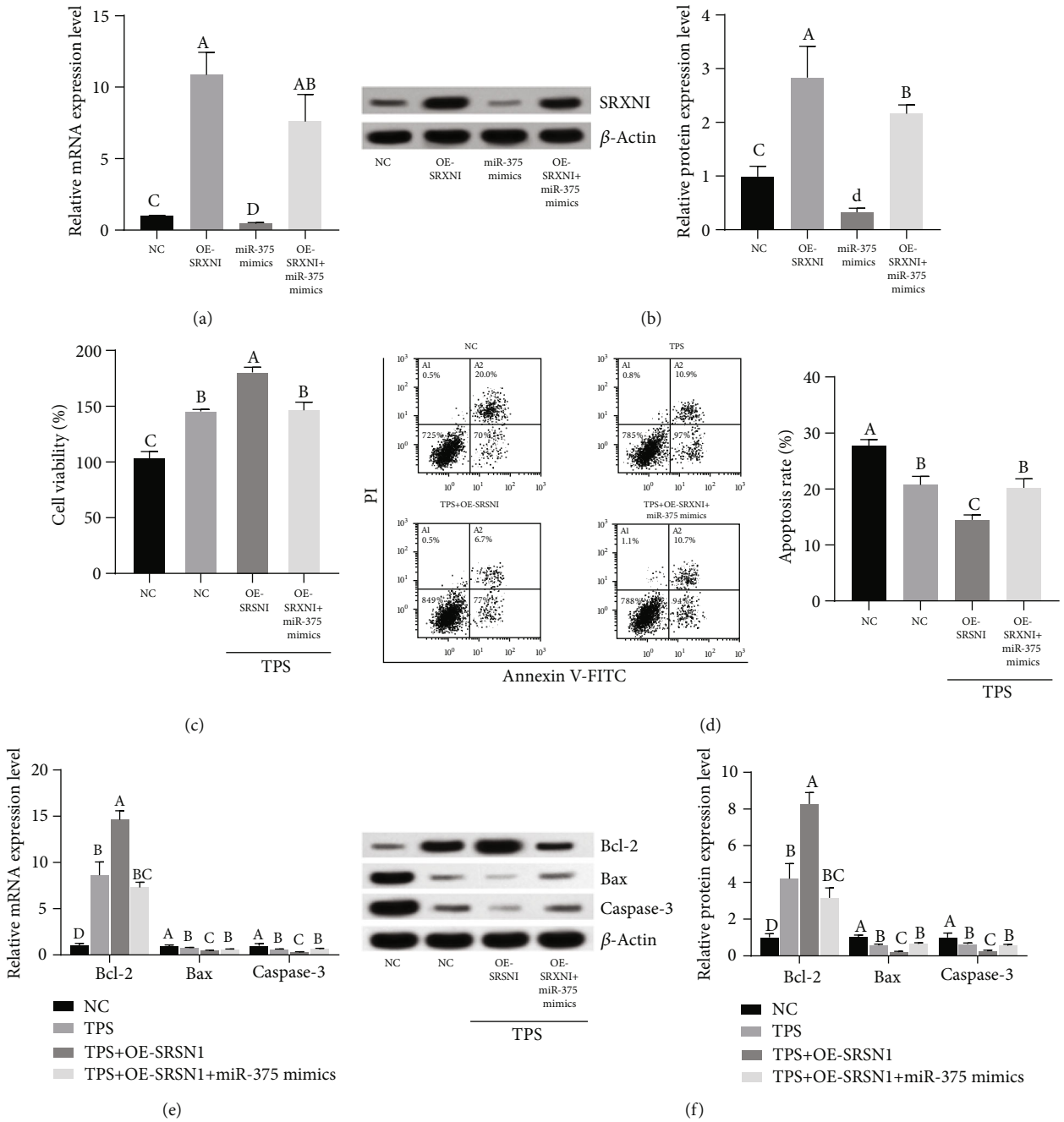

Figure 5: TPS alleviated damage of OGD/R AS via regulating miR-375/SRXN1 axis. (a) Transfection efficiency of OE-SRXN1 and/or miR-375 mimics and the effect of miR-375 on SRXN1 mRNA expression level. (b) Transfection efficiency of OE-SRXN1 and/or miR-375 mimics and the effect of miR-375 on SRXN1 protein expression level. (c) Cell viability of AS. (d) Cell apoptosis rate of AS. (e) Relative mRNA expression level of apoptosis-related protein. (f) Relative protein expression level of apoptosis-related protein. Note: each treatment in the figure has different lowercase letters, which means that the difference between the different treatments is significant ($P < 0.05$). NC: negative control.

apoptosis by regulating miR-375/SRXN1 axis. This provides a theoretical basis for the TPS clinical treatment in ischemia-reperfusion injury.

Data Availability

The data and materials used to support the findings of this study are included within the published article.

Conflicts of Interest

The authors declare that they have no conflicts of interest.

Acknowledgments

The article is supported by grant NSFC81300346 from the National Natural Science Foundation of China.

References

[1] T. Gattringer, A. Posekany, K. Niederkorn et al., "Predicting early mortality of acute ischemic stroke," *Stroke*, vol. 50, no. 2, pp. 349–356, 2019.

[2] V. Janardhan and A. I. Qureshi, "Mechanisms of ischemic brain injury," *Current Cardiology Reports*, vol. 6, no. 2, pp. 117–123, 2004.

[3] Y. P. Zhang, Y. Zhang, Z. B. Xiao et al., "CFTR prevents neuronal apoptosis following cerebral ischemia reperfusion via regulating mitochondrial oxidative stress," *Journal of Molecular Medicine*, vol. 96, no. 7, pp. 611–620, 2018.

[4] S. Michinaga and Y. Koyama, "Dual roles of astrocyte-derived factors in regulation of blood-brain barrier function after brain damage," *International Journal of Molecular Sciences*, vol. 20, no. 3, p. 571, 2019.

[5] A. Kinsner, V. Pilotto, S. Deininger et al., "Inflammatory neurodegeneration induced by lipoteichoic acid from Staphylococcus aureus is mediated by glia activation, nitrosative and oxidative stress, and caspase activation," *Journal of Neurochemistry*, vol. 95, no. 4, pp. 1132–1143, 2005.

[6] S. G. Rhee, W. Jeong, T. S. Chang, and H. A. Woo, "Sulfiredoxin, the cysteine sulfinic acid reductase specific to 2-Cys peroxiredoxin: its discovery, mechanism of action, and biological significance," *Kidney International*, vol. 72, pp. S3–S8, 2007.

[7] J. Wu, Y. Chen, S. Yu et al., "Neuroprotective effects of sulfiredoxin-1 during cerebral ischemia/reperfusion oxidative stress injury in rats," *Brain Research Bulletin*, vol. 132, pp. 99–108, 2017.

[8] A. P. Vivancos, E. A. Castillo, B. Biteau et al., "A cysteine-sulfinic acid in peroxiredoxin regulates H2O2-sensing by the antioxidant Pap 1 pathway," *Proceedings of the National Academy of Sciences*, vol. 102, no. 25, pp. 8875–8880, 2005.

[9] F. X. Soriano, F. Léveillé, S. Papadia et al., "Induction of sulfiredoxin expression and reduction of peroxiredoxin hyperoxidation by the neuroprotective Nrf 2 activator 3H-1, 2-dithiole-3-thione," *Journal of Neurochemistry*, vol. 107, no. 2, pp. 533–543, 2008.

[10] Y. Zhou, Y. Zhou, S. Yu, J. Wu, Y. Chen, and Y. Zhao, "Sulfiredoxin-1 exerts anti-apoptotic and neuroprotective effects against oxidative stress-induced injury in rat cortical astrocytes following exposure to oxygen-glucose deprivation and hydrogen peroxide," *International Journal of Molecular Medicine*, vol. 36, no. 1, pp. 43–52, 2015.

[11] L. Guo, Q. Liang, and X. Du, "Effects of molecular characteristics of on konjac glucomannan glass transitions of potato amylose, amylopection and their mixtures," *Journal of the Science of Food and Agriculture*, vol. 91, no. 4, pp. 758–766, 2011.

[12] W.-Y. Huang, S. T. Davidge, and J. Wu, "Bioactive natural constituents from food sources-potential use in hypertension prevention and treatment," *Critical Reviews in Food Science and Nutrition*, vol. 53, no. 6, pp. 615–630, 2013.

[13] D. Ren, Y. Hu, Y. Luo, and X. Yang, "Selenium-containing polysaccharides from Ziyang green tea ameliorate high-fructose diet induced insulin resistance and hepatic oxidative stress in mice," *Food function*, vol. 6, no. 10, pp. 3342–3350, 2015.

[14] P. Xu, J. Wu, Y. Zhang, H. Chen, and Y. Wang, "Physicochemical characterization of puerh tea polysaccharides and their antioxidant and α-glycosidase inhibition," *Journal of Functional Foods*, vol. 6, pp. 545–554, 2014.

[15] Y. Wang, S. Shao, P. Xu et al., "Fermentation process enhanced production and bioactivities of oolong tea polysaccharides," *Food Research International*, vol. 46, no. 1, pp. 158–166, 2012.

[16] M. Pu, J. Chen, Z. Tao et al., "Regulatory network of miRNA on its target: coordination between transcriptional and post-transcriptional regulation of gene expression," *Cellular and Molecular Life Sciences*, vol. 76, no. 3, pp. 441–451, 2019.

[17] R. Herzog, A. Zendedel, L. Lammerding, C. Beyer, and A. Slowik, "Impact of 17beta-estradiol and progesterone on inflammatory and apoptotic microRNA expression after ischemia in a rat model," *The Journal of Steroid Biochemistry and Molecular Biology*, vol. 167, pp. 126–134, 2017.

[18] Y. Liu and Y. Zhang, "Lycium barbarum polysaccharides alleviate hydrogen peroxide-induced injury by up-regulation of miR-4295 in human trabecular meshwork cells," *Experimental and Molecular Pathology*, vol. 106, pp. 109–115, 2019.

[19] Y. Ruan, H. Li, L. Pu, T. Shen, and Z. Jin, "Tremella fuciformis polysaccharides attenuate oxidative stress and inflammation in macrophages through miR-155," *Analytical Cellular Pathology*, vol. 2018, Article ID 5762371, 10 pages, 2018.

[20] Y. Cao, H. Liu, J. Zhang, and Y. Dong, "Circular RNA cZNF292 silence alleviates OGD/R-induced injury through up-regulation of miR-22 in rat neural stem cells (NSCs)," *Artificial Cells, Nanomedicine, and Biotechnology*, vol. 48, no. 1, pp. 594–601, 2020.

[21] H. Chen, Z. Qu, L. Fu, P. Dong, and X. Zhang, "Physicochemical properties and antioxidant capacity of 3 polysaccharides from green tea, oolong tea, and black tea," *Journal of Food Science*, vol. 74, no. 6, pp. C469–C474, 2009.

[22] R. Eilam, M. Segal, R. Malach, M. Sela, R. Arnon, and R. Aharoni, "Astrocyte disruption of neurovascular communication is linked to cortical damage in an animal model of multiple sclerosis," *Glia*, vol. 66, no. 5, pp. 1098–1117, 2018.

[23] M. Mann, A. Mehta, J. L. Zhao et al., "An NF-κB-microRNA regulatory network tunes macrophage inflammatory responses," *Nature Communications*, vol. 8, no. 1, p. 851, 2017.

[24] J. Guo, C. Yang, S. Zhang et al., "MiR-375 induces ROS and apoptosis in ST cells by targeting the HIGD1A gene," *Gene*, vol. 685, pp. 136–142, 2019.

[25] X. Yu, W. Zhao, X. Yang, Z. Wang, and M. Hao, "miR-375 affects the proliferation, invasion, and apoptosis of HPV16-positive human cervical cancer cells by targeting IGF-1R," *International Journal of Gynecological Cancer*, vol. 26, no. 5, pp. 851–858, 2016.

[26] L. Li, L. Jia, and Y. Ding, "Upregulation of miR-375 inhibits human liver cancer cell growth by modulating cell proliferation and apoptosis via targeting ErbB2," *Oncology Letters*, vol. 16, no. 3, pp. 3319–3326, 2018.

[27] V. J. Findlay, H. Tapiero, and D. M. Townsend, "Sulfiredoxin: a potential therapeutic agent?," *Biomedicine & Pharmacotherapy*, vol. 59, no. 7, pp. 374–379, 2005.

[28] K. F. Bell, B. al-Mubarak, J. H. Fowler et al., "Mild oxidative stress activates Nrf2 in astrocytes, which contributes to neuroprotective ischemic preconditioning," *Proceedings of the National Academy of Sciences*, vol. 108, no. 1, pp. E1–E2, 2011.

[29] S. Liebner, R. M. Dijkhuizen, Y. Reiss, K. H. Plate, D. Agalliu, and G. Constantin, "Functional morphology of the blood-brain barrier in health and disease," *Acta Neuropathologica*, vol. 135, no. 3, pp. 311–336, 2018.

[30] B. J. Andreone, B. W. Chow, A. Tata et al., "Blood-brain barrier permeability is regulated by lipid transport-dependent suppression of caveolae-mediated transcytosis," *Neuron*, vol. 94, no. 3, pp. 581–594.e5, 2017.

Hindawi
Advances in Polymer Technology
Volume 2020, Article ID 3591508, 9 pages
https://doi.org/10.1155/2020/3591508

Research Article

Anti-Inflammatory Effects of Cerium Dioxide Nanoparticles on Peritonitis in Rats Induced by *Staphylococcus epidermidis* Infection

Yan Li,[1] Hongmei Sun,[2] Zhiqi Yin,[1] Xuexi Guo,[1] and Jun Yan[1]

[1]*Department of Pathology, Tianjin First Center Hospital, Tianjin, 300192, China*
[2]*Department of Out-patient, Tianjin First Center Hospital, Tianjin, 300192, China*

Correspondence should be addressed to Jun Yan; yanhuang2@163.com

Received 3 February 2020; Revised 23 February 2020; Accepted 28 February 2020; Published 25 March 2020

Guest Editor: Jianxun Ding

Objective. To investigate the effects of cerium dioxide (CeO_2) nanoparticles on the inflammatory response of peritonitis rats induced by *Staphylococcus epidermidis* infection. *Methods*. Green tea polyphenol CeO2 nanoparticles were synthesized and characterized by transmission microscopy, ultraviolet-visible spectroscopy, FT-IR, and powder diffractometer. 40 male adult SD rats were randomly divided into 4 groups ($n = 10$ each): a control group, a model group, a CeO2 group, and a CeO2 + model group. *Staphylococcus epidermidis* solution was injected intraperitoneally with 10^7 CFU/ml of bacterial solution in the model group, while the control group was injected intraperitoneally with the same amount of normal saline, and the CeO2 and CeO2 + model groups were injected with 0.5 mg/kg CeO2 nanoparticles through the tail vein for 2 h and then injected with saline or bacterial solution for 2 h, respectively. After 0 h, 3 h, 12 h, 24 h, and 48 h of model construction, rats were sacrificed, and serum and peritoneal lavage fluid were collected. The total number of leukocytes and the percentage of each type of leukocytes in the peritoneal lavage fluid were determined. Enzyme-linked immunosorbent assay (ELISA) was used to detect the level of inflammatory factor TNF-α in serum and peritoneal lavage fluid, and myeloperoxidase (MPO) activity in peritoneal tissue was also measured. In addition, real-time fluorescence quantitative PCR (RT-PCR) was used to measure the expression of TLR2 and TLR4 in peritoneal tissue, and western blotting was used to detect the expression of TLR2, TLR4, and the activation of NF-κB signaling pathways as well. *Results*. The CeO2 has an average size of 37 ± 3 nm with binding activity to proteins, phenolic compounds, and alkaloids. After counting the white blood cells in the peritoneal lavage fluid, it was found that the total number of white blood cells and the percentage of neutrophils in the model group were significantly increased (both $P < 0.05$), and CeO2 treatment significantly reversed the above changes (both $P < 0.05$). The ELISA results showed that compared with the control group, the TNF-α in the peritoneal lavage fluid and serum of the model group increased in a time-dependent manner (all $P < 0.05$); however, there was no significant change in the CeO2 group ($P > 0.05$); at the same time in the CeO2 + model group, the TNF-α content was significantly reduced (all $P < 0.05$). Detection of MPO activity in peritoneal tissue revealed that MPO activity was significantly increased under peritonitis (all $P < 0.05$), and CeO2 treatment could mitigate that increase (all $P < 0.05$). RT-PCR results showed that compared with the control group, the expression of TLR2 and TLR4 mRNA levels in the peritoneum of the model group were increased in a time-dependent manner (all $P < 0.05$), and there was no significant change in the CeO2 group ($P > 0.05$); however, TLR2 and TLR4 mRNA levels were significantly reduced in the CeO2 + model group (all $P < 0.05$). Western blotting test was performed on the peritoneal tissue collected after 48 h of the model establishment. Compared with the control group, the levels of TLR2, TLR4, p–NF–κB, and p-IκBα protein in the model group were significantly increased (all $P < 0.05$), while CeO2 group showed no significant changes ($P > 0.05$) and administration of CeO2 before model construction can significantly reverse the above protein activation (all $P < 0.05$). *Conclusion*. CeO2 nanoparticles have anti-inflammatory effects in peritonitis caused by *Staphylococcus epidermidis* infection.

1. Background

Although the diagnosis and treatment of diseases have progressed with the development of medicine, the incidence of deaths associated with celiac infection and severe peritonitis remains high. Peritonitis can occur when infectious pathogens/microorganisms or their toxic metabolites are present in the peritoneum [1]. If the infection is aggravated due to improper handling and other reasons, it often develops into diffuse peritonitis and organ dysfunction. Peritoneal dialysis is also an important cause of peritonitis. It is often referred to as peritoneal dialysis-related peritonitis and among which, *Staphylococcus epidermidis* infection is the most common type [2]. It is reported that most of the organ damage in peritonitis is caused by the development of systemic inflammatory response syndrome (SIRS). In the occurrence and development of SIRS, there is an increase in inflammatory cytokines, tissue reactive oxygen levels, and an increase of monocytes, macrophages, and neutrophils infiltration in different organs; all of these combined together can cause tissue damage [3].

Cerium is a lanthanide series metal that can undergo a redox cycle from Ce^{4+} (oxidation) to Ce^{3+} (reduction) state and often exists in the form of cerium dioxide (CeO2). Previous studies have confirmed that CeO2 nanoparticles can act as superoxide dismutase mimics [4] and catalase mimics [5] and can reduce pulmonary hypertension [6] and reduce hypoxia-induced oxidative stress [7] as well as inhibiting cyclophosphamide-induced apoptosis [8]. In the study of peritonitis, CeO2 nanoparticles have been reported to reduce peritonitis-related SIRS [2], and other studies have found that CeO2 nanoparticles can improve diaphragmatic dysfunction caused by peritonitis [9]. In addition, green tea polyphenols, as the main ingredients of antioxidants, are well known for their antioxidant, anti-inflammatory, anticancer, anticardiolipin, antimicrobial, antihyperglycemic, and antiobesity properties [10].

In this study, a rat model of *Staphylococcus epidermidis*-induced peritonitis was established to investigate the effects of biosynthetic CeO2 nanoparticles on the inflammation of this model.

2. Materials and Methods

2.1. Plant Collection and Extraction. Green tea leaves were collected and dried to make a powder. 10 g of dried tea powder was added to a 250 ml beaker, and 100 ml of distilled water was added for continuous boiling for 10 min. The boiling solution was filtered through filter paper, and the filtrate was collected and stored at 4°C.

2.2. Synthesis of Polyphenol CeO2 Nanoparticles. 20 ml of the above filtrate was added to the conical flask, heated to boiling, and when it was cooled to 50°C, ammonium cerium nitrate solution (1 g in 50 ml of distilled water) was mixed with the filtrate and stirred until the solution turned to milky yellow. The solution was then transferred to a clean centrifuge tube and was centrifuged (12,000 rpm/min) at 4°C for 10 minutes. The supernatant was then discarded, and the milky solid precipitate at the bottom of the centrifuge tube was transferred to a quartz crucible and placed in a muffle furnace (calcined at 600°C for 1 h). A yellow-white solid was obtained after 1 h, and CeO2 nanoparticles were obtained by further grinding [11].

2.3. Characterization of Synthetic CeO2 Nanoparticles. The synthesized CeO2 nanoparticles were observed using a transmission microscope (JEM-2010, JEOL, Japan) and characterized and identified by UV-visible spectroscopy (125 spectrophotometers, PerkinElmer, Germany), and an FT-IR instrument (JASCO, USA) was used for infrared spectrum analysis. In addition, a powder diffractometer (D8, BRUKER-AXS, Germany) was used to analyze the XRD pattern.

2.4. Experimental Design and Establishment of the Rat Model of Peritonitis. 40 male Sprague Dawley rats (10-week-old, 250–300 g) were purchased from Changzhou Cavins Experimental Animal Co., Ltd. The rats were housed in a cage with an indoor temperature of 20°C–24°C and alternating light and dark cycles (12 h each) within 2 weeks of the experiment. The rats had free access to standard rodent food and water. This study was reviewed and approved by the ethics committee of our hospital, and all surgical procedures were performed in accordance with the guidelines. The rats were randomly divided into 4 groups ($n = 10$ each): the control group, the model group, the CeO2 group, and the CeO2 + model group. For the preparation of *Staphylococcus epidermidis* solution, please refer to the related literature [12]. Specifically, *Staphylococcus epidermidis* strain (ATCC 35984) was inoculated into 300 ml of conventional culture medium and shaken at 250 rpm/min at 37 °C overnight. The next day, it was centrifuged at 10,000 rpm/min for 5 minutes at 4°C. The supernatant was discarded and the pellet was collected. The pellet was then suspended in 50 ml of prechilled normal saline, centrifuged, and washed at 5000 rpm/min for 5 minutes, which was repeated three times. The final pellet was then resuspended in prechilled normal saline to prepare *Staphylococcus epidermidis* solution with a concentration of 10^7 CFU/ml. The solution was stored at 4°C for subsequent experiments. Rats in the control group were injected intraperitoneally with saline; model group was injected intraperitoneally with *Staphylococcus epidermidis* solution 10^7 CFU/ml; CeO2 group was injected with 0.5 mg/kg CeO2 nanoparticles (dissolved in 200 ml sterilized water) via tail vein 2 h before intraperitoneal saline injection; CeO2 + model group was intraperitoneally injected with 0.5 mg/kg CeO2 nanoparticles as well (dissolved in 200 ml of sterilized water) via tail vein 2 h before model construction and *Staphylococcus epidermidis* solution injection. Rats were then sacrificed at 0 h, 3 h, 12 h, 24 h, and 48 h after model construction and whole blood was centrifuged to obtain serum, peritoneal lavage fluid, and peritoneal tissue for the subsequent experiment.

2.5. Counting the Number of White Blood Cells in the Peritoneal Lavage Fluid. The peritoneal lavage fluid was centrifuged at 1,000 rpm for 10 min at room temperature, and the supernatant was collected and stored at−80°C for subsequent detection of inflammatory factors. The pellet was collected and resuspended in 200 μl PBS containing 0.6 mM EDTA. Density gradient centrifugation and Wright-Giemsa staining were used to count the white blood cells.

2.6. Detection of Inflammatory Factors in Serum and Peritoneal Lavage Fluid by ELISA. The concentration of TNF-α in peritoneal lavage fluid and serum was determined using the ELISA kit (R&D, USA) according to the manufacturer's instructions.

2.7. Detection of Myeloperoxidase Levels in Peritoneal Tissue. 3 ml of 0.05 M K-phosphate buffer (pH = 6.0) containing 0.5% cetyltrimethylammonium bromide was added to a total of 200 mg peritoneal sample and sonicated for 20 s to prepare a homogenate. Homogenate was then freeze-thawed for 3 times and centrifuged at 10,000 rpm for 15 min. Then, 0.1 ml supernatant was added and mixed to a 2.9 ml 0.05 M K-phosphate buffer (pH = 6.0) containing 0.53 mM o-diphenylamine and 0.15 mM H_2O_2. A spectrophotometer was used to measure the solution absorbance at 460 nm every 15 s continuously for 5 min. The MPO activity is expressed in U (units)/mg protein, and 1 U is defined as the degradation of 1 μM peroxide/min at 25 °C [13].

2.8. TLR2 and TLR4 mRNA Levels in Peritoneal Tissue Detected by Real-Time Fluorescence Quantitative PCR (RT-PCR). Total RNA was extracted from peritoneal tissue using an RNA extraction kit (DP420, Tiangen, China), and the concentration and purity were determined by a spectrophotometer. 1 μg of RNA was reverse transcribed into cDNA, followed by SYBR Green real-time fluorescence quantitative amplification. The primer sequences are shown in Table 1. β-Actin was used as the internal reference gene, and the relative expression of the target gene was calculated using the $2^{-\triangle\triangle Ct}$ method.

2.9. Expression of TLR2, TLR4, and NF-κb Signaling Pathway Proteins in Peritoneal Tissue Determined by Western Blotting. After washing the tissue with prechilled PBS, a certain amount of RIPA strong lysate and protease inhibitor (both purchased from Biyuntian, China) was added, and the tissue was completely lysed under ultrasound. The total protein from the peritoneal tissue was then extracted and the BCA protein concentration determination kit (Biyuntian, China) was used for protein quantification before protein was heated to denature. A certain amount of protein was added to the SDS-PAGE gel wells for electrophoresis before transferring to membranes. The membranes were then blocked, and primary antibodies were added. After incubation, membrane washing, secondary antibody incubation, membrane washing, and other steps, ECL luminescent solution was dropped on the membrane for fluorescence development. TLR2, TLR4, NF-κB p65, phosphorylated NF-κB p65 (p–NF–κB p65), IκBα, p-IκBα, and β-actin were purchased from Cell Signaling Technology, USA.

2.10. Statistical Analysis. Measurement data in this study were expressed in the form of mean ± standard deviation. t test was used for comparisons between the two groups and ANOVA analysis was used for comparison within groups under univariate conditions. $P < 0.05$ was considered statistically significant.

3. Results

3.1. Transmission Electron Microscopy and UV-Visible Spectrum Analysis of CeO2 Nanoparticles. The transmission electron microscope image of CeO2 nanoparticles is shown in Figure 1(a). The UV-visible spectrum analysis of polyphenol CeO2 nanoparticle mixtures was performed every 30 minutes. As shown in Figure 1(b), the surface plasmon resonance peak observed at 267 nm indicates the formation of CeO2 nanoparticles.

3.2. FT-IR Analysis of CeO2 Nanoparticles. As shown in Figure 2, the functional group wavelengths of polyphenol CeO2 nanoparticles were from 400 cm^{-1} to 4000 cm^{-1}. And at 3423 cm^{-1} (COOH–OH), 2960 cm^{-1} (CH), 1618 cm^{-1} (amide II band or N-diamine), 1421 cm^{-1} (COH), 1270 cm^{-1} and 1067 cm^{-1} (thio and vinyl), 916 cm^{-1}, and 831 cm^{-1} (organic sulfur compounds), CeO2 reached the peak, confirming the existence of multiple functional groups in tea polyphenols. FT-IR analysis of CeO2 nanoparticles synthesized by polyphenols showed that CeO2 nanoparticles can be combined with compounds such as proteins, phenolic compounds, and alkaloids. These chemicals play a capping reagent role in the synthesis of nanoparticles.

3.3. XRD Analysis of CeO2 Nanoparticles. As shown in Figure 3, the intensity of XRD was recorded from 20° to 80° at two angles. All the peaks obtained from the diffraction pattern were well characterized by CeO2 nanoparticles. The intensities of the narrow-tip diffraction peaks appearing at 2θ were 28.02, 33.08, 47.01, 57.45, 59.37, 69.39, and 78.43, corresponding to the lattice planes 111, 200, 220, 311, 222, 400, and 331 of CeO2 nanoparticles. The above results showed that CeO2 nanoparticles are spherical. The Debye–Scherrer equation was adopted to calculate the average size of the nanoparticles that was 37 ± 3 nm [13].

3.4. Number of Leukocytes in Peritoneal Lavage Fluid of Rats in Each Group. As shown in Figure 4(a), compared with the control group, the total number of white blood cells in the peritoneal lavage fluid of the model group was significantly increased (all $P < 0.05$) and was time-dependent (all $P < 0.05$); however, there was no significant difference in the CeO2 group ($P > 0.05$), whereas compared with the model group as shown in Figure 4(b), 4(c), and 4(d), pretreatment with CeO2 significantly reduced the total number of white

Table 1: Primer sequence.

Primer	Forward (5′-3′)	Reverse (5′-3′)
TLR2	TGGAGGTCTCCAGGTCAAATC	TTCCGCTGGACTCCAATGTC
TLR4	CCGCTCTGGCATCATCTTCA	TGGGTTTTAGGCGCAGAGTT
β-actin	CGCGAGTACAACCTTCTTGC	CGTCATCCATGGCGAACTGG

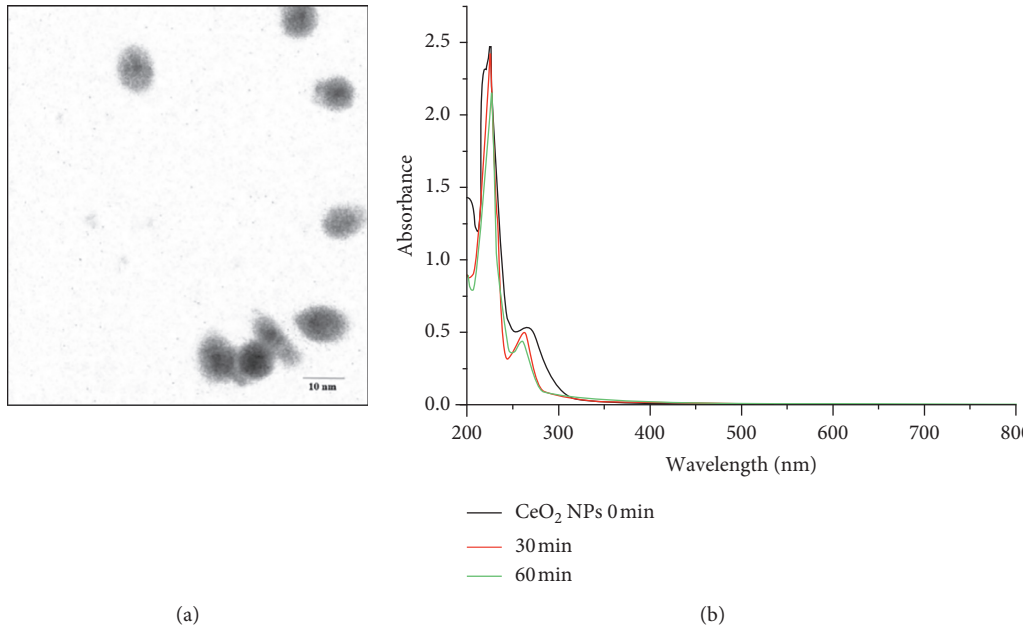

Figure 1: Transmission electron microscopy and UV-visible spectrum analysis of CeO2 nanoparticles.

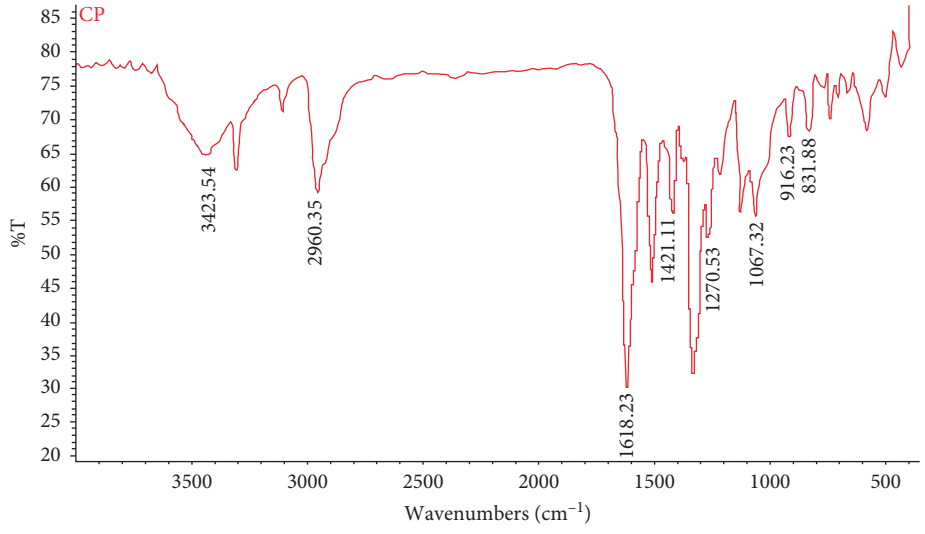

Figure 2: FT-IR analysis of CeO2 nanoparticles.

blood cells (all $P < 0.05$). The changes in the percentage of neutrophils in each group were consistent with the changes in the total number of white blood cells, while the percentage changes in macrophages and lymphocytes were the opposite.

3.5. Expression of Inflammatory Factors in Peritoneal Lavage Fluid and Serum of Rats in Each Group. As shown in Table 2, compared with the control group, TNF-α levels in the peritoneal lavage fluid of the model group rats were increased in a time-dependent manner during the period of 3–48 h after *Staphylococcus epidermidis* stimulation ($P < 0.05$); however, compared with the control group, there was no significant difference in CeO2 group ($P > 0.05$). On the other hand, compared with the model group, the administration of CeO2 before infection significantly reduced

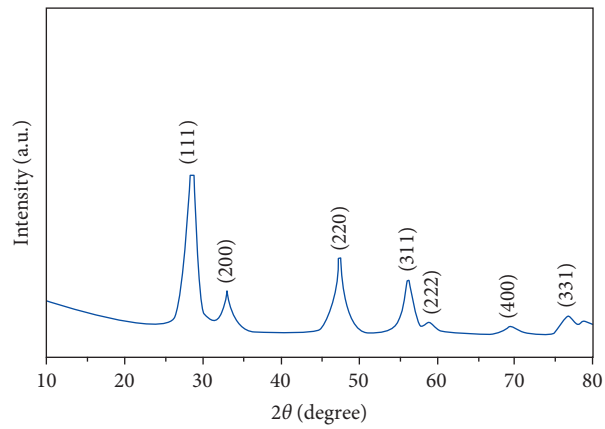

Figure 3: XRD analysis of CeO2 nanoparticles.

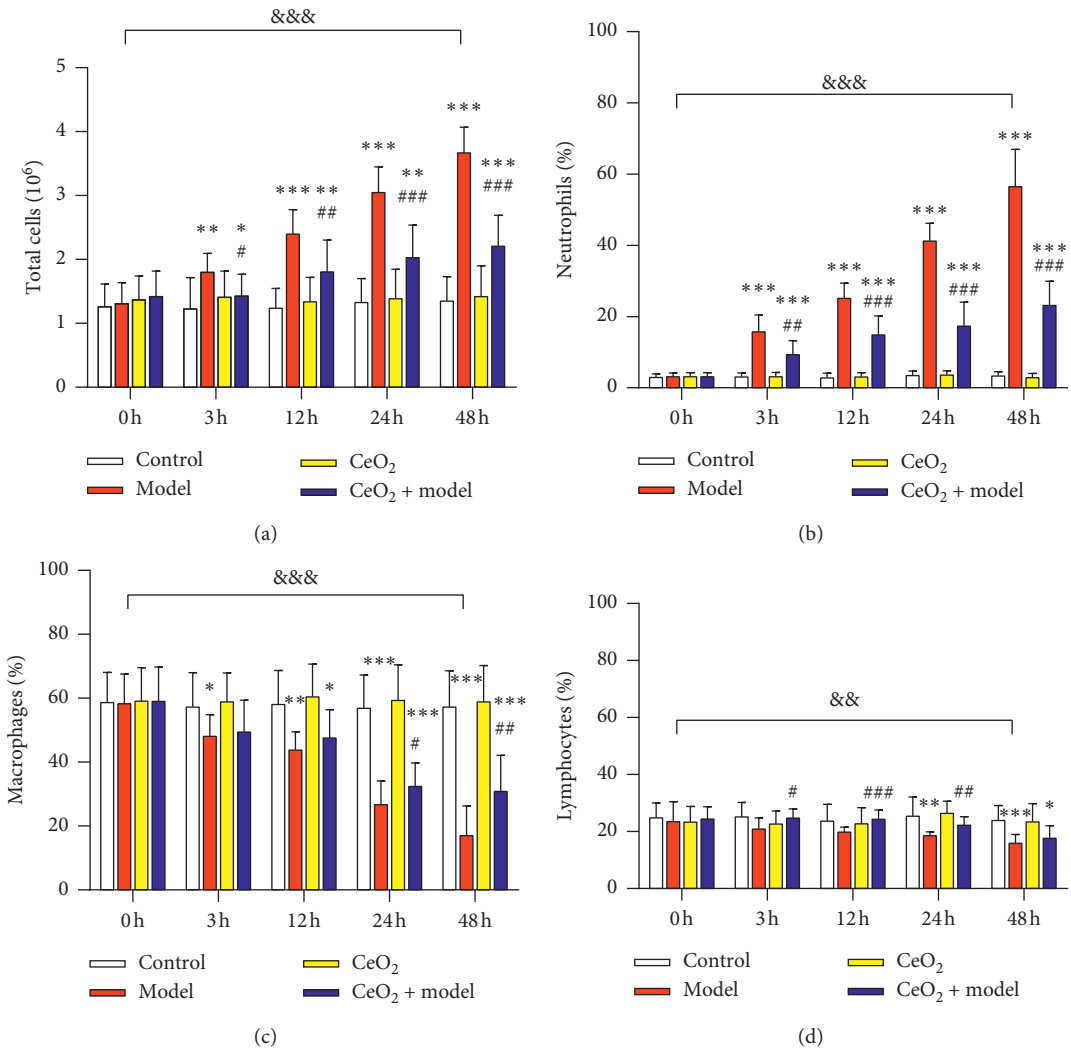

Figure 4: Differential counting of leukocytes in the peritoneal lavage fluid of each group of rats: (a) white blood cell count, (b) percentage of neutrophils, (c) percentage of macrophages, and (d) percentage of lymphocytes. Compared with the control group, $^{*}P < 0.05$, $^{**}P < 0.01$, $^{***}P < 0.001$; differences within the model group, $^{\&\&}P < 0.01$, $^{\&\&\&}P < 0.001$; compared with the model group, $^{\#}P < 0.05$, $^{\#\#}P < 0.01$, $^{\#\#\#}P < 0.001$.

Table 2: TNF-α levels in peritoneal lavage fluid of each group of rats (pg/ml).

Groups	0 h	3 h	12 h	24 h	48 h
Control	47.78 ± 3.17	44.02 ± 2.81	49.47 ± 5.11	43.01 ± 8.21	46.28 ± 4.01
Model	42.84 ± 6.38	$130.28 \pm 10.34^{**\&\&}$	$289.33 \pm 19.23^{***\&\&}$	$331.90 \pm 22.24^{**\&\&}$	$377.84 \pm 25.34^{**\&\&}$
CeO2	48.29 ± 2.34	41.02 ± 7.81	49.65 ± 2.33	47.01 ± 4.82	49.52 ± 3.11
CeO2 + model	49.88 ± 2.88	$77.12 \pm 5.34^{*\#\#\#}$	$87.32 \pm 11.34^{**\#\#\#}$	$100.24 \pm 12.54^{**\#\#}$	$130.23 \pm 14.23^{*\#\#\#}$

Note. Compared with the control group, $^{*}P < 0.05$, $^{**}P < 0.01$, $^{***}P < 0.001$; differences within the model group, $^{\&\&}P < 0.01$; compared with the model group, $^{\#\#}P < 0.01$, $^{\#\#\#}P < 0.001$.

TNF-α levels ($P < 0.05$). Table 3 shows that the serum results were consistent with the results obtained from peritoneal lavage fluid.

3.6. MPO Activity in Peritoneal Tissue of Rats in Each Group. As shown in Figure 5, compared with the control group, the MPO activity in the peritoneal tissue of the model group was significantly higher (all $P < 0.05$) and was time-dependent (all $P < 0.001$). No significant difference in the CeO2 group ($P > 0.05$) was observed compared to the control group. However, compared with the model group, the administration of CeO2 before infection significantly reduced MPO activity (all $P < 0.05$).

3.7. mRNA Levels of TLR2 and TLR4 in the Peritoneal Tissue of Rats in Each Group. As shown in Figure 6, RT-PCR results showed that compared with the control group, mRNA expression levels of TLR2 and TLR4 in the peritoneal tissue of the model group rats increased gradually after infection with *Staphylococcus epidermidis* (all $P < 0.05$), but there was no significant difference in CeO2 group ($P > 0.05$). However, compared with the model group, mRNA expression levels of TLR2 (Figure 6(a)) and TLR4 (Figure 6(b)) in the CeO2 + model group were reduced, and the difference was significant (all $P < 0.05$). ELISA and RT-PCR results suggested that with the establishment of the model, the inflammatory response gradually increased with time. Therefore, in the western blotting experiment, 48 h was chosen as the final detection time point.

3.8. Expression of TLR2, TLR4, and NF-κB Signaling Pathway Proteins in the Peritoneal Tissue of Each Group of Rats. As shown in Figure 7, western blot results showed that compared with the control group, the levels of TLR2, TLR4, p–NF–κB, and p-IκBα protein in the model group were significantly increased (all $P < 0.05$). However, no significant changes were found in the CeO2 group ($P > 0.05$). Compared with the model group, the levels of TLR2, TLR4, p–NF–κB, and p-IκBα protein in the CeO2 + model group were significantly reduced (all $P < 0.05$).

4. Discussion

Peritonitis is a major complication of peritoneal dialysis, a technique used to treat end-stage renal disease [14]. Among others, *Staphylococcus epidermidis* is an important pathogenic bacterium in the peritonitis with extremely strong drug resistance, so it is very difficult to completely remove them. In the occurrence of peritonitis, pathogenic bacteria can enter the abdominal cavity through the catheter or catheter outlet, activating peritoneal mesothelial cells and macrophages, which in turn releases a series of products including pro-inflammatory mediators to cause an inflammatory response [15].

Nanotechnology has shown great potential in improving the quality of daily life and has been widely used in the fields of new material production, industry, consumer goods, and medical applications. Studies have found the positive effects of CeO2 nanoparticles in antioxidant therapy, neuroprotection, radiation protection, and eye protection [16]. Meldrum et al. have confirmed that CeO2 nanoparticles can affect the occurrence of allergic airway diseases by regulating the pulmonary inflammation caused by exhaust particles and allergens [17]. With the in-depth study of nanomedicine, the organic combination of nanoparticles and bioactive drugs has gradually become a research hotspot. Green tea polyphenols, as the main component of antioxidants, have anti-inflammatory properties [10]. In view of the anti-inflammatory advantages of CeO2 nanoparticles, and no related reports on the effects of CeO2 nanoparticles on peritonitis, in this study, CeO2 nanoparticles were first biosynthesized based on the literature, and the nanoparticles were further characterized and identified by transmission microscope observation, ultraviolet-visible spectrum, infrared spectrum, and XRD pattern and then peritonitis induced by *Staphylococcus epidermidis* in rats was established to explore the role of biosynthesized CeO2 nanoparticles on the inflammatory response to peritonitis.

The NF-κB pathway is a typical proinflammatory signaling pathway, which plays an important role in the pathogenesis of inflammatory reactive diseases. NF-κB can be activated through the activation of Toll-like receptors (TLRs) to upregulate proinflammatory genes including cytokines, chemokines, and adhesion molecules [18]. TLRs are single, type I transmembrane glycoprotein that plays an important defensive role by activating immune cell responses in both innate and adaptive immune responses [19]. When the ligand binds to TLRs, it can trigger the myeloid differentiation primary response protein 88-TNFα receptor-related factor 6-transforming growth factor β-activated kinase 1-IκB kinase protein phosphorylation, leading to activation of NF-κB light chain enhancer, thereby promoting the production of inflammatory factors and inducing an inflammatory response. In this study, by detecting the mRNA and protein expression levels of TLR2 and TLR4, we found that the expression of the two receptors increased to

Table 3: TNF-α levels in serum of each group of rats (pg/ml).

Groups	0 h	3 h	12 h	24 h	48 h
Control	7.74 ± 1.26	7.90 ± 2.36	8.14 ± 2.77	9.04 ± 1.17	8.22 ± 1.77
Model	7.10 ± 1.87	$15.24 \pm 3.44^{*}\&\&$	$23.22 \pm 5.34^{**}\&\&$	$27.99 \pm 7.14^{**}\&\&\&$	$30.22 \pm 5.88^{***}\&\&\&$
CeO2	6.95 ± 2.70	6.15 ± 2.66	7.23 ± 3.01	7.29 ± 1.99	6.90 ± 1.73
CeO_2 + model	7.04 ± 2.01	$10.12 \pm 4.24^{**}\#\#\#$	$14.23 \pm 4.99^{***}\#\#\#$	$16.20 \pm 4.33^{***}\#\#$	$18.11 \pm 5.39^{***}\#\#\#$

Note. Compared with the control group, $^{*}P < 0.05$, $^{**}P < 0.01$, $^{***}P < 0.001$; differences within the model group, $^{\&\&\&}P < 0.001$; compared with the model group, $^{\#\#}P < 0.01$, $^{\#\#\#}P < 0.001$.

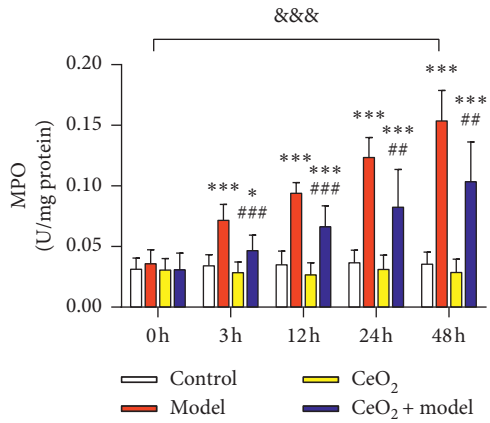

Figure 5: MPO activity changes in peritoneal tissue of rats in each group. Compared with the control group, $^{*}P < 0.05$, $^{***}P < 0.001$; differences within the model group, $^{\&\&\&}P < 0.001$; compared with the model group, $^{\#\#}P < 0.01$, $^{\#\#\#}P < 0.001$.

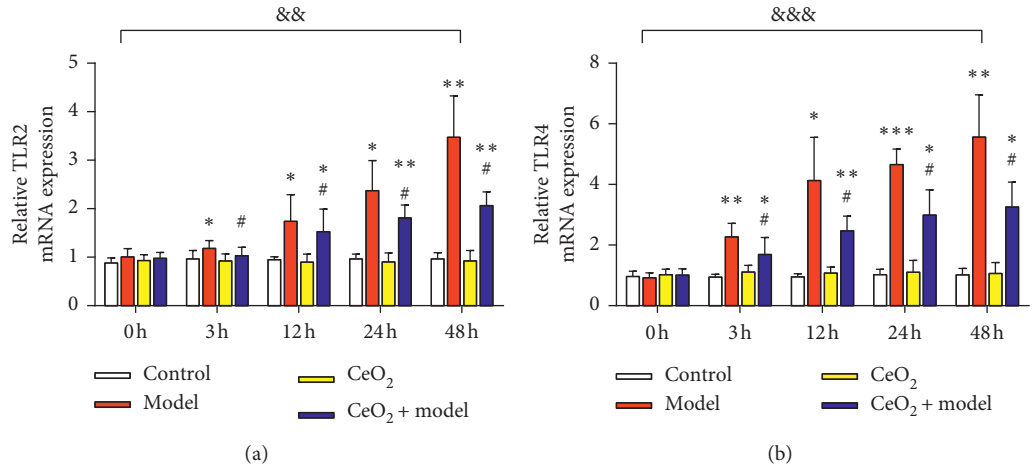

Figure 6: mRNA expression changes in the peritoneal tissue of each group of rats: (a) changes in mRNA expression levels of TLR2; (b) changes in mRNA expression levels of TLR4. Compared with the control group, $^{*}P < 0.05$, $^{**}P < 0.01$, $^{***}P < 0.001$; differences within the model group, $^{\&\&}P < 0.01$, $^{\&\&\&}P < 0.01$; compared with the model group, $^{\#}P < 0.05$.

varying degrees under the condition of peritonitis. By further testing the downstream IκBα and NF-κB signaling pathways, we found their phosphorylation levels were increased, suggesting that this signaling pathway was activated. In addition, the number of white blood cells in the peritoneal lavage fluid and the percentage of various types of white blood cells, the activity of myeloperoxidase, and the protein expression level of the inflammatory factor TNF-α were also measured in this study. The white blood cell count and the proportion of neutrophils can directly reveal the inflammatory status of the cells; MPO is a heme protein synthesized during the myeloid differentiation process. As a special component in neutrophils, its concentration is related to the severity of inflammation; TNF-α is a proinflammatory factor secreted by monocytes and is known for its strong inflammatory effect. This study tested the above indicators to confirm that the peritonitis status can increase the total number of white blood cells and the proportion of neutrophils, enhance MPO activity, and induce a significant increase in TNF-α levels in peritoneal lavage fluid and

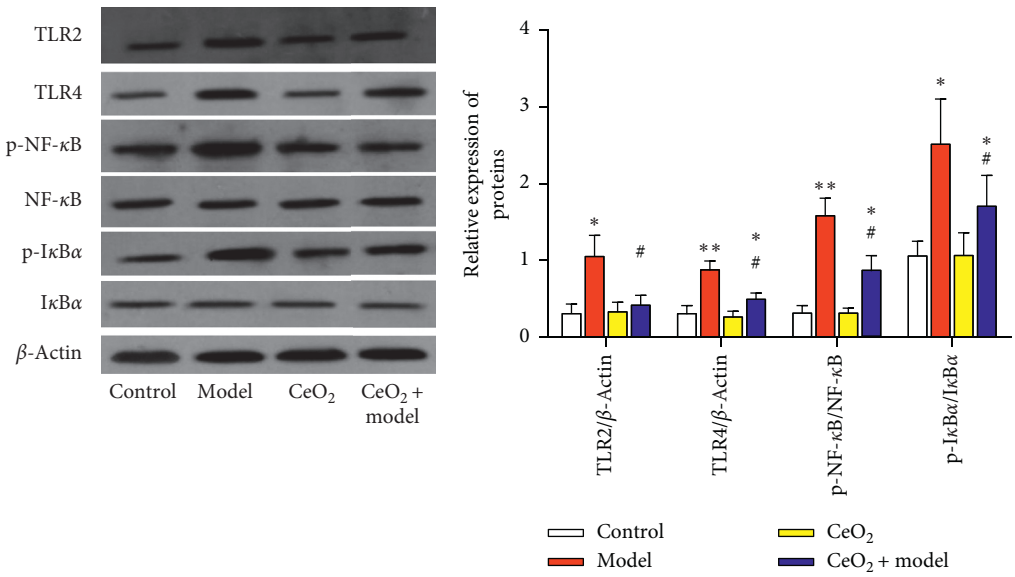

FIGURE 7: Changes of protein expression in peritoneal tissue of rats in each group. Compared with the control group, $^{*}P < 0.05$, $^{**}P < 0.01$; compared with the model group, $^{\#}P < 0.05$.

serum. And CeO2 nanoparticles can reduce the levels of the above indicators to different degrees and thus exert the anti-inflammatory effects.

In summary, this study found that in the occurrence and development of peritonitis caused by *Staphylococcus epidermidis*, CeO2 inhibited the transcription of TLR2 and TLR4 genes, inhibited the activation of the NF-κB signaling pathway, and further inhibited its downstream inflammatory factor TNF-α and reduced the number of white blood cells, thereby mitigating the occurrence of inflammatory reactions. Therefore, it is suggested that CeO2 plays a protective role in *Staphylococcus epidermidis*-induced peritonitis and provides new ideas for the treatment of this disease.

Data Availability

The data used to support the findings of this study are included within the article.

Conflicts of Interest

The authors declare that they have no conflicts of interest.

Acknowledgments

This study was supported by grant NSFC81300346 from the National Natural Science Foundation of China.

References

[1] J. O. A. M. van Baal, K. K. Van de Vijver, R. Nieuwland et al., "The histophysiology and pathophysiology of the peritoneum," *Tissue and Cell*, vol. 49, no. 1, pp. 95–105, 2017.

[2] N. D. P. K. Manne, R. Arvapalli, N. Nepal et al., "Therapeutic potential of cerium oxide nanoparticles for the treatment of peritonitis induced by polymicrobial insult in sprague-dawley rats," *Critical Care Medicine*, vol. 43, no. 11, pp. e477–e489, 2015.

[3] M. Bosmann and P. A. Ward, "The inflammatory response in sepsis," *Trends in Immunology*, vol. 34, no. 3, pp. 129–136, 2013.

[4] V. Baldim, N. F. Bedioui, and I. MargaillBerret, "The enzyme-like catalytic activity of cerium oxide nanoparticles and its dependency on Ce3+ surface area concentration," *Nanoscale*, vol. 10, no. 15, pp. 6971–6980, 2018.

[5] B.-H. Chen and B. Stephen Inbaraj, "Various physicochemical and surface properties controlling the bioactivity of cerium oxide nanoparticles," *Critical Reviews in Biotechnology*, vol. 38, no. 7, pp. 1003–1024, 2018.

[6] M. B. Kolli, N. D. P. K. Manne, R. Para et al., "Cerium oxide nanoparticles attenuate monocrotaline induced right ventricular hypertrophy following pulmonary arterial hypertension," *Biomaterials*, vol. 35, no. 37, pp. 9951–9962, 2014.

[7] A. Arya, N. Sethy, S. Singh, and M. Das, "Cerium oxide nanoparticles protect rodent lungs from hypobaric hypoxia-induced oxidative stress and inflammation," *International Journal of Nanomedicine*, vol. 8, no. 8, pp. 4507–4520, 2013.

[8] M. Hamzeh, S. J. Hosseinimehr, A. Karimpour, A. R. Mohammadi, and F. Talebpour Amiri, "Cerium oxide nanoparticles protect cyclophosphamide-induced testicular toxicity in mice," *International Journal of Preventive Medicine*, vol. 10, no. 1, p. 5, 2019.

[9] S. Asano, R. Arvapalli, N. Manne et al., "Cerium oxide nanoparticle treatment ameliorates peritonitis-induced diaphragm dysfunction," *International Journal of Nanomedicine*, vol. 10, pp. 6215–6225, 2015.

[10] M. Prasanth, B. Sivamaruthi, C. Chaiyasut, and T. Tencomnao, "A review of the role of green tea (camellia sinensis) in antiphotoaging, stress resistance, neuroprotection, and autophagy," *Nutrients*, vol. 11, no. 2, p. 474, 2019.

[11] X.-Li Tencomnao, Li Sun, Yi Fan et al., "Effects of curcumine on expressions of toll-like receptor 2 and 6 in rat peritoneum during acute peritonitis," *Chinese Journal of Nephrology, Dialysis and Transplantation*, vol. 21, pp. 244–248, 2012.

[12] G. Chen and Y. Xu, "Biosynthesis of cerium oxide nanoparticles and their effect on lipopolysaccharide (LPS) induced sepsis mortality and associated hepatic dysfunction in male sprague dawley rats," *Materials Science and Engineering: C*, vol. 83, pp. 148–153, 2018.

[13] Y. Xia and J. L. Zweier, "Measurement of myeloperoxidase in leukocyte-containing tissues," *Analytical Biochemistry*, vol. 245, no. 1, pp. 93–96, 1997.

[14] R. Mehrotra, O. Devuyst, S. J. Davies, and D. W. Johnson, "The current state of peritoneal dialysis," *Journal of the American Society of Nephrology*, vol. 27, no. 11, pp. 3238–3252, 2016.

[15] C. C. Johnson and S. J. Jenkins, "The biology of serous cavity macrophages," *Cellular Immunology*, vol. 330, pp. 126–135, 2018.

[16] S. Hussain, F. Al-Nsour, A. B Rice et al., "Cerium dioxide nanoparticles do not modulate the lipopolysaccharide-induced inflammatory response in human monocytes," *International Journal of Nanomedicine*, vol. 7, pp. 1387–1397, 2012.

[17] K. Meldrum, S. Robertson, I. Römer et al., "Diesel exhaust particle and dust mite induced airway inflammation is modified by cerium dioxide nanoparticles," *Environmental Toxicology and Pharmacology*, vol. 73, p. 103273, 2020.

[18] S. Mitchell, J. Vargas, and A. Hoffmann, "Signaling via the NFκB system," *Wiley Interdisciplinary Reviews: Systems Biology and Medicine*, vol. 8, no. 3, pp. 227–241, 2016.

[19] A. M. Hosseini, J. Majidi, B. Baradaran et al., "Toll-like receptors in the pathogenesis of autoimmune diseases," *Advanced Pharmaceutical Bulletin*, vol. 5, no. 1, p. p605, 2015.

Hindawi
Advances in Polymer Technology
Volume 2020, Article ID 4239207, 7 pages
https://doi.org/10.1155/2020/4239207

Research Article

Preparation and Characterization of PEG4000 Palmitate/PEG8000 Palmitate-Solid Dispersion Containing the Poorly Water-Soluble Drug Andrographolide

Qingyun Zeng, Liquan Ou, Guowei Zhao, Ping Cai, Zhenggen Liao, Wei Dong, and Xinli Liang

Key Laboratory of Modern Preparation of Traditional Chinese Medicine, Ministry of Education, Jiangxi University of Traditional Chinese Medicine, Nanchang 330004, China

Correspondence should be addressed to Guowei Zhao; weiweihaoyunqi@163.com

Received 4 December 2019; Revised 21 January 2020; Accepted 20 February 2020; Published 19 March 2020

Guest Editor: Yu Tao

Solid dispersion (SD) is the effective approach to improve the dissolution rate and bioavailability of class II drugs with low water solubility and high tissue permeability in the Biopharmaceutics Classification System. This study investigated the effects of polyethylene glycol (PEG) molecular weight in carrier material PEG palmitate on the properties of andrographolide (AG)-SD. We prepared SDs containing the poorly water-soluble drug AG by the freeze-drying method. The SDs were manufactured from two different polymers, PEG4000 palmitate and PEG8000 palmitate. The physicochemical properties of the AG-SDs were characterized by Fourier transform infrared spectroscopy, thermogravimetric analysis, differential scanning calorimetry, powder X-ray diffraction, scanning electron microscopy, dissolution testing, and so on. We found that AG-PEG4000 palmitate-SD and AG-PEG8000 palmitate-SD were similar in the surface morphology, specific surface area, and pore volume. Compared with the AG-PEG4000 palmitate-SD, the intermolecular interaction between PEG8000 palmitate and AG was stronger, and the thermal stability of AG-PEG8000 palmitate-SD was better. In the meanwhile, the AG relative crystallinity was lower and the AG dissolution rate was faster in AG-PEG8000 palmitate-SD. The results demonstrate that the increasing PEG molecular weight in the PEG palmitate can improve the compatibility between the poorly water-soluble drug and carrier material, which is beneficial to improve the SD thermal stability and increases the dissolution rate of poorly water-soluble drug in the SD.

1. Introduction

Oral administration is the most common route of administration due to its convenience, low cost, and flexible design. However, a major disadvantage of oral administration is the low bioavailability, usually due to poor water solubility and low permeability of active pharmaceutical ingredients (API) [1].

Although Class II drugs in the Biopharmaceutics Classification System (BCS) have high tissue permeability, their oral bioavailability is commonly low. This means that bioavailability is solubility dependent [1]. Therefore, one of the major challenges of the pharmaceutical industry is to apply strategies which can improve the solubility of these drugs to develop such problematic APIs into orally bioavailable and therapeutic effective drugs [2, 3] Solid dispersion (SD) is one of the most effective approaches to improve the solubility, dissolution rate, and the bioavailability of poorly water-soluble drugs [4–7]. SD has a wide range of advantages, such as reducing particle size to the molecular level, preventing the agglomeration of the drug particles by the interactions between the drug and carrier material, and releasing drug at supersaturated state, which can improve drug absorption.

Polyethylene glycol (PEG) has a very low melting point and is easily soluble in water and organic solvents. Therefore, PEG is suitable for the preparation of SD by the melting method and the solvent method [8, 9], and it is one of the most commonly used carrier materials in SD. However, PEG

is a hydrophilic polymer and most of Class II drugs are hydrophobic compounds, so the solubility of most drugs in PEG is very limited. The hydrophobic drug in SD is often in a supersaturated state and has a tendency to recrystallize in the preparation process (cooling or solvent removal) and during storage of SD [10–13]. Therefore, in the previous research [14], the carbon chain was grafted on PEG to increase the lipophilicity of the hydrophilic carrier material, and the effect of the carrier material lipophilicity on the physicochemical properties and dissolution behavior of SD was studied. The results showed that in the andrographolide (AG)-SD prepared by PEG-saturated fatty acid ester with different long carbon chains as a carrier material, the crystallinity and the melting temperature reduced and the dissolution rate of AG increased with the increase of the length of carbon chain of PEG-saturated fatty acid ester. This indicated that the increase of carrier material lipophilicity is beneficial to the thermal stability of SD, the decrease of crystallinity, and the increase of dissolution rate of poorly water-soluble drug in the SD.

Andrographolide (AG), a diterpenoid lactone, is isolated from the Chinese herb *Andrographis paniculata*. It has been proved to have many pharmacological actions, such as analgesic, antipyretic, anti-inflammatory, antiviral, and anticancer [15–18]. The potential use of AG has attracted great attention in recent years. AG has low aqueous solubility (74 μg/ml). The therapeutic use of AG is restricted by its poor solubility in water, which results in low bioavailability after oral administration. Therefore, AG was still chosen as a model drug to further study the effect of PEG molecular weight on the SD properties when PEG fatty acid was used as the carrier material for preparing SD.

2. Materials and Methods

2.1. Materials. Andrographolide (AG) was purchased from Hao-Xuan Biotechnology Co., Ltd. (Xi'an, China). The PEG4000 palmitate and PEG8000 palmitate were synthesized in the laboratory.

2.2. Preparation of Physical Mixture (PM). The physical mixtures of AG and the carrier material with a batch size of 3 g were prepared by mixing the components with a pestle in a mortar and using geometric dilution. The mixtures were sieved using a mesh of 250 μm. The drug: carrier weight ratio was 1 : 3 (w/w) [14]. The samples were labeled as AG-PEG4000 palmitate-PM and AG-PEG8000 palmitate-PM, respectively. The samples were stored in a desiccator over silica gel prior to use to decrease the potential effect of hygroscopicity.

2.3. Preparation of AG-SD by Freeze-Drying Method. The PM was dissolved in 30% ethanol using a magnetic stirrer. The solution was frozen at liquid nitrogen for 1 h and subsequently freeze-dried for 24 h at −40°C using a FreeZone freeze-dryer (Labconco Corp., USA). The powder was collected and then stored in a desiccator over silica gel prior to use to decrease the potential effect of hygroscopicity. The prepared SDs were labeled as AG-PEG4000 palmitate-SD and AG-PEG8000 palmitate-SD, respectively.

2.4. Fourier Transform Infrared Spectroscopy (FT-IR). A Spectrum Two FT-IR spectrometer (PerkinElmer Corp., USA) was used for collecting the spectra. A small amount of each sample was placed in a mortar with potassium bromide and triturated with a pestle, which was compressed into a disc by using a FW-4A powder compressing instrument (Uncommon Sci. Tech. Development Co., Ltd., Tianjin, China). The spectral region from 400 to 4000 cm^{-1} was collected as an accumulation of 64 scans.

2.5. Thermogravimetric (TG) Analysis. TG analysis of SDs and physical mixtures was determined by a TG/DTA6300 thermal analysis instrument (SII Nano Technology Inc., Japan). The samples (~5 mg) were placed in open aluminum pans and heated from 30°C to 500°C at 10°C/min.

2.6. Powder X-Ray Diffraction (XRD). XRD analysis of samples was conducted by using an X-ray diffractometer (D8 Advance, Bruker) with a copper anode (Cu Kα radiation). The operating voltage and current were set to 40 kV and 40 mA, respectively. The diffraction pattern was measured at room temperature with 2θ scanning from 5° to 55°.

2.7. Differential Scanning Calorimetry (DSC). The samples (~5 mg) were placed in standard aluminum pans and sealed. The crimped pans were heated from 20°C to 270°C at a scanning rate of 10°C/min using nitrogen gas (20 mL/min) to purge the DSC. A Diamond DSC instrument (PerkinElmer Corp., USA) was calibrated using pure indium before measurement.

2.8. Scanning Electron Microscopy (SEM). A Quanta 250 scanning electron microscope (FEI Corp., USA) was used to generate electron micrograph images. The SDs and physical mixtures were mounted on an aluminum stub using double-sided adhesive tape. The samples were then sputter-coated with gold for 60 s. Micrographs with different magnifications were taken to determine the surface morphology of SDs and physical mixtures.

2.9. Specific Surface Area and Pore Volume. The surface area and pore volume of different grades of SDs and physical mixtures were determined by nitrogen adsorption technique using a TriStar3000 surface area and pore volume analyzer (Micromeritics Instrument Corp., USA) [19, 20]. Moisture was removed from the samples prior to the surface area measurement by nitrogen flow at room temperature overnight using a Flow Pre-degasser (Micromeritics Instrument Corp., USA).

2.10. High-Performance Liquid Chromatography (HPLC) Analysis. An Agilent 1260 HPLC system (Agilent Corp.,

USA) with a C_{18} column (150 mm × 4.6 mm, 5 μm) was used for the AG analysis. A mobile phase of methanol and water (60 : 40, *V*: *V*) was used at a flow rate of 1 mL/min. A UV detector was utilized, and the absorption peak for AG was investigated at a maximum wavelength of 225 nm.

2.11. Dissolution Testing. The drug release was performed using the Chinese Pharmacopoeia paddle method with a ZRS-8G dissolution tester (Tianda Tianfa Technology Co., Ltd., China). The 900 mL redistilled water in the dissolution vessels was heated and maintained at 37 ± 0.5°C. The samples (0.10 g) were placed into the dissolution vessels at a rotation rate of 100 rpm. The 1.5 mL aliquots were withdrawn at predetermined time intervals (5, 10, 15, 30, 45, 60, 90, and 120 min) and filtered with a 0.22 μm membrane filter. An equal volume of fresh medium was added to keep an invariable dissolution volume in the meantime. The obtained filtrates were analyzed according to the aforementioned HPLC condition.

2.12. Statistical Analysis. The cluster analysis was calculated using SPSS19.0 software.

3. Results and Discussion

3.1. FT-IR. Figure 1 shows the FT-IR spectra of pure AG, physical mixtures, and SDs. The –OH absorption peak in pure AG is at 3317 cm^{-1}, the absorption peak position was not shifted or shifted slightly in all the physical mixtures, and the absorption peak position in the AG-PEG4000 palmitate-SD and the AG-PEG8000 palmitate-SD was blue shifted to 3326 cm^{-1} and 3339 cm^{-1}, respectively. This indicated that there was an intermolecular interaction between AG and PEG palmitate after the preparation of SD, which may form a hydrogen bond. The intermolecular hydrogen bonds between the drug and the carrier material facilitated the stability of the SD during storage [21, 22]. Moreover, compared with AG-PEG4000 palmitate-SD, the blue shift of the –OH absorption peak in AG-PEG8000 palmitate-SD was greater. This may be due to the increase of the PEG molecular weight in PEG palmitate, which can increase the lipophilicity of the carrier material, and thus improve the compatibility of PEG palmitate with the poorly water-soluble drug AG.

3.2. TG. The TG analysis of pure AG, physical mixtures, and SDs is shown in Figure 2. The 5% weight-loss temperature (T_i) of all samples is listed in Table 1. As can be seen from Table 1, the T_i of the prepared SDs and physical mixtures was significantly higher than that of pure AG. The T_i of the SD was 1°C–3°C higher than the corresponding physical mixture. This indicated that the interaction between AG and the carrier material in the SD was greater than the physical mixture. This was due to the fact that AG and carrier materials are in contact with each other in the molecular form in the preparation process of SD, which is more advantageous to enhance the intermolecular interaction than the preparation process of physical mixtures.

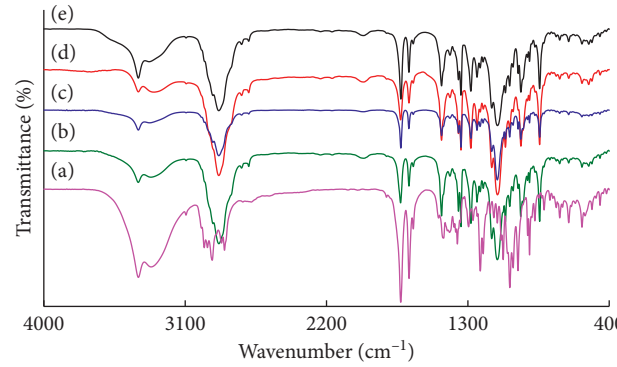

Figure 1: FT-IR spectra of (a) pure AG, (b) AG-PEG4000 palmitate-PM, (c) AG-PEG4000 palmitate-SD, (d) AG-PEG8000 palmitate-PM, and (e) AG-PEG8000 palmitate-SD.

The T_i of the physical mixture and SD prepared with PEG8000 palmitate as a carrier material was significantly increased as compared to the physical mixture and SD prepared with PEG4000 palmitate as a carrier material. This may be due to the higher compatibility of PEG8000 palmitate with poorly water-soluble drug AG, thereby increasing the thermal stability of the SD and physical mixture prepared with PEG8000 palmitate as the carrier material.

3.3. XRD. To confirm the crystalline structure of AG and the effect of carriers on it, XRD patterns of pure AG, SDs, and physical mixtures were studied, which are shown in Figure 3. The intense diffraction peaks were observed at 9.78, 11.97, 14.78, 15.67, 17.67, 18.44, and 22.62 2θ degrees, which revealed high crystallinity of AG. Both the SDs and physical mixtures showed the overlap of XRD patterns related to AG. Compared with physical mixtures, the intensity of AG diffraction peaks decreased significantly in the prepared SDs. This indicated that AG was not in the completely crystal state and was in a partial-amorphous and partial-crystal state in the as-prepared SDs.

3.4. DSC. The DSC thermograms of pure AG, physical mixtures, and SDs are shown in Figure 4. Figure 4(a) shows pure AG to have a sharp melting point of 243°C confirming its crystallinity. All the two physical mixtures and two SDs had a strong endothermic peak (T_{m1}) at about 60°C and a weak endothermic peak (T_{m2}) near 210°C–230°C. The T_{m1} and T_{m2} were the endothermic peaks of PEG palmitate and AG, respectively.

It was observed that the endothermic peak of AG and no glass transition on DSC thermograms of the SDs indicated that AG was not in 100% amorphous state in the SDs. The T_{m2} of SD was about 8°C lower than the corresponding physical mixture (see in Figure 4 and Table 1), which indicated that the existential state of AG in SD was different from that in the corresponding physical mixture. The above results showed that AG existed in partial-crystal and partial-amorphous state in the prepared AG-PEG palmitate-SDs. The result was consistent with that of XRD.

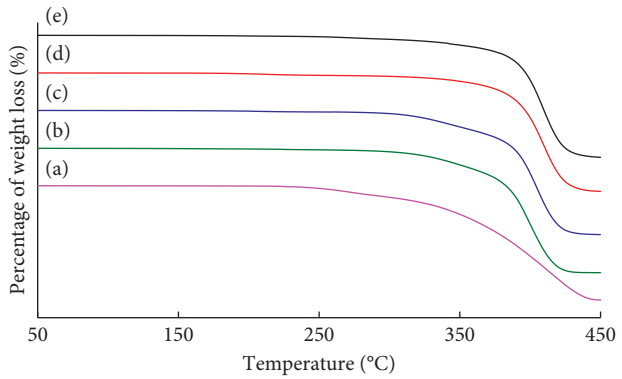

Figure 2: TG curves of (a) pure AG, (b) AG-PEG4000 palmitate-PM, (c) AG-PEG4000 palmitate-SD, (d) AG-PEG8000 palmitate-PM, and (e) AG-PEG8000 palmitate-SD.

Table 1: T_i and T_m of pure AG, physical mixtures (PM) and SD.

Sample	T_i (°C)	T_{m1} (°C)	T_{m2} (°C)
AG	272		243
AG-PEG4000 palmitate-PM	318	60	228
AG-PEG4000 palmitate-SD	319	57	220
AG-PEG8000 palmitate-PM	323	64	226
AG-PEG8000 palmitate-SD	326	61	218

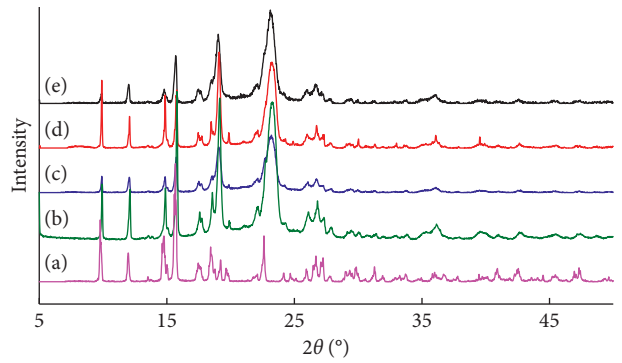

Figure 3: XRD patterns of (a) pure AG, (b) AG-PEG4000 palmitate-PM, (c) AG-PEG4000 palmitate-SD, (d) AG-PEG8000 palmitate-PM, and (e) AG-PEG8000 palmitate-SD.

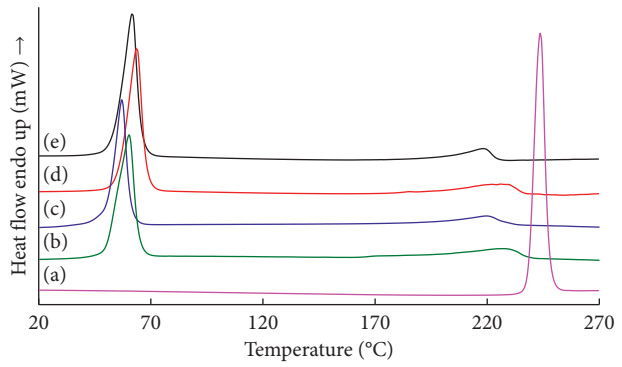

Figure 4: DSC thermograms of (a) pure AG, (b) AG-PEG4000 palmitate-PM, (c) AG-PEG4000 palmitate-SD, (d) AG-PEG8000 palmitate-PM, and (e) AG-PEG8000 palmitate-SD.

Table 1 shows that the T_m of AG-PEG8000 palmitate-SD is lower than that of the AG-PEG4000 palmitate-SD, which indicates that increasing the molecular weight of PEG in the carrier material can improve the compatibility of the carrier material with the poorly water-soluble drug AG. Therefore, the relative crystallinity of AG in SD prepared by PEG8000 palmitate was decreased.

3.5. SEM. In order to determine the surface morphology of SDs, SEM analysis of the samples was performed. As shown in Figure 5, pure AG was a smooth block-shaped crystal, the physical mixtures were an irregular block-shaped particle with a rough surface, and SD showed sheet-like particles.

3.6. Specific Surface Area and Pore Volume. Table 2 shows the specific surface area and pore volume of the physical mixtures and SDs. The specific surface area and pore volume of SDs increased significantly compared to the physical mixtures. This was because the SD powders prepared by the freeze-drying method were loose and showed sheet-like particles; therefore, they had a larger specific surface area and pore volume.

3.7. Dissolution Testing. The dissolution of a poorly water-soluble drug is crucial where it is the rate-limiting step in the oral absorption process from a solid dosage form and is an important parameter related to bioavailability [23–25]. Results of dissolution testing for pure AG, physical mixtures, and SDs are presented in Figure 6. The physical mixtures displayed dissolution profiles superior to that of pure AG, whereas the SDs displayed dissolution profiles superior to that of pure AG and the physical mixtures.

In order to further study the effect of carrier material on the dissolution behavior of AG in the SDs, the difference factor (f_1) [26] was used to compare the dissolution curves of AG in AG-PEG8000 palmitate-SD and AG-PEG4000 palmitate-SD. An f_1 value between 0 and 15 indicates that the dissolution behavior of the experimental formulation is similar to that of the reference formulation. The f_1 is calculated according to the following equation:

$$f_1 = \frac{\sum_{t=1}^{n} |R_t - T_t|}{\sum_{t=1}^{n} R_t}, \quad (1)$$

where R_t was the dissolution rate of reference formulation (AG-PEG4000 palmitate-SD) at different time points and T_t was the dissolution rate of experimental formulation (AG-PEG8000 palmitate-SD) at different time points. The f_1 value of AG-PEG8000 palmitate-SD versus AG-PEG4000 palmitate-SD was calculated to be 41. The results showed that increasing the molecular weight of PEG could improve the compatibility of the carrier material with the poorly water-soluble drug AG, thus promoting the dissolution of AG from SD.

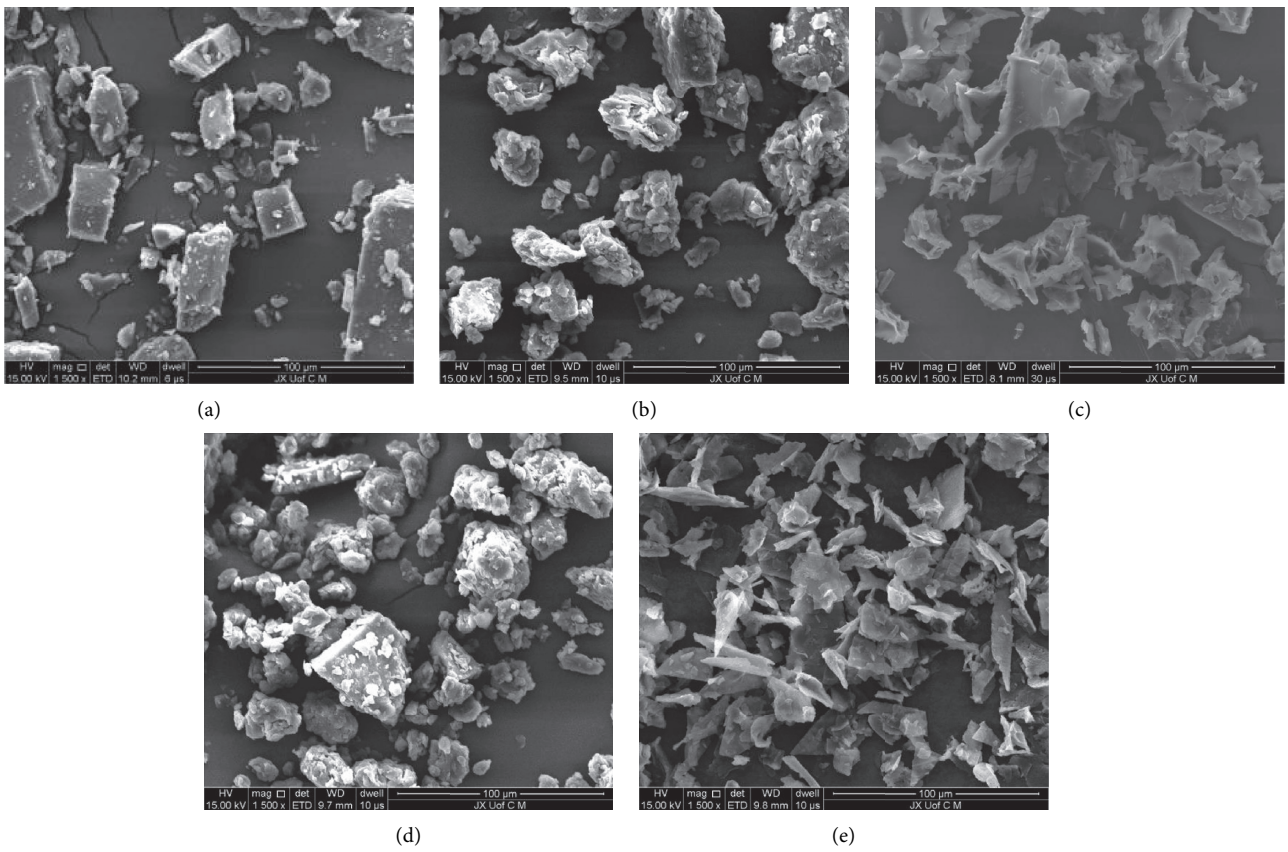

Figure 5: SEM photographs of (a) pure AG, (b) AG-PEG4000 palmitate-PM, (c) AG-PEG4000 palmitate-SD, (d) AG-PEG8000 palmitate-PM, and (e) AG-PEG8000 palmitate-SD.

Table 2: Specific surface area and pore volume of physical mixtures (PM) and SDs.

Sample	Specific surface area (m^2/g)	Pore volume ($\times 10^{-3}$, m^3/g)
AG-PEG4000 palmitate-PM	0.4084	1.784
AG-PEG4000 palmitate-SD	1.7350	7.155
AG-PEG8000 palmitate-PM	0.3340	2.694
AG-PEG8000 palmitate-SD	2.5646	5.376

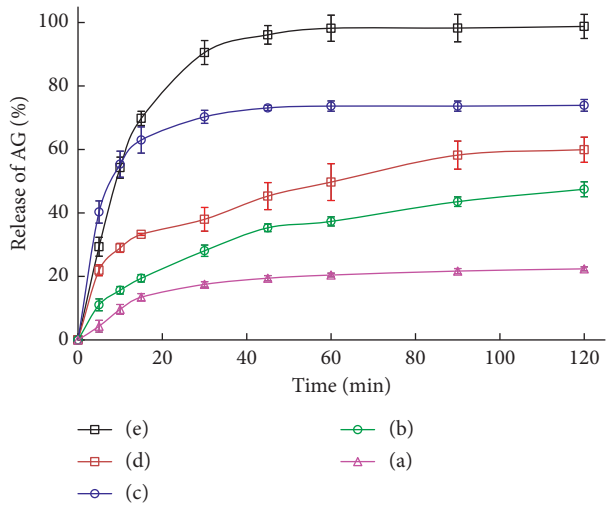

Figure 6: Dissolution profiles of (a) pure AG, (b) AG-PEG4000 palmitate-PM, (c) AG-PEG4000 palmitate-SD, (d) AG-PEG8000 palmitate-PM, and (e) AG-PEG8000 palmitate-SD. The error bars represent the standard deviation of measurements in six separate samples ($n = 6$).

4. Conclusions

In this work, the effects of the PEG molecular weight in carrier material PEG palmitate on the properties of AG-SD were investigated. AG-PEG4000 palmitate-SD and AG-PEG8000 palmitate-SD are similar in surface morphology, specific surface area, and pore volume. Compared with the SD with PEG4000 palmitate as a carrier material, the intermolecular interaction between PEG8000 palmitate and AG was stronger and the thermal stability of AG-PEG8000 palmitate-SD was better. In the meanwhile, the AG relative crystallinity was lower and the AG dissolution rate was faster in AG-PEG8000 palmitate-SD. The results demonstrate that increasing the PEG molecular weight in PEG palmitate could improve the compatibility between the poorly water-soluble drug and carrier material, which is beneficial to improve the SD thermal stability and increases the dissolution rate of poorly water-soluble drug in the SD.

Data Availability

The data used to support the findings of this study are available from the corresponding author upon request.

Conflicts of Interest

The authors declare that there are no conflicts of interest regarding the publication of this paper.

Authors' Contributions

Qingyun Zeng and Liquan Ou contributed equally to this work.

Acknowledgments

This research was supported by the National Natural Science Foundation of China (no. 81560654); the Traditional Chinese medicine Administration of Jiangxi Provincial of China (no. 2019A010); the PhD research start up foundation of Jiangxi University of Traditional Chinese Medicine (2019WBZR001); the First-class Discipline of Traditional Chinese Medicine of Jiangxi University of Traditional Chinese Medicine (no. JXSYLXK-ZHYAO058).

References

[1] Y. S. R. Krishnaiah, "Pharmaceutical technologies for enhancing oral bioavailability of poorly soluble drugs," *Journal of Bioequivalence and Bioavailability*, vol. 2, no. 2, pp. 28–36, 2010.

[2] G. Van den Mooter, "The use of amorphous solid dispersions: a formulation strategy to overcome poor solubility and dissolution rate," *Drug Discovery Today: Technologies*, vol. 9, no. 2, pp. e79–e85, 2012.

[3] Y. Kawabata, K. Wada, M. Nakatani, S. Yamada, and S. Onoue, "Formulation design for poorly water-soluble drugs based on biopharmaceutics classification system: basic approaches and practical applications," *International Journal of Pharmaceutics*, vol. 420, no. 1, pp. 1–10, 2011.

[4] C. L.-N. Vo, C. Park, and B.-J. Lee, "Current trends and future perspectives of solid dispersions containing poorly water-soluble drugs," *European Journal of Pharmaceutics and Biopharmaceutics*, vol. 85, no. 3, pp. 799–813, 2013.

[5] R. J. Chokshi, H. Zia, H. K. Sandhu, N. H. Shah, and W. A. Malick, "Improving the dissolution rate of poorly water soluble drug by solid dispersion and solid solution-pros and cons," *Drug Delivery*, vol. 14, no. 1, pp. 33–45, 2007.

[6] N.-Q. Shi, Y.-S. Lei, L.-M. Song, J. Yao, X.-B. Zhang, and X.-L. Wang, "Impact of amorphous and semicrystalline polymers on the dissolution and crystallization inhibition of pioglitazone solid dispersions," *Powder Technology*, vol. 247, pp. 211–221, 2013.

[7] K. Jo, J. M. Cho, H. Lee et al., "Enhancement of aqueous solubility and dissolution of celecoxib through phosphatidylcholine-based dispersion systems solidified with adsorbent carriers," *Pharmaceutics*, vol. 11, no. 1, pp. 1–14, 2018.

[8] S. Bialleck and H. Rein, "Preparation of starch-based pellets by hot-melt extrusion," *European Journal of Pharmaceutics and Biopharmaceutics*, vol. 79, no. 2, pp. 440–448, 2011.

[9] J. O. Eloy and J. M. Marchetti, "Solid dispersions containing ursolic acid in Poloxamer 407 and PEG 6000: a comparative study of fusion and solvent methods," *Powder Technology*, vol. 253, pp. 98–106, 2014.

[10] P. J. Marsac, T. Li, and L. S. Taylor, "Estimation of drug-polymer miscibility and solubility in amorphous solid dispersions using experimentally determined interaction parameters," *Pharmaceutical Research*, vol. 26, no. 1, pp. 139–151, 2009.

[11] P. J. Marsac, S. L. Shamblin, and L. S. Taylor, "Theoretical and practical approaches for prediction of drug-polymer miscibility and solubility," *Pharmaceutical Research*, vol. 23, no. 10, pp. 2417–2426, 2006.

[12] P. J. Marsac, H. Konno, A. C. F. Rumondor, and L. S. Taylor, "Recrystallization of nifedipine and felodipine from amorphous molecular level solid dispersions containing poly(vinylpyrrolidone) and sorbed water," *Pharmaceutical Research*, vol. 25, no. 3, pp. 647–656, 2008.

[13] H. Chauhan, C. Hui-Gu, and E. Atef, "Correlating the behavior of polymers in solution as precipitation inhibitor to its amorphous stabilization ability in solid dispersions," *Journal of Pharmaceutical Sciences*, vol. 102, no. 6, pp. 1924–1935, 2013.

[14] G. Zhao, Q. Zeng, S. Zhang et al., "Effect of carrier lipophilicity and preparation method on the properties of andrographolide-solid dispersion," *Pharmaceutics*, vol. 11, no. 2, pp. 74–91, 2019.

[15] C. Calabrese, S. H. Berman, J. G. Babish et al., "A phase I trial of andrographolide in HIV positive patients and normal volunteers," *Phytotherapy Research*, vol. 14, no. 5, pp. 333–338, 2000.

[16] P. K. Singha, S. Roy, and S. Dey, "Protective activity of andrographolide and arabinogalactan proteins from *Andrographis paniculata* nees. Against ethanol-induced toxicity in mice," *Journal of Ethnopharmacology*, vol. 111, no. 1, pp. 13–21, 2006.

[17] N. Sermkaew, W. Ketjinda, P. Boonme, N. Phadoongsombut, and R. Wiwattanapatapee, "Liquid and solid self-microemulsifying drug delivery systems for improving the oral bioavailability of andrographolide from a crude extract of *Andrographis paniculata*," *European Journal of Pharmaceutical Sciences*, vol. 50, no. 3-4, pp. 459–466, 2013.

[18] Y. Zhang, X. Hu, X. Liu et al., "Dry state microcrystals stabilized by an HPMC film to improve the bioavailability of

andrographolide," *International Journal of Pharmaceutics*, vol. 493, no. 1-2, pp. 214–223, 2015.

[19] J. J. Sousa, A. Sousa, F. Podczeck, and J. M. Newton, "Factors influencing the physical characteristics of pellets obtained by extrusion-spheronization," *International Journal of Pharmaceutics*, vol. 232, no. 1-2, pp. 91–106, 2002.

[20] G. Zhao, X. Liang, C. Wang, Z. Liao, Z. Xiong, and Z. Li, "Effect of superfine pulverization on physicochemical and medicinal properties of qili powder," *Revista Brasileira de Farmacognosia*, vol. 24, no. 5, pp. 584–590, 2014.

[21] E. Karavas, E. Georgarakis, M. P. Sigalas, K. Avgoustakis, and D. Bikiaris, "Investigation of the release mechanism of a sparingly water-soluble drug from solid dispersions in hydrophilic carriers based on physical state of drug, particle size distribution and drug-polymer interactions," *European Journal of Pharmaceutics and Biopharmaceutics*, vol. 66, no. 3, pp. 334–347, 2007.

[22] Y. Shibata, M. Fujii, M. Kokudai et al., "Effect of characteristics of compounds on maintenance of an amorphous state in solid dispersion with crospovidone," *Journal of Pharmaceutical Sciences*, vol. 96, no. 6, pp. 1537–1547, 2007.

[23] R. N. Shamma and M. Basha, "Soluplus®: a novel polymeric solubilizer for optimization of carvedilol solid dispersions: formulation design and effect of method of preparation," *Powder Technology*, vol. 237, pp. 406–414, 2013.

[24] G. Mohammadi, M. Barzegar-Jalali, H. Valizadeh et al., "Reciprocal powered time model for release kinetic analysis of ibuprofen solid dispersions in oleaster powder, microcrystalline cellulose and crospovidone," *Journal of Pharmacy & Pharmaceutical Sciences*, vol. 13, no. 2, pp. 152–161, 2010.

[25] L. Zhao, J. Ding, C. Xiao, X. Chen, G. Gai, and L. Wang, "Poly(L-glutamic acid) microsphere: preparation and application in oral drug controlled release," *Acta Chimica Sinica*, vol. 73, no. 1, pp. 60–65, 2015.

[26] P. Costa and J. M. Sousa Lobo, "Modeling and comparison of dissolution profiles," *European Journal of Pharmaceutical Sciences*, vol. 13, no. 2, pp. 123–133, 2001.

Hindawi
Advances in Polymer Technology
Volume 2020, Article ID 7145738, 7 pages
https://doi.org/10.1155/2020/7145738

Research Article

Improved Therapeutic Effect of Puerarin-Encapsulated PEG-PLGA Nanoparticle on an In Vitro Cerebral Infarction Model

Lei Li,[1] Yan Li,[2] Cheng Miao,[1] and Rui Liu[3]

[1]*Department of Neurology, Xinxiang Central Hospital, Xinxiang 453000, Henan, China*
[2]*Clinical Medical College of Tianjin Medical University, Tianjin 300270, China*
[3]*Xinxiang Medical University, Xinxiang 453000, Henan, China*

Correspondence should be addressed to Rui Liu; liurui@xxmu.edu.cn

Received 21 October 2019; Revised 11 December 2019; Accepted 30 December 2019; Published 28 February 2020

Guest Editor: Mingqiang Li

This study was to explore the therapeutic effect and mechanism of puerarin (PUE) combined with PEGylated nanoparticles on a rat cerebral infarction cell model. In this context, PEG-PLGA/PUE nanoparticles were prepared by the thin-film hydration method, and the toxicity of PEG-PLGA/PUE nanoparticles to brain capillary endothelial cell (BCEC) was detected by MTT. The BCEC/TF cell model was obtained by induction of BCEC cells with TNF-α. The BCEC/TF cell model was identified by immunofluorescence; the protein expression was detected by western blotting; the expression level of miR-424 in cells was measured by RT-qPCR; the targeting relationship between miR-424 and PDCD4 was confirmed by dual-luciferase reporter assay. We found that PEG-PLGA/PUE nanoparticles prepared by the thin-film hydration method had uniform particle size, regular shape, and good stability and were not toxic to cells. The vWF was widely expressed in the cytoplasm in BCECs. The BCEC/TF cell model was obtained after TNF-α treatment, and tissue factor (TF) was widely expressed on the cell membrane of BCEC/TF cells. Furthermore, it was observed that the PEG-PLGA/PUE nanoparticles showed better therapeutic effect on the BCEC/TF cell model than PUE. PEG-PLGA/PUE nanoparticles and PUE inhibited the expression of PDCD4 protein by increasing the expression of miR-424 in BCEC/TF cells. In summary, the therapeutic effect of PEG-PLGA/PUE nanoparticles on the in vitro cell model of cerebral infarction is better than that of PUE. Moreover, PEG-PLGA/PUE inhibits the expression of PDCD4 protein by lowering the expression level of miR-424 in cells, thereby reducing the hazard of cerebral infarction.

1. Introduction

Puerarin (PUE), an isoflavone active ingredient extracted from the rhizoma of legumes *Pueraria lobata and Kadsura kadsura*, has antioxidant, cholesterol-lowering, and blood pressure lowering effects and is commonly used in the treatment of cardiovascular and cerebrovascular diseases [1]. However, the clinical application of PUE is limited by its low solubility, short half-life, low concentration in the brain tissue, and low absolute bioavailability in the human body.

Nano-based drug delivery systems have been used in recent years to target drugs to specific sites to improve drug bioavailability. However, ordinary nanoparticles are rapidly cleared after intravenous injection, and this clearance should be avoided during drug delivery to tissues other than the liver. A layer of hydrophilic polymer is formed by physical adsorption on the surface of ordinary nanoparticles, and such nanoparticles are called PEGylated nanoparticles. Polyethylene glycol-poly lactic-co-glycolic acid (PEG-PLGA) copolymer is used as a nanopolymer carrier and has the characteristic. The PEG-PLGA polymer is amphiphilic because of having both hydrophilic and lipophilic sides. Moreover, possessing good biocompatibility and non-immunogenicity, it has a broad application prospect in the field of PEGylated nanoparticles. Based on the above advantages, PEG-PLGA nanoparticles can therefore prolong the circulation time of the nanodrug loading system in the blood, thereby targeting specific tissues or organs and

exerting sustained release and prolonged efficacy [2]. It has been documented [3] that PEG-PLGA nanoparticles can achieve deep penetration and have a long residence time in tumor tissues. As both the cerebral infarction site and the tumor tissue have similar inflammatory infiltration, it was speculated that PEG-PLGA nanoparticles could exert similar effects at the cerebral infarction site. Therefore, the therapeutic effect and underlying mechanism of PUE combined with PEG-PLGA nanoparticles on a rat cerebral infarction cell model were explored to provide a new theoretical basis for the treatment of cerebral infarction.

2. Materials, Objects, and Methods

2.1. Research and Design. This experimental protocol was designed based on an in vitro control study.

2.2. Research Materials

Animals. Clean SD male rats (50–60 g) were purchased from Hunan Silaike Jingda Laboratory Animal Co., Ltd.

2.3. Drugs and Reagents

Drugs. Puerarin (purity ≥ 98.0%) was purchased from Shanghai Aladdin Bio-Chem Technology Co., Ltd.

Reagents. PEG-PLGA was purchased from Shanghai Shunna Biological Technology Co., Ltd.; methanol, 75% ethanol, 4% paraformaldehyde, and glycerol were purchased from Shandong Baiyao Chemical Co., Ltd.;MTT kit, D-Hanks, Percoll gradient centrifugation solution, BSA, and collagenase II were purchased from Beijing Kanglong Kangtai Biotechnology Co., Ltd.;polyclonal rabbit anti-human VWF antibody, rabbit anti-rat TF polyclonal antibody, and DAPI were purchased from Sangon Biological Engineering (Shanghai) Co., Ltd.;TNF-α was purchased from Shanghai Enzyme Lian Biological Technology Co., Ltd.; total RNA extraction kit and cDNA reverse transcription kit were purchased from Shanghai Yiyan Biological Technology Co., Ltd.; total protein extraction kit, ECL kit, and dual-luciferase reporter assay kit were purchased from Nanjing Camilo Biological Engineering Co., Ltd..

2.4. Experimental Method

2.4.1. Preparation of PEG-PLGA/PUE Nanoparticles. PEG-PLGA/PUE nanoparticles were prepared by the thin-film hydration method with the following process: a certain amount of PUE and PEG-PLGA were weighed and completely dissolved in a certain volume of methanol. The solution was placed in a rotary flask at 35°C and protected by argon. The heating was stopped when a dry film is formed. After 10 h vacuuming at room temperature, the remaining organic solvent was removed and the film was hydrated by adding PBS buffer, which was followed by hydration at suitable temperature for 60 min, ultrasonic for 20 min, and standing at room temperature for 1 h. Afterwards, the precipitate was removed by filtering 3 to 4 times with 0.2 μm micropores to make the nanoparticles uniform in particle size, and PEG-PLGA/PU nanoparticles were obtained by being freeze-dried for 24 h.

2.4.2. Determination of Encapsulation Efficiency and Drug Loading. The 500 μL of PEG-PLGA/PUE nanoparticles after micropore filtration was centrifugated at 12000 rpm for 10 min, with high speed and low temperature, and the upper layer was drug-loaded nanoparticles. The encapsulation structure of the nanoparticles was destroyed by adding 10 volumes of methanol solution to completely release PUE, and the drug loading of PUE in the nanoparticles was measured by HPLC and recorded as $M_{\text{-load}}$. The same method was used to calculate the total amount of drug in 500 μL of nanoparticles, recorded as $M_{\text{-total}}$, and the PUE encapsulation efficiency was worked out by using the following formula: PUE encapsulation efficiency = $M_{\text{-load}}/M_{\text{-total}}$.

An appropriate amount of PEG-PLGA/PUE nanoparticle lyophilized powder was weighed, with its mass recorded as W_1. The encapsulation structure of the nanoparticles was then destroyed by adding 10 volumes of methanol to the powder, and the amount of drug in the nanoparticles was measured by HPLC and recorded as W_0. The PUE drug loading was worked out by using the following formula: PUE drug loading = W_0/W_1.

2.4.3. Identification of PEG-PLGA/PUE Nanoparticles. An appropriate amount of prepared PEG-PLGA/PUE nanoparticles was diluted with distilled water and evenly distributed with the use of ultrasound. One drop of nanoparticle suspension was placed onto a copper grid with the excess liquid sucked off and dried at room temperature. The morphology of the nanomicelles was then observed under a transmission electron microscope when there was no liquid on the copper grid. The particle size distribution of the PEG-PLGA/PUE nanoparticles was determined with a zeta potentiometer (Zetasizer Nano-ZS; Malvern Instruments). An appropriate number of nanoparticles were diluted to 10 mg/mL using distilled water, and 0.5 mL of nanoparticle solution was added to 2.5 mL of sodium sulfate solution at different concentrations. The solution was allowed to stand for 10 min at 37° C followed by the measurement of the absorbance of the nanoparticles at 560 nm using a spectrophotometer, by which the stability of the nanoparticles was evaluated.

2.4.4. MTT Assay for Cell Viability. Cells in the logarithmic phase of growth were digested with trypsin, and single-cell suspensions with a cell density of 5×10^4 cells/mL were adjusted. The cells were seeded in a 96-well plate at a concentration of 100 μL per well, and the intervention drug was added after the cells covered the bottom of the well. Six replicate wells were set in each group, and a blank control was set. The cells were incubated for 72 h at 37°C, 5% CO_2. Afterwards, each well was added 10 μL of 0.5% MTT solution

followed by another 4 hours of incubation. After the blank control group was set for zero adjustment, the absorbance A at each wavelength of 570 nm was determined by using a microplate reader. Cell viability was calculated using the formula: cell viability (%) = A experimental group/A control group × 100%.

2.4.5. Isolation and Identification of Rat BCEC Cells. Isolation. Three-week-old clean SD male rats were sacrificed by cervical dislocation and immersed in 75% ethanol for 3 min. The rat brain was obtained by isolating the cortex and rinsed 3 times with ice D-Hanks after the meninges were removed. The brain tissue cut into a 1 mm^3 cube was then digested with 0.1% collagenase II for 90 min, and the supernatant was removed by centrifugation at 1000 rpm for 20 min at 4 °C. BSA (20%) was added to 1 mL of brain tissue in the pellet. The solution was again centrifuged at 1000 rpm for 20 min at 4°C after the precipitate was dispersed. Again 0.1% collagenase was added at 37°C for digestion for 60 min, and the solution was centrifuged again with the supernatant discarded. The dispersed precipitate was then spread evenly on the Percoll gradient solution, and after centrifugation at 4°C for 10 min, obvious stratification was observed. The yellowish-white microvascular fragments were aspirated, rinsed twice, and cultured with medium for microvascular endothelial cells containing MVGS at 37°C in 5% CO_2.

Identification. Fixation was performed using 4% paraformaldehyde at room temperature for 20 min followed by three times of PBS rinsing, 5 min for each time. The cells were incubated with 10% goat serum for 30 min at 37°C, cultured with rabbit anti-vWF polyclonal antibody (1 : 200) at 4 ° C overnight, and rinsed 3 times with PBS buffer for 5 min each time. The next day, the cells rinsed with PBS buffer three times for 5 min each were incubated with DAPI (1 μg/mL) for 10 min at room temperature and then rinsed with PBS buffer three times for 5 min each. The slides were finally mounted in 50% glycerol and observed using a confocal laser scanning microscope.

2.4.6. Construction and Identification of the BCEC/TF Model

Construction. The rat BCECs were seeded in 6-well plates and then incubated with TNF-α (100 ng/mL) after 2 d for 12 h to stimulate TF expression.

Identification. After fixation with 4% paraformaldehyde, immunofluorescence staining was performed using rabbit anti-rat TF polyclonal antibody (1 : 200) according to the procedure described previously. A confocal laser scanning microscope was used for observation after mounting.

2.4.7. Protein Expression Measured by Western Blotting. Total cellular proteins were extracted using a kit, transferred to a membrane after sodium dodecyl sulfate polyacrylamide gel electrophoresis, and blocked with skimmed milk powder for 1 h. Corresponding antibodies were added, and secondary antibodies were added after the membrane was washed. Afterwards, ECL was added for color development, which was photographed using a gel imager for observation.

2.4.8. The Expression Levels of miRNAs Measured by RT-qPCR. The cells were seeded at a density of 1×10^6/well in a 6-well plate, and after 24 h, the culture medium was discarded before transfection. After 24 hours of transfection, the total RNA was extracted using an RNA extraction kit and the RNA was then reverse-transcribed into cDNA. The upstream primer of miR-424 was 5′- CAGCAGCAATTCATGTTTT-GAA-3′; the downstream primer was 5′-TTGTCGTC GTTAAGTACAAAAC-3′; the upstream primer of internal reference U6 was 5′- CTCGCTTCGGCAGCACA-3′; the downstream primer was 5′-AACGCTTCACGAATTT GCGT -3′. The reaction was performed in 10 μl of 2 × All-in-One qPCR Mix, 2 μl universal adaptor PCR primer, 2 μl All-in-One miRNA qPCR primer, 2 μl cDNA, and 4 μl ddH2O. Reaction conditions were as follows: 95°C, 10 s; 95°C, 3 s; 80°C, 20 s; and 72°C, 20 s for a total of 40 cycles.

2.4.9. Dual-Luciferase Reporter Assay. Primers for miRNA and protein mRNA were predicted and designed and were inserted into pDCD4-wt and pDCD-mut plasmids after being identified by sequencing. After cotransfection of cells with 20 ng of plasmid, miR-424 mimics and miR-NC plasmid, fluorescence intensity was measured using the dual-luciferase reporter assay.

2.5. Statistical Treatment. Statistical analysis was performed using SPSS 20.0. Data were compared between groups using *t*-test and among multiple groups using one-way analysis of variance, and the specific data were represented by mean ± standard deviation.

3. Results

3.1. Characterization and Evaluation of PEG-PLGA/PUE Nanoparticles. The PUE encapsulation efficiency and drug loading in PEG-PLGA/PUE nanoparticles were 83.6% and 9.7%, respectively, suggesting that PEG-PLGA/PUE nanoparticles were successfully prepared. Figure 1(a) shows the determination of PEG-PLGA/PUE nanoparticles by transmission electron microscopy (TEM). Figure 1(b) exhibits particle size distribution of PEG-PLGA/PUE nanoparticles, and it can be seen that PEG-PLGA/PUE formed a uniform monodisperse nanosolution (PDI = 0.13) with an average particle size of 116.4 nm under the influence of water-soluble vitamin E. Figure 1(c) shows the absorbance value of the nanoparticle system at 560 nm measured by using a spectrophotometer. When the concentration of sodium sulfate was lower than 0.45 mol/L, the absorbance value of the nanoparticle system did not change significantly, while the absorbance value of the nanoparticle system rose significantly when the concentration of sodium sulfate was greater than 0.45 mol/L. That is, the critical flocculation concentration of PEG-PLGA/PUE nanoparticles was 0.45 mol/L,

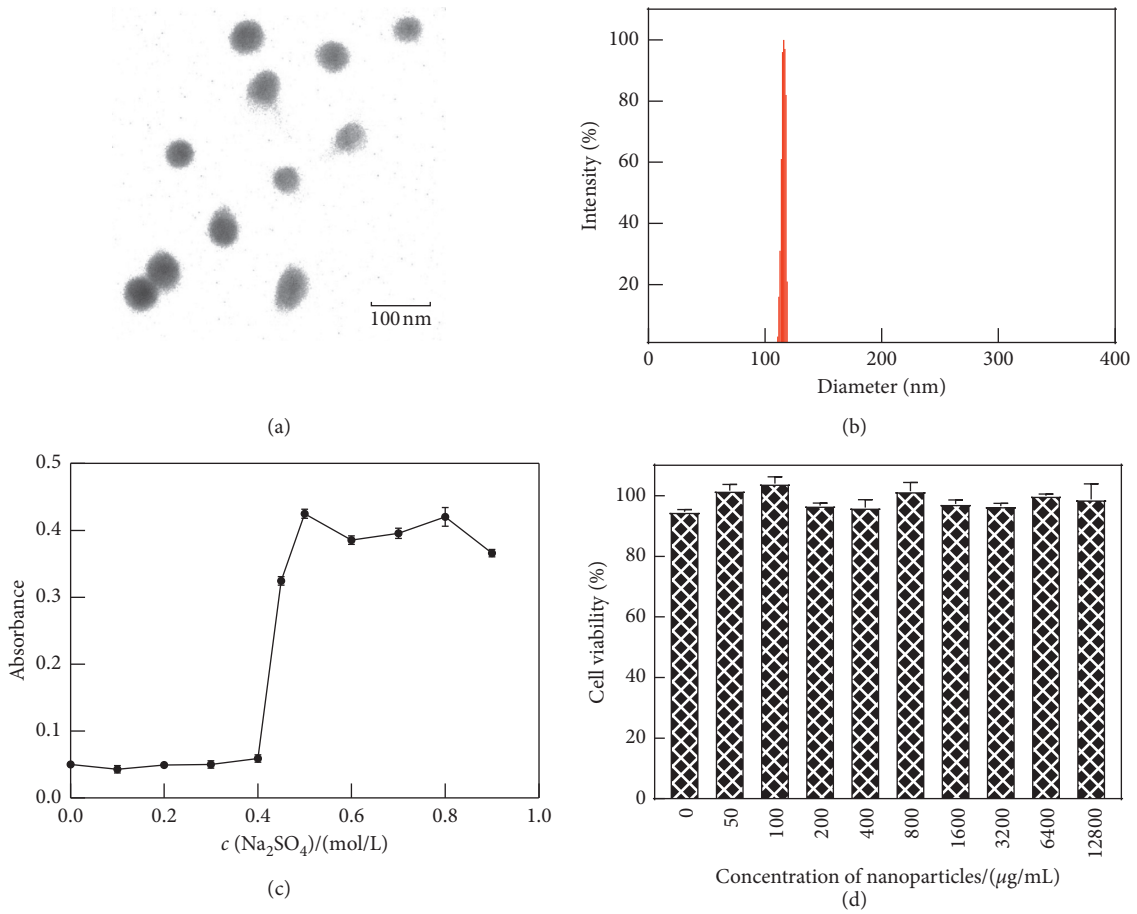

Figure 1: Characterization of PEG-PLGA/PUE nanoparticles. (a, b) Size distribution and TEM image of PEG-PLGA/PUE nanoparticles. (c) Absorbance of nanoparticles. (d) Cell viability (data are shown by mean ± SD, $N = 3$).

which was much greater than the electrolyte concentration in human blood, suggesting that PEG-PLGA/PUE nanoparticles have good stability. Figure 1(d) shows the measurement of cytotoxicity using MTT assay. After 72 h of coincubation of rat BCECs and PEG-PLGA/PUE nanoparticles, the survival rates of rat BCECs were all between 94.1% and 105.6%, indicating that PUE-PEG-PLGA nanoparticles had good biocompatibility.

3.2. BCEC/TF Model Construction and Identification. The product obtained by centrifugation was inoculated into a 6-well plate with a medium for microvascular endothelial cells containing MVGS. After about two weeks, the basically confluent rat BCECs were in long spindle shape, forming a tight single-cell layer at the bottom of the plate, and significant contact inhibition could be observed. Rat BCECs were then subcultured. After the third-generation cells were fused, it was observed that rat BCECs showed "flagstone" appearance and the cells presented turbulence arrangement. Immunofluorescence staining results showed that rat BCECs strongly expressed vWF, an early vascular endothelial cell activation marker, mainly in the cytoplasm (Figure 2(a)). Rat BCECs were treated with TNF-α for 12 h, and it was observed that TF was strongly expressed on the cell membrane of rat BCECs, while there was only trace TF expression in rat BCECs without TNF-α treatment (Figure 2(b)).

3.3. Evaluation of the Effect of PEG-PLGA/PUE on BCEC/TF Cells. Thrombomodulin (TM) and interleukin (IL-6) produce corresponding changes with the occurrence of cerebral infarction; thus, detection of the expression levels of TM and IL-6 in BCEC/TF cells by western blotting can reflect the therapeutic effect of drugs on cerebral infarction. The results of western blotting showed that the expression of TM and IL-6 in rat BCEC/TF cells of the control group was the highest, whereas that of TM and IL-6 in BCEC/TF cells cocultured with PEG-PLGA/PUE (PUE concentration of 0.5 mg/ml) was the lowest ($P < 0.001$), corresponding to a lower expression of TM and IL-6 in BCEC/TF cells cocultured with PUE (0.8 mg/ml) ($P < 0.01$) (Figure 3). The above experimental results indicated that PEG-PLGA/PUE nanoparticles have better efficacy on BCEC/TF cells than PUE.

3.4. Mechanism of Action of PEG-PLGA/PUE on BCEC/TF Cells. The RT-qPCR results showed that the expression level of miR-424 in BCEC/TF cells was significantly lower than that in BCEC cells ($P < 0.05$), but the expression level of

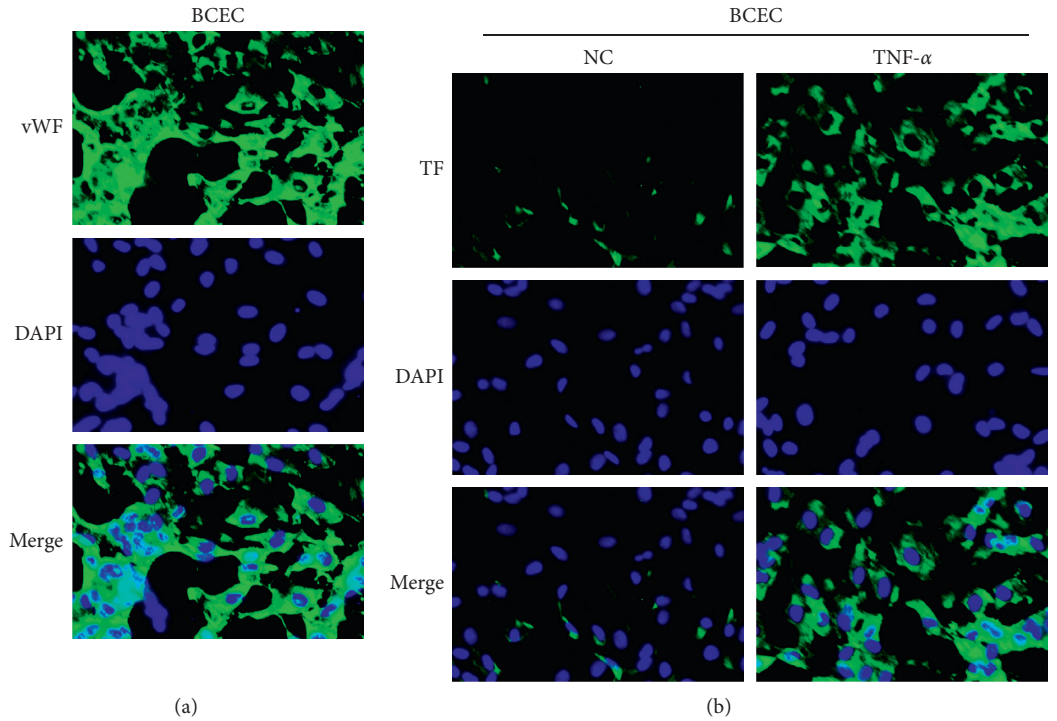

Figure 2: BCEC/TF model construction and identification. (a) The vWF expression level. (b) The TF expression level (data are shown by mean ± SD, $N = 3$).

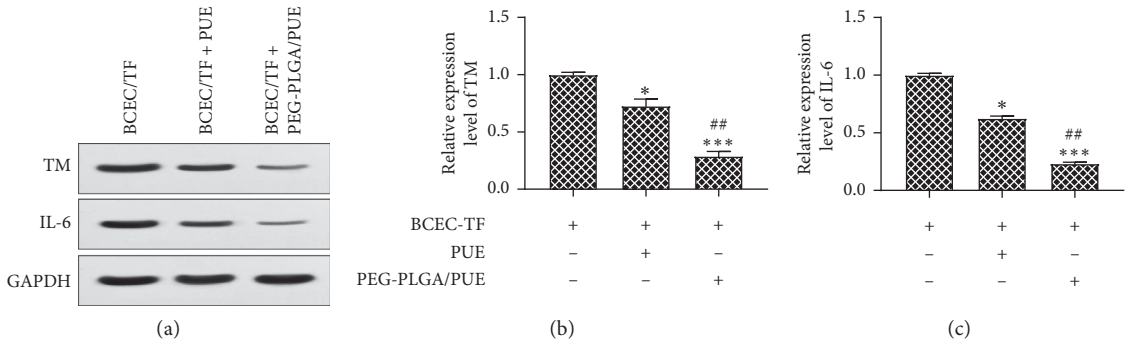

Figure 3: Expression levels of TM and IL-6 in BCEC/TF cells (data are shown by mean ± SD, $N = 3$; $^{*}P < 0.05$ and $^{***}P < 0.001$ vs. BCEC/TF group; $^{\#\#}P < 0.01$ vs. PUE + BCEC/TF group).

miR-424 in BCEC/TF cells increased after intervention with puerarin or PEG-PLGA/PUE nanoparticles, and the difference was statistically significant ($P < 0.05$). Furthermore, the expression level of miR-424 was the highest after coculture of BCEC/TF with PEG-PLGA/PUE nanoparticles (Figure 4(a)). The miRDB database predicted that the programmed cell death factor PDCD4 might be the target gene of miR-424 (Figure 4(b)), which was confirmed by the results of the dual-luciferase reporter assay (Figure 4(c)). The western blotting results showed that the expression of programmed cell death 4 (PDCD4) was decreased in BCEC/TF cells transfected with miR-424 mimics vector (Figure 4(d)). The expression of PDCD4 in BCEC/TF cells cocultured with PUE or PEG-PLGA/PUE nanoparticles was also reduced, and the difference was statistically significant ($P < 0.05$) (Figure 4(e)). In summary, PEG-PLGA/PUE nanoparticles can effectively enhance the expression of miR-424 in BECE/TF cells and realize targeted inhibition of the expression of PDCD4 protein.

4. Discussion

Cerebral infarction is a common and frequent cerebrovascular disease that occurs at any age, and brain tissue necrosis varies with both the location and the size of thrombus. Most patients suffer massive cerebral infarction, which commonly develops in the middle cerebral artery and carotid artery. Modern pharmacological studies have shown that PUE can increase cerebral blood flow, dilate brain blood vessels, and improve brain microcirculation in patients with cerebral infarction, thereby effectively repairing the cerebral lesions [4–6]. Although some studies have shown that PUE is more

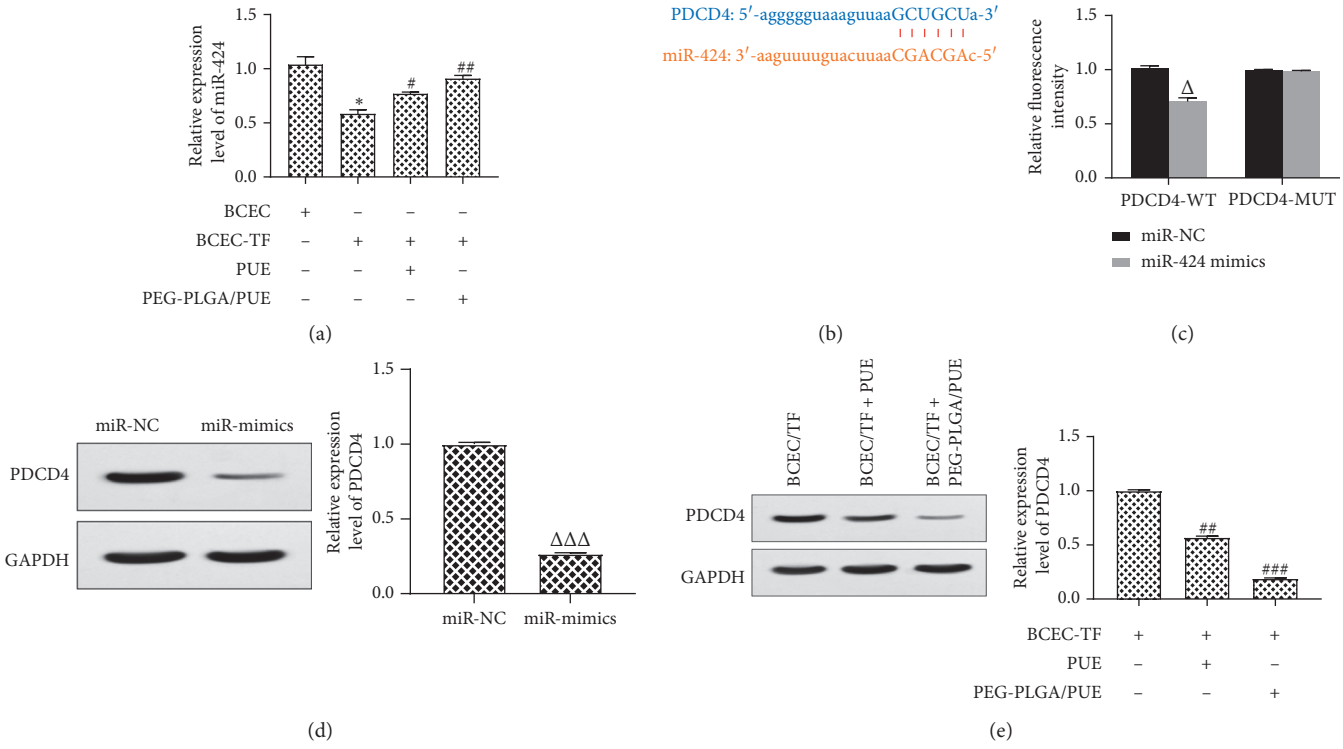

Figure 4: Mechanism of action of PEG-PLGA/PUE on BCEC/TF cells. (a) Relative expression of miR-424 on cells. (b) Gene sequence binding site. (c) Relative fluorescence intensity. (d, e) Protein expression level (data are shown by mean ± SD, $N = 3$; $^{*}P < 0.05$ vs. BCEC group; $^{\#}P < 0.05$, $^{\#\#}P < 0.01$, and $^{\#\#\#}P < 0.001$ vs. BCEC/TF group; $^{\Delta}P < 0.05$ and $^{\Delta\Delta\Delta}P < 0.001$ vs. miR-NC group).

effective in the treatment of patients with acute cerebral infarction, its application in clinical practice is still limited due to poor solubility and extremely low bioavailability in the human body [7]. The blood-brain barrier (BBB), a unique protective structure formed by the brain during the long-term evolution, is formed in close association with brain capillary endothelial cells and prevents most substances in the blood from entering the brain, including drugs acting on brain diseases. Therefore, there is still a lack of effective drugs for some brain diseases because of the barrier that impedes the drugs with good activity from reaching the focus. Tissue factor (TF) is the cellular receptor for coagulation factor VIIa in plasma, and the TF-VIIa complex can activate FIX and FX to hydrolyze prothrombin to form thrombin, which in turn coagulates blood. TF is normally distributed outside the blood circulation, and blood cells contact TF-expressing cells to initiate the clotting process to form thrombus only in case of blood vessels and endothelial disruption. Therefore, TF with the above characteristics has become a research hotspot for brain-targeted drug delivery [8, 9], and the BCEC/TF cell model has been a common model for studying cerebral infarction or cerebral thrombosis in vitro. In this study, BCEC cells were obtained by isolating rat brain tissues and TF-expressing rat BCEC cells were obtained using TNF-α induction for experiments.

Nanoparticles, as drug carriers, can modulate drug release rate and enhance drug penetration, thus increasing drug bioavailability. However, ordinary nanoparticles are rapidly cleared after entering the human body, which cannot achieve the desired effect, so nanoparticles with "invisible" ability have attracted more and more attention from scholars. Polylactic acid modified by polyethylene glycol (PEG) makes copolymer of polylactic and polyglycolic acids (PLGA) amphiphilic, which leads to better hydrophilic nature of the nanoparticle surface, and can reduce recognition or removal by RES [10]. PEG-PLGA nanoparticles have longer circulation time in human blood after being combined with drugs, leading to the greatly improved bioavailability of drugs [11, 12]. It was speculated that PEG-PLGA/PUE nanoparticles are more effective than PUE in the cell model of cerebral infarction in vitro, and it was proved in this study that PEG-PLGA/PUE nanoparticles had a stronger inhibitory effect on the expression of TM and IL-6 proteins in rat EC/TF cells than PUE.

MicroRNAs (miRNAs), small noncoding RNA molecules about 22 nucleotides in length, are involved in a variety of physiological activities in the human body. Studies have shown that the expression intensity of miR-424 in the serum of patients with cerebral infarction is lower than that in the serum of healthy individuals and miR-424 over expression can inhibit the activation and translation of the G1/S transforming factor, which can be used as a new intervention target for cerebral infarction [13]. In this study, we found that the expression intensity of miR-424 was significantly reduced in rat BCEC/TF cells, while its expression increased again after the intervention of PUE and PEG-PLGA/PUE nanoparticles. The miRDB database prediction results showed that PDCD4 might be a downstream target gene of

miR-424, which was confirmed by dual-luciferase reporter assay. Guo et al. reported that the reduction of PDCD4 expression could promote regeneration while inhibiting apoptosis of nerve cells, thereby bridging nerve defects in patients with cerebral infarction [14]. Furthermore, we found that the expression level of PDCD4 protein in BCEC/TF cells was significantly higher than that in BCEC cells. The overexpression of miR-424 was followed by the decreased expression of PDCD4 protein in BCEC/TF cells.

In summary, the therapeutic effect of PEG-PLGA/PUE nanoparticles on the in vitro cell model of cerebral infarction was better than that of PUE, and PEG-PLGA/PUE reduced the hazard of cerebral infarction by increasing the expression level of miR-424 in cells while inhibiting that of PDCD4 protein.

Data Availability

The data used to support the findings of this study are included within the article.

Conflicts of Interest

The authors declare that they have no conflicts of interest.

Acknowledgments

This study was supported by grants from the Key Science and Technology Project of Henan Science and Technology Department (122102310013).

References

[1] X. S. Xie, Y. Z. Dong, D. P. Mu, X. L. Pan, and F. Y Zhang, "Evaluation on safety of puerarin injection in clinical use," *Zhongguo Zhong Yao Za Zhi*, vol. 43, no. 19, pp. 3956–3961, 2018.

[2] X. Y. Liu, Z. B. Jiang, J. Luo, J. H. Li, and X. B. Hu, "In vitro evaluation, cellular uptake and anti-acute myocardial ischemia effect of puerarin PEG-PLGA micelles," *Zhongguo Zhong Yao Za Zhi*, vol. 44, no. 11, pp. 2244–2250, 2019.

[3] Z. B. Zhao, J. Long, Y. Y. Zhao et al., "Adaptive immune cells are necessary for the enhanced therapeutic effect of sorafenib-loaded nanoparticles," *Biomater Sci*, vol. 6, no. 4, pp. 893–900, 2018.

[4] Y. Chang, C.-Y. Hsieh, Z.-A. Peng et al., "Neuroprotective mechanisms of puerarin in middle cerebral artery occlusion-induced brain infarction in rats," *Journal of Biomedical Science*, vol. 16, no. 1, p. 9, 2009.

[5] H. P. Pan, J. Z. Yang, X. L. Mo et al., "Protection of puerarin on the cerebral injury in the rats with acute local ischemia," *Zhongguo Zhong Yao Za Zhi*, vol. 30, no. 6, pp. 457–459, 2005.

[6] R. Zhang, H. N. Guo, H. Q. Wu, H. X. Cheng, and H. Q. Wang, "Protective effect of puerarin against calcium overload after focal cerebral ischemia injury in rats," *Nan Fang Yi Ke Da Xue Xue Bao*, vol. 30, no. 6, pp. 1268–1271, 2010.

[7] H. T. Hu, F. Fen, and M. P. Ding, "Effects of puerarin with aspirin on the markers of damaged vascular endothelial cells in patients with acute cerebral infarction," *Zhongguo Zhong Yao Za Zhi*, vol. 33, no. 23, pp. 2827–2829, 2008.

[8] C. C. Visser, S. Stevanović, L. Heleen Voorwinden et al., "Validation of the transferrin receptor for drug targeting to brain capillary endothelial cells in vitro," *Journal of Drug Targeting*, vol. 12, no. 3, pp. 145–150, 2004.

[9] C. C. Visser, S. Stevanović, and L. Heleen Voorwinden, "Targeting liposomes with protein drugs to the blood-brain barrier in vitro," *European Journal of Pharmaceutical Sciences*, vol. 25, no. 2-3, pp. 299–305, 2005.

[10] K. Zhang, X. Tang, J. Zhang et al., "PEG-PLGA copolymers: their structure and structure-influenced drug delivery applications," *Journal of Controlled Release*, vol. 183, pp. 77–86, 2014.

[11] Z. He, J. Huang, Y. Xu et al., "Co-delivery of cisplatin and paclitaxel by folic acid conjugated amphiphilic PEG-PLGA copolymer nanoparticles for the treatment of non-small lung cancer," *Oncotarget*, vol. 6, no. 39, pp. 42150–42168, 2015.

[12] H. Li, Y. Tong, L. Bai et al., "Lactoferrin functionalized PEG-PLGA nanoparticles of shikonin for brain targeting therapy of glioma," *International Journal of Biological Macromolecules*, vol. 107, no. Pt A, pp. 204–211, 2018.

[13] H. Zhao, J. Wang, L. Gao et al., "MiRNA-424 protects against permanent focal cerebral ischemia injury in mice involving suppressing microglia activation," *Stroke*, vol. 44, no. 6, pp. 1706–1713, 2013.

[14] Y.-B. Guo, T.-F. Ji, H.-W. Zhou, and J.-L. Yu, "Effects of microRNA-21 on nerve cell regeneration and neural function recovery in diabetes mellitus combined with cerebral infarction rats by targeting PDCD4," *Molecular Neurobiology*, vol. 55, no. 3, pp. 2494–2505, 2018.

Hindawi
Advances in Polymer Technology
Volume 2020, Article ID 1640208, 9 pages
https://doi.org/10.1155/2020/1640208

Research Article

Effects of Lentinan on Endothelial Cell Activity, Inflammatory Response, Endoplasmic Reticulum Stress, and Apoptosis in Sepsis

Yan Xu and Yeping Du

Emergency Department, Huai'an Second People's Hospital, Huai'an 223002, JiangSu, China

Correspondence should be addressed to Yeping Du; yepingdu2008@163.com

Received 1 January 2020; Revised 21 January 2020; Accepted 5 February 2020; Published 26 February 2020

Guest Editor: Mingqiang Li

The aim of this study is to explore the protective effects of lentinan on endoplasmic reticulum stress, inflammation, and apoptosis in sepsis endothelial cells. Firstly, lentinan was extracted, purified, and analyzed. When the concentration of lentinan was in the range of 0.04–4 μM, there was no obvious effect on the morphology of HUVECs. When the concentration reached 10 M, the cells were obviously contracted and necrotic. CCK-8 cell activity experiment showed that when the concentration of lentinan reached 4 μM, the cell activity decreased significantly ($P < 0.001$), and it was in a dose-dependent manner. Then, the cells were divided into the control group (0 μM lentinan), sepsis group, sepsis + lentinan 1.2 μM group, and sepsis + lentinan 2 μM group. Enzyme-linked immunosorbent assay showed that lentinan could significantly reduce the expression of TNF-α, IL-1β, and IL-6 in sepsis endothelial cells ($P < 0.001$). In addition, flow cytometry and TUNEL staining showed that compared with the control group, the apoptosis of cells in the sepsis group increased significantly ($P < 0.001$), and lentinan could inhibit apoptosis ($P < 0.001$). In terms of mechanism research, the mRNA and protein expression of endoplasmic reticulum stress-related protein in endothelial cells were detected by real-time fluorescent quantitative PCR (qPCR) and Western blotting, respectively. It was found that the expression of SIRT1, the upstream factors of endoplasmic reticulum stress in sepsis cells, was obviously inhibited ($P < 0.001$), and the expression of CHOP, GRP78, IRE1α, and ATF6 was significantly increased ($P < 0.001$), However, the pretreatment of lentinan could significantly reverse the above changes ($P < 0.001$). Besides, lentinan could also reduce the expression of phosphorylated p65 protein (the activation marker of NF-κb) and iNOS. *Conclusion*. When sepsis occurs, lentinan can protect endothelial cells from ERS inflammation and apoptosis induced by sepsis. Thus, lentinan is expected to be a new target for the treatment of sepsis-induced endothelial damage.

1. Introduction

Sepsis is a complex systemic inflammatory response syndrome (SIRS). It is one of the critical causes of death in patients in the intensive care unit. It can affect the heart, liver, kidney, lung, and other organ systems leading to the occurrence of multi-organ dysfunction syndrome (MODS) [1]. Although life support system technology is continuously optimized with the advancement of science and technology, the prognosis of sepsis, especially septic shock, is still very poor. The current treatment mainly involves the broad-spectrum antibiotics for infectious pathogens. However, this method largely ignores the development of sepsis, which could lead to inflammatory damage to cells and other serious complications.

When sepsis occurs, bacterial endotoxin activates monocytes to produce proinflammatory cytokines and chemokines, induces endothelial cells to transition to the proinflammatory stage, and can activate endothelial cells to produce inflammatory cytokines, such as tumor necrosis factor α (TNF-α), interleukin 1β (IL-1β), increased caspase-3 activity, thereby promoting the occurrence of apoptosis, necrosis, and other reactions in endothelial cells [2]. In addition, the release of early response cytokines can lead to the production of anti-inflammatory mediators, such as compensatory anti-inflammatory response syndrome (CARS), which can cause vascular instability and microvascular occlusion, and ultimately lead to organ dysfunction and failure [3]. In the occurrence and development of sepsis,

SIRS and CARS are parallel to each other [4]. Therefore, effective treatment should be targeted at the early proinflammatory-anti-inflammatory stage of sepsis to prevent organ damage caused by the activation of endothelial cells.

When looking for anti-inflammatory drugs to treat sepsis, mild natural compounds caught our attention. For example, Dagmar et al. studied the effect and mechanism of Sini decoction, Baihu decoction, and Xuebi decoction in the treatment of sepsis endothelial cell model and found that the above traditional Chinese medicine has anti-inflammatory and antiapoptotic effects in sepsis [5]. It is well known that natural compounds containing β-glucan can be used to improve human health. For example, lentinan containing 1,3-β-glucan is an active ingredient extracted from lentinan. Various studies have shown the anti-inflammatory, antibacterial, and anticancer potential of lentinan [6, 7]. For example, through in vitro experiments, Nishitani et al. confirmed that lentinan can affect the expression of IL-8 and TNFR1 in intestinal epithelial cells, thereby exerting anti-inflammatory activity [8]. Mizuno also reported a similar discovery that lentinan can downregulate the IL-8 mRNA expression of TNF-α-induced Caco-2-expressing leukocytes [9]. However, in terms of sepsis research, there are few studies on lentinan, for instance, Wang et al. established a mouse model of burn sepsis and found that lentinan polysaccharides play a protective role by inhibiting the expression of inflammatory factors [10]. Therefore, this study intends to establish a model of endothelial cells with sepsis in vitro with the pretreatment of lentinan to investigate whether lentinan treatment has a protective effect on sepsis endothelial cells and explore its potential mechanism.

2. Materials and Methods

2.1. Extraction of Polysaccharides. Lentinan was extracted by water extraction and alcohol precipitation [11]. After the filtrate was obtained, it was concentrated, alcoholized with 95% ethanol overnight, and dried after centrifugation to obtain the crude lentinan powder, followed by the freeze-thaw classification, deproteinization, and purification of the crude lentinan, and finally obtained lentinan powder [12].

2.2. Determination of Polysaccharide Content. The total sugar and reducing sugar content were measured by the phenol-sulfuric acid method and the 3, 5-dinitrosalicylic acid colorimetry, respectively. The polysaccharide content (%) = total sugar content (%) – reducing sugar content (%) [13].

2.3. Polysaccharide Purity Identification and Component Analysis. Lentinan (3 mg) was dissolved in 1 ml of deionized water, and the purity was determined by high-performance liquid chromatography (HPLC, type 1260, Agilent, USA) with SHODEX SB-806HQ column (8.0 mm × 300 mm) and RID-10A parallax refractometer. In addition, gas chromatography (GC, Shimadzu, Japan) was used with a capillary column DB-1 (0.25 mm × 30 m) and an FID detector to detect the components of lentinan.

2.4. Cell Culture. Primary human umbilical vein endothelial cells (HUVECs) were isolated from human umbilical veins within 10 hours after delivery. This study was approved by the ethics committee of the hospital, and the umbilical cord was provided by volunteers with signed informed consent. The umbilical vein was perfused with M199 (M199/HEPES/PS) containing 0.02 M HEPES and 100 mM penicillin-streptomycin, and endothelial cells were obtained by digestion. HUVECs were cultured in M199 medium containing 0.02 M HEPES, 20% fetal bovine serum, 100 mM double antibody, 10 μg/mL epidermal cell growth supplement (ECGS, BD Biosciences, USA), and 15 IU/ml heparin (Baxter, Austria). HUVECs cells between passages 4–7 were used in subsequent experiments. Human mononuclear cell line THP-1 was purchased from ATCC (USA) and cultured in RPMI-1640 medium (Sigma-Aldrich, USA) containing 10% fetal bovine serum, 0.02 mM HEPES, and 100 mM double antibody at 37°C with 5% CO_2.

2.5. Observation of Morphological Changes of HUVECs Treated with Lentinan. HUVECs cells were seeded in a 24-well cell culture plate and cultured to 60–80% confluency and were treated with lentinan at concentrations of 0, 0.04, 0.4, 0.8, 1.2, 2, 4, and 10 μM. 24 h later cell morphology was observed with an optical microscope (Leica CRT6000, Germany).

2.6. Cell Viability Assay. Cell counting kit-8 (CCK-8, Donjindo, Japan) method was used to evaluate the proliferation activity of HUVECs. Specifically, cells were first seeded in a 96-well tissue culture plate at a density of 1×10^4 cells/well, and the next day, cells were treated with 0, 0.04, 0.4, 0.8, 1.2, 2, 4, and 10 μM lentinan for 24 h. After the treatment, 10 μL of CCK-8 solvent was added to the cell culture medium for 1 hour, and the cell viability was evaluated by measuring the absorbance of the cells at 450 nm, and the cell viability was expressed using the following formula: cell viability = OD value of treated cells/average OD value of control cell × 100%.

2.7. Preparation of Conditioned Medium (CdM) for HUVECs Stimulation and Lentinan Treatment. THP-1 cells were seeded into a 24-well cell culture plate at a density of 1×10^6 cells/well; after 10-h culture, 10 ng/mL lipopolysaccharide was added; and the cells were cultured in the original culture environment for another 4 h. Subsequently, the cell suspension was centrifuged at 1000 g for 5 minutes, and the obtained CdM was stored at −80°C until use. This method of obtaining TNF-α by treating mononuclear cells with lipopolysaccharide has been researched and confirmed, and the method is extensively used [14]. For stimulation, HUVECs were inoculated into T25 cell culture flasks (Corning, USA) and were treated with 1.2, 2 μM lentinan for 24 h. After the treatment, the cells were washed with 3 mL M199/HEPES/PS and then stimulated with 5 mL CdM for 24 h.

2.8. Analysis of Changes in Protein Expression with Western Blotting. Cell proteins were extracted using RIPA lysis buffer (Biyuntian, Beijing). The BCA™ Protein Detection Kit (Takara, Japan) was used to measure total protein concentration via the comparison with protein standards. A 20 μg protein sample was then added to a prepared SDS-PAGE gel for electrophoretic separation. After separation, proteins were transferred to a PVDF membrane. After blocking, primary antibodies including CCAAT enhancer-binding protein (CHOP) (ab10444, Abcam, UK), glucose-regulating protein 78 (GRP78) (ab21685, Abcam, UK), inositol-requiring enzyme 1α (IRE1α) (ab37117, Abcam, UK), activating transcription factor 6 (ATF6) (65880, cell signaling technology, UK), SIRT1 (8469, cell signaling technology, UK), NF-κB phosphorylation p65 (ab97726, Abcam, United Kingdom), p65 (ab16502, Abcam, United Kingdom), inducible nitric oxide synthase (iNOS) (EPR16635, Abcam, United Kingdom), and internal reference protein β-actin (ab8277, Abcam, United States) were added and incubated overnight. The next day, the primary antibody was removed, and an HRP-conjugated secondary antibody was added at room temperature for incubation. After washing, images were developed with ECL luminescent liquid (Biyuntian, China).

2.9. RNA Extraction and Measurement of mRNA Expression with Real-Time Quantitative PCR (qPCR). Total cellular RNA was extracted by TRIzol (Invitrogen, USA) method, and the cellular RNA concentration was measured spectrophotometrically. Reverse transcription into cDNA (Takara, Japan) was performed according to the instructions, and qPCR was performed by SYBR Green (Takara, Japan) method. The experimental data were analyzed by the relative Ct value method ($2^{-\triangle\triangle Ct}$ method) for relative quantitative comparative analysis, and β-actin was used as the reference gene. The target primer sequences are shown in the following Table 1.

2.10. Detection of Cytokines. Enzyme-linked immunosorbent assay (ELISA, Baosai, China) was used to determine the levels of inflammatory factors including tumor necrosis factor α (TNF-α), interleukin 1β (IL-1β), and IL-6.

2.11. Detection of Apoptosis by Flow Cytometry and TUNEL Staining. The Annexin V (FITC)/propidium iodide (PI) method was used to detect apoptosis. Apoptosis detection kit was purchased from Beijing Baosai Biotechnology Co., Ltd. Specifically, cells were seeded at a density of 1×10^5 cells/well in a 6-well plate for culture. After treatment, cells were washed twice with prechilled PBS and centrifuged and resuspended in binding buffer. Then, 5 μL of Annexin V-FITC solution was added and gently mixed, after which the samples were incubated for 15 minutes in the dark. Then, 5 μL of the PI solution was added. Apoptosis was detected by flow cytometry (Beckman, USA). In terms of TUNEL staining, cells were treated according to TUNEL's instructions (Biyuntian, China), observed under a laser confocal microscope, and each field was randomly selected under a high-power microscope (×400) to count the number of apoptotic cells and the total number of cells.

2.12. Statistical Analysis. Statistical analysis was performed using SPSS IBM Statistics 21 (US) software. All results were expressed as mean ± standard deviation. *T*-test was used for comparison between two groups, and univariate analysis of variance was used for comparison between multiple groups. $P < 0.05$ was considered statistically significant.

3. Results

3.1. Purity Determination and Component Analysis of Lentinan. The lentinan was analyzed by HPLC and showed a single narrow symmetrical peak with a relative molecular weight of about 7037 Da, see Figure 1.

The polysaccharide content of lentinan was 43.71%, determined by phenol-sulfuric acid and the 3,5-dinitrosalicylic acid colorimetric methods. Gas chromatography analysis showed that it is composed of various monosaccharides including glucose, galactose, and mannose, fucose, and its molar ratio was 9.28 : 3.57 : 1.92 : 1.03, respectively, as shown in Figure 2.

3.2. Effects of Lentinan on HUVECs Activity. Lentinan was added to the culture medium at a final concentration of 0 (control group), 0.04, 0.4, 0.8, 1.2, 2, 4, and 10 μM, and cells were incubated for 24 h. The morphological changes of the cells were observed under a light microscope. As shown in Figure 3, compared with the control group, the morphology in the lentinan treatment groups with concentrations of 0.04, 0.4, 0.8, 1.2, 2, and 4 μM did not change significantly, whereas the cells in the 10 μM group atrophied, degenerated, and showed the state of cell death.

3.3. Concentration-Dependent Effect of Lentinan on HUVECs Activity. The CCK-8 assay was used to detect activity changes of HUVECs treated with different concentrations of lentinan. As shown in Figure 4, compared with the control group, when the concentration of lentinan was 0.04, 0.4, 0.8, 1.2, and 2 μM, there was no significant difference in cell viability ($P > 0.05$). However, when the concentration of lentinan reached 4 μM, the cell viability was significantly lower than that of the control group ($P < 0.001$), which was further reduced ($P < 0.001$) when the concentration of lentinan was 10 μM. Therefore, in subsequent experiments, 1.2 and 2 μM lentinan were used to treat cells.

3.4. Lentinan Reduces Endoplasmic Reticulum Stress Response in HUVECs with Sepsis. To investigate whether the protective effect of lentinan on sepsis endothelial cells is related to endoplasmic reticulum stress, we examined the mRNA and protein expression levels of endoplasmic reticulum stress-related factors using the qPCR and Western blotting methods, respectively. The qPCR results (Figure 5(a)) showed that compared with the control group, the expression of CHOP,

Table 1: The primer sequences.

Gene	Forward primers (5′-3′)	Reverse primers (5′-3′)
CHOP	GGAAACAGAGTGGTCATTCCC	CTGCTTGAGCCGTTCATTCTC
GRP78	CATCACGCCGTCCTATGTCG	CGTCAAAGACCGTGTTCTCG
IRE1α	CACAGTGACGCTTCCTGAAAC	GCCATCATTAGGATCTGGGAGA
ATF6	TCCTCGGTCAGTGGACTCTTA	CTTGGGCTGAATTGAAGGTTTTG
SIRT1	TAGCCTTGTCAGATAAGGAAGGA	ACAGCTTCACAGTCAACTTTGT
β-actin	CATGTACGTTGCTATCCAGGC	CTCCTTAATGTCACGCACGAT

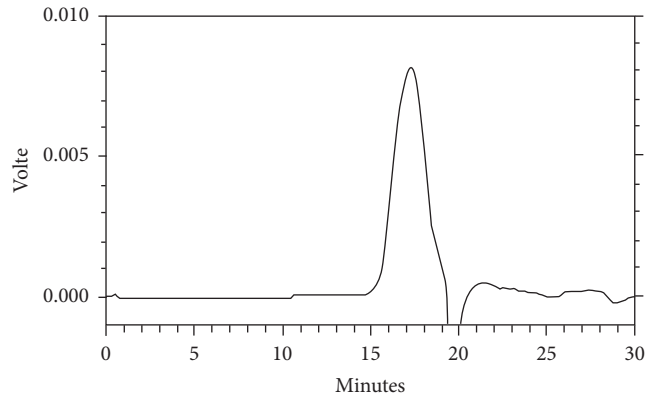

Figure 1: HPLC result of lentinan.

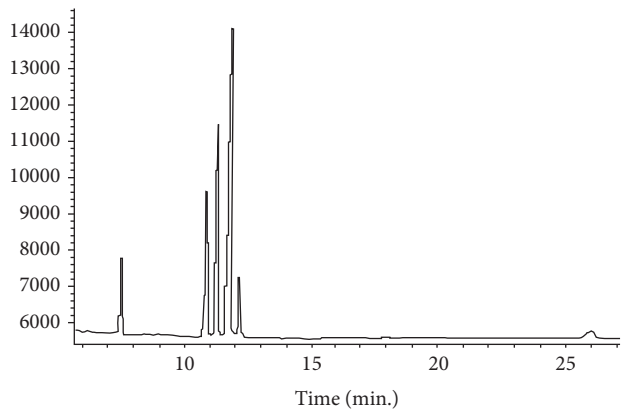

Figure 2: Gas chromatogram of lentinan.

GRP78, IRE1α, and ATF6 in sepsis cells was significantly increased ($P < 0.001$). However, when the cells were pretreated with 1.2 and 2 μM lentinan, expression levels of these factors were significantly reduced ($P < 0.001$). The Western blotting results (Figure 5(b)) were consistent with the qPCR results ($P < 0.001$). SIRT1 is a key medium for reducing endoplasmic reticulum stress. In this study, the mRNA (Figure 5(c)) and protein (Figure 5(d)) expression levels of SIRT1 were therefore also measured. The results showed that SIRT1 expression of endothelial cells was inhibited ($P < 0.001$) in sepsis. However, when HUVECs were pretreated with 1.2 and 2 μM lentinan, the inhibitory effect of SIRT1 expression was reversed ($P < 0.001$). The above results suggest that lentinan can inhibit endoplasmic reticulum stress response by upregulating SIRT1 expression in HUVECs in vitro sepsis model.

3.5. Lentinan Inhibits the Production of Inflammatory Cytokines in Sepsis Endothelial Cells. To explore the protective mechanism of lentinan on endothelial cells, we quantified the inflammatory cytokines released by HUVECs cells. The ELISA results (Figure 6(a)–6(c)) showed that compared with the control group, CdM has a stronger activation effect on the secretion of TNF-α, IL-1β, and IL-6 inflammatory cytokines ($P < 0.001$). However, pretreatment with 1.2 and 2 μM lentinan cells significantly inhibited the secretion of inflammatory cytokines ($P < 0.001$). In addition, we found that sepsis state can increase the expression of the inflammatory factor upstream mediator p65-phosphorylated protein and the downstream target iNOS protein, and pretreatment with lentinan can reverse this change (Figure 6(d)).

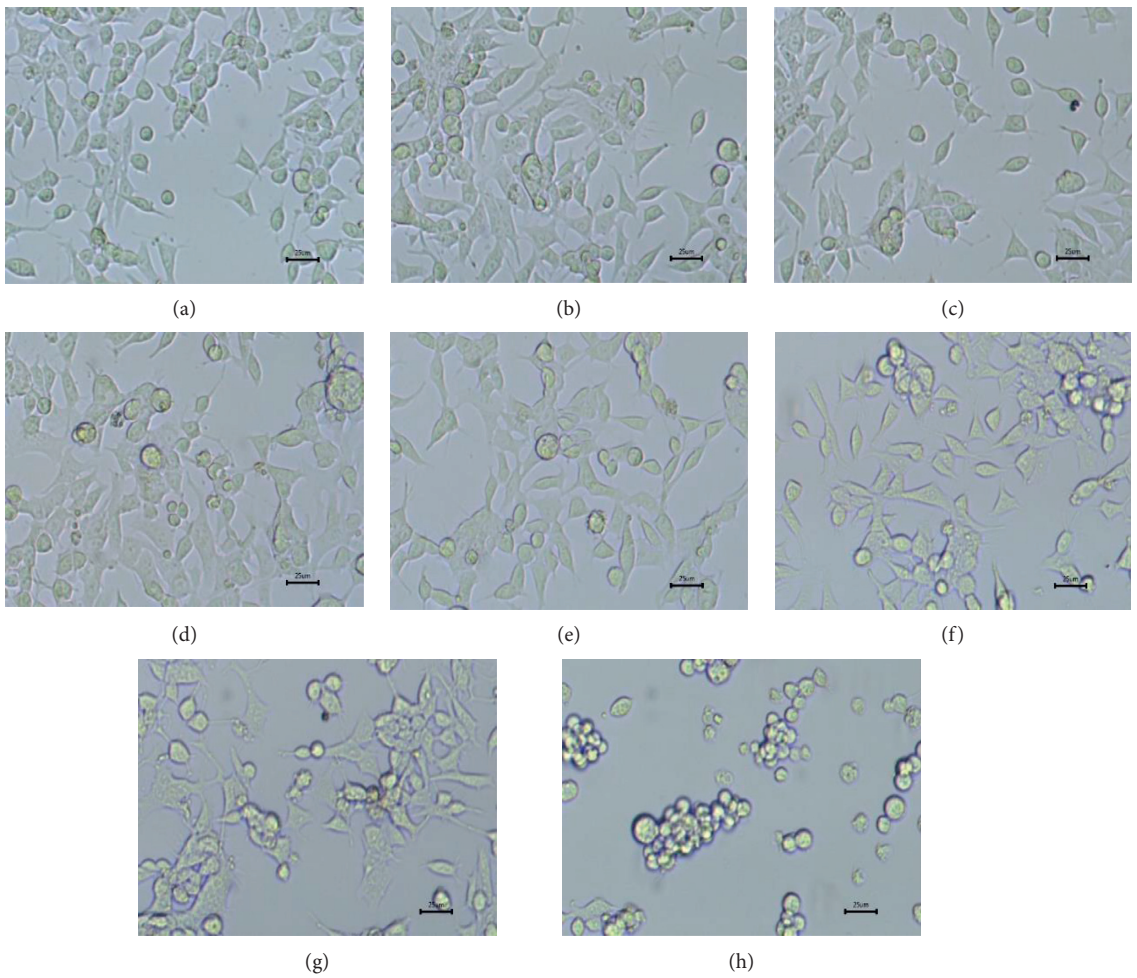

Figure 3: Concentration-dependent cytotoxic effects of lentinan on HUVECs. Figures A-H are HUVECs treated with lentinan at concentrations of 0, 0.04, 0.4, 0.8, 1.2, 2, 4, and 10 μM, respectively. Scale bar = 25 μm.

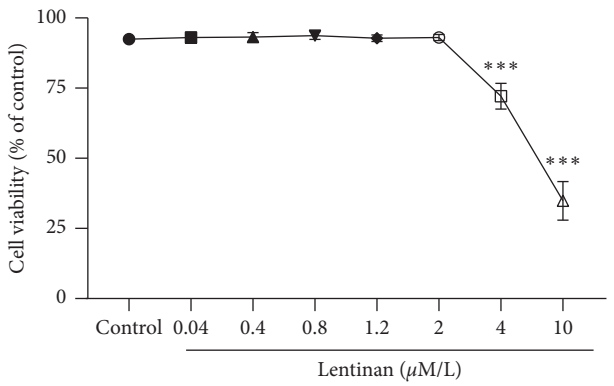

Figure 4: Viability of HUVECs treated with different concentrations of lentinan. Lentinan concentrations were 0 (control group), 0.04, 0.4, 0.8, 1.2, 2, 4, and 10 μM, and the values were expressed as mean ± standard deviation ($n = 4$). Compared with the control group, $^{***}P < 0.001$.

3.6. Lentinan Inhibits Sepsis Endothelial Cell Apoptosis. To study the effects of lentinan on the cell apoptosis, Annexin V-FITC/PI double staining and TUNEL staining were used to detect the apoptosis of endothelial cells in the control group, sepsis group, sepsis + LNA 1.2 μM group, and sepsis + LNA 2 μM group. Figure 7(a) shows that compared with the control group, the apoptotic rate of the sepsis group was significantly increased ($P < 0.001$), which was significantly reduced when 1.2 and 2 μM of lentinan were administered ($P < 0.001$). Figure 7(b) shows that the TUNEL results are consistent with the flow cytometry results ($P < 0.001$). These results suggest that lentinan can protect cells from sepsis-induced apoptotic damage.

4. Discussion

Endothelial cell activation and dysfunction is an important feature of sepsis and can play a key role in the development of sepsis. In this study, the HUVECs model of sepsis was established in vitro to investigate the inhibitory effect of lentinan on endothelial cell injury induced by sepsis. We found that a low concentration of lentinan had no obvious toxic effect on HUVECs. However, when the concentration of lentinan exceeded 2 μM, the cell viability was significantly reduced, and the cytotoxicity of lentinan was dose-dependent. We found that when HUVECs pretreated with 1.2 and

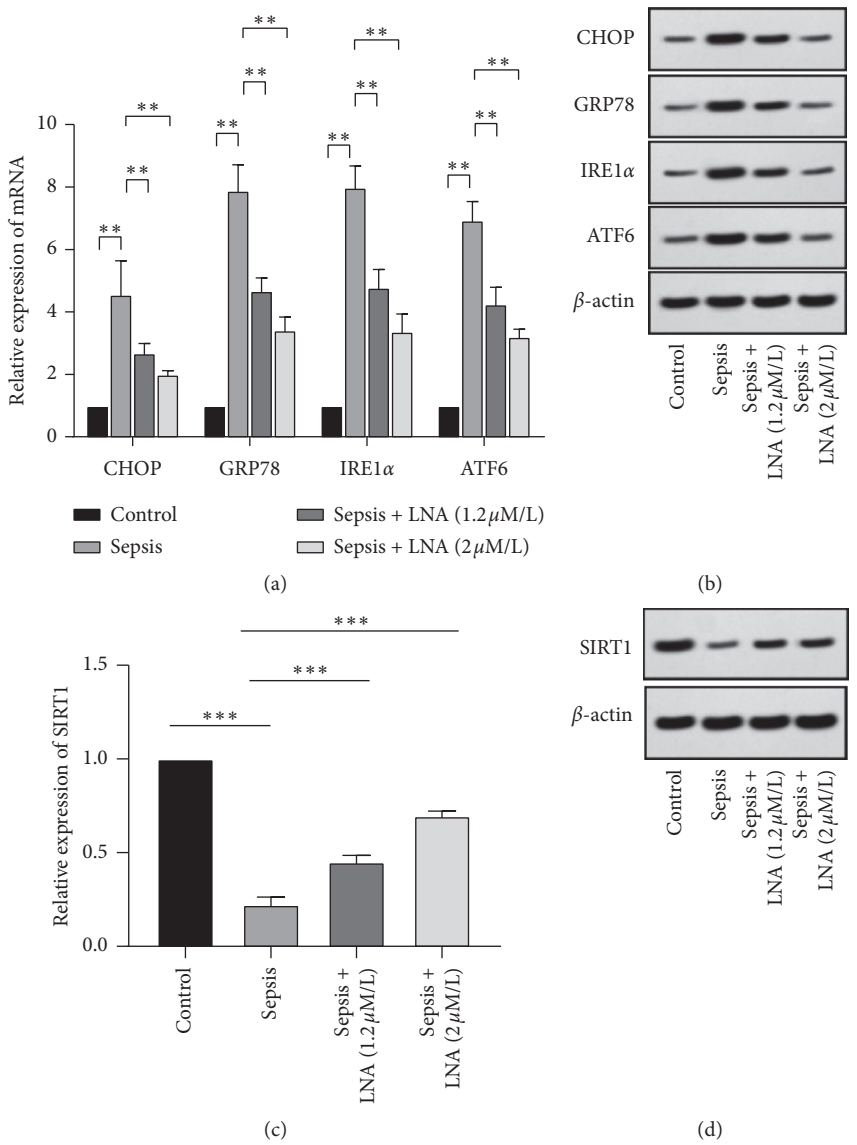

Figure 5: Lentinan reduces endoplasmic reticulum stress response in sepsis HUVECs. (a, b) mRNA and protein expressions of CHOP, GRP78, IRE1α, and ATF6 in endothelial cells of the control group, sepsis group, sepsis + LNA 1.2 μM group, and sepsis + LNA 2 μM group were measured by qPCR and Western blotting. (c, d) mRNA and protein expression of SIRT1 in endothelial cells of the control group, sepsis group, sepsis + LNA 1.2 μM group, and sepsis + LNA 2 μM group were measured by qPCR and Western blotting. Values are expressed as mean ± standard deviation ($n = 3$). Compared with the control group or sepsis model group, $^{**}P < 0.01$, $^{***}P < 0.001$.

2 μM lentinan and then stimulated with sepsis CdM, lentinan significantly reduced the expression of inflammatory factors such as TNF-α, IL-1β, and IL-6 in sepsis, thereby reducing the inflammatory response. In addition, we found that treatment with a certain level of lentinan can inhibit endoplasmic reticulum stress in the cells; specifically, we found reduced expression of ER stress-related factors including CHOP, GRP78, IRE1α, and ATF6. The inhibitory effect may be due to the regulation of lentinan on SIRT1 expression. Endoplasmic reticulum stress is known to cause apoptotic responses. This study also found that lentinan can inhibit the apoptotic response of sepsis cells and reduce the inflammatory factor upstream regulatory mediator phosphorylation of p65 protein (NF-κB activation marker), and downstream targets iNOS.

Sepsis is known to be a proinflammatory and anti-inflammatory coexisting complex SIRS. Endoplasmic reticulum stress plays an important role in it. Some studies have found that endoplasmic reticulum stress is involved in the occurrence and development of sepsis [15]. Endoplasmic reticulum stress can induce the release of proinflammatory factors by activating downstream signaling pathways of the inflammatory response [16], and cascade activation of inflammation further aggravates programmed cell death and

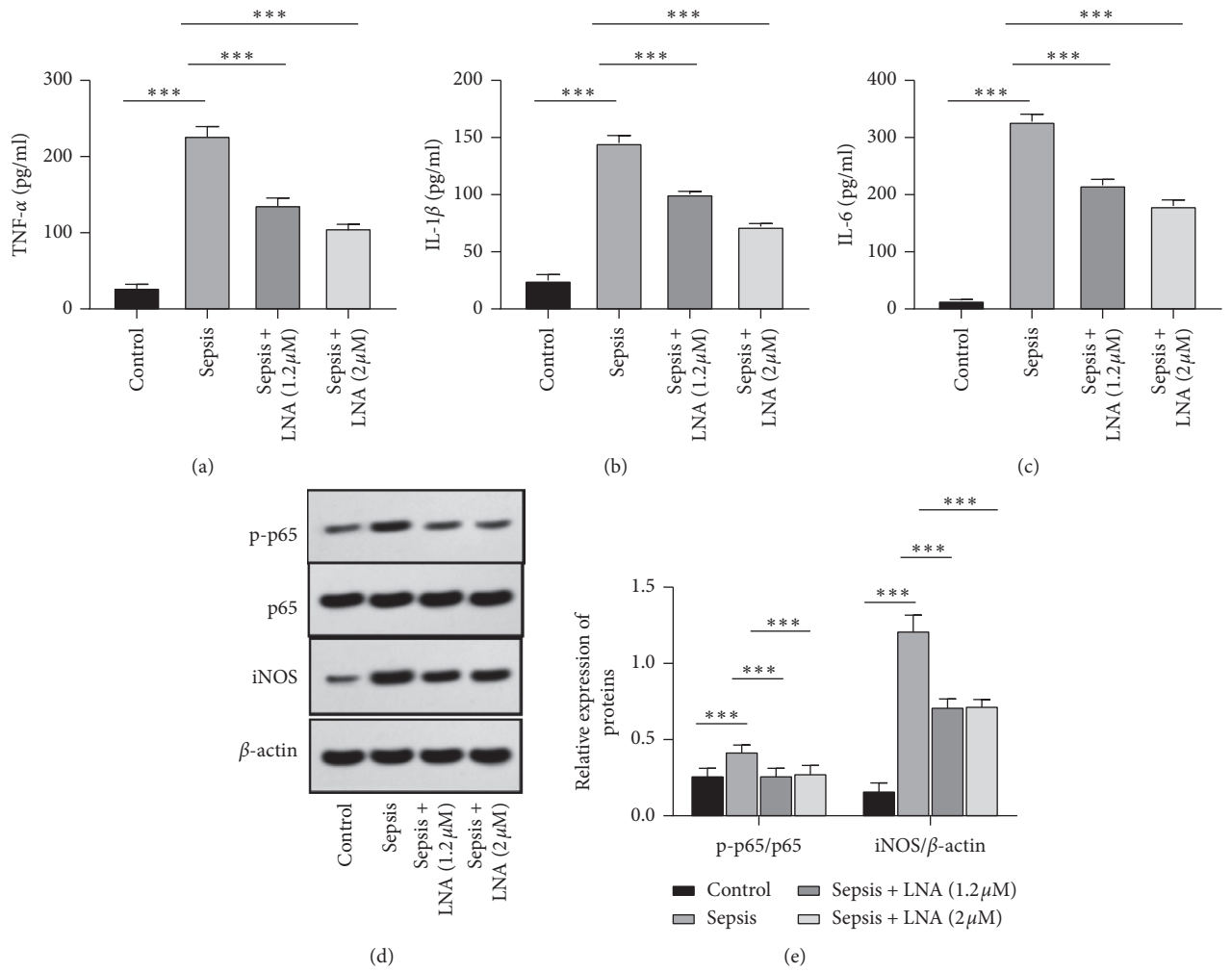

Figure 6: Lentinan reduces the inflammatory response of endothelial cells in sepsis. (a–c) Levels of TNF-α, IL-1β, and Il-6 secreted by HUVECs cells in the control group (lentinan 0 μM), sepsis group (sepsis group), sepsis + lentinan 1.2 μM group (sepsis + LNA 1.2 μM group), and sepsis + lentinan 2 μM group (sepsis + LNA 2 μM group); (d) detection of the p65 protein phosphorylation level and iNOS protein expression level by Western blotting. Values are expressed as mean ± standard deviation ($n = 4$). Compared with the control group or the sepsis model group, $^{***}P < 0.001$.

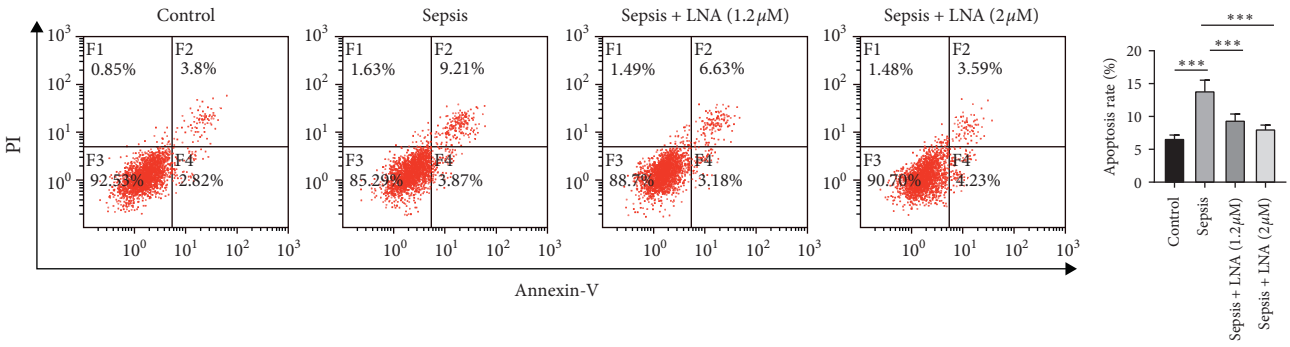

(a)

Figure 7: Continued.

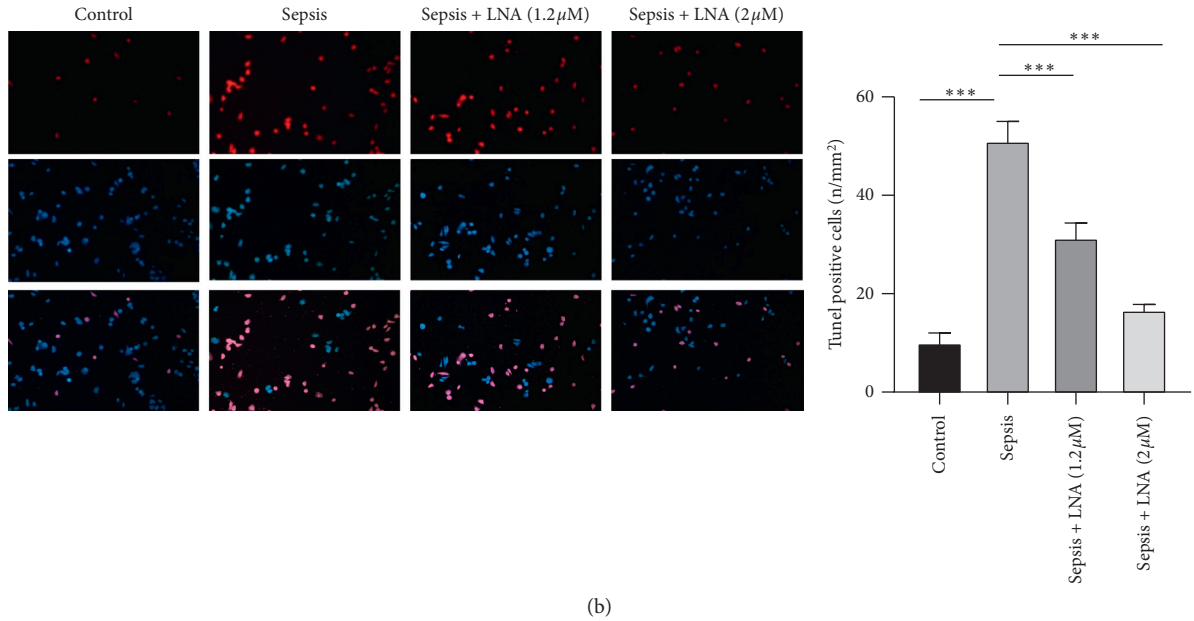

(b)

Figure 7: Lentinan inhibits apoptosis of endothelial cells in sepsis and expression of apoptosis-related proteins p65 and iNOS. In the control group, sepsis group, sepsis + LNA 1.2 μM group, and sepsis + LNA 2 μM group, (a) the flow cytometry Annexin V-FITC/PI double-labeling method was used to detect apoptosis and (b) TUNEL staining was used to detect apoptosis. Red dots denote that the nucleus stained positively by the TUNEL method, blue the nucleus of DAPI staining, while purple double staining. Values are expressed as mean ± standard deviation ($n = 3$). Compared with the control group or sepsis model group, $^{**}P < 0.01$ and $^{***}P < 0.001$.

tissue damage. Lentinan is a biological response modifier, which has the effect of reducing oxidative damage. At present, no significant adverse reaction has been reported in the human intake of lentinan [17]. Previous studies have found that lentinan can improve the immune defense system of mice by regulating inflammatory cytokines and chemokines [18]. In addition, it has been reported that lentinan can regulate the immune response by changing the structure and composition of the intestinal microbial community [18]. Zhang et al. demonstrated that lentinan can protect cardiomyocytes, inhibit apoptosis, and reduce hypoxia-induced cell damage by regulating microRNA-22/SIRT1 in primary neonatal rat cardiomyocytes [19]. However, no studies have reported the role and mechanism of lentinan in sepsis endothelial cells.

The endoplasmic reticulum stress signaling pathway is closely related to cellular inflammation, and downstream signaling pathways activated by endoplasmic reticulum stress can strongly stimulate the production of proinflammatory cytokines [20]. As important regulators of endoplasmic reticulum stress, CHOP, GRP78, IRE1α, and ATF6 have all been shown to play a role in regulating apoptosis [21]. Therefore, we established a model of sepsis endothelial cell in vitro, tested the expression of endoplasmic reticulum stress-related proteins under the intervention of lentinan, and demonstrated that lentinan can reduce endoplasmic reticulum stress response by inhibiting the expression of endoplasmic reticulum stress-related proteins such as CHOP, GRP78, IRE1α, and ATF6. In addition, as a downstream response to endoplasmic reticulum stress, the inflammatory response is an important cellular response process. Our study found that lentinan can significantly reduce the production of inflammatory factors including TNF-α, IL-1β, and IL-6, thereby reducing the inflammatory response. Furthermore, apoptosis is one of the cell outcomes caused by sepsis. In this study, flow cytometry and TUNEL staining were also used to detect apoptosis, and it was found that lentinan can significantly inhibit apoptosis and reduce the expression of the related protein.

Therefore, we believe that lentinan can protect endothelial cells and reduce damage when sepsis occurs in the body, and lentinan is expected to become a new target for treating endothelial damage caused by sepsis.

Data Availability

The data used to support the study are available from the corresponding author upon request.

Conflicts of Interest

The authors declare that there are no conflicts of interest regarding the publication of this paper.

Acknowledgments

This study was supported by the Science and Technology Funding of Huai'an (No. HAS2013008).

References

[1] L. Yang, D. Li, Y. Zhuo, S. Zhang, X. Wang, and H. Gao, "Protective role of liriodendrin in sepsis-induced acute lung injury," *Inflammation*, vol. 39, no. 5, pp. 1805–1813, 2016.

[2] J. Cohen, "The immunopathogenesis of sepsis," *Nature*, vol. 420, no. 6917, pp. 885–891, 2002.

[3] M. F. Osuchowski, C. Thiemermann, and D. G. Remick, "Sepsis-3 on the block," *Shock*, vol. 47, no. 5, pp. 658–660, 2017.

[4] A. R. Novotny, D. Reim, V. Assfalg et al., "Mixed antagonist response and sepsis severity-dependent dysbalance of pro- and anti-inflammatory responses at the onset of postoperative sepsis," *Immunobiology*, vol. 217, no. 6, pp. 616–621, 2012.

[5] D. Brislinger, C. Daxböck, E. Rossmanith, M. Stückler, I. Lang, and D. Falkenhagen, "Bai Hu Tang, Si Ni Tang, and Xue Bi Tang amplify pro-inflammatory activities and reduce apoptosis in endothelial cells in a cell culture model of sepsis," *Journal of Ethnopharmacology*, vol. 225, pp. 309–318, 2018.

[6] M.-F. Moradali, H. Mostafavi, S. Ghods, and G.-A. Hedjaroude, "Immunomodulating and anticancer agents in the realm of macromycetes fungi (macrofungi)," *International Immunopharmacology*, vol. 7, no. 6, pp. 701–724, 2007.

[7] L. Ren, C. Perera, and Y. Hemar, "Antitumor activity of mushroom polysaccharides: a review," *Food & Function*, vol. 3, no. 11, pp. 1118–1130, 2012.

[8] Y. Nishitani, L. Zhang, M. Yoshida et al., "Intestinal anti-inflammatory activity of lentinan: influence on IL-8 and TNFR1 expression in intestinal epithelial cells," *PLoS One*, vol. 8, no. 4, Article ID e62441, 2013.

[9] M. Mizuno, Y. Nishitani, T. Hashimoto, and K. Kanazawa, "Different suppressive effects of fucoidan and lentinan on IL-8 mRNA expression inin vitroGut inflammation," *Bioscience, Biotechnology, and Biochemistry*, vol. 73, no. 10, pp. 2324-2325, 2009.

[10] C. Kupfahl, G. Geginat, and H. Hof, "Lentinan has a stimulatory effect on innate and adaptive immunity against murine listeria monocytogenes infection," *International Immunopharmacology*, vol. 6, no. 4, pp. 686–696, 2006.

[11] H. Zhu, K. Sheng, E. Yan, J. Qiao, and F. Lv, "Extraction, purification and antibacterial activities of a polysaccharide from spent mushroom substrate," *International Journal of Biological Macromolecules*, vol. 50, no. 3, pp. 840–843, 2012.

[12] Y.-j. Zhang, L.-x. Zhang, J.-f. Yang, and Z.-y. Liang, "Structure analysis of water-soluble polysaccharide CPPS3 isolated from *Codonopsis pilosula*," *Fitoterapia*, vol. 81, no. 3, pp. 157–161, 2010.

[13] Z. J. Zhang, W. Sun, L. I. Yong-Liang et al., "Determination of polysaccharide in rhizoma polygonatii by phenol-sulfuric acid and DNS methods," *Chinese Journal of Experimental Traditional Medical Formulae*, vol. 6, pp. 106–109, 2012.

[14] A. Schildberger, E. Rossmanith, V. Weber, and D. Falkenhagen, "Monitoring of endothelial cell activation in experimental sepsis with a two-step cell culture model," *Innate Immunity*, vol. 16, no. 5, pp. 278–287, 2010.

[15] M. M. Khan, W.-L. Yang, and P. Wang, "Endoplasmic reticulum stress in sepsis," *Shock*, vol. 44, no. 4, pp. 294–304, 2015.

[16] R. Iscimen, R. Cartin-Ceba, M. Yilmaz et al., "Risk factors for the development of acute lung injury in patients with septic shock: an observational cohort study," *Critical Care Medicine*, vol. 36, no. 5, pp. 1518–1522, 2008.

[17] G. Ren, K. Li, Y. Hu, M. Yu, J. Qu, and X. Xu, "Optimization of selenizing conditions for Seleno-Lentinan and its characteristics," *International Journal of Biological Macromolecules*, vol. 81, pp. 249–258, 2015.

[18] X. Xu and X. Zhang, "Lentinula edodes-derived polysaccharide alters the spatial structure of gut microbiota in mice," *PLoS One*, vol. 10, no. 1, Article ID e0115037, 2015.

[19] S. Zhang and Y. Zhao, "Lentinan protects cardiomyocytes against hypoxia-induced injury by regulation of microRNA-22/Sirt1," *Artificial Cells, Nanomedicine, and Biotechnology*, vol. 47, no. 1, pp. 3938–3946, 2019.

[20] F. Martinon, X. Chen, A.-H. Lee, and L. H. Glimcher, "TLR activation of the transcription factor XBP1 regulates innate immune responses in macrophages," *Nature Immunology*, vol. 11, no. 5, pp. 411–418, 2010.

[21] R. Sano and J. C. Reed, "ER stress-induced cell death mechanisms," *Biochimica et Biophysica Acta (BBA)-Molecular Cell Research*, vol. 1833, no. 12, pp. 3460–3470, 2013.

Hindawi
Advances in Polymer Technology
Volume 2020, Article ID 8486039, 7 pages
https://doi.org/10.1155/2020/8486039

Research Article

Effects of Huaier Polysaccharide SP1 on Gastric Cancer Cell Proliferation, Apoptosis, Migration, and Invasion by Regulating TGF-β/SMAD Signaling Pathway

Miaoliang Chen,[1] Ying Lu,[2] Ruili Zhang,[1] Tienan Bi,[1] and Shenkang Zhou[1]

[1]*Department of Gastrointestinal Surgery, Taizhou Hospital of Zhejiang Province, Wenzhou Medical University, Taizhou, Zhejiang 317000, China*
[2]*Pharmacy Department, Taizhou Hospital of Zhejiang Province, Wenzhou Medical University, Taizhou, Zhejiang 317000, China*

Correspondence should be addressed to Shenkang Zhou; zhousk@enzemed.com

Received 6 November 2019; Revised 8 December 2019; Accepted 19 December 2019; Published 8 February 2020

Guest Editor: Mingqiang Li

Objective. To study the effects of Huaier polysaccharide SP1 on the proliferation, apoptosis, migration, and invasion of gastric cancer cell line MGC-803 and the underlying mechanism. *Methods*. MGC-803 cells were cultured in vitro and treated with SP1. The effects of SP1 on the proliferation, apoptosis, migration, and invasion of MGC-803 cells were detected by CCK-8 assay, flow cytometry analysis, and Transwell assay, respectively. Western blot and qRT-PCR were used to detect the expression of related genes. *Results*. Our study showed that Huaier polysaccharide SP1 could inhibit proliferation, migration, invasion, and promote the apoptosis of MGC-803 cells in vitro in a dose-dependent manner. Huaier polysaccharide SP1 could inhibit the activation of TGF-β/SMAD signal pathway by upregulating SMAD7 expression, thereby downregulating the expression of SOX4, ZEB2, MMP9, Snail, and Slug. *Conclusion*. Huaier polysaccharide SP1 can regulate the proliferation, apoptosis, migration, and invasion of gastric cancer cells by promoting the expression of SMAD7 and inhibiting the activation of TGF-β/SMAD signal pathway as well as the expression of the downstream oncogenes.

1. Introduction

Gastric cancer, one of the common malignancies in the world, has seen great development in its therapeutic strategies such as radical surgery, traditional chemotherapy, radiation therapy, and targeted therapy in recent years. However, it still has a high mortality rate [1, 2], which is mainly because there is no better treatment for patients with advanced and/or metastatic gastric cancer, and systemic chemotherapy remains the main option [3, 4]. As conventional chemotherapeutics are causing higher drug resistance, and cytotoxic and serious side effects [5, 6], it is of great significance to find a novel, highly effective anticancer drug with few side effects for treating gastric cancer and reducing the chemotherapy-induced adverse effects.

Trametes robiniophila Murr, also called Huaier, is a Chinese medicinal fungus [7]. Recent studies have found that polysaccharides extracted from Huaier have inhibitory effects on various tumor cells such as those of breast cancer [7, 8], liver cancer [9, 10], and clear cell renal cell carcinoma (CCRCC) [11]. Moreover, Huaier polysaccharides exert anticancer effects in various ways. For example, Luo et al. reported that Huaier polysaccharide SP1 caused apoptosis in breast cancer MCF-7 cells by downregulating MTDH protein [8]; Li et al. proved that Huaier polysaccharides suppressed liver cancer growth and metastasis by inhibiting angiogenesis [9]; Fang et al. found that Huaier polysaccharide HP-1 inhibited the progression of CCRCC by inhibiting epithelial-mesenchymal transition and improved the efficacy of sunitinib [11]. So far, there have been no

studies on Huaier polysaccharides in gastric cancer, and the underlying mechanism remains unknown.

According to the method of Luo et al. [8], we extracted Huaier polysaccharide SP1 from Trametes robiniophila Murr, explored its function in gastric cancer cell line MGC-803, and further explained the corresponding mechanism, thus providing a theoretical basis for the application of Huaier polysaccharide SP1 as a chemotherapeutic agent in the treatment of gastric cancer.

2. Materials and Methods

2.1. Extraction and Identification of Huaier Polysaccharide SP1. Huaier polysaccharide SP1 was extracted according to the method reported by Luo et al. [8]. First, sandy and beige powdered water-soluble crude polysaccharide (SCP) was isolated and purified from the fruiting bodies of Trametes robiniophila Murr. Next, SCP was further purified by DEAE cellulose and agarose CL-6B gel filtration chromatography to obtain polysaccharides with different average molecular weight distributions. The water-soluble neutral fraction SP1 was collected and lyophilized for further study, and the products were identified by high-performance liquid chromatography. A single peak indicated the homogeneity of the products, with an average molecular weight of approximately 56 kDa (Figure 1). Gas chromatography analysis showed that SP1 was composed of galactose, arabinose, and glucose in a molar ratio of 3.1 : 1.1 : 1.1 : 3.3.

2.2. Cell Culture and Treatment. Human gastric cancer cell line MGC-803 was purchased from ATCC, USA. The MGC-803 cell line was routinely cultured with DMEM high glucose medium containing 10% fetal bovine serum, 100 μ/ml penicillin, and 100 g/ml streptomycin. The cells were cultured in a humidified incubator containing 5% carbon dioxide at 37 C.

2.3. Cell Viability Test. MGC-803 cells were seeded in 96-well plates at a density of 3000 cells/well and preincubated for 24 hours. Different concentrations of SP1 were then added, and CCK-8 reagent (Dojindo, Japan) was added at 24, 48, and 72 h respectively. The absorbance (A) at 450 nm was measured on a spectrophotometer. Relative cell activity = (the treatment group value − the blank background value)/(the control group value − the blank background value) × 100%.

2.4. Cell Migration Assay. Cell migration ability was detected using a scratch assay. MGC-803 cells treated with different concentrations of SP1 were cultured to a confluency rate of 95%. A straight line was scratched on the cells perpendicular to the culture plate with a tip, followed by PBS washing to remove detached cells. Serum-free DMEM high glucose medium with different concentrations of SP1 was then added. The cells were cultured in a cell culture incubator and photographed at 24 hours. Cell mobility was calculated.

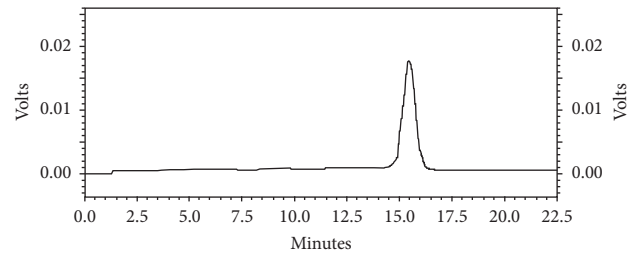

Figure 1: Identification of Huaier polysaccharide SP1 by high-performance liquid chromatography.

Relative cell mobility = (0 h scratch width − after-culture scratch width)/0 h scratch width × 100%.

2.5. Apoptosis Detection. MGC-803 cells were seeded in 12-well plates and treated with different concentrations of SP1 for 72 h in an incubator. Cells were collected, washed twice with PBS, and stained using the Annexin V-FITC/PI Apoptosis kit. Samples were analyzed on a flow cytometer. Apoptosis rate (%) = early apoptosis rate (%) + late apoptosis rate (%).

2.6. Cell Invasion Assay. Cell invasion ability was measured using a Transwell assay. A 100 μl mixture of matrix gel (Corning, USA) and serum-free DMEM medium (1 : 8) was coated on the upper transwell chamber (Corning). The cells (5×10^4) were seeded in the upper chamber with DMEM containing no serum 4 h after the matrix gel had solidified, and DMEM medium containing 10% fetal bovine serum was added to the lower chamber. The cells were cultured for 24 hours, fixed with methanol and stained with crystal violet, and cells on the lower surface of the membrane were photographed and counted using a microscope.

2.7. Western Blot. The proteins extracted with RIPA lysate were quantified using a BCA protein assay kit, and equal amounts of proteins were electrophoresed on 10% SDS-PAGE followed by immunoblotting on nitrocellulose membranes. Membranes were blocked with 5% skim milk for 2 h at room temperature and then incubated with primary antibodies overnight at 4 C. After incubation with HRP-conjugated secondary antibodies, the proteins were visualized on an ECL gel imaging system. Primary antibodies were purchased from Abcam.

2.8. qRT-PCR. Total cellular RNA was extracted with TRIzol reagent (Takara, Japan), and cDNA was synthesized using Prime Script RT reagent kit (Takara). All reactions were performed with the use of TaqMan Gene Expression Assay system (Applied Biosystems, USA) and TaqMan Universal PCR Master Mix reagents (Thermo Fisher Scientific, USA). The relative gene expression levels were calculated using the $2^{-\Delta\Delta ct}$ method with β-actin as an internal reference. All experiments were repeated at least three times. All primers used in the experiments are listed in Table 1.

Table 1: qRT-PCR Primer sequence.

Genes	Forward primers (5′–3′)	Reverse primers (5′–3′)
SMAD7	TTCCTCCGCTGAAACAGGG	CCTCCCAGTATGCCACCAC
SOX4	GACCTGCTCGACCTGAACC	CCGGGCTCGAAGTTAAAATCC
ZEB2	CAAGAGGCGCAAACAAGCC	GGTTGGCAATACCGTCATCC
MMP9	GGGACGCAGACATCGTCATC	TCGTCATCGTCGAAATGGGC
Snail	TCGGAAGCCTAACTACAGCGA	AGATGAGCATTGGCAGCGAG
Slug	CGAACTGGACACACATACAGTG	CTGAGGATCTCTGGTTGTGGT
β-actin	CATGTACGTTGCTATCCAGGC	CTCCTTAATGTCACGCACGAT

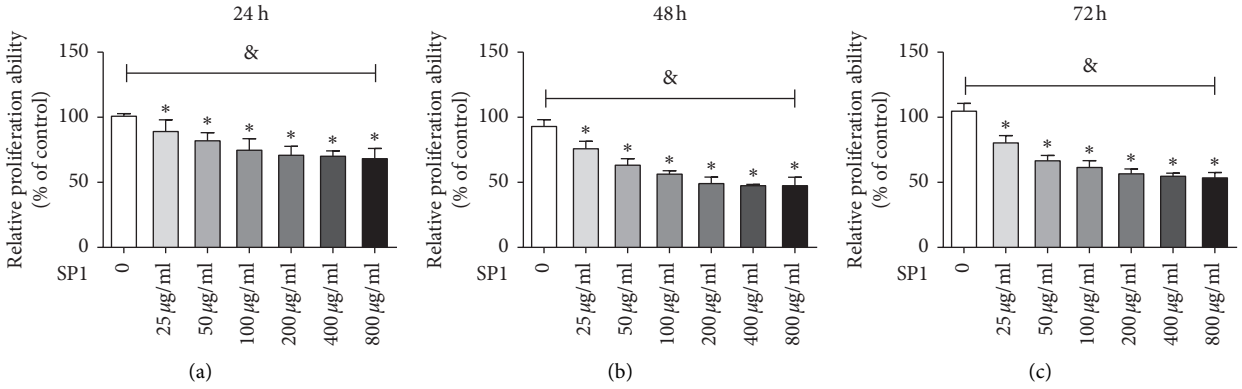

Figure 2: Results of relative cell viability of MGC-803 cells treated with different concentrations of SP1 (0, 25, 50, 100, 200, 400, and 800 μg/ml) for 24, 48, and 72 hours, respectively. Compared with 0 μg/ml SP1-treated (control) group, $^{*}P < 0.05$; $^{\&}P < 0.05$ for comparison between groups under different concentrations of SP1 treatment.

2.9. Statistical Analysis. Data were presented as mean ± standard deviation, and each experiment was independently repeated at least three times. Statistical analysis was performed using SPSS 20.0 software. Comparisons between the experimental and control groups were performed using Student's t-test and one-way ANOVA. $P < 0.05$ was considered statistically significant.

3. Results

3.1. SP1 Inhibited MGC-803 Cell Proliferation. Figure 2 showed that MGC-803 cells had a dose-dependent inhibition on the growth of MCF-7 cells after exposure to different concentrations of SP1 (25, 50, 100, 200, 400, and 800 μg/ml) for 24, 48, and 72 hours ($P < 0.05$). As the SP1 concentration increased to 50 μg/ml, cell viability decreased significantly over all time periods. However, the decreasing trends of cell viability were similar at a concentration above 200 μg/ml. Therefore, SP1 could suppress MGC-803 cell proliferation.

3.2. SP1 Promoted Apoptosis in MGC-803 Cells. As shown in Figure 3, flow cytometric analysis revealed that MGC-803 cells after exposure to different concentrations of SP1 (25, 50, 100, and 200 μg/ml) for 72 hours showed significantly increased proportion of apoptosis with increasing doses of SP1 ($P < 0.05$), indicating that SP1 could promote MGC-803 cell apoptosis.

3.3. SP1 Inhibited Migration of MGC-803 Cells. As shown in Figure 4, the scratch assay revealed that MGC-803 cells treated with 25, 50, 100, and 200 μg/ml of SP1 showed a marked decrease in cell migration in a dose-dependent manner ($P < 0.05$), suggesting that SP1 could inhibit MGC-803 cell migration.

3.4. SP1 Inhibited MGC-803 Cell Invasion. As shown in Figure 5, the transwell assay revealed that MGC-803 cells treated with 25, 50, 100, and 200 μg/ml of SP1 showed a significant decrease in cell invasion in a dose-dependent manner ($P < 0.05$), demonstrating that SP1 could inhibit MGC-803 cell invasion.

3.5. SP1 Inhibited the Activation of the TGF-β/SMAD Signaling Pathway. After treatment of MGC-803 cells with 200 μg/ml of SP1 for 72 h, we found that SP1 could significantly elevate SMAD7 mRNA and protein levels (Figures 6(a) and 6(b)), which in turn inhibited the expression of TGF-βRI. Meanwhile, SP1 could significantly reduce the phosphorylation levels of SMAD2 and SMAD3, and downstream proteins of TGF-βRI (Figure 6(b)).

3.6. SP1 Inhibited the Expression of Downstream Oncogenes in the TGF-β/SMAD Signaling Pathway. We examined mRNA and protein expressions of the proliferation, apoptosis, migration, and invasion-related downstream genes in the

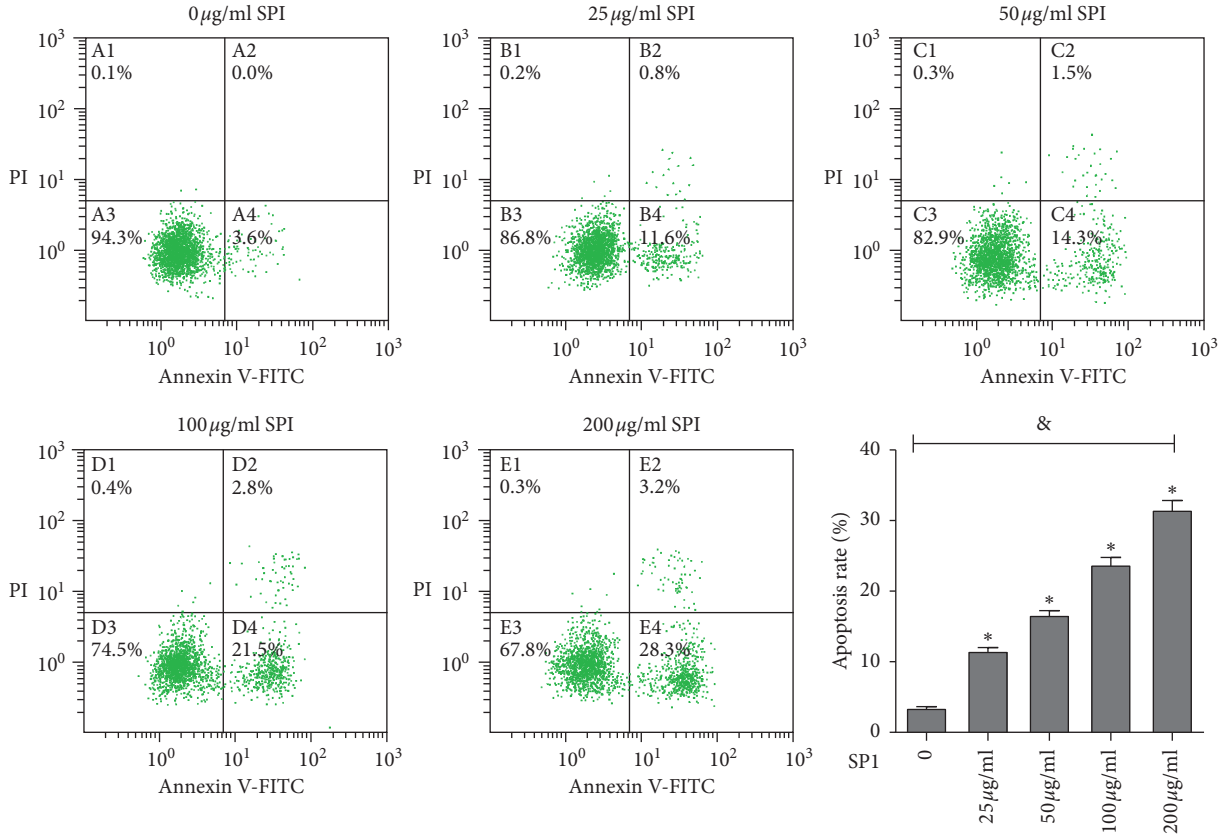

Figure 3: Apoptosis of MGC-803 cells treated with different concentrations of SP1 (0, 25, 50, 100, and 200 μg/ml) for 72 h was detected by flow cytometry. Compared with 0 μg/ml SP1-treated (control) group, $^{*}P < 0.05$; $^{\&}P < 0.05$ for comparison between groups under different concentrations of SP1 treatment.

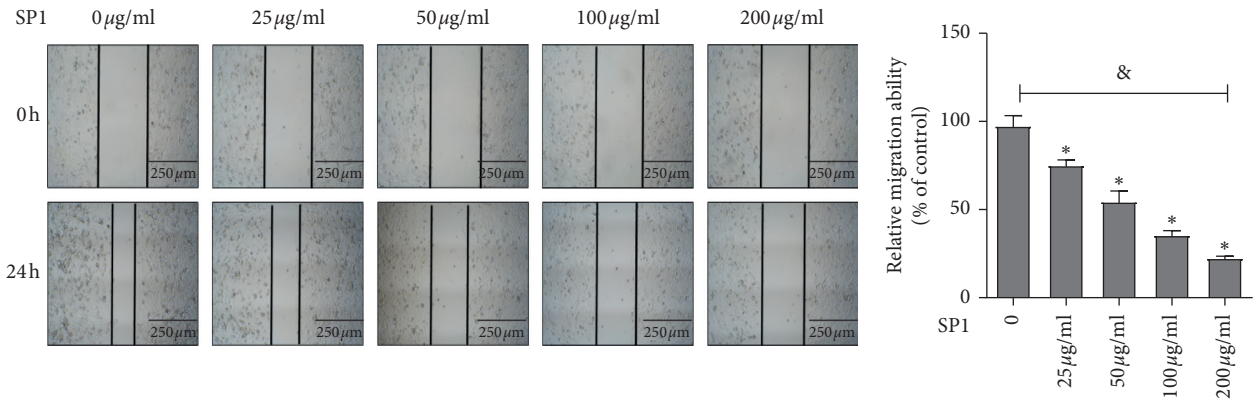

Figure 4: Scratch assay was used to detect the change of cell migration ability in MGC-803 cells treated with different concentrations of SP1 (0, 25, 50, 100, and 200 μg/ml) for 24 h Compared with 0 μg/ml SP1-treated (control) group, $^{*}P < 0.05$; $^{\&}P < 0.05$ for comparison between groups under different concentrations of SP1 treatment.

TGF-β/SMAD signaling pathway including SOX4, ZEB2, MMP9, Snail, and Slug and found that these gene expression levels were inhibited by SP1 (Figure 7).

4. Discussion

There is increasing evidence that herbs have antitumor effects. Huaier is a common medicinal fungus that has been used in traditional Chinese medicine for more than 1000 years [12]. Moreover, it has attracted more and more attention due to its antitumor and immune-promoting functions as well as negligible side effects. In this study, we isolated purified polysaccharide SP1 from Huaier and demonstrated that SP1 could exert antitumor effects by inhibiting the TGF-β signaling pathway.

In vitro studies revealed that Huaier polysaccharide SP1 could significantly inhibit the proliferation, migration, and invasion while it could promote the apoptosis of MGC-803

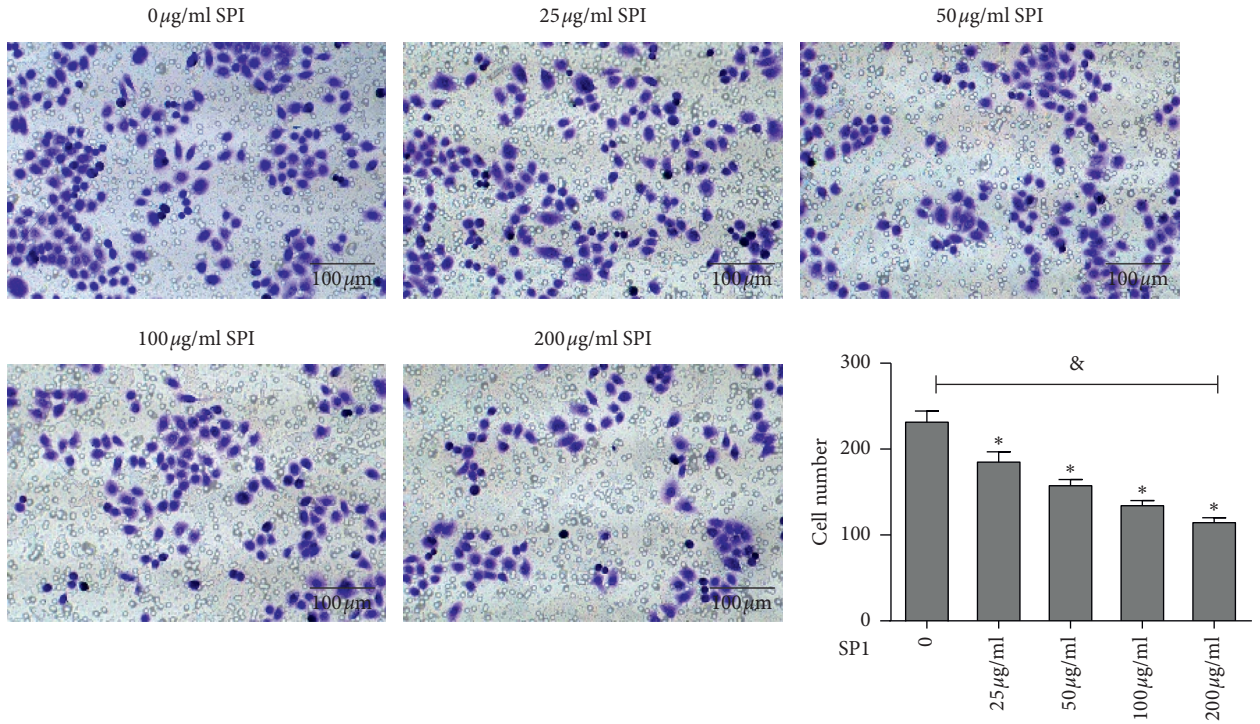

Figure 5: The invasion ability of MGC-803 cells treated with different concentrations of SP1 (0, 25, 50, 100, and 200 μg/ml) for 72 h was detected by transwell assay. Compared with 0 μg/ml SP1-treated (control) group, $^{*}P < 0.05$; $^{\&}P < 0.05$ for comparison between groups under different concentrations of SP1 treatment.

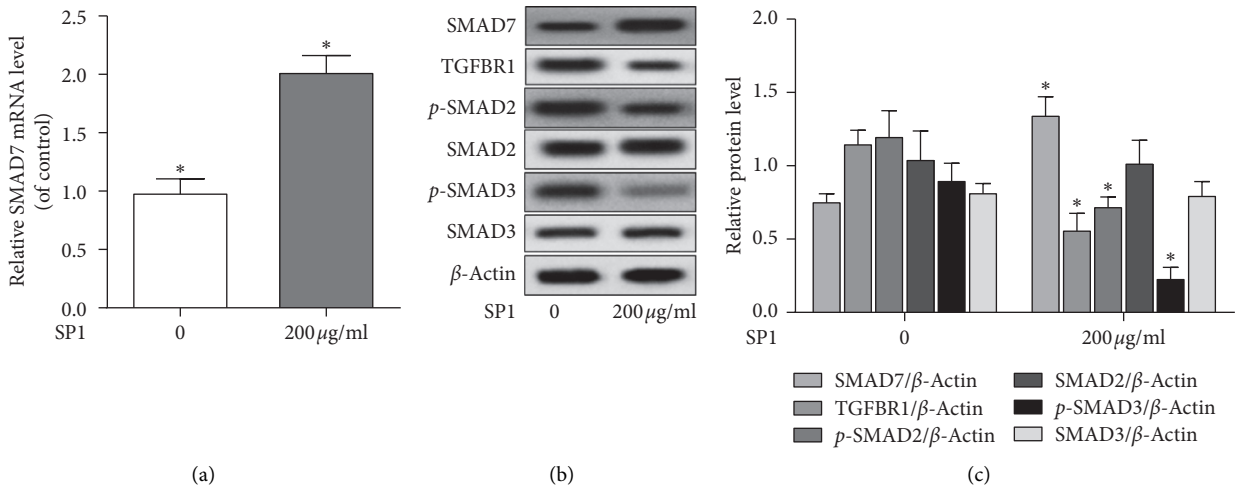

Figure 6: (a) The expression of SMAD7 mRNA in MGC-803 cells of the control group (SP1 0 μg/ml) and SP1 treatment group (200 μg/ml) for 72 h was detected by qRT-PCR. (b) The protein level of SMAD7 in MGC-803 cells of the control group (SP1 0 μg/ml) and SP1 treatment group (200 μg/ml) for 72 h was detected by Western blot. Compared with the control group, $^{*}P < 0.05$.

cells. However, there have been no studies on the effects of Huaier polysaccharides in gastric cancer, so we have proved for the first time that Huaier polysaccharide SP1 has a significant anticancer effect on gastric cancer and can be used as a chemotherapeutic or adjuvant drug in the treatment of gastric cancer. Through oral administration, Huaier polysaccharide SP1 can directly enter the stomach and act on gastric cancer, which may have better antitumor effects.

So far, the explanation for the mechanism of Huaier polysaccharides against cancer is still insufficient. In this study, we found that SP1 could inhibit the activation of TGF-β/SMAD signaling pathway by upregulating the expression of SMAD7. TGF-β, transforming growth factor β, is a pleiotropic cytokine that signals via membrane receptors and intracellular SMAD proteins, which then enter the nucleus after receptor activation and act as transcription

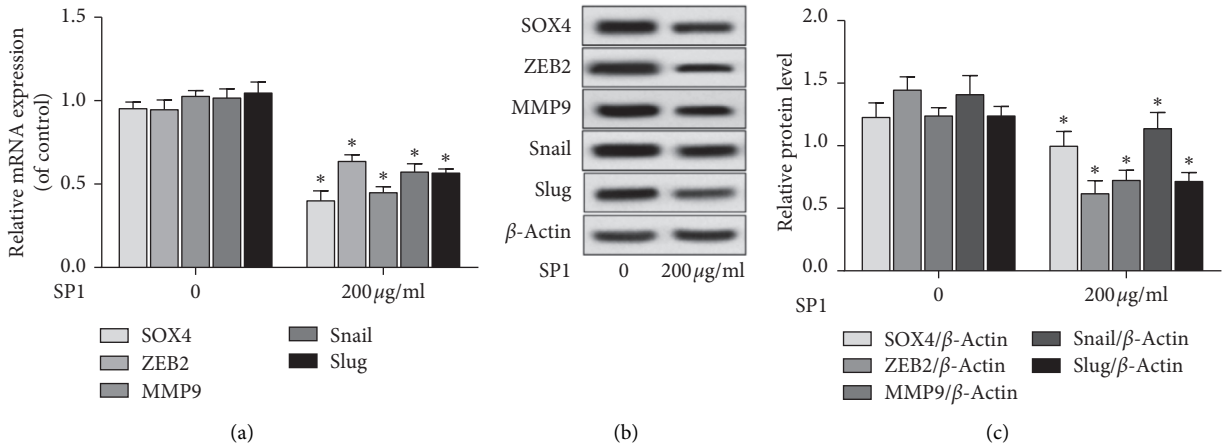

Figure 7: The expression of SOX4, ZEB2, MMP9, Snail, and Slug mRNA in MGC-803 cells of the control group (SP1 0 μg/ml) and SP1 treatment group (200 μg/ml) for 72 h was detected by qRT-PCR. (b) The protein levels of SOX4, ZEB2, MMP9, Snail, and Slug in MGC-803 cells of control group (SP1 0 μg/ml) and SP1 treatment group (200 μg/ml) for the 72 h were detected by Western blot. Compared with the control group, $^*P < 0.05$.

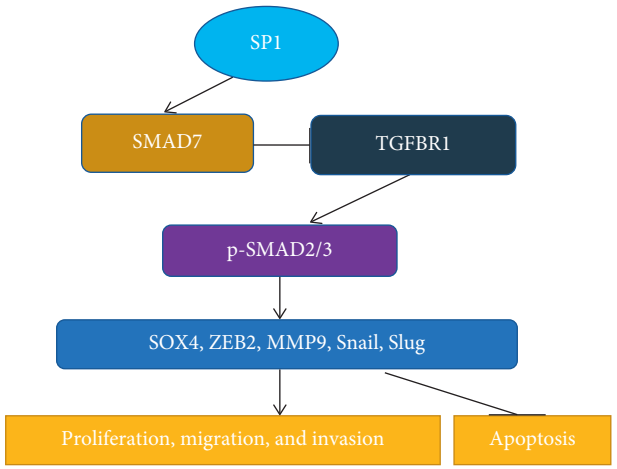

Figure 8: The effects of SP1 regulating TGF-β/SMAD signaling on gastric cancer cell proliferation, apoptosis, migration, and invasion.

factors. The TGF-β/SMAD signaling pathway plays a critical role in such malignant progressions of cancer cells as survival, EMT, migration, and invasion [13, 14]. Upon activation of transforming growth factor beta receptor 1 (TGF-βR1), the receptor-regulated SMAD proteins, SMAD2, and SMAD3 are recruited and phosphorylated for activation. Activated SMAD2 and SMAD3 continue to form oligomeric SMAD complexes with SMAD4, which together translocate into the nucleus, bind to DNA, and regulate the expression of target genes [15]. SMAD7 as a negative regulator of the TGF-β/SMAD signaling pathway can interact with TGF-βR1 in the cytoplasm, leading to TGF-βR1 degradation [16]. In this study, we found that SP1 could significantly increase the levels of SMAD7 mRNA and proteins and inhibit the expression of TGF-βRI, thus reducing the phosphorylation levels of downstream SMAD2 and SMAD3 of TGF-βRI.

Meanwhile, our study found that SP1 could inhibit the mRNA and protein expression of proliferation, apoptosis, migration, and invasion-related genes SOX4, ZEB2, MMP9, Snail, and Slug, which are all downstream molecules of TGF-β/SMAD signaling pathway [17, 18]. SOX4, a member of the C-subfamily of SOX transcription factors, promotes tumorigenesis by enabling cancer cells to survive, migrate, and invade [19]; MMP9, a member of the matrix metalloproteinase (MMP) family, plays an important role in tumor migration and invasion, angiogenesis, and apoptosis [20]; the transcription factors Snail and Slug are important molecules in the EMT process, which can promote tumor invasion and metastasis, and facilitate cell survival by regulating the cell cycle and apoptosis [21, 22]. Therefore, we suggest that SP1 regulates the proliferation, apoptosis, migration, and invasion of gastric cancer cells by inhibiting the TGF-β/SMAD signaling pathway and the expression of downstream molecules Sox4, Zeb2, Mmp9, Snail, and Slug (Figure 8).

In this study, we extracted the polysaccharide SP1 from Huaier and confirmed by in vitro experiments that SP1 could inhibit the activation of TGF-β/SMAD signaling pathway and the expression of downstream oncogenes SOX4, ZEB2, MMP9, Snail, and Slug by facilitating the expression of SMAD7, thereby regulating the proliferation, apoptosis, migration, and invasion of gastric cancer cells, which provided a theoretical basis for the use of SP1 in the treatment of gastric cancer.

Data Availability

The data used to support the findings of this study are available from the corresponding author upon request.

Conflicts of Interest

The authors declare that there are no conflicts of interest regarding the publication of this paper.

Authors' Contributions

Miaoliang Chen and Ying Lu contributed equally to this work.

Acknowledgments

This work was supported by the Zhejiang Basic Public Welfare Research Program (Grant no. LGF19H160017).

References

[1] C. E. Van, X. Sagaert, B. Topal et al., "Gastric cancer," *Lancet*, vol. 388, no. 10060, pp. 2654–2664, 2016.

[2] T. Huang, C. Song, L. Zheng et al., "The roles of extracellular vesicles in gastric cancer development, microenvironment, anti-cancer drug resistance, and therapy," *Molecular Cancer*, vol. 18, no. 1, p. 62, 2019.

[3] C. Hierro, M. Alsina, M. Sánchez, V. Serra, J. Rodon, and J. Tabernero, "Targeting the fibroblast growth factor receptor 2 in gastric cancer: promise or pitfall?" *Annals of Oncology*, vol. 28, no. 6, pp. 1207–1216, 2017.

[4] J. Lee, S. T. Kim, K. Kim et al., "Tumor genomic profiling guides patients with metastatic gastric cancer to targeted treatment: the VIKTORY umbrella trial," *Cancer Discovery*, vol. 9, no. 10, pp. 1388–1405, 2019.

[5] F. Lordick, K. Shitara, and Y. Y. Janjigian, "New agents on the horizon in gastric cancer," *Annals of Oncology*, vol. 28, no. 8, pp. 1767–1775, 2017.

[6] D. Y. Oh and Y. J. Bang, "HER2-targeted therapies-a role beyond breast cancer," *Nature Reviews Clinical Oncology*, vol. 17, no. 1, pp. 33–48, 2019.

[7] B. Hu, W. Yan, M. Wang et al., "Huaier polysaccharide inhibits the stem-like characteristics of ERα-36 high triple negative breast cancer cells via inactivation of the ERα-36 signaling pathway," *International Journal of Biological Sciences*, vol. 15, no. 7, pp. 1358–1367, 2019.

[8] Z. Luo, X. Hu, H. Xiong et al., "A polysaccharide from Huaier induced apoptosis in MCF-7 breast cancer cells via down-regulation of MTDH protein," *Carbohydrate Polymers*, vol. 151, pp. 1027–1033, 2016.

[9] C. Li, X. Wu, H. Zhang et al., "A Huaier polysaccharide restrains hepatocellular carcinoma growth and metastasis by suppression angiogenesis," *International Journal of Biological Macromolecules*, vol. 75, pp. 115–120, 2015.

[10] J. Zheng, C. Li, X. Wu et al., "Huaier polysaccharides suppresses hepatocarcinoma MHCC97-H cell metastasis via inactivation of EMT and AEG-1 pathway," *International Journal of Biological Macromolecules*, vol. 64, pp. 106–110, 2014.

[11] L. Fang, Y. Zhang, Y. Zang et al., "HP-1 inhibits the progression of ccRCC and enhances sunitinib therapeutic effects by suppressing EMT," *Carbohydrate Polymers*, vol. 223, p. 115109, 2019.

[12] Y. Tao, L. Shan, X. Xu et al., "Huaier augmented the chemotherapeutic sensitivity of oxaliplatin via downregulation of YAP in hepatocellular carcinoma," *Journal of Cancer*, vol. 9, no. 21, pp. 3962–3970, 2018.

[13] Y. Yu and X.-H. Feng, "TGF-β signaling in cell fate control and cancer," *Current Opinion in Cell Biology*, vol. 61, pp. 56–63, 2019.

[14] F. Dituri, C. Cossu, S. Mancarella, and G. Giannelli, "The interactivity between TGFβ and BMP signaling in organogenesis, fibrosis, and cancer," *Cells*, vol. 8, no. 10, p. 1130, 2019.

[15] S. Tu, W. Huang, C. Huang, Z. Luo, and X. Yan, "Contextual regulation of TGF-β signaling in liver cancer," *Cells*, vol. 8, no. 10, p. 1235, 2019.

[16] E. Troncone, I. Marafini, C. Stolfi, and G. Monteleone, "Transforming growth factor-β1/smad7 in intestinal immunity, inflammation, and cancer," *Frontiers in Immunology*, vol. 9, p. 1407, 2018.

[17] A. Chanda, A. Sarkar, and S. Bonni, "The SUMO System and TGFβ signaling interplay in regulation of epithelial-mesenchymal transition: implications for cancer progression," *Cancers (Basel)*, vol. 10, 2018.

[18] Y. E. Zhang, "Mechanistic insight into contextual TGF-β signaling," *Current Opinion in Cell Biology*, vol. 51, pp. 1–7, 2018.

[19] H. Hanieh, E. A. Ahmed, R. Vishnubalaji, and N. M. Alajez, "SOX4: epigenetic regulation and role in tumorigenesis," *Seminars in Cancer Biology*, 2019.

[20] T. C. Appleby, A. E. Greenstein, M. Hung et al., "Biochemical characterization and structure determination of a potent, selective antibody inhibitor of human MMP9," *Journal of Biological Chemistry*, vol. 292, no. 16, pp. 6810–6820, 2017.

[21] G. Assani and Y. Zhou, "Effect of modulation of epithelial-mesenchymal transition regulators snail1 and snail2 on cancer cell radiosensitivity by targeting of the cell cycle, cell apoptosis and cell migration/invasion," *Oncology Letters*, vol. 17, no. 17, pp. 23–30, 2019.

[22] J. Y. Wang, Z. Wang, M. Y. Li et al., "Dictamnine promotes apoptosis and inhibits epithelial-mesenchymal transition, migration, invasion and proliferation by downregulating the HIF-1α and slug signaling pathways," *Chemico-Biological Interactions*, vol. 296, pp. 134–144, 2018.

Hindawi
Advances in Polymer Technology
Volume 2020, Article ID 7472314, 6 pages
https://doi.org/10.1155/2020/7472314

Research Article

Ganoderma lucidum Polysaccharide (GLP) Inhibited the Progression of Oral Squamous Cell Carcinoma via the miR-188/BCL9/β-Catenin Pathway

Zhigang Zeng[1] **and Kaiyan Xiao**[2]

[1]*Department of Otorhinolaryngology, People's Hospital of Longyan, Longyan 364000, Fujian, China*
[2]*Department of Plastic and Reconstructive Surgery, Shanghai 9th People's Hospital, Shanghai Jiao Tong University School of Medicine, Shanghai 200011, China*

Correspondence should be addressed to Zhigang Zeng; gangzz1977@126.com and Kaiyan Xiao; xky7026@163.com

Received 21 November 2019; Accepted 26 December 2019; Published 3 February 2020

Guest Editor: Jianxun Ding

Objective. The effects of *Ganoderma lucidum* polysaccharide (GLP) on the proliferation and migration of oral squamous cell carcinoma (OSCC) cells (HSC-3) were investigated in this study. *Methods*. Oral squamous cell carcinoma (OSCC) cells (HSC-3) were cultured in vitro and were treated with different concentrations of GLP. CCK-8 assay and scratch assay were then used to detect the inhibitory effect of GLP on these cells. qRT-PCR and western blot were used to measure the expression changes of the genes involved in the miR-188 and β-catenin signaling pathways. *Results*. GLP had significant cytotoxicity to HSC-3 cells and was capable of inhibiting the proliferation and migration of HSC-3 cells. GLP upregulated the expression of miR-188 in HSC-3 cells and via which inhibited the proliferation and migration of HSC-3 cells. In addition, miR-188 inhibited the activation of the β-catenin signaling pathway through its target BCL9. *Conclusions*. GLP inhibited the proliferation and migration of OSCC cells (HSC-3) by regulating the miR-188/BCL9/β-catenin signaling pathway. The results in this study provided a theoretical basis for the treatment of OSCC with GLP.

1. Introduction

Oral squamous cell carcinoma (OSCC) is a malignant tumor that occurs in the oral cavity and is the eighth most common type of cancer in the world [1]. In China, the incidence of OSCC is about 3–6 per 100,000 people, and this number is increasing every year. Smoking, alcoholism, and chewing betel nut are believed to play an important role in the etiology of oral cancer. At present, although surgery, radiotherapy, and chemotherapy have made some progress in the treatment of OSCC, the mortality rate of OSCC is still high [2], in which tumor metastasis is the leading cause of death in OSCC patients [3]. Therefore, further research concerning the new or adjuvant treatment of OSCC to improve the prognosis of patients is urgently needed.

Ganoderma lucidum has been widely used as an auxiliary drug for antitumor therapy in clinical practice [4], and polysaccharide is one of the main bioactive components of *Ganoderma lucidum*. It has many biological functions such as improving immune function, preventing oxidative damage, and protecting the liver, while with little toxicity [5, 6]. Recently, the direct inhibitory effect of *Ganoderma lucidum* polysaccharide (GLP) on tumors has received extensive attention, for example, in colorectal cancer, GLP can promote the apoptosis of colorectal cancer cells by mediating the MAPK/ERK signaling pathway to regulate autophagy [7]; in prostate cancer, GLP can induce PC-3 cells apoptosis through NAG-1 [8] and can also inhibit prostate cancer cell migration through the arginine methyltransferase 6 signaling pathway [9]; in liver cancer, GLP can enhance the radiosensitivity of the liver cancer cell line HepG2 through the Akt signaling pathway [10]. However, the role of GLP in OSCC is unclear. Therefore, in this study, we investigated the effect of GLP on OSCC cells in vitro and explored the associated underlying mechanisms.

2. Material and Methods

2.1. Cell Culture and GLP Processing. Human oral squamous cell carcinoma HSC-3 cells were purchased from ATCC, USA, and the medium was DMEM containing 10% fetal calf serum and cells were cultured at 37°C with 5% CO_2. The cells in each group were treated with different concentrations of GLP including 0 mg/mL (control group), 0.5 mg/mL, 1.0 mg/mL, 2.0 mg/mL, 4.0 mg/mL, and 8.0 mg/mL, respectively. The preparation of GLP followed the method of Chen et al. [11]. The gas chromatographic analysis of GLP is shown in Figure 1. The monosaccharide composition of GLP is glucose and galactose, and the ratio of the amount of substance is 16.8 : 1.0.

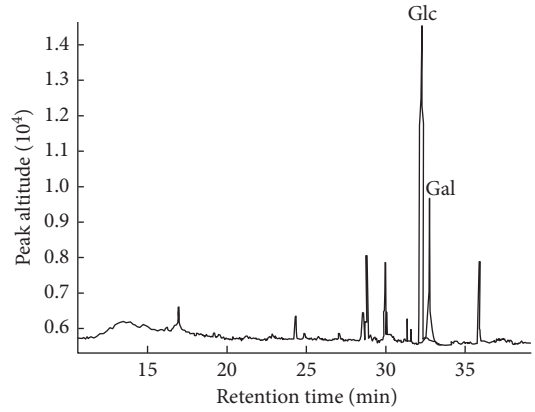

Figure 1: Gas chromatographic analysis of GLP.

2.2. Cell Transfection. One day before transfection, the cells were seeded into the culture plate in an appropriate number. According to the instructions, miR-188 mimics and miR-188 inhibitor were transfected into the cells using the Lipofectamine 3000 transfection reagent. The final concentration of miR-188 mimic transfection is 50 nM, and the final concentration of miR-188 inhibitor transfection is 100 nM.

2.3. Cell Activity Measured with CCK-8 Assay. HSC-3 cells were seeded in 96-well plates at approximately 5,000 cells per well and cultured for 24 h. After that, different treatments were applied to each group. After 24, 48, and 72 h, 10 μl of the CCK-8 reagent (Dojindo, Japan) was added to each well and mixed. The cells were then incubated for an appropriate period of time, and the absorbance at 450 nm was measured with a microplate reader. Inhibition rate = [(absorbance of control well − absorbance of the experimental well)/(absorbance of control well − absorbance of the blank well)] ∗ 100%.

2.4. In Vitro Scratch Assay. HSC-3 cells were seeded in a 12-well plate and cultured to form a monolayer, and a line was drawn in the layer using a pipette tip and then rinsed with PBS and treated accordingly. Scratches at different time periods were photographed using a microscope and statistical analysis was performed using ImageJ software.

2.5. miRNA Sequencing and Target Prediction. Total RNA was extracted from cells using the Trizol reagent (Invitrogen), followed with high-throughput sequencing of miRNAs on the Illumina platform. The expression profiles of miRNAs were analyzed using Cluster 3.0 software, and targets for miRNAs were predicted on the microRNA.org website.

2.6. qRT-PCR. Total RNA was extracted from the cells using the Trizol reagent (Invitrogen), and the RNA concentration was determined with a spectrophotometer. Reverse transcription was performed using the PrimeScript RT reagent kit (Takara). The resulting cDNA was then subjected to qRT-PCR analysis using the SYBR Premix Ex Taq kit (Takara). U6 snRNA was used as an internal reference for the quantification of miR-188 expression, and for the mRNA expression, β-actin was used as an internal reference. The relative expression level of the target gene was calculated by the $2^{-\Delta\Delta CT}$ method. Primer sequences are as follows: miR-188-F: ATGTACACAAGCACACCTTCTCATT; miR-188-R: TCAGAAAGCTCACCCTCCACCAT; U6-F: CTCGCTTCGGCAGCACACA; U6-R: AACGCTTCACGAATTTGCGT;-c-Myc-F: CAAGAGGCGAACACACAACGT; c-Myc-R: GGGCCTTTTCATTGTTTTCCA; CCND1-F: CTGGAGGTCTGCGAGGAACA; CCND1-R: CTTAGAGGCCACG AACATGCA; Slug-F: CATGCCTGTCATACCACAAC; Slug-R: GGTGTCAGATGGAGGAGGG; Vimentin-F: AAAGTGTGGCTGCCAAGAAC; Vimentin-R: AGCCTCAGAGAGGTCAGCAA; β-acti-F: GGCTCCGGCATGTGCAAG; β-acti-R: CCTCGGTCAGCAGCACGG.

2.7. Construction of Dual-Luciferase Reporter. The BCL9 3′-UTR sequences containing the wild type (wt) or mutant (mut) miR-188 binding site were synthesized and inserted into the pGL3 luciferase vector (Promega). The luciferase plasmid and miR-188 mimics or NC were cotransfected into cells using the Lipofectamine 2000 reagent (Invitrogen). After 48 h, luciferase activity was measured using the dual-luciferase reporter system (Promega) and Renilla luciferase activity was used as an internal reference.

2.8. Western Blot. Total cellular proteins were extracted with RIPA lysate, and nuclear proteins were extracted using the Nuclear and Cytoplasmic Extraction Reagent kit (Thermo Scientific). Western blot was performed using the standard method. The antibodies used in this experiment were purchased from Cell Signaling Technology.

2.9. Statistical Analysis. Data were analyzed using SPSS 18. 0 software and expressed as mean ± standard deviation. $P < 0.05$ was considered statistically significant.

3. Results

3.1. GLP Inhibited HSC-3 Cell Activity. As shown in Figure 2, compared with the control group, the inhibition rates of GLP (0.5, 1.0, 2.0, 4.0, 8.0 mg/mL) on the HSC-3 cells at 72 h were 44.0, 58.3, 59.7, 62.7, 71.7, and 93.3%, respectively. Also the IC50 for GLP at 24 h, 48 h, and 72 h were 5.43, 3.26, and 0.91 mg/mL, respectively. The results showed that GLP significantly reduced cell viability ($P < 0.05$) in a dose- and time-dependent manner, indicating that GLP has potent cytotoxicity against HSC-3 cells.

3.2. GLP Inhibited HSC-3 Cell Migration. As shown in Figure 3, the migration ability of HSC-3 cells was reduced in a dose-dependent manner ($P < 0.05$) after treatment with different concentrations of GLP for 48 h compared with the control group. Therefore, GLP had a significant inhibitory effect on the migration of HSC-3 cells.

3.3. GLP Upregulated the Expression of miR-188. After the treatment of HSC-3 cells with 1.0 mg/ml GLP for 48 h, cellular RNAs were extracted for high-throughput sequencing of miRNA. The result showed that the expression level of miR-188 was significantly increased (Figure 4). Furthermore, HSC-3 cells were also treated with different concentrations of GLP and the sequencing results were verified via qRT-PCR. The results confirmed that GLP upregulated the expression of miR-188 in a dose-dependent manner ($P < 0.05$) (Figure 4).

3.4. GLP Regulated HSC-3 Cell Proliferation and Migration via miR-188. Recovery experiments showed that transfection of the miR-188 inhibitor in GLP (1.0 mg/mL) treated cells significantly reversed GLP-induced inhibition on cell proliferation (Figure 5(a)) and migration (Figure 5(b)) ($P < 0.05$), which indicated that GLP inhibited the proliferation and migration of HSC-3 cells via miR-188.

3.5. miR-188 Regulated BCL9/β-Catenin Pathway in HSC-3 Cells. With microRNA.org, we found that BCL9 is a potential target for miR-188 (Figure 6(a)) and that was subsequently validated with the luciferase reporter gene (Figure 6(b)). In addition, we also found that miR-188 inhibited the activation of the β-catenin signaling pathway by downregulating the expression of BCL9, which in turn caused a decrease in the level of β-catenin in the nucleus (Figure 6(c)). Not surprisingly, the expression (mRNA and protein) of genes involved in the downstream of the β-catenin pathway including c-Myc, CCND1, Vimentin, and Slug was all downregulated by miR-188 (Figures 6(d) and 6(e)). The results mentioned above suggested that miR-188 regulated the BCL9/β-catenin pathway in HSC-3 cells.

4. Discussion

Studies have shown that GLP can exert antitumor effects by inhibiting tumorigenesis, tumor growth, and metastasis, as well as regulating immunity [12, 13]. However, there are a few research studies focusing on the effects of GLP in OSCC. The present study investigated the antitumor effect and corresponding mechanism of GLP in the OSCC cell line HSC-3.

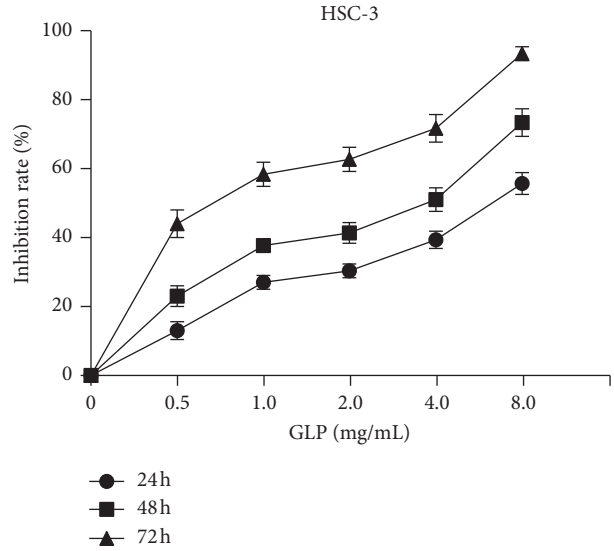

Figure 2: Cytotoxic effects of GLP on HSC-3 cells.

Firstly, we demonstrated that GLP is cytotoxic to HSC-3 and can significantly inhibit HSC-3 cell proliferation and migration. Our results demonstrated that GLP has a significant antitumor effect in OSCC cells.

Secondly, we explored the mechanism of the antitumor effects of GLP. We found that GLP promoted the expression of miR-188 in HSC-3 cells. Studies have shown that GLP can regulate the expression of some miRNA and exert its antitumor effect through these miRNAs [14, 15]. With the help of high-throughput sequencing, we found that GLP induced changes in miRNA expression in HSC-3 cells, and we subsequently focused on miR-188 in the present study. miR-188 has shown anticancer effects in many tumors, including OSCC [16]. The results of our experiments showed that GLP can inhibit HSC-3 cell proliferation and migration by upregulating the expression of miR-188.

There are few studies focusing on miR-188 in OSCC; therefore, we further explored the role of miR-188 in OSCC. We found and confirmed that BCL9 is a direct target for miR-188 and that miR-188 can inhibit the expression of BCL9 by binding to its' 3′-UTR. The BCL9 gene was originally discovered in lymphoblastic leukemia cells, which typically are overexpressed in a variety of malignancies and can activate the Wnt/β-catenin signaling pathway to promote cell proliferation, migration, invasion, and metastasis [17]. Our results showed that by inhibiting BCL9, miR-188 can inhibit the activation of the β-catenin signaling pathway and thus inhibits the expression of genes involved in the downstream of the β-catenin signaling pathway including c-Myc and CCND1, Vimentin and Slug, as shown by Zhuang et al. [18].

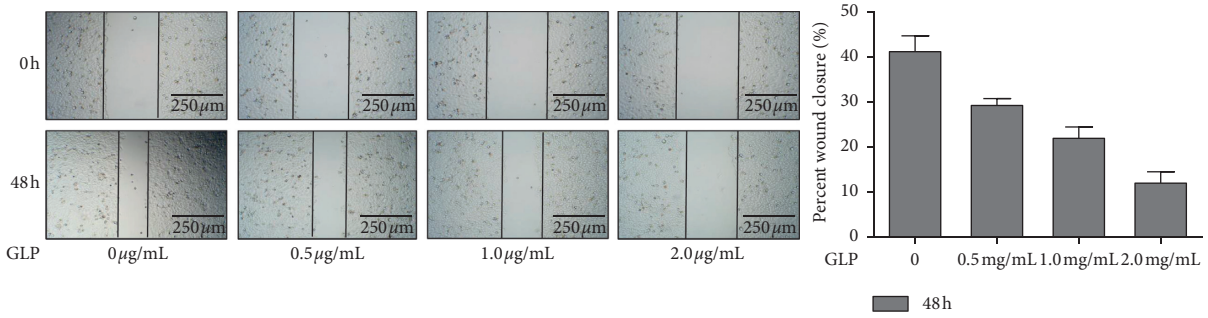

Figure 3: GLP inhibited HSC-3 cell migration.

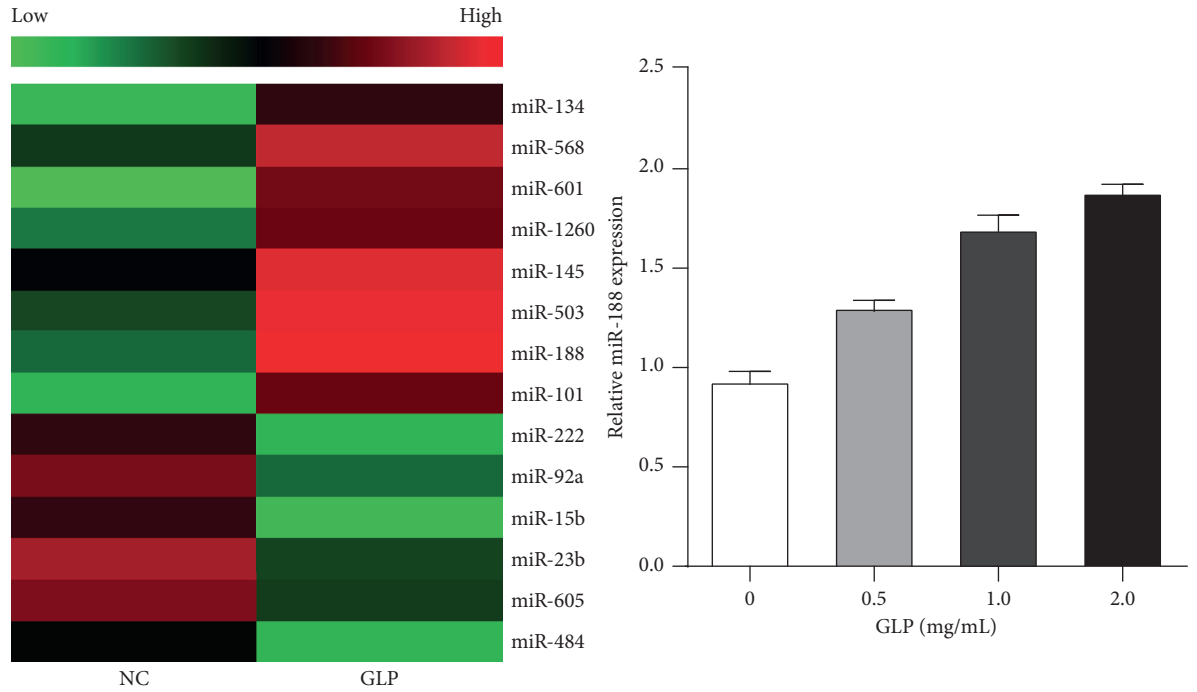

Figure 4: GLP upregulated the expression of miR-188.

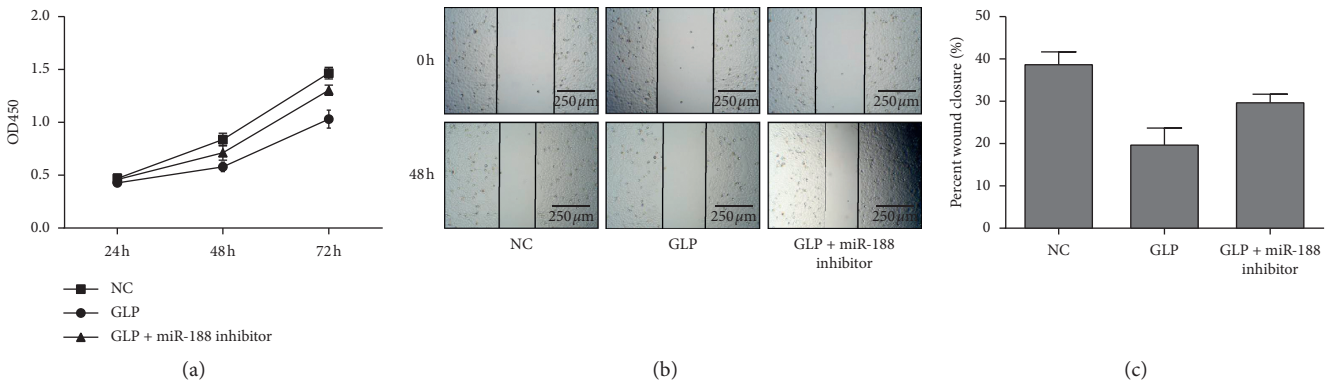

Figure 5: GLP inhibited the proliferation and migration of HSC-3 cells via miR-188. (a) Cell proliferation detected by the CCK-8 test; (b and c) cell migration measured by the scratch test.

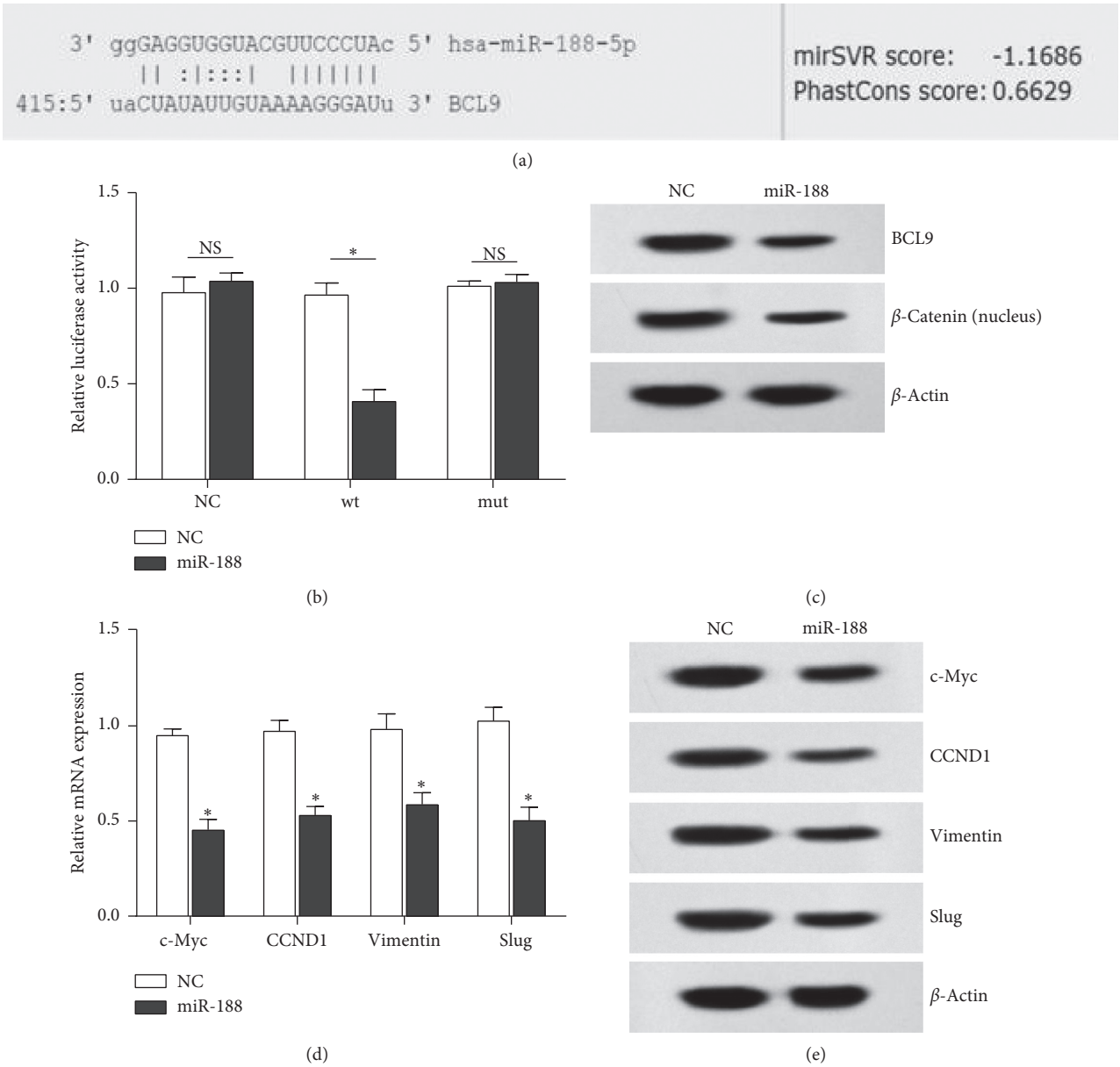

Figure 6: miR-188 regulated the β-catenin pathway by targeting BCL9. (a) BCL9 and miR-188 binding sites were predicted on the microRNA.org website; (b) verification of the binding sites via the luciferase reporter gene experiment; (c) miR-188 regulates BCL9 and nuclear β-catenin expression; (d and e) miR-188 regulates mRNA and protein expression of β-catenin downstream genes. $^{*}P < 0.05$

5. Conclusion

Taken together, our results demonstrated that GLP can inhibit the proliferation and migration of OSCC cells (HSC-3) by regulating the miR-188/BCL9/β-catenin signaling pathway. Therefore, the results in this study provide a theoretical basis for the treatment of OSCC with GLP.

Data Availability

The data used to support the findings of this study are available from the corresponding author upon request.

Conflicts of Interest

The authors declare that there are no conflicts of interest regarding the publication of this paper.

Acknowledgments

This work was supported by the National Natural Science Foundation (grant no. 81771568).

References

[1] J. Ferlay, H.-R. Shin, F. Bray, D. Forman, C. Mathers, and D. M. Parkin, "Estimates of worldwide burden of cancer in

2008: GLOBOCAN 2008," *International Journal of Cancer*, vol. 127, no. 12, pp. 2893–2917, 2010.

[2] S. Gupta, W. Kong, Y. Peng, Q. Miao, and W. J. Mackillop, "Temporal trends in the incidence and survival of cancers of the upper aerodigestive tract in Ontario and the USA," *International Journal of Cancer*, vol. 125, no. 9, pp. 2159–2165, 2009.

[3] J. Wikner, A. Gröbe, K. Pantel, and S. Riethdorf, "Squamous cell carcinoma of the oral cavity and circulating tumour cells," *World Journal of Clinical Oncology*, vol. 5, no. 2, pp. 114–124, 2014.

[4] Z. Xu, X. Chen, Z. Zhong, L. Chen, and Y. Wang, "*Ganoderma lucidum* polysaccharides: immunomodulation and potential anti-tumor activities," *The American Journal of Chinese Medicine*, vol. 39, no. 1, pp. 15–27, 2011.

[5] K. Pan, Q. Jiang, G. Liu, X. Miao, and D. Zhong, "Optimization extraction of *Ganoderma lucidum* polysaccharides and its immunity and antioxidant activities," *International Journal of Biological Macromolecules*, vol. 55, pp. 301–306, 2013.

[6] L. Guo, J. Xie, Y. Ruan et al., "Characterization and immunostimulatory activity of a polysaccharide from the spores of *Ganoderma lucidum*," *International Immunopharmacology*, vol. 9, no. 10, pp. 1175–1182, 2009.

[7] H. Pan, Y. Wang, K. Na et al., "Autophagic flux disruption contributes to Ganoderma lucidum polysaccharide-induced apoptosis in human colorectal cancer cells via MAPK/ERK activation," *Cell Death & Disease*, vol. 10, p. 456, 2019.

[8] K. Wu, K. Na, D. Chen, Y. Wang, H. Pan, and X. Wang, "Effects of non-steroidal anti-inflammatory drug-activated gene-1 on *Ganoderma lucidum* polysaccharides-induced apoptosis of human prostate cancer PC-3 cells," *International Journal of Oncology*, vol. 53, no. 6, pp. 2356–2368, 2018.

[9] X. Zhao, D. Zhou, Y. Liu et al., "*Ganoderma lucidum* polysaccharide inhibits prostate cancer cell migration via the protein arginine methyltransferase 6 signaling pathway," *Molecular Medicine Reports*, vol. 17, no. 1, pp. 147–157, 2018.

[10] Y. Yu, L. Qian, N. Du, and Y. Liu, X. Zhao, X. Zhang, *Ganoderma lucidum* polysaccharide enhances radiosensitivity of hepatocellular carcinoma cell line HepG2 through akt signaling pathway," *Experimental and Therapeutic Medicine*, vol. 14, no. 6, pp. 5903–5907, 2017.

[11] Y. Chen, M.-Y. Xie, S.-P. Nie, C. Li, and Y.-X. Wang, "Purification, composition analysis and antioxidant activity of a polysaccharide from the fruiting bodies of *Ganoderma* atrum," *Food Chemistry*, vol. 107, no. 1, pp. 231–241, 2008.

[12] X.-L. Zhu, A.-F. Chen, and Z.-B. Lin, "*Ganoderma lucidum* polysaccharides enhance the function of immunological effector cells in immunosuppressed mice," *Journal of Ethnopharmacology*, vol. 111, no. 2, pp. 219–226, 2007.

[13] B. Boh, "*Ganoderma lucidum*: a potential for biotechnological production of anti-cancer and immunomodulatory drugs," *Recent Patents on Anti-Cancer Drug Discovery*, vol. 8, no. 3, pp. 255–287, 2013.

[14] J. Shen, H.-S. Park, Y.-M. Xia, G.-S. Kim, and S. W. Cui, "The polysaccharides from fermented *Ganoderma lucidum* mycelia induced miRNAs regulation in suppressed HepG2 cells," *Carbohydrate Polymers*, vol. 103, pp. 319–324, 2014.

[15] A. Li, X. Shuai, Z. Jia et al., *Ganoderma lucidum* polysaccharide extract inhibits hepatocellular carcinoma growth by downregulating regulatory T cells accumulation and function by inducing microRNA-125b," *Journal of Translational Medicine*, vol. 13, no. 1, p. 100, 2015.

[16] L. Wang and H. Liu, "MicroRNA-188 is downregulated in oral squamous cell carcinoma and inhibits proliferation and invasion by targeting six1," *Tumor Biology*, vol. 37, no. 3, pp. 4105–4113, 2015.

[17] C. Yang, Y. Xu, F. Cheng et al., "miR-1301 inhibits hepatocellular carcinoma cell migration, invasion, and angiogenesis by decreasing Wnt/β-catenin signaling through targeting BCL9," *Cell Death & Disease*, vol. 8, no. 8, p. e2999, 2017.

[18] L. K. Zhuang, Y. T. Yang, X. Ma et al., "MicroRNA-92b promotes hepatocellular carcinoma progression by targeting smad7 and is mediated by long non-coding RNA XIST," *Cell Death and Disease*, vol. 7, no. 4, p. e2203, 2016.

Hindawi
Advances in Polymer Technology
Volume 2020, Article ID 1763245, 6 pages
https://doi.org/10.1155/2020/1763245

Research Article

Altered Frequency of NK Cells and Treg Cells by *Astragalus* Polysaccharide Combined with Budesonide in Asthma Model Mice

Wei Zhang [1] **and Kuifen Ma** [2]

[1]*Department of Respiratory Medicine, Affiliated Hangzhou First People's Hospital, Zhejiang University School of Medicine, Hangzhou 310006, China*
[2]*The First Affiliated Hospital of Medical School of Zhejiang University, Hangzhou 310003, China*

Correspondence should be addressed to Wei Zhang; bobbyzw@163.com

Received 21 August 2019; Accepted 28 October 2019; Published 12 January 2020

Guest Editor: Jianxun Ding

Objective. We investigated the efficacy of astragalus polysaccharide (APS) combined with budesonide and the effect on expressions of peripheral NK cells and Treg cells and the molecular mechanism in mice with bronchial asthma. *Methods*. In this study, we established a mouse model of asthma. Four groups of BaLB/C mice were developed; control group had no asthma induction, and the other three groups of mice were sensitized by OVA (Ovalbumin), OVA + budesonide, and OVA + APS + budesonide. Flow cytometry was used to determine the proportion of NK cells and Treg cells. Levels of cytokines IL-4 and IL-10 were detected using RT-PCR and ELISA. *Results*. Asthma mice treated with APS + budesonide showed alleviated airway resistance compared to model mice ($P < 0.05$). The percentage of dendritic cells (DCs) was reduced ($P < 0.05$), while anti-inflammatory NK cells and Treg cells significantly increased after APS + budesonide treatment ($P < 0.05$). Further, APS + budesonide treatment resulted in improvements in IL-4 and IL-10 mRNA and protein levels ($P < 0.05$). *Conclusion*. APS combined with budesonide medication may regulate expressions of DCs cells and related cytokines, reliving clinical symptom of bronchial asthma.

1. Introduction

Bronchial asthma is a common chronic airway inflammatory disease, and its pathogenesis includes a variety of cells and components. Based on epidemiological survey data, elderly people have a higher incidence of asthma [1]. At present, the main treatment is drug therapy, which can be classified as control patient's condition and relief symptoms. Long-term oral or intravenous use of glucocorticoid can cause immunosuppression and Cushing's syndrome and other side effects. Inhalation of common doses of glucocorticoid generally does not cause adverse reactions [2]. But after glucocorticoids inhalation, approximately 80–90% of the drug is deposited in the pharynx and swallowed into the gastrointestinal tract, eventually depositing glucocorticoid will cause pharyngeal or systemic adverse reactions.

Over the last decades, traditional Chinese medicine extracted from the root of *Astragalus membranaceus* was documented to have biological activities. *Astragalus* polysaccharide (APS), the extraction, is a polysaccharide consisting of glucose and arabinose sugar, possessing very low toxicity, with a wide range of immune enhancement and antiviral effect, which can relieve the plant hemagglutination (PHA) toxicity and resist the inhibitory effects of immunosuppressive drugs such as prednisolone and cyclophosphamide [3]. The therapeutic implication of APS has been confirmed in patients with lung cancer [4]. Budesonide, which is a commonly used inhaled hormone, has fewer systemic adverse reactions. However, there are a few clinical studies on the combined therapy for adult asthma.

Given the NK cells and regulatory T cells contribute to asthma pathogenesis, it is believed that combination of APS and budesonide may influence immune cell counts. In this study, the effects of APS combined with budesonide on pulmonary function and immune response in mice with bronchial asthma were observed, aiming to provide theoretical basis for clinical treatment.

2. Methods and Materials

2.1. Animals and Study Design. Forty female BaLB/c mice (8.7 ± 3.4 g) purchased from Shanghai Lab Animal Research Center (Shanghai, China) were divided into 4 groups: control group ($n = 8$), untreated asthma group ($n = 8$), budesonide group ($n = 8$) and APS + budesonide group ($n = 8$). Mouse model of asthma were induced as previously [5]. Briefly, 25 μg OVA (SIGMA-ALDRICH, O1641) dissolved in 200 μL PBS were injected intraperitoneally into the mice except those in control group. Mice in the control group were injected with same volume of PBS. On day 14, mice in the non-control group were kept in a closed container and inhaled 6% OVA solution by ultrasonic atomization to induce asthma 30 min/day for 7 days while mice in the control group inhaled PBS. On day 15, control and untreated asthma group was administered with atomized PBS; budesonide group, 3 μg/day budesonide; APS + budesonide group, 100 mg/kg body weight/day APS injected intraperitoneally and 3 μg/day budesonide inhaled. On day 29, mice were sacrificed to evaluate airway response and other biomarkers.

2.2. Bone-Marrow-Derived DCs (BMDCs) Generation. The tibial and femoral bone marrow was isolated from the mice and the BMDCs were prepared as previous reported [6]. Isolated BMDCs were cultured in RPMI-1640 containing 5% fetal bovine serum and stimulated with 1000 U/mL IL-4 and 500 U/mL granulocyte-macrophage colony-stimulating factor (GM-CSF). On day 7, non-adherent cells were harvested.

2.3. Flow Cytometric Analysis of NK, DCs and Treg Cells. A FC500 (Beckman Coulter, USA) was used to analyze the proportions of NK, DCs and Treg cells. The data was analyzed with CXP analysis software 2.3. NK cells were stained with FITC-CD16 and PE-CD56 (eBioscience, SanDiego, CA). The BMDCs were stained with rat anti-mouse monoclonal antibodies to FITC-CD11c and PE-CD86 (B7-2) (eBioscience, SanDiego, CA). Treg cells were stained with FITC-CD4 and PE-CD25 (eBioscience, SanDiego, CA).

2.4. Determination of Airway Hyper-Responsiveness. Airway hyper-responsiveness was measured using the FinePointe™ RC animal airway resistance and pulmonary compliance system (BUXCO, USA). On day 28, 60 mg/kg pentobarbital sodium was injected intraperitoneally, then a tracheal incision was performed. Respiratory frequency was set at 160 times/min. Mice were inhaled with 10 μL acetylcholine, at ascending concentrations of 0 mg/mL, 1 mg/mL, 2 mg/mL, 4 mg/mL, 8 mg/mL. The maximum airway resistance within 3 minutes was recorded.

2.5. Quantitative RT-PCR. Total RNA from the lung tissue was extracted using Trizol reagent (Takara, Dalian, China), and cDNA was synthesized using the Prime Script® RT reagent kit (Takara, Dalian, China), according to the manufacturer's instructions. Real-time RT-PCR was performed using SYBR® Premix Ex TapTM II (Takara). The primers used are as follows: IL4 (120 bp), forward prime, 5′-CATCGGCATTTTGAACGAG-3′, reverse prime, 5′-TTGGAAGCCCTACAGACGAG-3′; IL10 (165 bp), forward prime, 5′-TAACTGCACCCACTTCCCAG-3′, reverse prime, 5′-AAGGCTTGGCAACCCAAGTA-3′; GAPDH (104 bp), forward prime, 5′-CGTGTTCCTACCCCCAATGT-3′, reverse prime, 5′-TGTCATACTTGGCAGGTTTCT-3′. All experiments were conducted in triplicate and repeated three times. The PCR data were analyzed using the QuantStudio 7 Flex detection system (Applied Biosystems Co., Foster City, CA, USA). Cycle threshold (CT) values were calculated using the comparative CT ($\Delta\Delta$CT) method, and the relative amount of target mRNA ($2^{-\Delta\Delta CT}$) was obtained by normalizing to endogenous GAPDH levels.

2.6. ELISA Assay. Bronchoalveolar lavage fluid (BALF) was collected and analyzed for interleukin-4 (IL-4) and IL-10 contents by enzyme-linked immunosorbent assay (ELISA), according to the manufacturer's guidelines.

2.7. Statistical Analyses. All data were analyzed using SPSS13.0 software. The data are expressed as mean ± standard deviation. The inter-group comparisons of means were performed using univariate analysis of variance and pairwise comparison between groups, with $P < 0.05$, $P < 0.01$ or $P < 0.001$ as significantly different.

3. Results

3.1. Body Weight and Airway Resistance in Mice with Asthma Influences by APS and Budesonide. Compared to control group, mice in model group, and drug treated group had a loss and slight fluctuation in body weight (Figure 1(a)). Airway hyper-responsiveness was assessed in 4 groups. In untreated group, mice exposed to OVA showed significant airway resistance at acetylcholine concentrations of 1, 2, 4, and 8 mg/mL ($P < 0.01$; Figure 1(b)). To verify airway resistance, the airway resistance after acetylcholine challenge between untreated model mice and various treatment groups was compared. The mice of three various treated groups exhibited significantly less airway resistance at an acetylcholine concentration of 1, 2, 4, and 8 mg/mL ($P < 0.05$; Figure 1(b)). The mice in APS + budesonide showed significantly lower airway resistance than that in budesonide group ($P < 0.05$; Figure 1(b)).

3.2. Percentage of DCs, NK Cells, and Treg Cells Influences by APS and Budesonide. The frequency of NK cells and Treg cells in BALF has been analyzed. Compared with healthy controls, animals with experimental asthma showed attenuated DCs and attenuated cell numbers of NK cells and Treg cells ($P < 0.05$; Figure 2). However, the percentages of NK cells and Treg cells, were markedly increased in mice with drug treatment whether combined with APS ($P < 0.05$; Figure 2). The frequency of DCs in untreated asthma group was elevated when compared to control group ($P < 0.05$; Figure 2). By comparison, frequency of DCs in two treated groups was significantly alleviated ($P < 0.05$; Figure 2). In addition, the

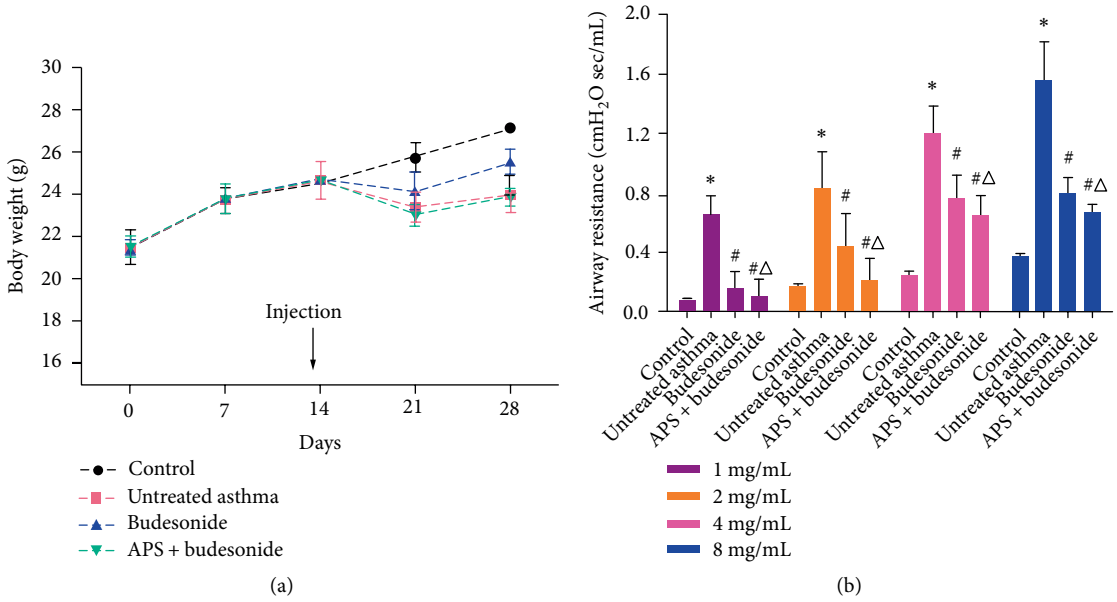

FIGURE 1: Body weight and airway resistance effected by APS and budesonide treatment. (a) The body weight change of mice in 4 groups ($n = 8$ per group) was monitored within 28 days. (b) Airway resistance in mice was measured after treatment. Mean ± SD is presented for each group. $^{*}P < 0.01$, compared with control group; $^{\#}P < 0.05$, compared with untreated asthma group; $^{\triangle}P < 0.05$, compared with budesonide group.

frequency of DCs in APS + budesonide group was significantly lower than that in budesonide group ($P < 0.05$; Figure 2).

3.3. mRNA Levels of IL4 and IL10 in Mice Influences by APS and Budesonide. As NK cells in the lungs have been considered to be regulators of Th1 or Th2 cytokine production, we analyzed the mRNA levels of inflammatory mediators: IL4 and IL10 in lung tissues of mice. Th2 cytokines IL4 and anti-inflammatory cytokines IL10 in mice model of asthma were significantly increased, compared to control group ($P < 0.05$; Figure 3). Administration of budesonide significantly reduced the mRNA levels of IL4 in mice with asthma ($P < 0.05$; Figure 3). Levels of IL4 and IL10 in APS + budesonide group were significantly decreased compared to budesonide group ($P < 0.05$; Figure 3).

3.4. Cytokine Levels in APS and Budesonide Treated Mice. Levels of the important Th2 cytokine IL-4 and inflammatory cytokine IL-10 in BALF and the spleen were measured by ELISA. As shown in Figure 4, levels of these cytokines in BALF significantly declined in APS + budesonide—treated mice, when compared with budesonide treated mice ($P < 0.05$; Figure 4). Levels of IL-4 and IL-10 in spleen were consistent with that in BALF.

4. Discussion

The etiology of asthma is complex, and airway hyperresponsiveness is the characteristic pathological manifestation of asthma. Leukotriene, a metabolite of arachidonic acid, is widely present in the airway of patients with bronchial asthma and mediates and induces inflammatory reactions. Previous clinical practice has shown that the clinical effect of montelukast alone as a leukotriene regulator in the treatment of bronchial asthma needs to be further improved. Polysaccharide served as anti-tumor drug has been well studied in various types of tumor cells [7, 8]. In the present study, we established a murine asthmatic model and demonstrated that asthma model mice, challenged with APS and budesonide, exhibited improved airway hyper-responsiveness.

Current studies have confirmed that the pathogenesis of bronchial asthma is closely related to cellular immune dysfunction. The cell types involved in the pathological process of asthma include Th2 cells, Th17 cells, NK cells, antigen presenting cells, B cells, etc. [9–13]. As an important natural immune cell, NK cells are the third type of lymphocytes along with T cells and B cells. Recent studies have shown that compared with healthy controls, NK cells isolated from the peripheral blood of asthmatic patients have a reduced killing ability against tumor cell lines, although they secrete more cytotoxic regulators [14]. The airway inflammatory immune response of bronchial asthma is associated with decreased cytotoxicity of NK cells and increased leukocyte count. Some studies have confirmed that NK cell subsets are significantly reduced in patients with allergic asthma, suggesting that the occurrence of asthma is related to the inhibition of NK function [15]. Moreover, the NK cells content in the remission phase of asthma was higher than that in the acute attack phase [16, 17]. NK cells is a necessary factor for naive T cells differentiating to Th2 cells.

Treg plays an important role in balancing the inflammatory response and regulating the immune response. Studies have found that in allergic patients, Treg content is reduced and function is impaired. In addition, Treg cells can negatively feedback regulate T cells through a variety of inhibitory mechanisms, such as down-regulating the expression of T cytokines and inhibiting the activation and differentiation of T cells [18]. DCs can be directly activated and indirectly activated by

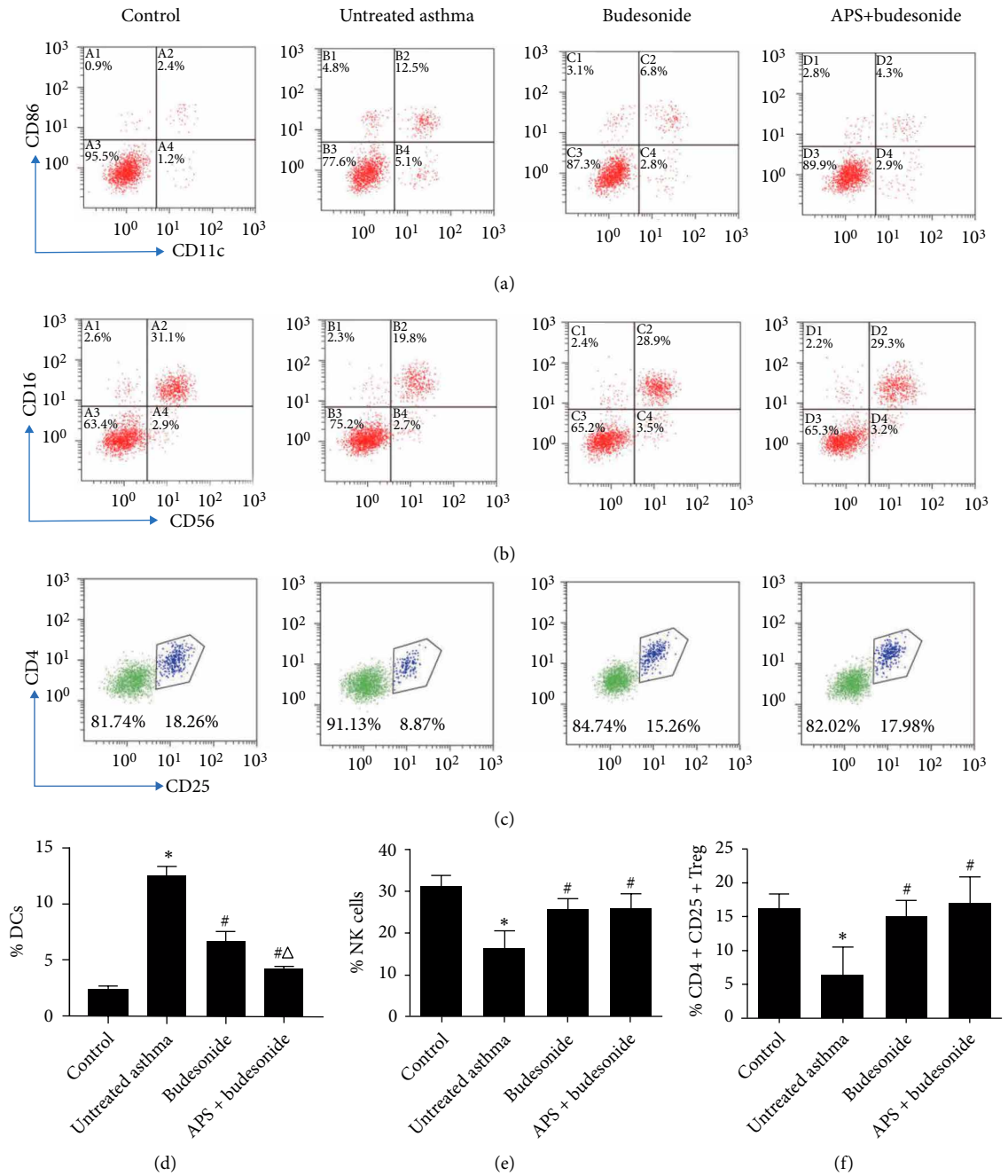

FIGURE 2: Flow cytometric analysis of DCs, NK cells, and Treg cells. (a–c) The percentage of DCs, NK cells, and Treg cells. (d–f) Results from gated cells were visualized by bar charts as percentages of DCs, NK cells, and Treg cells. Mean ± SD is presented for each group. $^{*}P < 0.01$, compared with control group; $^{\#}P < 0.05$, compared with untreated asthma group; $^{\triangle}P < 0.05$, compared with budesonide group.

epithelium when inhaling harmless allergens, which are sufficient to initiate Th2 immunity. Our results shed light upon how the polysaccharide influence the asthma model mice. Using the OVA-induced asthma model, our data showed that combination of APS and budesonide modulated the proportion of DCs, NK cells, and Treg cells. Notably, APS and budesonide had significant decrease of DCs compared to budesonide alone, suggesting the reliving immune response in treated-asthma mice.

It is documented that patients with asthma often had increased frequencies of IL-4-producing NK cells [19]. Impaired capacity of DCs to activate T cells results in incomplete maturation of specific inhibitory cytokines such as IL-10, which will suppress T-cell immune reactivity [20–22]. In this study, we observed the mRNA levels of IL-4 and IL-10 were alleviated by APS and budesonide treatment. Furthermore, both local (BALF) and systemic (spleen) levels of IL-4 and IL-10 in mice treated with APS and budesonide were significantly lower than in untreated model mice. Therefore, it is possible that APS and budesonide suppressed the production of IL-4 and IL-10 in gene and protein levels.

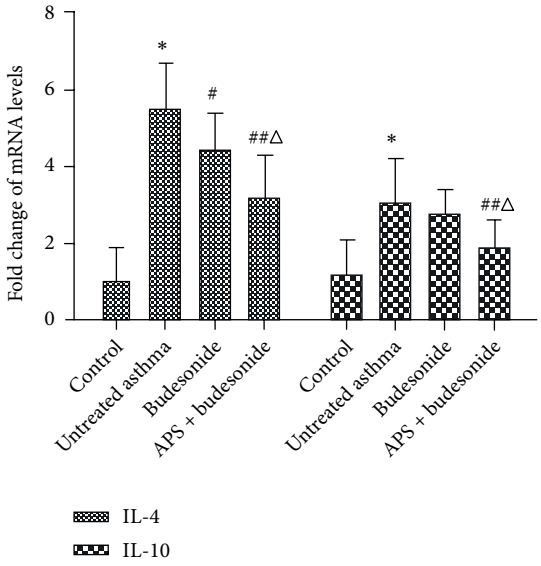

Figure 3: APS and budesonide suppressed mRNA levels of inflammatory mediators. Relative expression of IL4 and IL10 mRNA levels were measured by RT-PCR and is represented above. Every independent experiment was triplicated. Mean ± SD is presented for each group. $^{*}P < 0.01$, compared with control group; $^{\#}P < 0.05$, compared with untreated asthma group; $^{\triangle}P < 0.05$, compared with budesonide group.

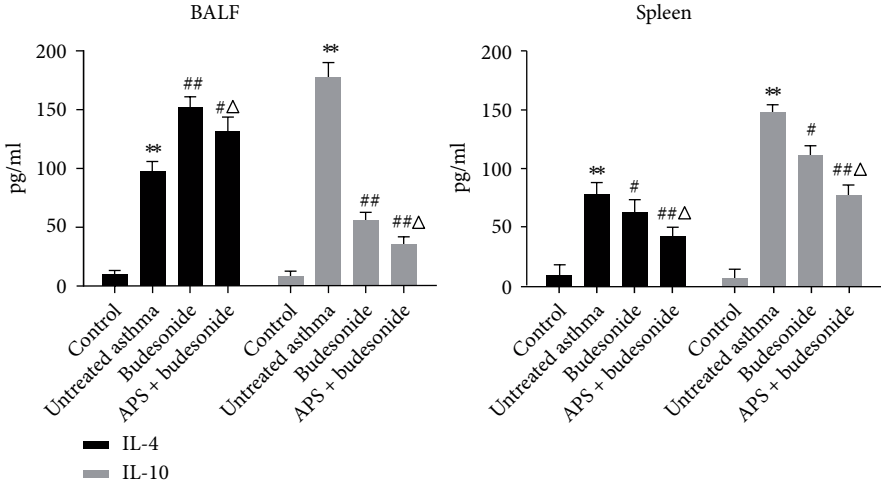

Figure 4: Cytokine levels of IL-4 and IL-10 in BALF and spleen were analyzed by ELISA. Every independent experiment was repeated twice. Mean ± SD is presented for each group. $^{**}P < 0.01$, compared with control group; $^{\#}P < 0.05$, $^{\#\#}P < 0.01$, compared with untreated asthma group; $^{\triangle}P < 0.05$, compared with budesonide group.

Taken together, these findings suggest that budesonide with or without APS treatment might induce protective immunity against asthma by the regulation of DCs, NK cells and Treg cells through IL-4 and IL-10 production. Apart from that, combination of APS and budesonide shows benefits in improving airway pressure maybe due to the modulation of DCs, IL-4 and IL-10, which provide a new strategy in the therapy of asthma.

Data Availability

The data used to support the findings of this study are available from the corresponding author upon request.

Conflicts of Interest

The authors declare that there are no conflicts of interest regarding the publication of this paper.

Acknowledgments

This work was supported by Zhejiang Provincial Health Department Project (Grant no. 2019KY486).

References

[1] I. Kuprys-Lipinska, J. Liebhart, C. Palczynski, P. Lacwik, M. Jonakowski, and P. Kuna, "Prevalence, risk factors and

underdiagnosis of asthma in the general population aged over 60 years," *Postepy Dermatologii I Alergologii*, vol. 36, no. 1, pp. 86–91, 2019.

[2] P. Nair and P. Barker, "Glucocorticoid sparing of benralizumab in asthma," *The New England Journal of Medicine*, vol. 377, no. 12, p. 1205, 2017.

[3] K. K. Auyeung and Q. B. Han, "*Astragalus membranaceus*: a review of its protection against inflammation and gastrointestinal cancers," *The American Journal of Chinese Medicine*, vol. 44, no. 1, pp. 1–22, 2016.

[4] O. A. Bamodu, K. T. Kuo, C. H. Wang et al., "Astragalus polysaccharides (PG2) enhances the M1 polarization of macrophages, functional maturation of dendritic cells, and T cell-mediated anticancer immune responses in patients with lung cancer," *Nutrients*, vol. 11, no. 10, p. 2264, 2019.

[5] S. Wu, G. Wang, and R. Yang, "Anti-inflammatory effects of polysaccharide on asthma pathology," *American Journal of Translational Research*, vol. 8, no. 10, pp. 4478–4489, 2016.

[6] K. J. Liu, S. J. Leu, C. H. Su, B. L. Chiang, Y. L. Chen, and Y. L. Lee, "Administration of polysaccharides from *Antrodiacamphorata* modulates dendritic cell function and alleviates allergen-induced T helper type 2 responses in a mouse model of asthma," *Immunology*, vol. 129, no. 3, pp. 351–362, 2010.

[7] H. Guo, F. Li, W. Xu et al., "Mucoadhesive cationic polypeptide nanogel with enhanced penetration for efficient intravesical chemotherapy of bladder cancer," *Advanced Science (Weinheims)*, vol. 5, no. 6, p. 1800004, 2018.

[8] J. Wang, W. Xu, S. Li et al., "Polylactide-cholesterol stereocomplex micelle encapsulating chemotherapeutic agent for improved antitumor efficacy and safety," *Journal of Biomedical Nanotechnology*, vol. 14, no. 12, pp. 2102–2113, 2018.

[9] Y. M. Du, Y. X. Zhuansun, R. Chen, L. Lin, Y. Lin, and J. G. Li, "Mesenchymal stem cell exosomes promote immunosuppression of regulatory T cells in asthma," *Experimental Cell Research*, vol. 363, no. 1, pp. 114–120, 2018.

[10] P. J. Barnes, "Targeting cytokines to treat asthma and chronic obstructive pulmonary disease," *Nature Reviews Immunology*, vol. 18, no. 7, pp. 454–466, 2018.

[11] M. C. Altman, E. Whalen, A. Togias et al., "Allergen-induced activation of natural killer cells represents an early-life immune response in the development of allergic asthma," *The Journal of Allergy and Clinical Immunology*, vol. 142, no. 6, pp. 1856–1866, 2018.

[12] D. C. Do, Y. Zhao, and P. Gao, "Cockroach allergen exposure and risk of asthma," *Allergy*, vol. 71, no. 4, pp. 463–474, 2016.

[13] M. H. Grayson, S. Feldman, B. T. Prince, P. J. Patel, E. C. Matsui, and A. J. Apter, "Advances in asthma in 2017: mechanisms, biologics, and genetics," *Journal of Allergy and Clinical Immunology*, vol. 142, no. 5, pp. 1423–1436, 2018.

[14] M. G. Duvall, C. Barnig, M. Cernadas et al., "Natural killer cell-mediated inflammation resolution is disabled in severe asthma," *Science Immunology*, vol. 2, no. 9, , 2017.

[15] B. Simons, M. E. Ferrini, S. Carvalho, D. J. P. Bassett, Z. Jaffar, and K. Roberts, "PGI2 controls pulmonary NK cells that prevent airway sensitization to house dust mite allergen," *Journal of Immunology*, vol. 198, no. 1, pp. 461–471, 2017.

[16] J. H. Kim and Y. J. Jang, "Role of natural killer cells in airway inflammation," *Allergy Asthma & Immunology Research*, vol. 10, no. 5, pp. 448–456, 2018.

[17] M. M. Gorska, "Natural killer cells in asthma," *Current Opinion in Allergy and Clinical Immunology*, vol. 17, no. 1, pp. 50–54, 2017.

[18] D. M. Richards, M. Delacher, Y. Goldfarb et al., "Treg cell differentiation: from thymus to peripheral tissue," *Progress in Molecular Biology and Translational Science*, vol. 136, pp. 175–205, 2015.

[19] A. K. Singh, S. Rhost, L. Löfbom, and S. L. Cardell, "Defining a novel subset of CD1d-dependent type II natural killer T cells using natural killer cell-associated markers," *Scandinavian Journal of Immunology*, vol. 90, no. 3, p. e12794, 2019.

[20] K. J. Liu, S. J. Leu, C. H. Su, B. L. Chiang, Y. L. Chen, and Y. L. Lee, "Administration of polysaccharides from *Antrodiacamphorata* modulates dendritic cell function and alleviates allergen-induced T helper type 2 responses in a mouse model of asthma," *Immunology*, vol. 129, no. 3, pp. 351–362, 2010.

[21] O. Sukhbaatar, D. Kimura, M. Miyakoda et al., "Activation and IL-10 production of specific CD4+ T cells are regulated by IL-27 during chronic infection with *Plasmodium chabaudi*," *Parasitology International*, vol. 74, p. 101994, 2020.

[22] D. M. Shaw, F. Merien, and A. Braakhuis, "T-cells and their cytokine production: the anti-inflammatory and immunosuppressive effects of strenuous exercise," *Cytokine*, vol. 104, pp. 136–142, 2018.

Hindawi
Advances in Polymer Technology
Volume 2020, Article ID 7879368, 12 pages
https://doi.org/10.1155/2020/7879368

Research Article

Influence of the Preparation Method on Some Characteristics of Alginate/Chitosan/Lovastatin Composites

Duc-Thuan Nghiem,[1] Thuy-Chinh Nguyen,[2,3] Minh-Thanh Do,[2] Thi-Huyen Nguyen,[4] Dai Lam Tran,[2,3] Tran-Dung Hoang,[2] Van-Quan Le,[1] Quoc-Trung Vu,[4] Duy-Trinh Nguyen,[5] and Hoang Thai[2,3]

[1]*Military Hospital 103, Vietnam Military Medical University, 261 Phung Hung, Phuc La, Ha Dong, Hanoi 100000, Vietnam*
[2]*Institute for Tropical Technology, Vietnam Academy of Science and Technology, 18 Hoang Quoc Viet, Cau Giay, Hanoi 100000, Vietnam*
[3]*Graduate University of Science and Technology, Vietnam Academy of Science and Technology, 18 Hoang Quoc Viet, Cau Giay, Hanoi 100000, Vietnam*
[4]*Hanoi National University of Education, No. 136 Xuan Thuy Road, Cau Giay, Hanoi 100000, Vietnam*
[5]*Nguyen Tat Thanh University, 300A Nguyen Tat Thanh, District 4, Ho Chi Minh City 700000, Vietnam*

Correspondence should be addressed to Thuy-Chinh Nguyen; thuychinhhn@gmail.com and Hoang Thai; hoangth@itt.vast.vn

Received 25 October 2019; Revised 30 November 2019; Accepted 12 December 2019; Published 4 January 2020

Guest Editor: Mingqiang Li

This study investigates the effects of direct and indirect dispersion methods for lovastatin solid dispersion (LSD) in alginate (AG)/chitosan (CS) composites on the characteristics and properties of the AG/CS/LSD composites. The preparation method significantly influences the structure, morphology, and LSD size distribution of the composites as well as the drug release of LSD from the samples. The differences in dispersion methods for LSD lead to differences in the interaction between the components, the structure, and the control drug release of LSD. Lovastatin was released from the samples containing LSD in two stages (a fast release stage and a slow release stage), and the drug release content prepared using the indirect method is lower than that prepared using the direct method in the same buffer solution. After 32 h of testing, the released LSD content from the indirect and direct LSD dispersion methods in pH 2 and pH 7.4 buffer solutions was 87–94% and 41–61%, respectively. Drug release kinetics from the above samples in solutions with different pH values was also set up.

1. Introduction

Lovastatin, a natural product with a potential inhibitory effect on HMG-CoA reductase, was synthesized in 1979 and first applied in medicine in 1987. It is absorbed rapidly in the small intestine if administered orally. The plasma concentration of lovastatin reaches its maximum within 4 h. It has a short half-life of 3 h and a low bioavailability of 5% [1]. Lovastatin is widely used to lower cholesterol and reduce the risk of cardiovascular diseases. As lovastatin has poor aqueous solubility, researchers face a great challenge to develop suitable and viable methods and technologies for the preparation of drug samples to enhance the saturation solubility and dissolution velocity of drugs. This shall allow for the achievement of optimum absorption in the systemic circulation as well as bioavailability of drugs in therapy.

Basavaraj et al. used nanotechnology to reduce the particle size of lovastatin from micron size to nanosize level by precipitation process without the use of surfactants or stabilizers [2]. The authors showed methanol and acetone to be suitable solvents for the preparation of lovastatin nanocrystal, at 3 mM concentration of drug. The dissolution rate of nanocrystal drug in methanol and acetone was doubled due to the contact of the drug particles with a larger

surface area of the dissolution medium, and oral bioavailability in biological fluid of nanocrystal drug was increased as compared to the pure lovastatin. Inclusion complex techniques were also used for the preparation of lovastatin systems by kneading method through the combination of excipients (B-cyclodextrin, hydroxypropyl-β-cyclodextrin, randomly methylated B-cyclodextrin, etc.), with lovastatin at different drug-carrier ratios. The solubility of lovastatin in these systems was 2.4 to 3.4 times higher than regular drug formulation [1, 3, 4]. Another technique used for increasing the solubility of lovastatin is the solubilization of surfactant by microemulsion or self-microemulsifying drug delivery system methods. The solubility of the drug in these systems was 1.3 to 2.27 times higher than raw lovastatin [5, 6]. Liquisolid compaction and mesoporous carrier techniques have been studied for the improvement of the solubility of lovastatin [7–10]. These are novel techniques, with complex requirements. The solubility of lovastatin in these systems was increased from 1.8 to 3.42 times.

Solid dispersion is the most popular technique for the preparation of lovastatin systems, with the solubility of lovastatin being 1.2–2.9 times higher than that of pure lovastatin [1]. Solid dispersions in which the drug may be present in the amorphous state offer an attractive means of increasing the solubility and, therefore, potentially increasing the oral bioavailability of these complex compounds. The advantages of the solid dispersion technique are the reduction of particle size of drug crystals, improvement of the drug wettability, and enhancement of the degree of porosity. Amongst the various methods (such as solvent evaporation, melt/cool, coprecipitation, dropping, fusion, physical mixture, kneading, freeze-drying, carrier, grinding, and hot-melt extrusion) and carrier options (for example, modified locust bean gum, sodium starch glycolate, crospovidone, poloxamer F68, polyethyleneglycol, soluplus, acetylsalicylic acid, and mannitol), solid dispersion technique has the potential to prepare lovastatin system for effective therapy [11–14]. In this technique, there are physicochemical interactions between lovastatin and carriers that help to deposit the drug on the surface of carriers.

Owing to the variation of the solid dispersion technique, we chose this technique to investigate the solubility of lovastatin in simulated body fluids. The materials as excipients including chitosan (CS), alginate (AG), crosslinking agent, and gelation agent are used in this study. Chitosan and AG are suitable due to their nontoxic, biocompatible, and biodegradable nature. Moreover, chitosan has a high specific area and high drug loading capacity and can interact with AG by electrostatic binding which occurs between protonated amine group of chitosan and COO^- group of AG [15–22]. AG dissolves well in water and is used in drug preparation as a stabilizer and emulsifier or for coating. The combination of chitosan with AG in the lovastatin solid dispersion could provide a good solubility of lovastatin in water and buffer solutions. Sodium tripolyphosphate (STPP) is a crosslinking agent for chitosan, and calcium chloride ($CaCl_2$) is a gelation agent for AG in the lovastatin solid dispersion. This study focuses on investigating the characterizations and solubility of lovastatin in simulated body fluids in two systems prepared according to two methods: directly combined and indirectly combined dropping methods. The aim is to provide detailed evaluation of the role of excipients and preparation method on the solubility of lovastatin. In the direct dropping method combined with solvent evaporation, we first add lovastatin, STPP, and $CaCl_2$ solution into the AG solution, following which we add this mixture solution into chitosan solution. The solution is then centrifuged to obtain the solid residue which is then freeze-dried to obtain a powder containing solid dispersion lovastatin (D-LSD) with the random dispersion of components. For the indirect dropping method, we first add the lovastatin and $CaCl_2$ solution into the AG solution. Following this, the mixture solution is centrifuged and freeze-dried to obtain the AG/lovastatin powder. Thereafter, the AG/lovastatin powder is covered by chitosan and STPP solution using 3D liquid printer to form chitosan-coated AG/lovastatin solid dispersion (ID-LSD) with bilayer structure on lovastatin.

2. Materials and Methods

2.1. Materials. The following materials and chemicals were purchased from Sigma-Aldrich Co.: AG (AG, viscosity of 300–500 mpa-s), AG (CS, deacetylation >75–85%, PDI = 1.61×10^5 Da), lovastatin (LVS, purity > 98%), and sodium tripolyphosphate (STPP, purity >85%). Some other chemicals are analysis reagents, which were used as received.

2.2. Preparation of Composites of Alginate (AG)/Chitosan (CS)/Lovastatin (LVS) Using Different Methods of LVS Dispersion

2.2.1. Direct Combination Dropping Method. The composites of AG/CS/LSD were prepared using the direct combination dropping method to form D-LSD samples as follows. Firstly, some separated solutions were produced, including 0.05 g of STPP in 10 mL of distilled water (solution S1), 15 mL of $CaCl_2$ 0.002 M (solution S2), 0.02 g of LVS in 10 mL of ethanol (solution S3), 0.1 g of AG in 50 mL of distilled water (solution S4), and 0.1 g of CS in 50 mL of acetic acid 1% (solution S5). Secondly, solutions S1, S2, and S3 were mixed together to obtain a homogenous solution (solution S6). Under ultrasonicating at 20000 rpm, solution S6 was dropped into S4 to form solution S7 and kept in this status for 30 min before dropping into S5 to form solution S8, which was ultrasonicated at 20000 rpm for 60 min before centrifuging to obtain the solid part. The solid part was freeze-dried on a FreeZone 2.5 machine (Labconco, USA) to obtain a composite powder containing solid dispersion lovastatin (D-LSD). The schematic diagram of the preparation procedure of D-LSD samples is shown in Figure 1. The ratio of components and abbreviation of samples is listed in Table 1.

2.2.2. Indirect Combination Dropping Method. The composites of AG/CS/LVS were prepared by the indirect combination dropping method to form ID-LSD samples as follows. Firstly, some individual solutions were produced as follows: 15 mL of $CaCl_2$ 0.002 M (solution S1), 0.02 g of LVS in 10 mL

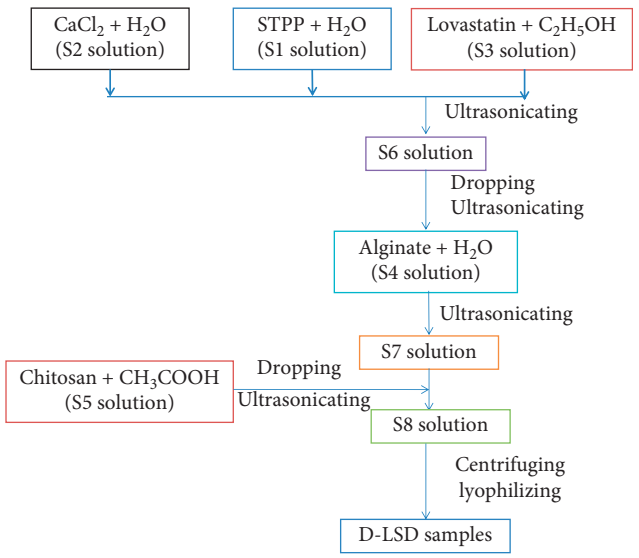

Figure 1: Schematic diagram describing the process of preparing the D-LSD samples.

of ethanol (solution S2), 0.1 g of AG in 50 mL of distilled water (solution S3). Secondly, S2 was dropped into S3 and ultrasonicated for 30 min to obtain a homogenous solution (solution S4). Following this, S4 was heated to 60–70°C and kept at this state for 30 min. At the same time, S1 was dropped into S4 to form AG gelation. This solution was then cooled to room temperature before centrifuging it to obtain the solid part. The solid part was freeze-dried on a FreeZone 2.5 machine (Labconco, USA) to obtain AG/LVS beads in powder.

Following this, 0.01 g of CS and 0.005 g of STPP were dissolved in 4 mL of acetic acid 1% (solution S5), and 0.1 g of the AG/CS beads dispersed into S5 to form solution S6. A total of 2 mL of S6 was pumped into the piston of the 3D liquid printer. Printing process was performed by compiling a g-code script designed for printing to control the nozzle moving in three coordinate axes to cover the surface of the 10×10 cm glass sheet that was heated to 75°C. The print ink (solution S6) was driven out of the printer head to form a 6×6 cm printed area. The printer control was performed by the Repetier-Host software on the computer. The printing process was carried out for 60 min at a speed of 5 mm/s. The width of the printing line was 0.6 mm, and the thickness of the printed layer was 0.2 mm. A total of 2 mL of the remaining S6 was carried out in a manner similar as above. The 3D liquid printer system connected to the computer is presented in Figure 2. The CS-coated AG/LVS beads were obtained in powder and signed as ID-LSD. The schematic diagram for the preparation procedure of ID-LSD samples is presented in Figure 3. The ratio of components and abbreviation of ID-LSD samples having a core-shell structure prepared by print ink solution and 3D liquid printer technique are presented in Table 2.

2.3. Characterization. Infrared (IR) spectra of the samples of AG/CS/LVS composites were recorded by using a Nicolet iS10 (Thermo Scientific, USA) at room temperature in the range of 400–4000 cm^{-1} with the resolution of 8 cm^{-1}. The sample was pressed with KBr to form a pellet before being taken to the IR chamber. Field-emission scanning electron microscope (FESEM) images of samples were taken by using an S-4800 FESEM instrument (Hitachi, Japan). Mean diameter, size distribution, and zeta potential of the samples were determined according to the dynamic light scattering (DLS) method by using a Zetasizer Ver 6.20 particle size analyzer (Malvern Instruments Ltd.). The samples were distributed in distilled water by ultrasonic stirring before being taken to the DLS chamber. *Differential Scanning Calorimetry (DSC) of the samples was measured on a* DSC-131 (SETARAM) in a temperature range from room temperature to 400°C, at a heating speed of 10°C/min in an argon atmosphere. Ultraviolet-visible spectroscopy (UV-Vis, Cintra 40, GBC, USA) was used to determine the drug loading capacity and drug release content from the investigated samples.

2.4. Determination of Drug Loading Capacity. 0.01 g of the sample was dispersed in 200 mL of ethanol, and this solution was stirred continuously for 3 h at 37°C. Then, 10 mL of this solution was withdrawn to record the UV-Vis spectrum. From the absorbance value, drug loading capacity was calculated based on the calibration equation of lovastatin in ethanol ($y = 0.301x + 31269$, with x being the concentration of lovastatin solution and y being absorbance, $\lambda_{max} = 245.547$ nm, linear regression coefficient $R^2 = 0.9931$).

2.5. In Vitro Drug Release Study. The release content of lovastatin from samples was determined by UV-Vis spectroscopy as follows: 0.01 g of samples was added into 200 mL of buffer solutions (simulated gastric fluid (SGF) and simulated intestinal fluid (SIF)), and the solution was stirred at a speed of 400 rpm for 32 hours at 37°C. A sample (5 ml) of the solution was withdrawn from this solution at hourly intervals. The samples were replaced with fresh medium at the same volume. Absorbance values of these solutions were measured by using a UV-Vis spectrophotometer. The percentage drug release was calculated according to the following equation:

$$\%\,\text{lovastatin} = \frac{m_t}{m_o} \cdot 100, \quad (1)$$

where m_t and m_o are the drug contents at t time and initial time, respectively. m_t was determined based on the calibration equations of lovastatin in SGF ($y = 6187x + 0.011$, $\lambda_{max} = 229.97$ nm, $R^2 = 0.996$) and SIF ($y = 3197.2x + 0.0188$; $\lambda_{max} = 239.147$ nm, $R^2 = 0.996$).

2.6. Drug Release Kinetics Study. Drug release kinetics of LVS from the LSD samples evaluated according to the drug release content versus testing time is a popular kinetic model and is as follows:

(i) Zero-order kinetics (ZO): $W_t = W_0 + K_1 \cdot t$ (2)

(ii) First-order kinetics (FO): $\log C = \log C_0 - K_2 \cdot t/2.303$ (3)

Table 1: Ratio of components and abbreviation of D-LSD samples.

No.	STPP weight (g)	$CaCl_2$ 0.002 M volume (mL)	Alginate weight (g)	Chitosan weight (g)	Lovastatin weight (g)	Signed samples
1	0.05	15	0.10	0.10	—	D-LSD1
2	0.05	15	0.10	0.10	0.01	D-LSD2
3	0.05	15	0.10	0.10	0.02	D-LSD3
4	0.05	15	0.10	0.10	0.03	D-LSD4

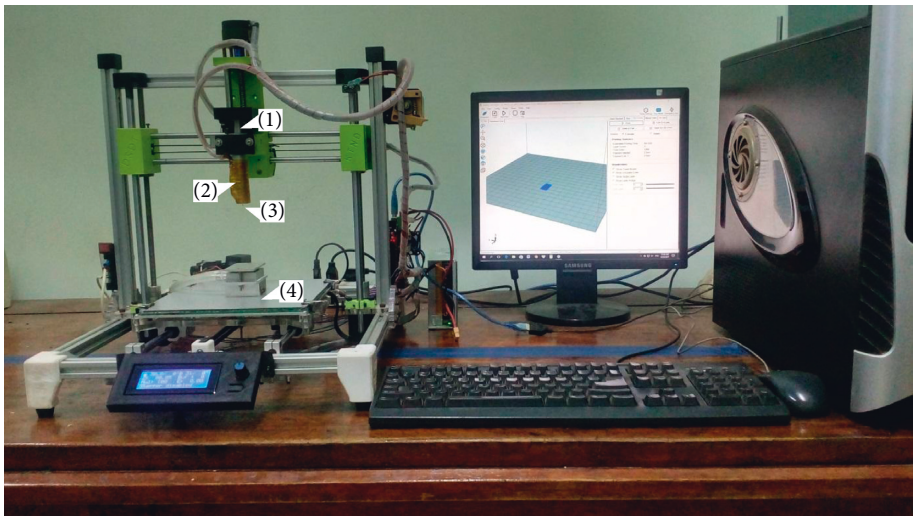

(1) Piston
(2) Cylinder for containing liquid sample
(3) Nozzle
(4) Heated bed

Figure 2: The 3D liquid printer system connected to a computer.

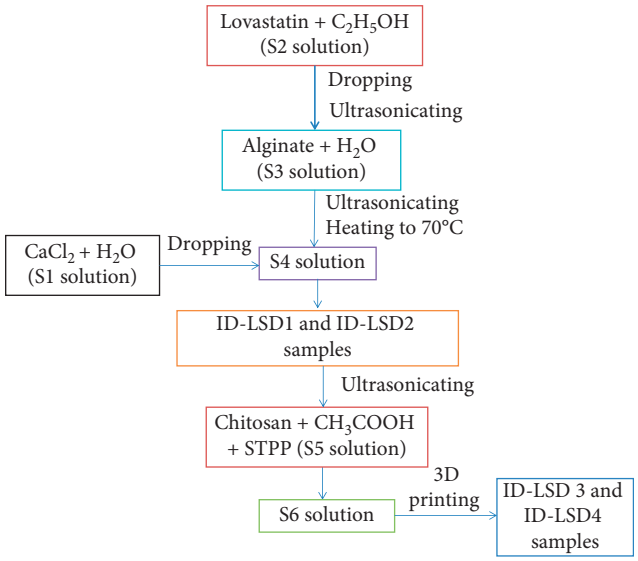

Figure 3: Schematic diagram describing the process of preparing the ID-LSD samples.

Table 2: Ratio of components and abbreviation of ID-LSD samples.

No.	STPP weight (g)	$CaCl_2$ 0.002 M volume (mL)	Alginate weight (g)	Chitosan weight (g)	Lovastatin weight (g)	ID-LSD weight (g)	Signed samples
1	—	15	0.10	—	0.01		ID-LSD1
2	—	15	0.10	—	0.02		ID-LSD2
3	0.05	—	—	0.01	—	0.10 (ID-LSD1)	ID-LSD3
4	0.05	—	—	0.01	—	0.10 (ID-LSD2)	ID-LSD4

(iii) Hixson–Crowell model (HC): $W_0^{1/3} - W_t^{1/3} = K_3 \cdot t$ (4)

(iv) Higuchi model (HG): $W_t = K_4 \cdot t^{1/2}$ (5)

(v) Korsmeyer–Peppas model (KP): $M_t/M_\infty = K_5 \cdot t^n$ (6)

where t is the testing time, K is the drug release constant, n is the diffusion constant, W_t is the weight of drug at the t time, W_0 is the weight of drug at the initial time, M_t/M_∞ is the drug released into the medium, C_0 is the concentration of drug at the initial time, and C is the concentration of drug at the t time.

3. Results and Discussion

3.1. Photo of LSD Samples. Figure 4 presents the photos of LSD samples prepared using direct and indirect dropping methods. The photos clearly indicate that the colors of these samples were not similar. The ID-LSD2 sample was white in color as it consisted of AG and LVS. The D-LSD3 and ID-LSD4 samples were light yellow in color owing to the presence of chitosan.

3.2. Morphology of LSD Samples. The SEM images of LVS, D-LSD, and ID-LSD samples are shown in Figure 5. The LVS has a crystal-bar shape with sizes ranging from 100 to 300 μm [23].

Figure 5 presents the FESEM images of the D-LSD and ID-LSD samples with different LVS contents. It is worth noting that the morphology of LVS had changed in terms of size and shape owing to variations in face dimensions or the appearance/disappearance of some crystal faces [23]. The size of LVS in the D-LSD samples decreased after loading to the AG/CS composites. The LVS was coated by polymers; thus, we did not observe any appearance of LVS bars in the structures of the D-LSD samples. This can be attributed to the formation of hydrogen bonds and electrical interactions between hydroxyl, amine, and carbonyl groups of AG and CS with hydroxyl and carbonyl groups of LVS. In contrast, for the ID-LSD1 and ID-LSD2 samples, the LVS became bar shaped with size ranging from 500 to 3000 nm. The surface of the LVS bars was coated by a thin AG film. As coated by CS (ID-LSD3 and ID-LSD4), the LVS/AG bars were entirely covered by CS layers to form a bilayer structure on the surface of the LVS bars. There was a difference in the morphologies of the D-LSD and ID-LSD samples due to the preparation methods. This variation could cause a modification in the relative crystal degree as discussed later.

3.3. Functional Groups in LSD Samples. The functional groups of LSD samples were indicated in their IR spectra (Figures 6 and 7). In the IR spectra of D-LSD samples (Figure 6), there was a vibration of -CH, -OH, -NH, -C=O, and -C-O groups. The IR spectra of ID-LSD1 and ID-LSD2 were different from the IR spectra of ID-LSD3 and ID-LSD4 because of the CS coating on their surface (Figure 7). The wavenumbers characterized for vibrations of some main functional groups such as -CH, -OH, -NH, -C=O, and -C-O groups in CS, AG, LVS, D-LSD, and ID-LSD samples are listed in Table 3. The shift of position of peaks for -OH, -NH, -C=O, and -C-O groups on the IR of D-LSD and ID-LSD samples as compared with the corresponding peaks on the IR spectrum of AG, CS and LVS confirmed the existence of hydrogen bond and charge interactions between AG, CS, and LVS in investigated samples, as well as the resonance of functional groups. Moreover, the preparation method also affected the functional groups of LSD samples by a slight difference in wavenumbers of functional groups as listed in Table 3.

3.4. Thermal Behavior of LSD Samples. DSC parameters of the D-LSD and ID-LSD samples are listed in Table 4. It can be seen that most LSD samples had the melting temperature that was lower and melting enthalpy that was higher than the equivalent for AG, CS, and LVS. This was caused by the interactions between AG, CS, and LVS. The melting enthalpy of samples was increased remarkably with rising LVS content due to the presence of crystal structure in LVS (D-LSD3 and D-LSD4, ID-LSD1 and ID-LSD2, and ID-LSD3 and ID-LSD4). This phenomenon provides further evidence of the effect of LVS crystal structure on the melting of AG and CS. The melting enthalpy of the ID-LSD samples was higher than that of D-LSD samples. This shows that the preparation method can have an impact on the arrangement of LVS crystal structure in investigated samples [23].

3.5. Size Distribution of LSD Samples. Table 5 and Figure 8 describe the size distribution of LSD samples. The size distribution of D-LSD1 samples ranged from 190.1 nm to 615.1 nm, with the average particle size of 341.3 ± 34.7 nm. As loading LVS, the average particle size of D-LSD2, D-LSD3, and D-LSD4 samples increased but some smaller particles (around 100 nm) were observed at the same time, with the particle intensity percentage of ca. 13%. The increase of particle size followed a general trend for polymer/drug systems because of the appearance of drug-drug and drug-polymer interactions [24].

The preparation method also affected the size distribution of LSD samples. For ID-LSD1 and ID-LSD2, the particle size was 160.7 ± 4.1 nm and 188.8 ± 2.9, respectively. For ID-LSD3 and ID-LSD4, the particle size was 615.1 ± 17.7 nm and 645.7 ± 26.1 nm, respectively. Coating AG/LVS particles by CS was the main reason for the increase in particle size of ID-LSD samples. The transition of zeta potential of ID-LSD3 and ID-LSD4 to a more positive potential as compared to zeta potential of ID-LSD1 and ID-LSD2 also confirmed the coating of CS onto AG/LVS particles due to CS protonated in acidic environment (zeta potentials of ID-LSD1, ID-LSD2, ID-LSD3, and ID-LSD4 are −6.8 mV, −14.8 mV, 5.45 mV, and −9.02 mV, respectively).

3.6. Drug Release of LSD Samples in Different Simulated Body Fluids. Figures 9 and 10 present the drug released content from LVS control, D-LSD, and ID-LSD samples in pH 2 and pH 7.4 solutions. It is clear from the figures that the

(a) (b) (c)

Figure 4: Photos of the LSD samples prepared using different methods: (a) D-LSD3, (b) ID-LSD2, (c) and ID-LSD4.

preparation method had a strong effect on the drug release content from LSD samples. The drug content released from D-LSD samples was much higher than that from the ID-LSD samples at the same testing time. The main reasons for this were the nature of the polymer, combined way of polymers in processing as well as interactions between the drug and polymers. In the D-LSD samples, AG, CS, and LVS were combined, so when D-LSD samples were added into buffer solutions, polymers could swell and dissolve. Hence, LVS placed near the surface of particles would be first diffused into solution, and then, it was the turn of LVS inside of particles. For the ID-LSD samples, LVS was carried by AG before coated with CS; therefore, when taking the ID-LSD samples into buffer solutions, CS layer could limit the diffusion of drug from particles into solutions. As a result, the drug release content from ID-LSD particles was smaller than that from D-LSD samples.

As can be seen from Figures 9 and 10, there was almost no release of LVS from the LVS control in pH 2 solution (only reaching 4.1% after 9 testing hours) and a very fast release in pH 7.4 solution. In contrast, the LVS released from LSD samples in both pH 2 and pH 7.4 solutions and the release of LVS from LSD samples in pH 7.4 solution was much slower than that from the control solution. It was due to the difference in the structure and morphology of LSD sample from LVS control sample. This result confirms that LSD system helped to improve the solubility of LVS in a different pH solution, leading to the enhancement in bioavailability of LVS in treatment.

Again, as can been seen from Figures 9 and 10, LVS released from the LVS control was released in one stage but LVS released from the LSD samples was released in two stages: a fast release stage for the 10 starting hours of the test and a slow release stage in the following hours. After 10 h of testing, the LVS content reached 82.59–92.55% and 41.24–57.19% corresponding to the D-LSD samples and ID-LSD samples, respectively. With increasing LVS content in LSD samples, there is a decreasing trend of the LVS released content. This may be due to the drug-drug interaction leading to the agglomeration of drug in particles when using high drug content, resulting in lowering the diffusion ability of drug from particles into solution.

Figures 9 and 10 also show that pH of the solution had a slight effect on the drug release content from LSD samples. In pH 2 solution, the amine groups in CS were protonated by a proton in the acid environment to form a proton layer around particles leading to the prevention of the release of an LVS part into the solution [16, 25]. Moreover, calcium ion cross-linked with the AG exchanging with ion H^+ leading to the carrier material being converted to water-soluble alginic acid. Sodium ion cross-linked with the chitosan exchanging with ion H^+ but the protonation of amine groups in CS prevailed. Therefore, the drug release content from LSD samples in pH 7.4 solution was higher than that in pH 2 solution.

The LVS content released from ID-LSD3 and ID-LSD4 samples in both investigated pH solutions was generally higher than that from ID-LSD1 and ID-LSD2 samples. For ID-LSD3 and ID-LSD4 samples, the CS content was higher and the drug release was lower. In case of using a higher LVS content (0.03 g of LVS in ID-LSD sample), the drug release content from ID-LSD samples in both pH 2 and pH 7.4 solutions is lower than 20% after 32 h of testing. This is a reason why we do not report about the ID-LSD samples containing 0.03 g of LVS in this article. The drug release from ID-LSD samples was quite complex, and we investigated the reasons behind this phenomenon.

3.7. Drug Release Kinetics of LSD Samples in Different Simulated Body Fluids. Tables 6 and 7 show the LVS release constant and regression coefficient obtained from kinetics equations reflecting LVS released from the samples in pH 2 and pH 7.4 solutions. Zero-order release kinetics describes the process of constant drug release from a drug delivery system when the level of the drug in the blood remains constant throughout the delivery. First-order release kinetics states that change in concentration with respect to change in time is dependent only on concentration. *Hixson–Crowell's* cube root equation is a mathematical *model* used to describe powder dissolution or *drug release* from specific formulations where there is a change in surface area and diameter of particles or tablets. Hence, particles of regular area are proportional to the cube root of its volume. The Higuchi models described the rate of drug release from matrix devices where the drug loading exceeds the solubility in the matrix medium. *Korsmeyer–Peppas model* derived a simple relationship

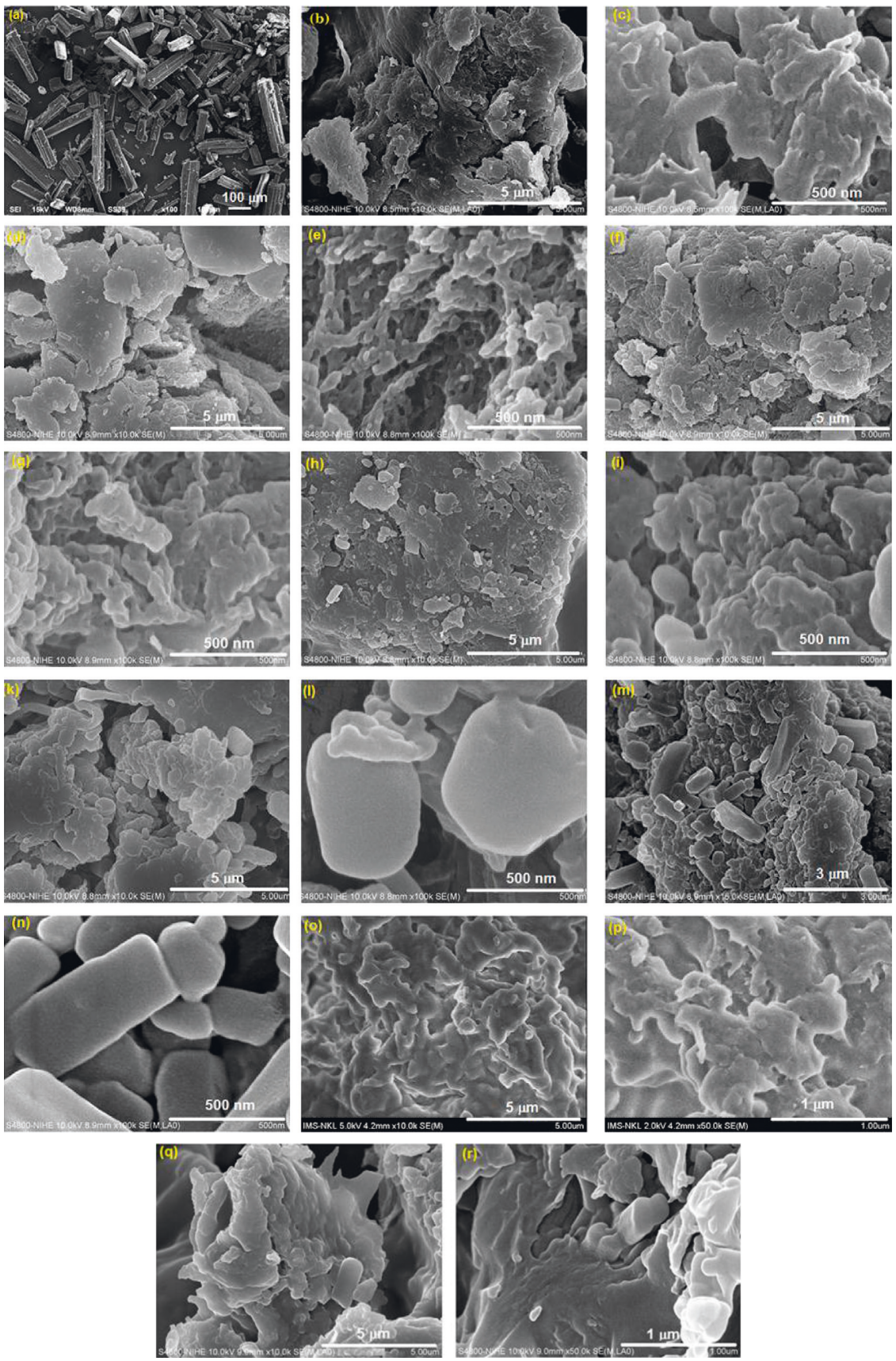

Figure 5: SEM images of (a) lovastatin, (b, c) D-LSD1, (d, e) D-LSD2, (f, g) D-LSD3, (h, i) D-LSD4, (k, l) ID-LSD1, (m, n) ID-LSD2, (o, p) ID-LSD3, and (q, r) ID-LSD4.

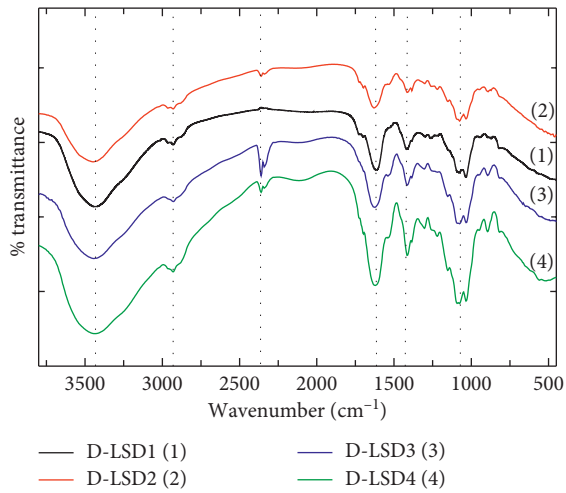

Figure 6: IR spectra of the D-LSD samples.

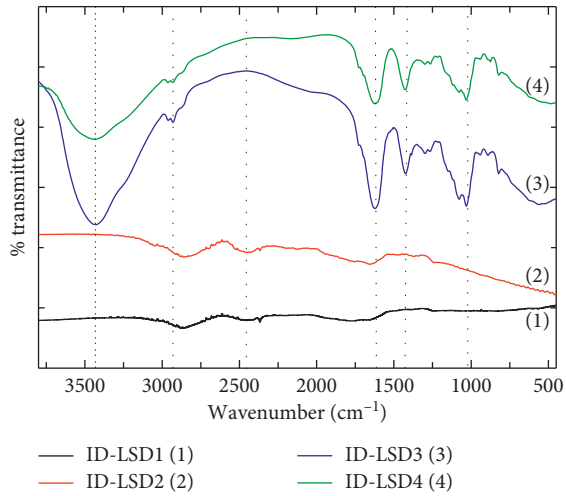

Figure 7: IR spectra of the ID-LSD samples.

Table 3: Vibrations of main functional groups of AG, CS, LVS, D-LSD, and ID-LSD samples.

Sample	Vibration Wavenumbers (cm^{-1})				
	$\nu_{-OH;}\ \nu_{-NH2}$	ν_{-CH}	$\nu_{-C=O}$	δ_{-NH2}	ν_{-C-O}
AG	3448.16	2923.65	1626.64	—	1032.10
CS	3442.46	2924.08	1644.18	1418.87	1027.40
LVS	3540.99	2965.06	1702.02	—	1074.50
D-LSD1	3439.20	2964.77	1613.75	1416.66	1080.70
D-LSD2	3448.76	2930.00	1629.72	1414.02	1075.60
D-LSD3	3444.02	2928.96	1625.30	1414.77	1076.06
D-LSD4	3440.85	2930.04	1629.72	1414.02	1075.60
ID-LSD1	3426.62	2930.06	1622.16	1423.94	1081.54
ID-LSD2	3441.26	2926.46	1621.47	1426.97	1082.90
ID-LSD3	3460.66	2926.28	1630.28	1426.79	1088.00
ID-LSD4	3460.66	2924.26	1619.98	1422.89	1092.69

equation which described which type of dissolution *was followed by a drug release* from a polymeric system. The LVS was released from the samples in two stages: rapid

Table 4: DSC parameters of D-LSD and ID-LSD samples.

Sample	Endothermic peak (°C)	Melting enthalpy (ΔH, $J{\cdot}g^{-1}$)
AG	119.7	358.6
CS	106.8	48.0
LVS	174.6	90.3
D-LSD3	85.3	236.7
D-LSD4	93.8	405.6
ID-LSD1	106.9	547.0
ID-LSD2	104.9	631.1
ID-LSD3	100.6	497.4
ID-LSD4	98.3	584.1

Table 5: Size distribution of D-LSD and ID-LSD samples.

Sample	Size distribution range (nm)	Main particle size		Average particle size (nm)
		nm	%	
D-LSD1	190.1–615.1	341.3	100	341.3 ± 34.7
D-LSD2	295.3–712.4	449.9	100	449.9 ± 47.3
D-LSD3	58.8–825	99.4	13.8	99.4 ± 10.1
D-LSD4	68.1–825	460.8 118.7 420.5	86.2 13.3 86.7	460.8 ± 68.5 118.7 ± 12.9 420.5 ± 70.9
ID-LSD1	122–190	160.7	100	160.7 ± 4.1
ID-LSD2	142–220	188.8	100	188.8 ± 2.9
ID-LSD3	53–712	615.1	100	615.1 ± 17.7
ID-LSD4	459–825	645.7	100	645.7 ± 26.1

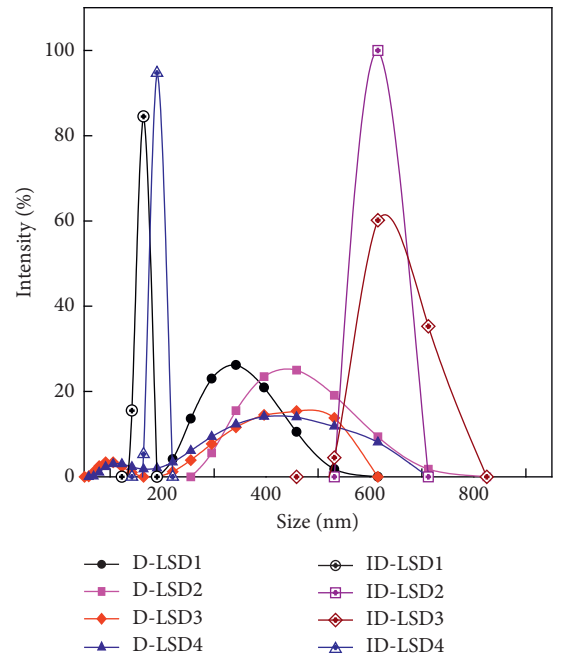

Figure 8: Size distributions of the LSD samples.

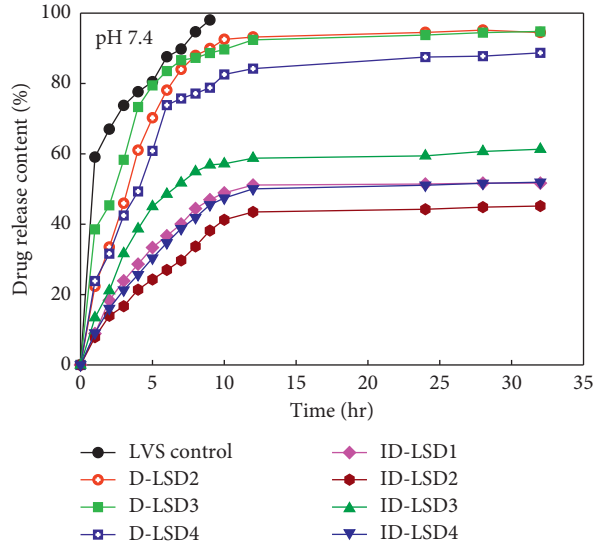

Figure 9: LVS release content from D-LSD and ID-LSD samples in pH 7.4 solution.

Table 6: Release constant (k) and regression coefficient (R^2) obtained from kinetic equations reflecting LVS release from D-LSD and ID-LSD samples in pH 7.4 solution.

Sample		ZO		FO		HG		HC		KP		
		k	R^2	k	R^2	k	R^2	k	R^2	k	n	R^2
D-LSD1	Fast stage	3.10^{-5}	0.9281	−0.1457	0.8359	0.0001	0.9774	-1.10^{-5}	0.9281	0.6521	0.2276	0.9825
	Slow stage	6.10^{-7}	0.9286	−0.0016	0.9315	5.10^{-6}	0.8963	-2.10^{-7}	0.9286	0.0307	0.8620	0.8654
D-LSD2	Fast stage	4.10^{-5}	0.8506	−0.0898	0.7988	0.0002	0.9275	-1.10^{-5}	0.8506	0.4051	0.3820	0.9537
	Slow stage	9.10^{-7}	0.9938	−0.0013	0.9939	8.10^{-6}	0.9888	-3.10^{-7}	0.9938	0.0256	0.8668	0.9785
D-LSD3	Fast stage	7.10^{-5}	0.9278	−0.1336	0.8698	0.0003	0.9659	-2.10^{-5}	0.9278	0.5851	0.2287	0.9821
	Slow stage	2.10^{-6}	0.9740	−0.0026	0.9729	2.10^{-5}	0.9855	-8.10^{-7}	0.9740	0.0517	0.7411	0.9215
ID-LSD1	Fast stage	0.0001	0.8039	−0.2226	0.8487	0.0004	0.8783	-3.10^{-5}	0.8039	0.8007	0.0652	0.9876
	Slow stage	2.10^{-6}	0.9821	−0.0044	0.5808	2.10^{-5}	0.982	-7.10^{-7}	0.9821	0.1477	0.2593	0.8233
ID-LSD2	Fast stage	0.0001	0.9446	−0.1847	0.9016	0.0004	0.987	-4.10^{-5}	0.9446	0.7243	0.1013	0.9963
	Slow stage	1.10^{-6}	0.9551	−0.0053	0.6684	10^{-5}	0.9576	-4.10^{-7}	0.9551	0.1549	0.4023	0.8447
ID-LSD3	Fast stage	7.10^{-5}	0.9865	−0.1751	0.8396	0.0003	0.9894	-2.10^{-5}	0.9700	0.7865	0.1743	0.9916
	Slow stage	2.10^{-6}	0.9618	0.0014	0.8254	2.10^{-5}	0.9548	-6.10^{-7}	0.9618	0.0497	0.8201	0.9460
ID-LSD4	Fast stage	0.0002	0.9283	−0.1805	0.8938	0.0007	0.9830	-5.10^{-5}	0.9283	0.7779	0.0713	0.9994
	Slow stage	4.10^{-6}	0.9929	−0.0033	0.7872	4.10^{-5}	0.9843	-1.10^{-6}	0.9929	0.1160	0.3259	0.9135

ZO: zero-order kinetics; FO: first-order kinetics; HG: Higuchi model; HC: Hixson–Croswell model; KP: Korsmeyer–Peppas model.

release for the first 10 testing hours and slow release in the following hours. In both pH 7.4 and pH 2 solutions, LVS content released from the D-LSD and ID-LSD samples followed Korsmeyer–Peppas model (diffusion/relaxation model) for fast stage ($R^2 > 0.95$) and Hixson–Croswell model for slow stage ($R^2 > 0.92$). It means that in the fast release stage during the first 10 testing hours, the mechanism for LVS release from the D-LSD and ID-LSD samples into solution pH 7.4 was quite complex and combined by processes of polymer swelling, polymer dissolution, and drug diffusion, among others. These results agree with the LVS release process published in some studies [26, 27]. In the slow release stage, LVS content was released from a system having a change on surface area and a diameter of particles according to the erosion mechanism. Comparing regression coefficients obtained from zero-order kinetics and first-order kinetics, the release of LVS from the LSD samples was complied with zero-order kinetics. It confirms that the LVS release rate was constant over a period of testing time [28].

4. Conclusions

In conclusion, we successfully prepared the composites of AG/CS/LVS by using combination dropping methods to form D-LSD samples based on a one-step and two-step procedure, with LVS, AG, CS, $CaCl_2$, and STPP being used as components. For ID-LSD samples, for the first time, we used print ink solution and 3D liquid printer technique to prepare AG/CS/LVS composites having core-shell structure. The difference in combination of components leads to the formation of indirect LSD and direct LSD samples. The ID-

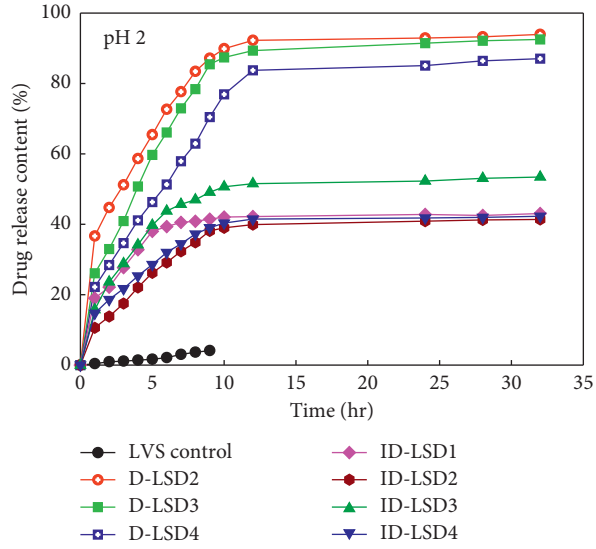

Figure 10: LVS release content from D-LSD and ID-LSD samples in the pH 2 solution.

Table 7: Release constant (k) and regression coefficient (R^2) obtained from kinetic equations reflecting LVS release from D-LSD and ID-LSD samples in pH 2 solution.

Sample		ZO		FO		HG		HC		KP		
		k	R^2	k	R^2	k	R^2	k	R^2	k	n	R^2
D-LSD1	Fast stage	2.10^{-5}	0.9856	−0.0978	0.9483	0.0001	0.9942	-8.10^{-6}	0.9856	0.4118	0.3447	0.9868
	Slow stage	3.10^{-7}	0.9286	−0.0008	0.9301	3.10^{-6}	0.8963	-1.10^{-7}	0.9286	0.0162	0.8855	0.8635
D-LSD2	Fast stage	5.10^{-5}	0.9868	−0.1334	0.9369	0.0002	0.9902	-2.10^{-5}	0.9868	0.5650	0.2384	0.9859
	Slow stage	1.10^{-6}	0.9905	−0.0018	0.9899	1.10^{-5}	0.9970	-4.10^{-7}	0.9905	0.0359	0.8173	0.9967
D-LSD3	Fast stage	6.10^{-5}	0.9986	−0.1313	0.9699	0.0003	0.9759	-2.10^{-5}	0.9986	0.5452	0.2018	0.9799
	Slow stage	2.10^{-6}	0.9506	−0.0019	0.9524	2.10^{-5}	0.9270	-6.10^{-7}	0.9506	0.0374	0.7619	0.9018
ID-LSD1	Fast stage	0.0001	0.9445	−0.1141	0.8909	0.0005	0.9816	-4.10^{-5}	0.9445	0.4716	0.1201	0.9775
	Slow stage	2.10^{-6}	0.9830	−0.0012	0.7870	2.10^{-5}	0.9794	-6.10^{-7}	0.9830	0.0844	0.2725	0.9253
ID-LSD2	Fast stage	0.0001	0.8626	−0.1702	0.9571	0.0006	0.9365	-5.10^{-5}	0.8626	0.6489	0.1213	0.9828
	Slow stage	6.10^{-7}	0.7560	−0.0030	0.8133	5.10^{-6}	0.7999	-2.10^{-7}	0.7560	0.1205	0.4222	0.9422
ID-LSD3	Fast stage	5.10^{-5}	0.9579	−0.1698	0.9181	0.0002	0.9892	-2.10^{-5}	0.9579	0.5584	0.3504	0.9979
	Slow stage	2.10^{-6}	0.8189	0.0063	0.7140	1.10^{-5}	0.8602	-5.10^{-7}	0.8189	0.0977	0.8786	0.8041
ID-LSD4	Fast stage	0.0002	0.9881	−0.1191	0.9566	0.0007	0.9816	-5.10^{-5}	0.9881	0.4619	0.0616	0.9897
	Slow stage	9.10^{-6}	0.8987	−0.0026	0.7216	7.10^{-5}	0.9291	-3.10^{-6}	0.8987	0.0426	0.1644	0.7707

ZO: zero-order kinetics; FO: first-order kinetics; HG: Higuchi model; HC: Hixson–Croswell model; KP: Korsmeyer–Peppas model.

LSD samples had an average particle size in the range of 160.7 ± 4.1–645.7 ± 26.1 nm while the D-LSD samples had a smaller average particle size from 99.38 ± 10.1 nm to 460.8 ± 68.5 nm. The FTIR spectra of LSD samples showed that LVS, CS, and AG interact together, and some peaks at the same position overlapped. The different preparation methods also influenced changes in crystal structure and morphology of LSD samples. The D-LSD samples had more regular morphology than the ID-LSD samples. The LVS released from the D-LSD and ID-LSD samples in pH 2 and pH 7.4 solutions was released in two stages: a rapid release for the first 10 testing hours and a slow release in the following hours. The LVS release content from D-LSD samples was higher than that from the ID-LSD samples. The LVS release content reached 82.59–92.55% and 41.24–57.19% corresponding to the D-LSD samples and ID-LSD samples after 10 testing hours, respectively. The Korsmeyer–Peppas model and Hixson–Croswell model were the most suitable for LVS release in fast stage and slow stage, respectively. The LVS releases process from LSD samples complied with the zero-order kinetics by release rate which was constant over a period of testing time. In general, the one-step method could make D-LSD samples have a more uniform distribution, better interaction of the components, higher drug release content, and better drug release control than ID-LSD samples prepared by the two-step method. These results provide an opportunity to use the D-LSD systems in future applications.

Data Availability

Data are provided in the Supplementary Information files.

Conflicts of Interest

The authors declare no conflicts of interest.

Acknowledgments

This work was supported by the National Foundation for Science and Technology Development in Vietnam (subject code 104.02-2017.17, period of 2017–2020). The authors would like to thank Editage (http://www.editage.com) for English language editing.

References

[1] N. F. Zolkiflee, M. M. R. Meor Mohd Affandi, and A. B. A. Majeed, "Lovastatin: history, physicochemistry, pharmacokinetics and enhanced solubility," *International Journal of Research in Pharmaceutical Sciences*, vol. 8, no. 1, pp. 90–102, 2017.

[2] K. N. Basavaraj, K. D. Ganesh, M. B. Hiren, K. N. Veerendra, and F. V. Manvi, "Design and characterization of nanocrystals of lovastatin for solubility and dissolution enhancement," *Journal of Nanomedicine and Nanotechnology*, vol. 2, no. 2, 2011.

[3] A. Rasheed, C. K. A. Kumar, and V. V. N. S. S. Sravanthi, "Cyclodextrins as drug carrier molecule: a review," *Scientia Pharmaceutica*, vol. 76, no. 4, pp. 567–598, 2008.

[4] A. Mehramizi, E. Asgari Monfared, M. Pourfarzib et al., "Influence of β - cyclodextrin complexation on lovastatin release from osmotic pump tablets (OPT)," *DARU Journal of Pharmaceutical Sciences*, vol. 15, no. 2, pp. 71–78, 2007.

[5] R. P. Patel and M. M. Patel, "Preparation and evaluation of inclusion complex of the lipid lowering drug lovastatin with β-Cyclodextrin," *Dhaka University Journal of Pharmaceutical Sciences*, vol. 6, no. 1, pp. 25–36, 2007.

[6] R. Emőke, B. Tőkés, and S. Emese, "Physical and chemical study of lovastatin inclusion complexes. Bioavailability improvement," *Acta Medica Marisiensis*, vol. 58, no. 5, pp. 326–328, 2012.

[7] V. Viswanath and G. Somasekhar, "Stability enhancement of lovastatin by liquisolid compaction technique," *Journal of Global Trends in Pharmaceutical Sciences*, vol. 5, no. 2, pp. 1933–1939, 2014.

[8] K. Neduri and S. K. Vermula, "Dissolution enhancement of lovastatin by liquisolid compact technique and study of effect of carriers," *International Journal of PharmTech Research*, vol. 6, no. 5, pp. 1624–1632, 2014.

[9] W. Chao, W. Jing, H. Yanchen et al., "Development of a novel starch derived porous silica monolith for enhancing the dissolution rate of poorly water soluble drug," *Materials Science and Engineering: C*, vol. 32, no. 2, pp. 201–206, 2012.

[10] Z. Peng, W. Lihong, S. Changshan et al., "Uniform mesoporous carbon as a carrier for poorly water soluble drug and its cytotoxicity study," *European Journal of Pharmaceutics and Biopharmaceutics*, vol. 80, no. 3, pp. 535–543, 2012.

[11] M. Patel, A. Tekade, S. Gattani, and S. Surana, "Solubility enhancement of lovastatin by modified locust bean gum using solid dispersion techniques," *AAPS PharmSciTech*, vol. 9, no. 4, pp. 1262–1269, 2008.

[12] D. Maji, S. Shaikh, D. Solanki, and K. Gaurav, "Safety of statins," *Indian Journal of Endocrinology and Metabolism*, vol. 17, no. 4, pp. 636–646, 2013.

[13] U. Verma, J. B. Naik, and V. J. Mokale, "Preparation of freeze-dried solid dispersion powder using mannitol to enhance solubility of lovastatin and development of sustained release tablet dosage form," *American Journal of Pharmaceutical Sciences and Nanotechnology*, vol. 1, no. 1, pp. 11–26, 2014.

[14] A. Górniak, M. Gajda, J. Pluta, H. Czapor-Irzabek, and B. Karolewicz, "Thermal, spectroscopic and dissolution studies of lovastatin solid dispersions with acetylsalicylic acid," *Journal of Thermal Analysis and Calorimetry*, vol. 125, no. 2, pp. 777–784, 2016.

[15] K. Agnieszka, M. Aleksandra, M. Justyna, A. Regiel-Futyra, and S. Victor, "Preparation and characterization of alginate/chitosan formulations for ciprofloxacin-controlled delivery," *Journal of Biomaterials Application*, vol. 32, no. 2, pp. 162–174, 2017.

[16] L. Segale, L. Giovannelli, P. Mannina, and F. Pattarino, "Calcium alginate and calcium alginate-chitosan beads containing celecoxib solubilized in a self-emulsifying phase," *Scientifica*, vol. 2016, Article ID 5062706, 8 pages, 2016.

[17] Y. Ji, C. Jie, P. Dan, W. Ying, and W. Zheng, "pH-sensitive interpenetrating network hydrogels based on chitosan derivatives and alginate for oral drug delivery," *Carbohydrate Polymers*, vol. 92, no. 1, pp. 719–725, 2013.

[18] M. Neeraj and K. Gurpreet, "Investigations on polymeric nanoparticles for ocular delivery," *Advances in Polymer Technology*, vol. 2019, Article ID 1316249, 14 pages, 2019.

[19] C. N. Ramesh, K. Rakesh, and J. K. Pandit, "Chitosan coated sodium alginate–chitosan nanoparticles loaded with 5-FU for ocular delivery: in vitro characterization and in vivo study in rabbit eye," *European Journal of Pharmaceutical Sciences*, vol. 47, no. 4, pp. 678–685, 2012.

[20] C. Tingting, L. Shunying, Z. Wenting, L. Zhi, and Z. Qingbing, "Self-assembly pH-sensitive chitosan/alginate coated polyelectrolyte complexes for oral delivery of insulin," *Journal of Microencapsulation*, vol. 36, no. 1, pp. 96–107, 2019.

[21] L. C. Cheng, G. Lu, Y. L. Xin et al., "Development of sustainable carrier in thermosensitive hydrogel based on chitosan/alginate nanoparticles for *in situ* delivery system," *Polymer Composites*, vol. 40, no. 6, pp. 2187–2196, 2019.

[22] P. Mukhopadhyay, S. Maity, S. Mandal, A. S. Chakraborti, A. K. Prajapati, and P. P. Kundu, "Preparation, characterization and in vivo evaluation of pH sensitive, safe quercetin-succinylated chitosan-alginate core-shell-corona nanoparticle for diabetes treatment," *Carbohydrate Polymers*, vol. 182, pp. 42–51, 2018.

[23] R. R. Thenge, S. V. Lonkar, N. M. Mahajan et al., "Modification and characterization of lovastatin crystals," *World Journal of Pharmacy and Pharmaceutical Sciences*, vol. 5, no. 1, pp. 1035–1045, 2015.

[24] C.-Y. Yu, X.-C. Zhang, F.-Z. Zhou, X.-Z. Zhang, S.-X. Cheng, and R.-X. Zhuo, "Sustained release of antineoplastic drugs from chitosan-reinforced alginate microparticle drug delivery systems," *International Journal of Pharmaceutics*, vol. 357, no. 1-2, pp. 15–21, 2008.

[25] T. A. Ahmed and K. M. El-Say, "Development of alginate-reinforced chitosan nanoparticles utilizing W/O nanoemulsification/internal crosslinking technique for transdermal delivery of rabeprazole," *Life Sciences*, vol. 110, no. 1, pp. 35–43, 2014.

[26] L. Ochoa, M. Igartua, R. M. Hernández, A. R. Gascón, M. A. Solinis, and J. L. Pedraz, "Novel extended-release formulation of lovastatin by one-step melt granulation: *In*

vitro and *in vivo* evaluation," *European Journal of Pharmaceutics and Biopharmaceutics*, vol. 77, no. 2, pp. 306–312, 2011.

[27] P. Sandhya, G. Kodali, and A. Fatima, "Formulation and in-vitro characterization of gastro retentive mucoadhesive tablets of Lovastatin," *International Journal of Biological & Pharmaceutical Research*, vol. 5, no. 1, pp. 71–77, 2014.

[28] G. Abhijit, "Achieving zero-order release kinetics using multi-step diffusion-based drug delivery," *Pharmaceutical Technology*, vol. 38, no. 5, pp. 38–42, 2014.

Hindawi
Advances in Polymer Technology
Volume 2020, Article ID 1796701, 7 pages
https://doi.org/10.1155/2020/1796701

Research Article

Effects of Ginsenoside Biopolymer Nanoparticles on the Malignant Behavior of Non-Small-Cell Lung Cancer

Weizheng Zhou,[1] Chengliang Cai,[1] Hui Shi,[2] Hai Jin,[1] and Xiaowei Wang[1]

[1]*Department of Thoracic Surgery, Changhai Hospital, Shanghai 200435, China*
[2]*Department of Respiratory, Changhai Hospital, Shanghai 200435, China*

Correspondence should be addressed to Hai Jin; projinhai@163.com and Xiaowei Wang; xiaoweiwang@genopub.com

Received 22 October 2019; Revised 4 December 2019; Accepted 12 December 2019; Published 3 January 2020

Guest Editor: Mingqiang Li

Objective. To explore the effects and mechanism of ginsenoside Rg3 nanoparticles on the malignant behavior of non-small-cell lung cancer. *Methods*. The nanoparticle carriers were prepared by using an electrostatic system, and the coverage of ginsenoside Rg3 was determined by HPLC after coating the nanoparticle carriers with the ginsenoside Rg3 monomer. The proliferation of H125 cells was measured using MTT assay, and the Transwell assay was used to detect the invasiveness of H125 cells. Cell scratch test was used to determine the migration ability of H125 cells, and Western blotting was used to measure the expression level of PTEN in H125 cells; the expression level of miR-192 in H125 cells was measured via RT-qPCR, and the apoptosis level of H125 cells was detected by Tunel assay. *Results*. Firstly, gelatin nanoparticles and hyaluronic acid nanoparticles were uniformly distributed, uniform in size and spherical in shape, and after coating ginsenoside Rg3, the sizes of the nanoparticles were significantly increased. Secondly, the expression level of miR-192 was upregulated in H125 cells, which could be effectively inhibited by the treatment of Rg3 monomer and HA-Rg3 nanoparticles. Thirdly, the knockdown of miR-192 significantly inhibited H125 cell proliferation, invasion, and migration and also enhanced H125 cell apoptosis. In addition, PTEN was demonstrated as a target gene of miR-192. Finally, by inhibiting the expression level of miR-192 in H125 cells, the Rg3 monomer and HA-Rg3 nanoparticles upregulated the expression of PTEN and thus exerted its antitumor effect; the effects of HA-Rg3 were comparatively more significant than those of the Rg3 monomer. *Conclusions*. The Rg3 monomer and HA-Rg3 nanoparticles mitigated the malignant behavior of human non-small-cell lung cancer H125 cells through the miR-192/PTEN molecular axis, and HA-Rg3 nanoparticles showed better antitumor effects.

1. Introduction

With the aging of the population and the deterioration of the living environment, lung cancer has become one of the most common malignant tumors worldwide, and both morbidity and mortality are on the rise. It has become a malignant tumor with the highest morbidity and mortality in China with about 80% to 85% of them being non-small-cell lung cancer [1]. Ginsenoside Rg3 is one of the active ingredients in the ginseng extract. According to clinical evidence, ginsenoside Rg3 can inhibit malignant behaviors of tumors such as tumor invasion and metastasis, can alleviate the toxic effects of chemoradiotherapy, and also can sensitize tumors to antitumor drugs. However, the ginsenoside Rg3 monomer has low solubility in the human body, thus resulting in low effectiveness. Several studies indicated that the nanometer-sized particle carrier can improve the solubility of the drug, therefore increasing the body's absorption and improving the bioavailability of the drug.

MicroRNAs (miRNAs) are a class of noncoding single-stranded RNA molecules that affect various biological behaviors. The mechanism of action is mainly through the interaction with 3′-UTR to affect the mRNA expression of target genes. Many studies have shown that [2] the change of miRNA expression will lead to the upregulation or downregulation of its target gene mRNA expression and then affect cell proliferation and apoptosis. In addition, the abnormal expression of miRNAs can also induce a series of

human diseases, including cancer. Previous studies have shown that miR-192 expression is significantly increased in non-small-cell lung cancer tissues. It is thus speculated that miR-192 is related to the occurrence and development of non-small-cell lung cancer. The tumor suppressor gene phosphatase and tensin homolog (PTEN) is a dual-specific protein and lipid phosphatase, which can block the PI3K signaling pathway by activating AKT to inhibit cell proliferation and survival. Therefore, PTEN has a certain inhibitory effect on cancer [3]. Through prediction, it was found that PTEN may be a downstream target gene of miR-192. It is, therefore, speculated that miR-192 might affect the occurrence and development of non-small-cell lung cancer by regulating the expression of PTEN. Therefore, in this study, the nanoparticle carriers covered with ginsenoside Rg3 monomer were prepared to investigate its effect on the malignant behavior of human non-small-cell lung cancer cell line H125 and its underlying mechanism.

2. Material and Methods

2.1. Cell Lines and Reagents. In this study, human normal lung epithelial cells BEAS-2B were purchased from the Chinese Academy of Sciences Cell Bank, and human non-small-cell cancer cells H125 were purchased from FuHeng Cell Center, Shanghai, China. Ginsenoside Rg3 (Shenyi Capsule) was purchased from Jilin Yatai Pharmaceutical Co., Ltd.; fetal bovine serum and DMEM medium were purchased from Suzhou Laisa Biotechnology Co., Ltd.; the MTT kit was purchased from Beijing Kanglong Kangtai Biotechnology Co., Ltd.; the Transwell chamber was purchased from American BD Company; the Tunel kit and RIPA cell lysate were purchased from Shanghai Biyuntian Biotechnology Co., Ltd.; the Lipofectamine 2000 kit and reverse transcription kit were purchased from Shanghai Kemin Biotechnology Co., Ltd.; the ECL development kit was purchased from China Solarbio, and the dual-luciferase reporter gene detection kit was purchased from Beijing YuanPingHao Biotechnology Co., Ltd.

2.2. Preparation of Nanoparticles. Gelatin and hyaluronic acid nanoparticles were prepared in an electrostatic field preparation system. In addition, 4 μL of the prepared ginsenoside Rg3 solution (25 mg/mL) was separately added to 996 μL of prepared gelatin and hyaluronic acid nanoparticles (final concentration of ginsenoside Rg3 was 100 μg/mL) for their coating in the electrostatic field preparation system. The coverage of ginsenoside Rg3 was then determined by HPLC.

2.3. Cell Culture and Transfection. H125 cells were seeded in the DMEM medium (containing 10% fetal bovine serum, 100 U/L penicillin, and 100 mg/L streptomycin) and cultured in a constant temperature incubator at 37°C with 5% CO_2. miR-192 inhibitor, miR-NC, pc-PTEN, pc-NC, and sh-PTEN were provided by Shanghai Jima. The cells in the logarithmic growth phase were transfected with miRNA mimics and siRNAs according to the Lipofectamine 2000 kit. After 48 h of transfection, the cells were harvested for subsequent experiments. The primer sequences used in this study are shown in Table 1.

2.4. MTT Experiment. The single-cell suspension was prepared by trypsinization of H125 cells in the logarithmic growth phase. The cell concentration was adjusted to 5×10^3 cell/well and inoculated into a 96-well plate. The cells were then cultured in an incubator at 37°C with 5% CO_2. After 24 h, the cells were treated according to the experimental design and then cultured at 37°C with 5% CO_2 for 24 h. The cells were washed twice with PBS buffer solution and then cultured in a DMEM medium containing 10% fetal calf serum for 48 h. 20 μL (5 mg/L) MTT solution was added to each well, and the proliferation activity of H125 cells was measured in strict accordance with the instructions of the MTT kit.

2.5. Transwell Experiment. The upper chamber of the Transwell chamber was coated with Matrigel, and the H125 cells in the logarithmic growth phase were taken and seeded at a concentration of 1×10^5 cell/well in the upper chamber of the Transwell chamber containing a serum-free medium. The DMEM medium containing 10% fetal bovine serum was added to the lower chamber. The cells were removed 24 h after inoculation, fixed with formaldehyde, stained with crystal violet for 5 min, washed 3 times with PBS buffer, photographed, and counted.

2.6. Cell Scratch Test. 5×10^5 cells were added to each well of a 6-well plate. When the cell fusion rate reached 95%, the cell membrane was streaked and washed slowly with PBS buffer 3 times, the delineated cells were removed, and serum-free medium was added. The plate was incubated in a 37°C, 5% CO^2 incubator for 24 h and photographed after 24 h, and the scratch distance was determined using ImageJ.

2.7. Western Blotting. H125 cells were transferred to EP tubes, lysed on ice for 30 min using the RIPA cell lysate, and then centrifuged at 14,000 rpm for 5 min at 4°C. The supernatant was extracted and a loading buffer was added to the supernatant. The sample was then denatured at 100°C for 10 min and then stored at −20°C. 25 μg of protein sample was then loaded and electrophoresed at 40 A for 100 min. After that, it was then transferred to the membrane at 100 V for 90 min. After adding the primary antibody, the membrane was incubated at 4°C overnight and then incubated at room temperature for 2 h after the addition of the secondary antibody. Image development was performed strictly based on the ECL kit instructions and the grayscale analysis of protein bands was performed using ImageJ software.

2.8. RT-qPCR. H125 cellular RNA was extracted and 2 μL of the extracted RNA was added to 98 μL of ddH_2O to measure the RNA content and purity based on the absorbance value obtained through an ultraviolet spectrophotometer. The

Table 1: Primer sequences.

Gene name	Primer sequence
miR-192	5′-GGGCTGACCTATGAATTG-3′ 5′-CAGTGCGTGTCGTGGAGT-3′
U6	5′-ACGATGCACCTGTACGATCA-3′ 5′-TCTTTCAACACGCAGGACAG-3′

Table 2: RT-qPCR reaction system (20 μL).

Reagent	Volume (μL)
SYBR premix Ex Taq (2x)	10
Forward primer (5 pmol/L)	1
Reverse primer (5 pmol/L)	1
cDNA	0.5
RNase-FREE WATER	7.5

cDNA was then synthesized according to the instructions of the reverse transcription kit. The PCR reaction was carried out according to Table 2; specifically, the reaction conditions were as follows: 95°C, 10 min; 95°C, 20 s; 60°C, 1 min, for a total of 40 cycles.

2.9. Detection of Apoptosis by Tunel Assay. After the treated sample was rinsed with PBS buffer, the liquid surrounding the sample was removed. 100 μL of the TdT enzyme reaction solution was added to each sample, the reaction was carried out in the dark at 37°C for 60 min, and then the diluted SSC solution was added to terminate the reaction. After rinsing with PBS buffer, the samples were blocked in 0.3% hydrogen peroxide/PBS and incubated for 4 min at room temperature. 100 μL of the streptavidin-HRP working solution was then added, and the reaction was carried out at 37°C for 60 min. The BAD chromogenic solution was added, followed by rinsing the cells with PBS buffer 3 times, and then sealed with a neutral resin and observed under a microscope.

2.10. Dual-Luciferase Reporter Gene Assay. After the 3′-UTR fragment of PTEN gene was amplified and inserted into the double luciferase reporter gene plasmid, the positive clone was screened, followed by sequencing, amplification, and purification of the plasmid. The miR-192 plasmid and the empty vector were obtained in a similar manner. The plasmid of the reporter gene, miR-192, and empty vector were cotransfected with well-grown H125 cells, and the cells were then cultured in a constant temperature incubator at 37°C, with 5% CO_2 for 24 h. After that, the protein was purified, and the substrate was added; luciferase activities were measured by using a fluorescence counter.

2.11. Statistical Analysis. SPSS (version 22.0) statistical software was used for the data analysis, the data obtained in this study were expressed as $\overline{x} \pm s$, the t-test was used for comparison between groups, and the comparison among multiple groups was analyzed by one-way ANOVA. The difference was statistically significant when $P < 0.05$ or $P < 0.01$.

3. Results

3.1. Nanoparticle Detection and Vector Screening. The prepared gelatin nanoparticle carriers and hyaluronic acid nanoparticle carriers were found uniformly distributed, uniform in size and spherical in shape under the electron transmission microscopy, and the particle sizes of the nanoparticle carriers were 4.5 ± 0.75 nm and 16.4 ± 4.2 nm, respectively. As shown in Figures 1(a) and 1(b), the results of MTT experiments showed that cell viability of H125 cells was significantly reduced when cocultured with 20 μL gelatin nanoparticle carrier suspension ($P < 0.05$), while similar significantly reduced cell viability of H125 cells was observed, and when cocultured with 40 μL hyaluronic acid nanoparticle carrier suspension ($P < 0.05$). After coculture of H125 cells with gelatin polymer or HA polymer, the activity of H125 cells is similar to that of gelatin or HA nanoparticles; see Figure 1(c). After coating ginsenoside Rg3, Gelatin-Rg3 nanoparticles and hyaluronic acid HA-Rg3 nanoparticles showed a small amount of particle agglomeration, and the particle sizes of the nanoparticles were significantly different from that before coating ($P < 0.01$); the particle sizes were 40.3 ± 5.8 nm and 31.2 ± 8.4 nm, respectively. The coverage of ginsenoside Rg3 on gelatin and hyaluronic acid nanoparticles measured by HPLC was 13.715 ± 1.985% and 36.410 ± 6.472%, respectively. Therefore, to reduce the impact of nanoparticle carriers on H125 cells, HA-Rg3 nanoparticles were selected for subsequent experiments.

3.2. Effect of HA-Rg3 Bio-Polymerized Nanoparticles on the Expression Level of miR-192. As shown in Figure 2(a), the expression level of miR-192 in H125 cells was significantly higher than that of BEAS-2B cells. However, the expression levels of miR-192 in H125 cells were significantly downregulated after cocultured with ginsenoside Rg3 and HA-Rg3 bio-polymerized nanoparticles ($P < 0.05$), and the expression levels of miR-192 achieved lowest when H125 cells were cocultured with HA-Rg3 ($P < 0.01$) as shown in Figure 2(b).

3.3. Effect of miR-192 on Malignant Behavior of H125 Cells. The results of RT-qPCR showed that the expression level of miR-192 in H125 cells was significantly downregulated compared with the control group after the transfection of miR-192 inhibitor ($P < 0.01$), as shown in Figure 3. And the knockdown of miR-192 significantly inhibited the activity of H125 cells ($P < 0.01$) as shown in MTT (Figure 4(a)), significantly inhibited the invasion of H125 cells ($P < 0.05$) as shown in Transwell results (Figure 4(b)), and also significantly inhibited the migration ability of H125 cells ($P < 0.05$) as shown in the results of cell scratch assay (Figure 4(c)). Furthermore, knockdown of miR-192 also significantly promoted the apoptosis of H125 cells ($P < 0.01$) as shown in Figure 4(d).

3.4. PTEN Is the Target Gene of miR-192. By using the ENCORI database, we predicted that the 3′-UTR end of

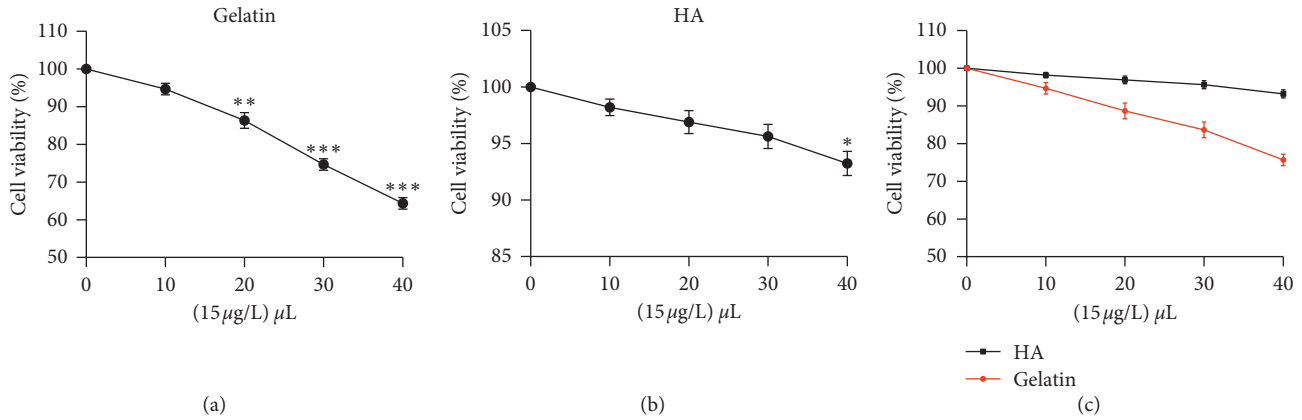

Figure 1: Nanoparticle detection and vector screening. (a, b) H125 cells proliferation activity. $^{*}P < 0.05$, $^{**}P < 0.01$, and $^{***}P < 0.001$ vs the 0 μL group.

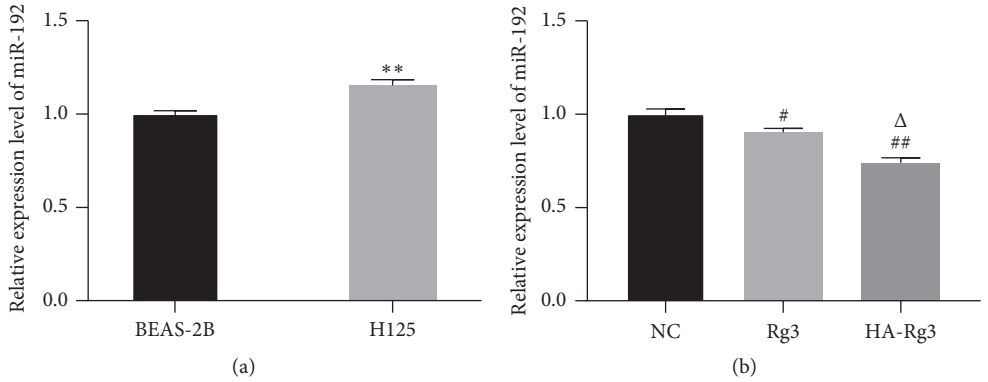

Figure 2: Effect of HA-Rg3 bio-polymerized nanoparticles on the expression level of miR-192. (a, b): The relative expression level of miR-192. $^{**}P < 0.01$ vs the BEAS-2B group; $^{\#}P < 0.05$ and $^{\#\#}P < 0.01$ vs the NC group; $^{\triangle}P < 0.05$ vs the NC group.

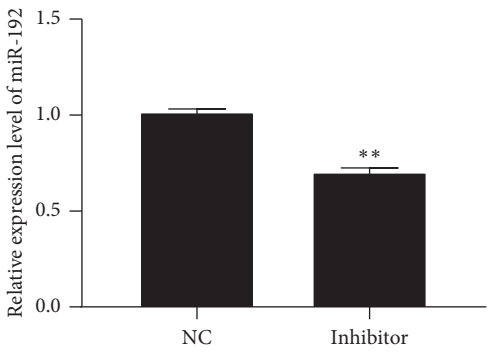

Figure 3: Effects of miR-192 on malignant behavior of H125 cells. $^{**}P < 0.01$ vs the NC group.

PTEN mRNA has a partial base sequence binding to the 5′-UTR end of miR-192 as shown in Figure 5(a). Western blotting results (Figure 5(b)) showed that the expression level of PTEN was significantly downregulated in H125 cells ($P < 0.05$), whereas the knockdown of miR-192 significantly enhanced the expression of PTEN in H125 cells ($P < 0.05$). Moreover, as shown in Figure 5(c), the results of the dual-luciferase assay verified that PTEN is the target gene of miR-192.

3.5. Mechanism of Action of HA-Rg3 Bio-Polymerized Nanoparticles on Non-Small-Cell Lung Cancer. The MTT assay showed that the proliferation activity of H125 cells in group I and group II was significantly lower than that in the NC group ($P < 0.01$), and the proliferation activity of H125 cells in group III and IV was significantly inhibited ($P < 0.001$), whereas the proliferation activity of H125 cells in the V group was not significantly different from that in the NC group. Moreover, the activity of H125 cells in group II was significantly inhibited when compared with group I ($P < 0.05$) as shown in Figure 4(a). Transwell results (Figure 4(b)) showed that the invasiveness of H125 cells in group I, II, III, and IV was inhibited compared with the NC group, and the difference was statistically significant ($P < 0.05$), whereas the invasion of H125 cells in group V was not significantly different from that of the NC group, and the invasiveness of H125 cells in group II was significantly lower than that of group I ($P < 0.05$). The scratch test results (Figure 4(c)) measuring the cell migration ability also showed that H125 cells in group I, II, III, and IV was inhibited compared with the NC group, and the difference was statistically significant ($P < 0.05$); the H125 cells in group V was not significantly different from that of the NC group, and the migration ability of H125 cells in group II was significantly lower than that of

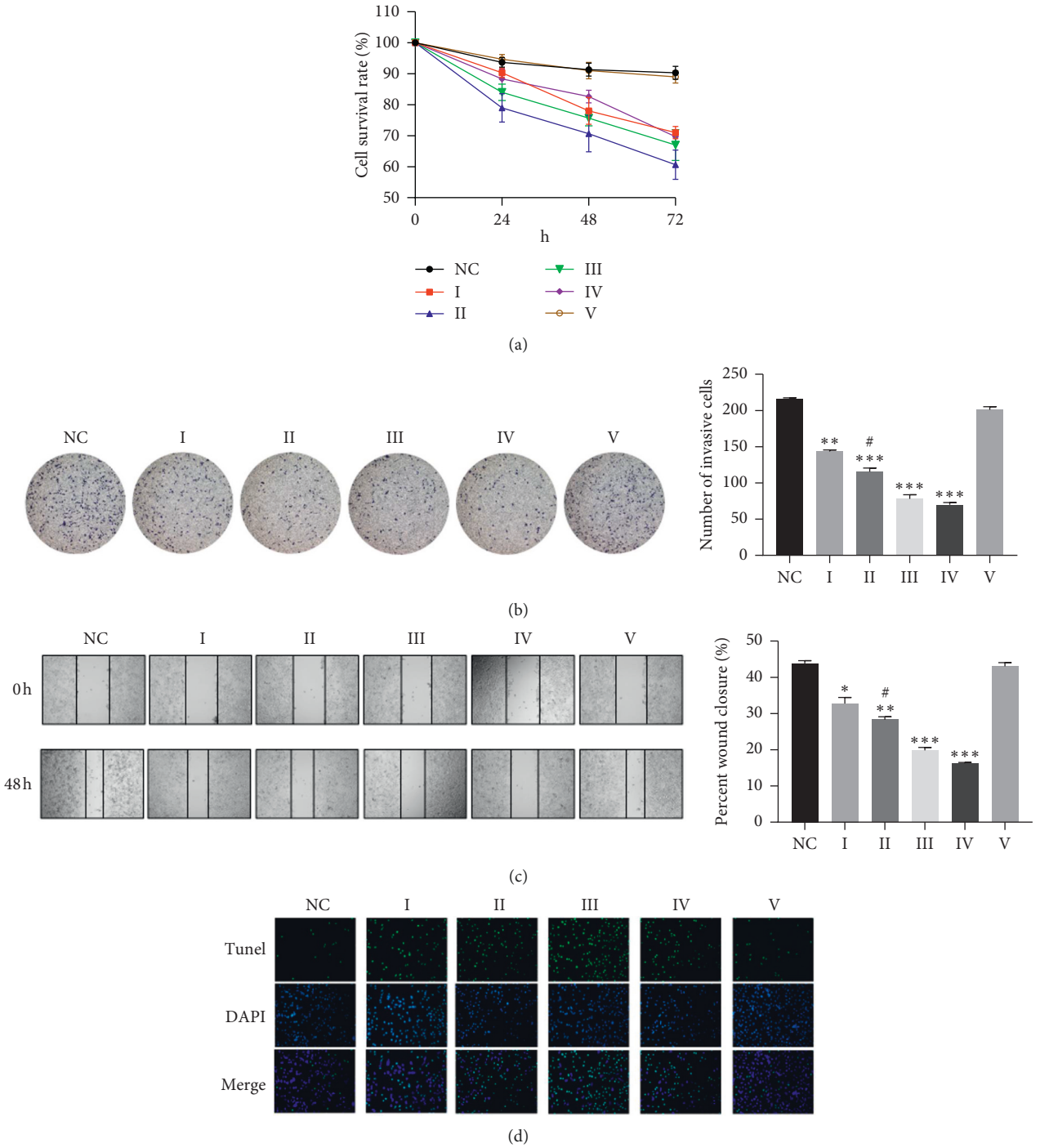

Figure 4: Mechanism of action of HA-Rg3 bio-polymerized nanoparticles on non-small-cell lung cancer. (a) H125 cells proliferation activity; (b) the invasion of H125 cells detected by Transwell assay; (c) the migration ability of H125 cells detected by wound healing; (d) the apoptosis of H125 cells was measured by Tunel assay. Groups (I) II, III, IV, and V were Rg3, HA-Rg3, miR-192 inhibitor, pc-PTEN, and miR-192 inhibitor + sh-PTEN, respectively. $^{**}P < 0.01$ vs the NC group.

group I ($P < 0.05$). The apoptosis results of Tunel assay (Figure 4(d)) showed that the number of apoptosis of H125 cells in group I, group II, group III, and group IV increased in different degrees compared with the NC group, and the difference was statistically significant ($P < 0.05$). There was no significant difference in the number of apoptosis of H125 cells in the V group compared with the NC group, and again the number of apoptosis of H125 cells in group II was significantly lower than that of group I ($P < 0.05$).

4. Discussion

Lung cancer is primary bronchial carcinoma, of which non-small-cell lung cancer is the most common type of cancer,

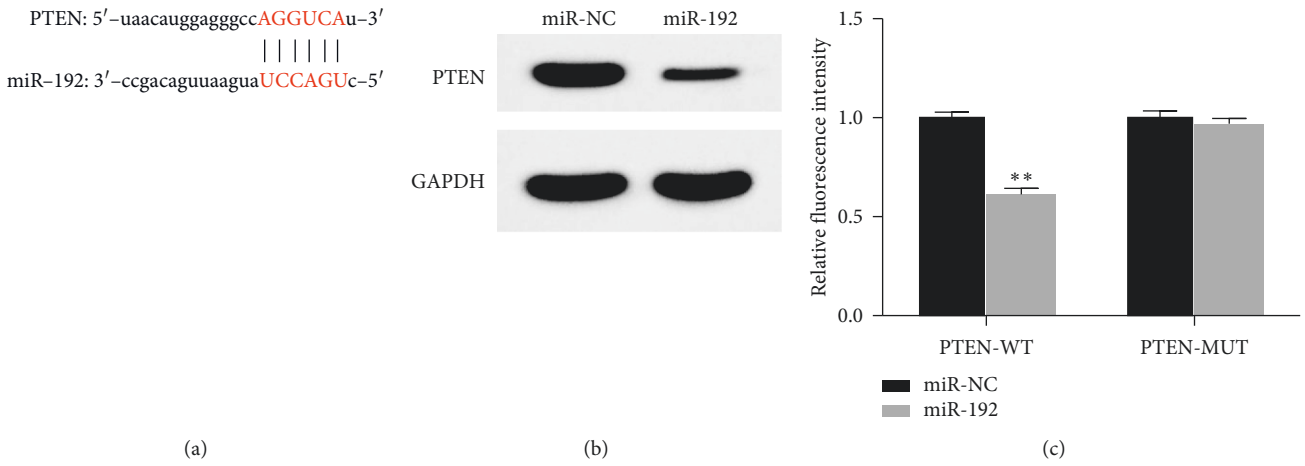

Figure 5: PTEN is the target gene of miR-192. (a) the predicted results of target genes; (b) detection of PTEN protein level by Western blotting; (c) detection of the Interaction between miR-192 and PTEN by DLRTM. $^{**}P < 0.01$ vs the miR-NC group.

accounting for 75% to 80% of the total number of lung cancer patients [4]. Due to the lack of early specific symptoms, lung cancer often develops into the advanced stage at the clinical diagnosis. Although surgery can be used to treat early-stage lung cancer, 70% of patients cannot be cured [4]. Recently, radiotherapy and chemotherapy are becoming mainstream methods for the treatment of lung cancer. However, with that comes the toxic side effects and higher recurrence rate, and it is also demanding in terms of the patient's physical quality. In recent years, the advantages of traditional Chinese medicine in cancer treatment have gradually gained attention, which can reduce the side effects of radiotherapy and chemotherapy on patients, prolong the quality lifespan of patients, and alleviate the drug resistance in the cancer treatments [5–7].

Ginsenoside Rg3 is the active ingredient extracted from ginseng. The main component of which is tetracyclic triterpenoid saponin, which can inhibit the formation of tumor blood vessels, block the invasion and metastasis of tumors, and improve the immunity and quality of life for the cancer patients. Wu et al. [8] reported that ginsenoside Rg3 can inhibit the proliferation of thyroid cancer in vitro and in vivo and significantly inhibit the metastasis of thyroid cancer. Dai et al. [5] showed that ginsenoside Rg3 could enhance the anticancer activity of gefitinib and enhance the sensitivity of non-small-cell lung cancer to gefitinib. At present, the "Senyi Capsule" containing ginsenoside Rg3 has been approved for marketing in China and has been used for clinical treatment of cancer, which has achieved a certain curative effect. However, the low solubility of monomeric ginsenoside Rg3 in the human body results in its low bioavailability thus its effectiveness. Because of the small particle diameter, the nanocarrier has been believed to be beneficial to increase the stability, solubility, and ultimately bioavailability of the drug in the human body. Studies have shown that biomimetic 50 nm nanoparticles coated with paclitaxel can prevent the drug from being absorbed by the normal lung cells of the human body because of its surface characteristics, which ultimately can more effectively deliver drugs and improve the bioavailability of the drug [9]. The results of our study showed that the hyaluronic acid nanoparticles coated with ginsenoside Rg3 showed better antitumor effect in vitro, compared with ginsenoside Rg3 monomer. It also more effectively inhibited the proliferation, invasion, and migration of H125 cells as well as promoting the apoptosis of H125 cells. Although ginsenoside Rg3 has certain antitumor curative effects, its mechanism of action has not yet been fully understood. Therefore, it is necessary and urgent to explore the mechanism of action of ginsenoside Rg3 and its biopolymer nanoparticles on non-small-cell lung cancer.

MicroRNAs (miRNAs) are a class of noncoding single-stranded RNA molecules consisting of approximately 22 nucleotides that regulate the expression of proteins in plants and animals. Studies have shown the abnormal expression of various miRNAs in cancer tissues or patients' serum. For example, the expression level of miR-125b in patients' serum can be used as a biomarker for the diagnosis and prognosis of epithelial ovarian cancer [10]. The expression levels of miR-21-5p, miR-141-3p, and miR-205-5p in urine can be used as biomarkers for the diagnosis of prostate cancer and bladder cancer [11]. By reviewing the literature, miR-192 was found upregulated in non-small-cell lung cancer and can be used as a biomarker for the diagnosis of non-small-cell lung cancer [12]. By summarizing the literature reviewed, it is speculated that miR-192 can affect various biological behaviors in H125 cells by regulating PTEN expression. The results in this study showed that the expression of miR-192 was upregulated in H125 cells and the knockdown of miR-192 significantly inhibited the malignant biological behavior of H125 cells. By double luciferase reporter gene experiments, PTEN was revealed as a downstream target of miR-192.

In summary, HA-Rg3 nanoparticles have more advantages in inhibiting H125 cell proliferation, invasion, migration, and promoting H125 cell apoptosis than monomeric ginsenoside Rg3. Further research indicates that ginsenoside Rg3 monomer and HA-Rg3 nanoparticles may inhibit non-small-cell lung cancer by downregulating the

expression level of miR-192 in H125 cells and thus promoting the expression of PTEN in H125 cells.

Data Availability

The data used to support the findings of this study are included within the article.

Conflicts of Interest

The authors declare that they have no conflicts of interest.

Authors' Contributions

Weizheng Zhou and Chengliang Cai contributed equally to this study.

Acknowledgments

This work was funded by the Wu Jieping Medical Fund (no. 320.6750.12213).

References

[1] N. Shriwash, P. Singh, S. Arora, M. Ali, S. Ali, and R. Dohare, "Identification of differentially expressed genes in small and non-small cell lung cancer based on meta-analysis of mRNA," *Heliyon*, vol. 5, no. 6, Article ID e01707, 2019.

[2] A. Lujambio and S. W. Lowe, "The microcosmos of cancer," *Nature*, vol. 482, no. 7385, pp. 347–355, 2012.

[3] B. D. Hopkins, C. Hodakoski, D. Barrows, S. M. Mense, and R. E. Parsons, "PTEN function: the long and the short of it," *Trends in Biochemical Sciences*, vol. 39, no. 4, pp. 183–190, 2014.

[4] R. L. Siegel, K. D. Miller, and A. Jemal, "Cancer statistics, 2017," *CA: A Cancer Journal for Clinicians*, vol. 67, no. 1, pp. 7–30, 2017.

[5] Y. Dai, W. Wang, Q. Sun, and J. Tuohayi, "Ginsenoside Rg3 promotes the antitumor activity of gefitinib in lung cancer cell lines," *Experimental and Therapeutic Medicine*, vol. 17, no. 1, pp. 953–959, 2018.

[6] X.-J. Wang, R.-J. Zhou, N. Zhang, and Z. Jing, "20 (S)-ginsenoside Rg3 sensitizes human non-small cell lung cancer cells to icotinib through inhibition of autophagy," *European Journal of Pharmacology*, vol. 850, pp. 141–149, 2019.

[7] Y. Zhang, X. Q. Wang, H. Liu et al., "A multicenter, large-sample, randomized clinical trial on improving the median survival time of advanced non-small cell lung cancer by combination of Ginseng Rg3 and chemotherapy," *Zhonghua Zhong Liu Za Zhi*, vol. 40, no. 4, pp. 295–299, 2018.

[8] W. Wu, Q. Zhou, W. Zhao et al., "Ginsenoside Rg3 inhibition of thyroid cancer metastasis is associated with alternation of actin skeleton," *Journal of Medicinal Food*, vol. 21, no. 9, pp. 849–857, 2018.

[9] H. Choi, T. Liu, H. Qiao et al., "Biomimetic nano-surfactant stabilizes sub-50 nanometer phospholipid particles enabling high paclitaxel payload and deep tumor penetration," *Biomaterials*, vol. 181, pp. 240–251, 2018.

[10] M. Zuberi, I. Khan, R. Mir, G. Gandhi, P. C. Ray, and A. Saxena, "Utility of serum miR-125b as a diagnostic and prognostic indicator and its alliance with a panel of tumor suppressor genes in epithelial ovarian cancer," *PLoS One*, vol. 11, no. 4, Article ID e0153902, 2016.

[11] N. Ghorbanmehr, S. Gharbi, E. Korsching, M. Tavallaei, B. Einollahi, and S. J. Mowla, "miR-21-5p, miR-141-3p, and miR-205-5p levels in urine-promising biomarkers for the identification of prostate and bladder cancer," *The Prostate*, vol. 79, no. 1, pp. 88–95, 2019.

[12] X. Du, F. Qi, S. Lu, Y. Li, and W. Han, "Nicotine upregulates FGFR3 and RB1 expression and promotes non-small cell lung cancer cell proliferation and epithelial-to-mesenchymal transition via downregulation of miR-99b and miR-192," *Biomedicine & Pharmacotherapy*, vol. 101, pp. 656–662, 2018.

Hindawi
Advances in Polymer Technology
Volume 2019, Article ID 6090965, 13 pages
https://doi.org/10.1155/2019/6090965

Research Article

Development and *In-Vitro* Evaluation of pH Responsive Polymeric Nano Hydrogel Carrier System for Gastro-Protective Delivery of Naproxen Sodium

Rai Muhammad Sarfraz,[1] **Muhammad Rouf Akram**,[1] **Muhammad Rizwan Ali**,[1] **Asif Mahmood**,[2] **Muhammad Usman Khan**,[1] **Husnain Ahmad**,[1] **and Muhammad Naeem Qaisar**[1]

[1]*College of Pharmacy, University of Sargodha, Sargodha 40100, Punjab, Pakistan*
[2]*Department of Pharmaceutics, Faculty of Pharmacy, University of Lahore, Lahore, Pakistan*

Correspondence should be addressed to Rai Muhammad Sarfraz; sarfrazrai85@yahoo.com

Received 17 September 2019; Revised 8 November 2019; Accepted 21 November 2019; Published 29 December 2019

Guest Editor: Mingqiang Li

Current research work was carried out for gastro-protective delivery of naproxen sodium. Polyethylene glycol-g-poly (methacrylic acid) nanogels was developed through free radical polymerization technique. Formulation was characterized for swelling behaviour, entrapment efficiency, Fourier transform infrared (FTIR) spectroscopy, Differential scanning calorimetry (DSC), and Thermal Gravimetric Analysis (TGA), Powder X-ray diffraction (PXRD), Zeta size distribution, and Zeta potential measurements, and *in-vitro* drug release. pH dependent swelling was observed with maximum drug release at higher pH. PXRD studies confirmed the conversion of loaded drug from crystalline to amorphous form while Zeta size measurement showed size reduction. On the basis of these results it was concluded that prepared nanogels proved an effective tool for gastro-protective delivery of naproxen sodium.

1. Introduction

Naproxen, a propionic acid derivative, is widely used either in the form of free acid or sodium salt in the treatment of musculoskeletal and joint disorders. It is also used in management of headache including migraine, dysmenorrhoea, soft-tissue disorders, postoperative pain, and acute gout as well as antipyretic agent [1]. Along with the benefits, there are many gastro intestinal risk factors associated with chronic use of these agents, such as mucosal damage and development of peptic ulcers [2]. The inhibition of biosynthesis of endogenous prostaglandin by nonsteroidal anti-inflammatory drugs (NSAIDs) is the primary mechanism that leads to damage of the gastric mucosa [3]. Secondary to this mechanism, acid-mediated direct topical effect of NSAIDs also resulted into breakdown of mucosal defence by depletion of the mucus barrier [4–6]. Different strategies have been reported to modify the local damage of the gastric mucosa caused by NSAIDs thus reducing the complications. These include; prodrug formulation, complex formation with biocompatible materials, and varying the route of drug delivery thus decreasing local contact of these agents to the gastric mucosa [7–10]. Targeted delivery of NSAIDs to the intestine in the form of delayed release formulations provided the change in absorption site for these agents from stomach to intestine with reduced frequency of gastric ulceration [11]. Furthermore, decreasing the particle size and changing the drug from crystalline to amorphous form is also effective in order to minimize NSAIDs related complications to the gastric mucosa [5, 12].

Previously various techniques have been studied for gastro-protective delivery of NSAIDs [13]. In many studies application of nanogels carrier systems has been reported as tool for controlled and targeted delivery of pH sensitive therapeutic agents i.e. peptides and proteins through oral route in order to bypass gastric environment [14]. Due to this characteristic, nanogels carrier system is getting the attention of researchers for targeted delivery of NSAIDs. Nanogels are nano-scale

hydrogels particulate systems (hydrogel nanoparticles) that possess the characteristics of hydrogels as well as of nanoparticles at the same time [15, 16]. Furthermore, these systems are also a preferred tool for reducing the particle size of the drug [17, 18]. This novel drug delivery approach provided the enhancement in bioavailability of drugs as well as reduction in drug related side effects [14, 19, 20]. Moreover, Chemical cross-linking in nanogels enable these systems to retain their mechanical stability thus stably holding the loaded drug [21]. Many researchers have formulated nanogels drug carrier systems that are sensitive to external stimuli especially pH and temperature by employing several natural and synthetic biodegradable polymers. By modifying the properties of polymeric networks through conjugation with pH sensitive moiety, these systems have been enabled to release the active pharmaceutical moiety at specific pH in order to achieve targeted drug delivery [14].

Poly ethylene glycol (PEG) is a nontoxic, water soluble polymer that exhibits the resistance to recognition by the immune system and presented rapid clearance from the body. Due to these advantages, PEG based nanogels are considered good candidates as biomaterials for drug delivery. These systems have been used in drug delivery, wound healing, and a variety of other biomedical applications. These drug delivery systems are often used in combination with other polymers in order to prepare an appropriate biomaterial. Previously these systems have been studied extensively for targeted delivery of peptides and protein through oral route. PEG based systems also have been used as controlled release devices. The rate of drug release from these systems was found to be dependent not only on the method of preparation, but also on the crosslinking density, molecular weight of the PEG anionic chains, and drug solubility [22].

In the present work, PEG-6000 based pH sensitive nanogels are synthesized by grafting with methacrylic acid. These pH sensitive nanogels are then employed as a carrier system for targeted delivery of naproxen sodium in order to bypass gastric release of the drug. Such formulations will be helpful to provide gastro-protective effect through site specific drug delivery with reduced complications associated with chronic use of NSAIDs.

2. Materials and Methods

2.1. Chemicals. Naproxen sodium was obtained as a gift from the Global Pharmaceuticals Islamabad, Pakistan, PEG-6000 was gifted from the Trison Research Laboratories (Pvt.) Ltd., Sargodha, Pakistan, methacrylic acid and methylene bisacrylamide was purchased from Merck KGaA, Darmstadt, Germany. All other chemicals used were of analytical grade.

2.2. Preparation of Nanogels Particulate System of PEG and MAA. The polymer was mixed with monomer in different molar ratio. Methylene bisacrylamide was added as a cross linking agent in a suitable amount. This mixture was added to a three necked reaction flask supplied with inlet of nitrogen and continuous stirring on a hot plate magnetic stirrer at temperature 37°C. Nitrogen was purged continuously through this mixture for 30 minutes in order to remove the dissolved oxygen. Potassium persulfate (KPS) was then added to the mixture with continuous stirring in order to start polymerization. Formed mixture was poured to a test tube, sealed with aluminium foil and allowed to stand in a water bath at 70°C for 6 hrs. After completion of polymerization reaction, the prepared hydrogel was removed from the test tubes, cut into small slices, and washed with water–methanol mixture 50:50 thrice. Small slices of hydrogel were crushed in wet form and passed through suitable sieve in order to achieve particulate system of uniform size. Particulate systems were dried at 50°C in a hot air oven until constant weight and stored for further analysis [23–25]. Chemical structure of individual ingredients and formulations are presented in Figure 1. In a similar way with varying concentration of polymer, monomer, and cross linking agent, 9 formulations were prepared as presented in Table 1.

2.3. Drug Loading. The drug solution was prepared in 0.1 M phosphate buffer of pH 6.8 (USP). A known quantity of dried nanogels particulate were accurately weighed and immersed in the drug solution and placed at 25°C. After 48 hrs, pH of the solution was decreased to 1.2 by the addition of 0.1 M HCL solution for the locking of the drug loaded nanogels. The mixture was filtered and the residue was also washed with 100 mL of distilled water to remove unentrapped drug. Drug loaded nanogels were dried at low temperature in a hot air oven and stored for further analysis [26–28].

3. *In-Vitro* Characterization of Nanogels Particulate Systems

3.1. Product Yield. Product yield for different formulations was determined in order to evaluate the efficiency of the process with the help of Equations (1) and (2) [17],

$$\text{Product yield} = 100 - \text{Mass loss}, \tag{1}$$

$$\text{Mass loss (\%)} = \frac{M_o - M_1}{M_o} \times 100, \tag{2}$$

where, M_o = initial weight of all ingredients, M_1 = final weight of nanogels.

3.2. Calculation of Entrapment Efficiency. A known quantity of drug loaded nanogels were pulverized and added to 10 mL of 6.8 pH buffer solution and was subjected to stirring for 24 hrs at room temperature. The resulting suspension was filtered and the residue was washed with the same buffer solution. The filtrate drug contents were measured with the help of a double beam UV/Vis spectrophotometer at 332 nm. The entrapment efficiency and the percentage drug loading was calculated with the help of Equations (3) and (4) [29],

$$\text{Drug loading(\%)} = \frac{\text{Amount of drug in particles}}{\text{Amount of drug loaded particles}} \times 100, \tag{3}$$

$$\text{Entrapment efficiency(\%)} = \frac{\text{Actual loading}}{\text{Theoretical loading}} \times 100. \tag{4}$$

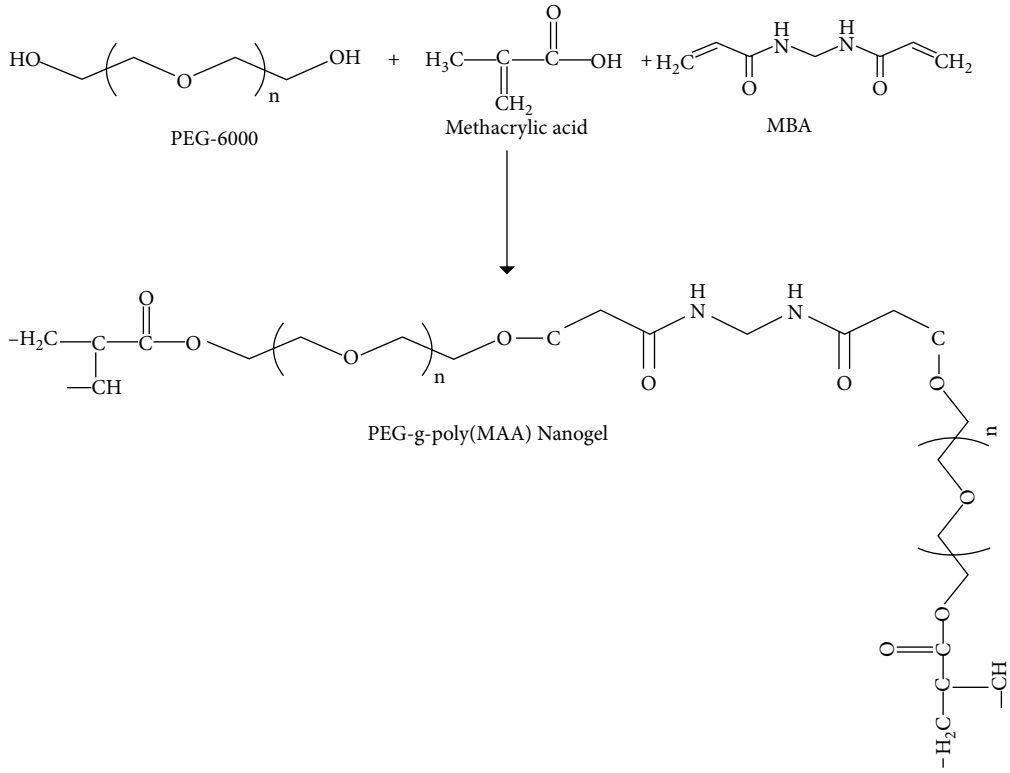

Figure 1: Proposed structure of PEG-g-poly (methacrylic acid) nanogels.

Table 1: Composition of PEG-g-poly (MAA) nanogels and calculation of sol–gel fraction.

Code	Ethylene glycol: MAA (mol)	Cross linker (% of total wt. of PEG + MAA)	Initiator (% of total wt. of PEG + MAA)	W_i (mg)	W_e (mg)	Sol fraction (%) $= \frac{W_i - W_e}{W_i} \times 100$	Gel fraction (%) = 100 − Sol fraction
N1	1:1	1	1	200	176	12	88
N2	2:1	1	1	200	162	19	81
N3	3 : 1	1	1	200	148	26	74
N4	1:2	1	1	200	181	9.5	90.5
N5	1:3	1	1	200	187	6.5	93.5
N6	1:4	1	1	200	191	4.4	95.5
N7	1:1	2	1	200	179	10.5	89.5
N8	1:1	3	1	200	186	7	93
N9	1:1	4	1	200	190.2	4.9	95.1

3.3. Sol–Gel Fraction Determination. The gel fraction of prepared formulations was determined with the help of the Soxhlet apparatus at 85°C for 12 hrs. Discs of hydrogel were cut into uniform small size slices, dried in a hot air oven at 50°C until constant weight and then subjected to extraction in distilled water. After the specified time, slices of hydrogel were taken off from the water and subjected to drying for 72 hrs at 50°C. By using the Equations (5) and (6), Sol fraction and gel fraction was calculated [30],

$$\text{Sol fraction} = \frac{M_i - M_e}{M_i} \times 100, \tag{5}$$

where M_i = initial mass, M_e = mass after extraction,

$$\text{Gel fraction} = 100 - \text{Sol fraction}. \tag{6}$$

3.4. Swelling Behaviour. Swelling index of the prepared formulations was studied in 0.1M buffer solutions of pH 1.2 and 6.8 while maintaining the temperature at 37°C. Weighed quantity of grafted nanogels particulate were taken in a tea bag and immersed in specified buffer solution. After a specific time interval the tea bags were removed from solution and excess of water was removed with the help of tissue paper and weighed on a weighing balance. This process was continued until constant weight. Degree of swelling (Q) of prepared formulations was calculated at different pH values by using Equation (7) [31],

$$Q = \frac{M_s}{M_d}, \tag{7}$$

where M_s = mass of swelled particles, M_d = mass of dried particles before immersing.

3.5. Micromeritic Properties. Micromeritic properties of prepared nanogels particulate system were determined in order to estimate the flow characteristics of formulations. Angle of repose, Bulk density, Tapped density, Carr's compressibility index, and Hausner's ratio was calculated as previously describe in study performed by Sarfraz et al. [25].

3.6. Particle Size Analysis. Average particle size of prepared nanogels particulate systems was evaluated with the help of particles size analyzer. For this purpose nanogels particulate systems were suspended in ultrapure water and particle size analysis was performed by the Particle size analyzer (Zetasizer Ver System; Malvern Instruments, Malvern, UK) using Dynamic Light Scattering (DLS) method [32, 33].

3.7. Zeta Potential Measurement. Measurement of Zeta potential of the drug loaded nanogels was also carried out in order to confirm the stability. Meanwhile, ionization of prepared formulation were also studied with the help of zeta potential.

3.8. FTIR Spectroscopy. FTIR spectra of PEG-6000, MAA, MBA, pure drug NPS, and drug loaded nanogels were measured between 400 and 4000 cm^{-1} with the help of IR spectrophotometer for the confirmation of grafting. For this purpose, samples were prepared by mixing the finely grounded prepared formulations with KBr and was placed on disc slit and the IR spectra was recorded [34].

3.9. Thermal Analysis. For the determination of thermal stability of ingredients in grafted nanogels, thermal analysis of individual ingredients and prepared formulations were performed through DSC and TGA. DSC of samples was performed under nitrogen environment by gradually applying heat stress from ambient to 400°C at the rate of 10°C/min while TGA analysis was performed in a temperature range of 0–800°C [25].

3.10. Powder X-Ray Diffraction Studies. Powder X-Ray diffraction studies of pure drug, polymers, and drug loaded formulations were performed and results were compared. Powder XRDs were calculated at 5–50°C at 2Θ in order to evaluate the crystalline or amorphous nature of the drug [35, 36].

3.11. In-Vitro Drug Release. A calibrated USP type-2 dissolution apparatus (Paddle apparatus) was used in order to perform the dissolution studies of drug loaded formulations at pH 1.2 and 6.8 respectively. 900 mL of each solution was used as a medium while maintaining the temperature at 37°C ± 0.2 and paddles speed at 50 rpm. At specified time intervals 5 mL of the samples were withdrawn and replaced with the same amount of fresh medium. The cumulative drug released was calculated by measuring the absorbance with the help of UV/Vis spectrophotometer at 332 nm. For each formulation, the same procedure was adopted to study the dissolution parameters [29].

3.12. Release Kinetics. By applying different model-dependent approaches, i.e. zero order, first order, Korsmeyer–Peppas and Higuchi, dissolution data from all prepared formulations were analyzed in order to study the kinetics of the drug release.

3.12.1. Zero-Order Model

$$M_t = K_o t. \tag{8}$$

In this equation, k_o represent the Zero-order rate constant while M_t is the amount of drug released at time t.

3.12.2. Higuchi Model. Where drug release is a function of square root of time, these systems are described under Higuchi model i.e. insoluble matrix,

$$M_t = K_H t^{1/2}, \tag{9}$$

where K_H represents the Higuchi rate constant.

3.12.3. Korsmeyer–Peppas Model. In order to evaluate the mode of drug release, the data of drug release were fitted to Korsmeyer–Peppas model as given,

$$\frac{M_t}{M_\infty} = K t^n, \tag{10}$$

where M_t/M_∞ = Fraction of drug released at time interval t, K = Rate constant of drug release, n = Drug release exponent.

The value of "n" calculated from this equation was used to describe the mode of drug release, as these are interrelated. If the value of "n" is greater than 0.89 then it is Super case-II transport, equal to 0.89, Case-II transport, between 0.45 and 0.89, Anomalous (nonFickian) diffusion or equal to 0.45, shows Fickian diffusion. All the data of dissolution studies was analyzed by using DD Solver [31, 36].

4. Results and Discussion

4.1. Sol–Gel Fraction. A decrease in gel fraction was observed while increasing the concentration of polymer (Table 1).

This reduction in gel fraction was observed because of the fact that when the concentration of the polymer increased, less cross linking took place that resulted in increase in un-reacted contents. Similar findings were reported in a study of Jalil et al. [30] where they synthesized the copolymer of sodium alginate and acrylic acid through free radical polymerization technique. They also reported the reduction in gel fraction with increase in concentration of polymer.

An increase in gel fraction was observed with increase in concentration of monomer or cross linking agent. This phenomenon was seen because of the fact that, an increase in proportion of monomer or cross linking agent resulted into more entanglement of polymer and monomer that led to higher degree of cross linking with less proportion of unreacted contents. These findings of our study also shown an agreement with a study performed by Sarfraz et al. [18] where they prepared hydrogel micro particles of β-cyclodextrin and methacrylic acid and reported an increase in gel fraction with increasing the proportion of monomer or cross linking agent.

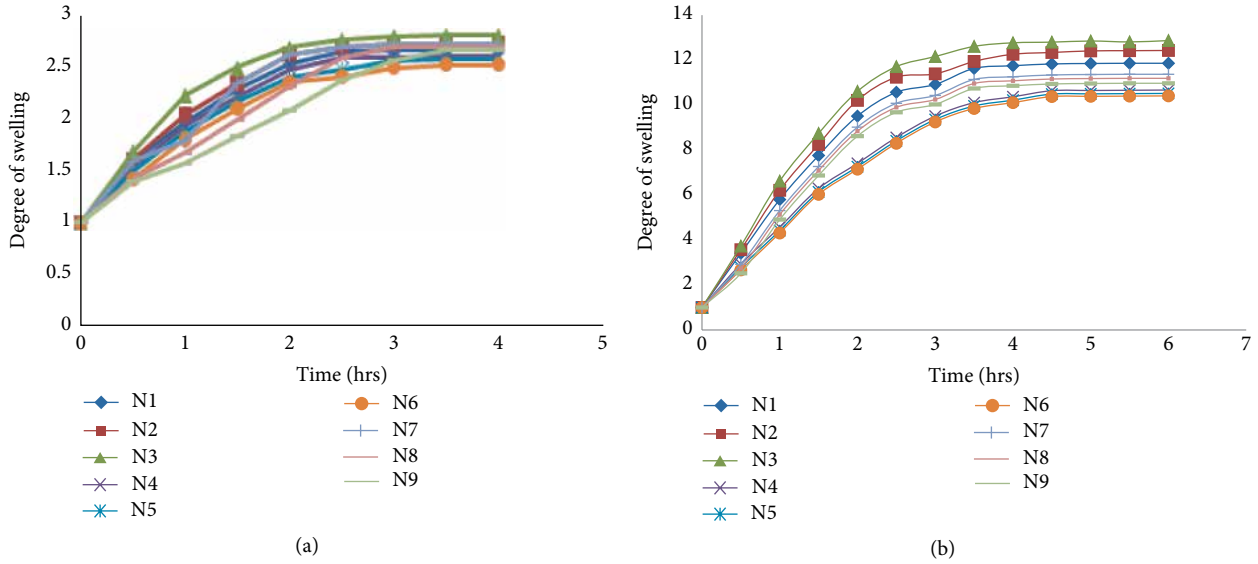

Figure 2: (a) Degree of swelling of formulation N1–N9 at pH 1.2. (b) Degree of swelling of formulation N1–N9 at pH 6.8.

Table 2: Entrapment efficiency and product yield of PEG-g-poly (MAA) nanogels.

Formulation	Entrapment efficiency (%)	Product yield (%)
N1	82.56 ± 0.24	90.00 ± 0.51
N2	82.87 ± 0.25	89.90 ± 0.27
N3	83.01 ± 0.23	92.00 ± 0.35
N4	84.89 ± 0.19	88.50 ± 0.42
N5	85.45 ± 0.18	87.10 ± 0.31
N6	88.40 ± 0.27	85.00 ± 0.32
N7	82.78 ± 0.21	87.10 ± 0.27
N8	81.98 ± 0.22	91.50 ± 0.21
N9	80.45 ± 0.27	87.70 ± 0.51

Average of three determinations, ±SD (standard deviation).

4.2. Swelling Behaviour. Prepared nanogels presented a pH dependent swelling behaviour as shown in Figures 2(a) and 2(b). At lower pH i.e. 1.2, formulation presented less swelling and appeared in condensed form. In acidic environment, due to high concentration of free hydrogen ions (H^+), carboxylic group of methacrylic acid (a weak acid) remain in unionized form as reported by Sarfraz et al. [18] and Elliot et al. [37]. Thus polymeric network remain in condensed form and less water is penetrated that lead to less swelling of nanogels.

At higher pH i.e. 6.8 a remarked increase in swelling was observed. This type of swelling behaviour was observed due to ionization of carboxylic group of methacrylic acid by releasing hydrogen ions (H^+) and thus attaining negative charge. Presence of successive negative charged groups resulted in activation of electrostatic repulsive forces that lead to the expansion of polymeric network and thus swelling of nanogels. Similar expansion of polymeric network was reported in a study performed by Tu et al. [38] due to ionization of the carboxylic group of the methacrylic acid at higher pH.

A decrease in swelling was observed when concentration of the monomer and cross linker was increased as shown in the case of formulations N4–N9. This decrease in swelling was seen because of the increase in cross linking density of formulations that resulted into decrease in water absorption capacity of nanogels and ultimately less swelling. A similar reduction in swelling with increasing the concentration of monomer was reported in studies performed by Rashid et al. [39] and Huang et al. [40]. Mahmood et al. [17] and Li and Mooney [41] also prepared methacrylic acid based hydrogel where with increase in concentration of monomer a decrease in swelling of hydrogel was observed.

4.3. Entrapment Efficiency and Product Yield. For the determination of efficiency of the prepared nanogels carrier systems, entrapment efficiency is considered as an important parameter. Results for entrapment efficiency of all prepared nanogels formulation is presented in Table 2 that ranges from 80.45% to 88.40%.

Results for product yield of all prepared nanogels were in the ranges of 85–92%. These results were in acceptable limit that depicted the good efficiency of process used for the synthesis of these formulations. These findings were in agreement with studies performed by Sarfraz et al. [25] and Mahmood et al. [31] where they prepared the β-cyclodextrin based hydrogel microparticulate system grafted with methacrylic acid and reported the good process efficiency as product yield was observed in the range of 85–93%.

4.4. Flow Properties. For formulations that are in powder form or particulate systems, determination of rheological parameters is very important in product development process. Materials with poor flow properties are not good candidates for use in solid dosage form thus may lead to improper mixing and loading of drugs as reported by Sarfraz et al. [18]. All the results for rheological parameters were found within pharmacopeial limits (Table 3). As the values of angle of repose ranged from 24.30θ to 28.9θ, (below 30) thus presented the good flow properties by all the prepared formulations. Similar results were reported in studies performed by Sarfraz et al. [25], Hafeezullah et al. [34], Singh and Sameer [42], and Minhas et al. [43].

Table 3: Results of micromeritics properties of formulations N1–N9.

Code	Bulk density (g/mL)	Tapped density (g/mL)	Angle of repose (θ)	Hausner's ratio	Carr's index (%)
N1	0.721	0.861	27.9	1.194	16.26
N2	0.642	0.743	26.5	1.157	13.59
N3	0.515	0.629	28.9	1.221	18.12
N4	0.701	0.831	26.8	1.186	15.64
N5	0.763	0.889	27.8	1.165	14.17
N6	0.804	0.963	26.4	1.198	16.51
N7	0.716	0.851	27.6	1.188	15.86
N8	0.749	0.872	28.1	1.164	14.10
N9	0.779	0.902	26.9	1.158	13.64

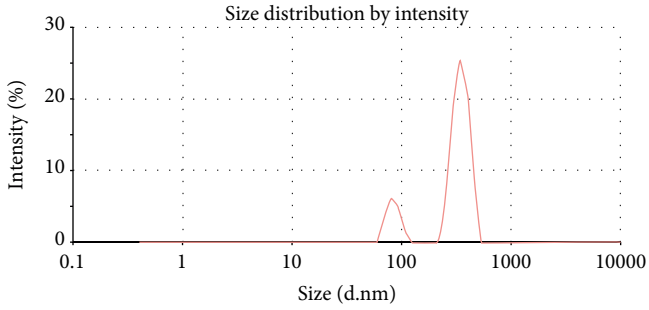

Figure 3: Average particles size of nanogels.

4.5. Particle Size Analysis. As depicted by peak size and peak area, particle size range for nanogels particulate system was 100–400 nm with maximum percentage at 300 nm (Figure 3). These results confirmed size of the prepared formulations in nano range as previously reported by Hamidi et al. [44] and Van Thienen et al. [45].

4.6. Zeta Potential. Zeta potential of prepared nanogels particulate system of formulation was neutral that demonstrate the stability of nanogels thus can be dispersed easily in aqueous media (Figure 4(a)). Results of this study also showed an agreement with a study performed by Tummala et al. [46] where they also reported the presence of net neutral charge on microparticulate system resulted into improvement in stability of the formulation.

When zeta potential of prepared formulations was studied at pH 6.8 (intestinal environment) it presented an increase in the value of zeta potential (Figure 4(b)). This increase in value of zeta potential is the indication of ionization of neutral surface of nanogels as previously reported by Cruz et al. [47] Presence of charges on the surface leads to electrostatic repulsion among similar charges and ultimately results into expansion of condensed structure.

4.7. FTIR Spectroscopic Analysis. Results for FTIR spectra is presented in Figures 5(a)–5(e). FTIR spectra of PEG-6000 presented the characteristic peaks at 1109 and 2870 cm^{-1} that was related to stretching of the ether group (C-O-C) and the alkyl group (R-CH_2) respectively. Absorption for hydroxyl group (OH) was indicated in the region of 3200–3300 cm^{-1} as reported previously by Mansur et al. [48]. FTIR spectra of MAA presented the characteristic peaks at 1708, 1635, and 2970 cm^{-1} that are corresponding to stretching of the carboxylic group (–C=O), double bond (C=C), and methyl group (–C–H) respectively. FTIR spectra of MBA presented the characteristic peaks at 1627 cm^{-1}, 1537 cm^{-1}, and 3228 that are related to stretching of the carbonyl group (C=O), amine group (NH), and methylene group (C=C–H) respectively.

FTIR spectra of grafted copolymeric nanogels of PEG-6000 (PEG-g-poly (MAA) presented the different absorption pattern as compared to individual ingredients. Disappearance of the absorption peak in region of 3200–3300 cm^{-1} and addition of new absorption peak in region of 1720–1730 cm^{-1} was observed that was corresponding to the involvement of the hydroxyl groups (OH) of PEG in the grafting process and addition of the carbonyl group (C=O) from monomer, MAA respectively. Results of this study also supported by findings of the study performed by Sarfraz et al. [25] where they prepared the β-CD-g-poly (MAA) hydrogels and confirmed the grafting process of copolymeric network system through disappearance of the characteristic peaks of the functional groups involved in the cross linking process.

FTIR spectra of naproxen sodium presented the absorption peaks at 1033 cm^{-1}, 1571 cm^{-1}, and 1670 cm^{-1} that were corresponding to the ether group (–OR), aromatic benzene ring, and carbonyl group (C=O) respectively. FTIR spectra of drug loaded formulations were also recorded and compare with spectra of the pure drug. This comparative analysis indicated that the drug (Naproxen) is in intact form as major peaks were in their original position i.e. 1033 cm^{-1} and 1571 cm^{-1} as in pure drug and the drug is physically entrapped in nanogels particulate systems as previously reported by Minhas et al. [43].

4.8. Thermal Analysis. Results for thermal analysis are presented in Figures 6(a) and 6(b). TGA curve of PEG presented an initial weight loss at 200°C that was because of the loss of moisture that presented a gradual mass loss and at 352°C only 12% mass of PEG was left. Similarly TGA curve of MBA showed the gradual mass loss at 187.64°C, 226.51°C, and 344.52°C. When degradation pathway of PEG-g-poly (MAA) nanogels (N3) was studied it showed the more thermal stability as compared to individual ingredients and even at higher temperature i.e. 401°C only 64% loss of mass occurred.

This improved thermal stability of prepared nanogels formulation also confirmed the grafting and development of copolymeric network systems that ultimately provided the targeted release of drug. Finding of TGA analysis also shown an agreement with the study performed by Mahmood et al. [17] and Chen et al. [49] where they confirmed the formation of the complex by improved thermal stability of chitosan based hydrogel.

A clear difference was observed in DSC thermogram of individual ingredients and nanogels formulations Figure 6(b). In DSC thermogram of PEG and MBA a specific pattern of endothermic peaks at 280°C and 212°C was observed that is followed by exothermic peaks at 358°C and 362°C respectively that indicating the loss of moisture content followed by thermal

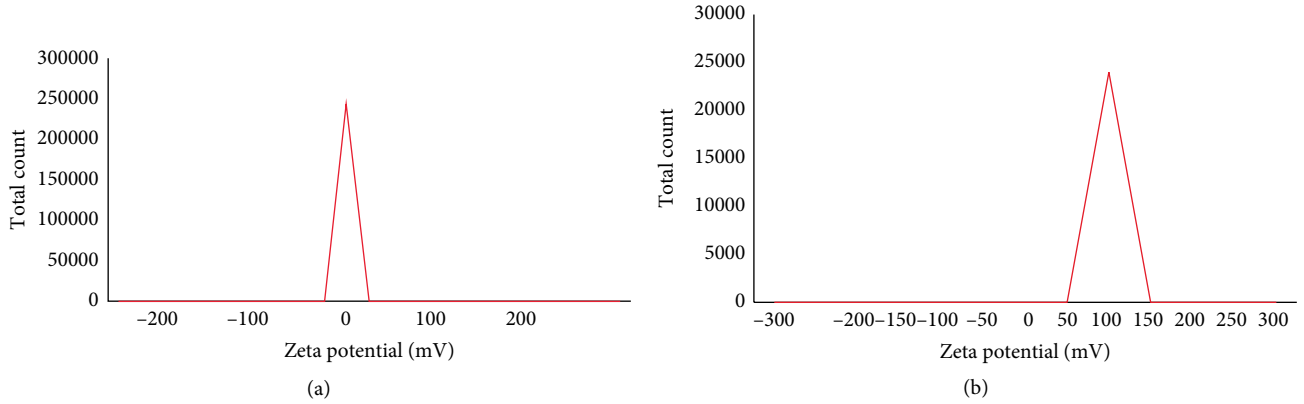

Figure 4: (a) Zeta potential measurement of nanogels in distilled water. (b) Zeta potential measurement of nanogels at pH 6.8.

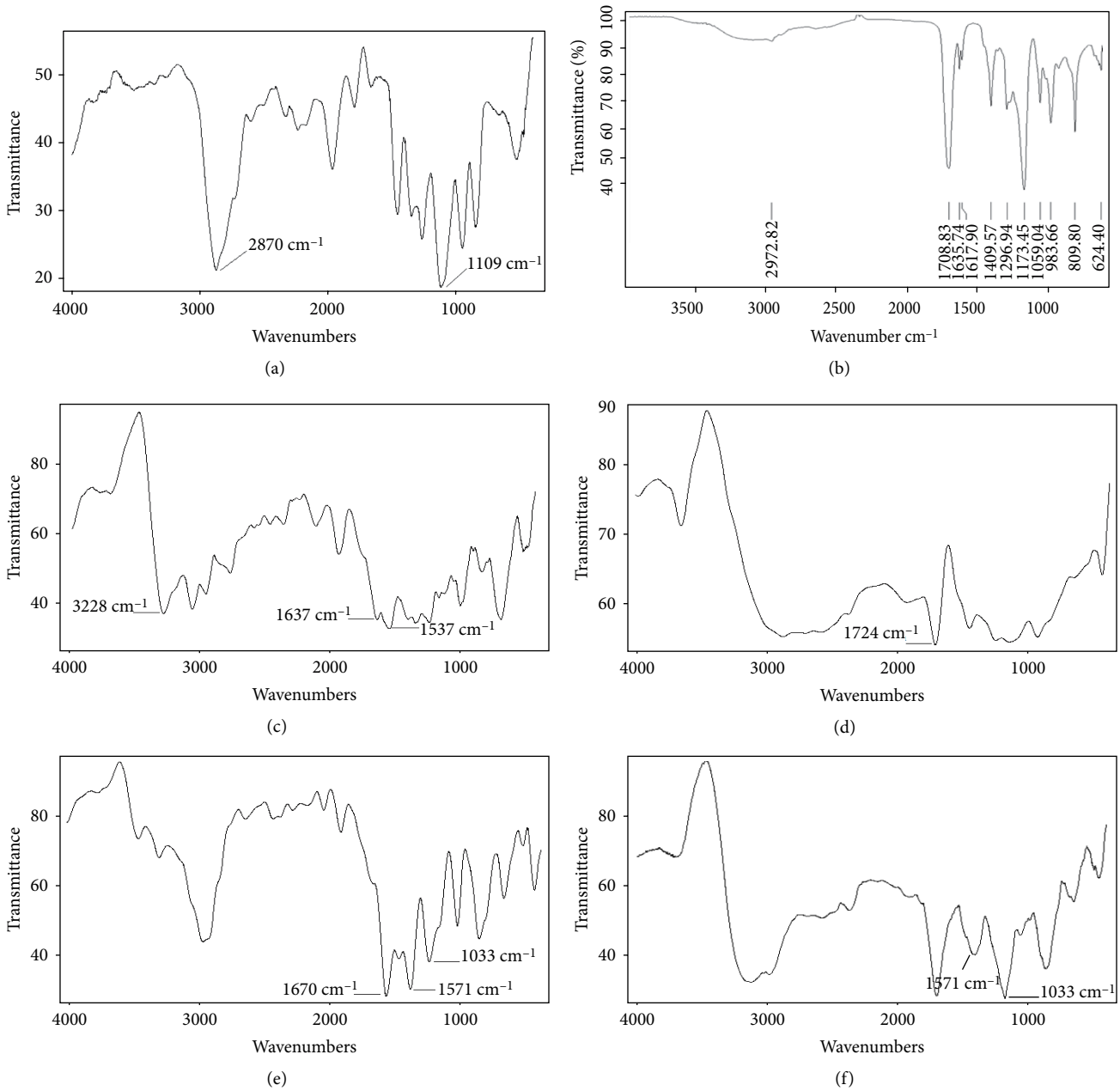

Figure 5: (a) FTIR spectra of PEG. (b) FTIR spectra of methacrylic acid. (c) FTIR spectra of MBA. (d) FTIR spectra of PEG-p (MAA). (e) FTIR spectra of naproxen sodium. (f) FTIR spectra of drug loaded nanogels.

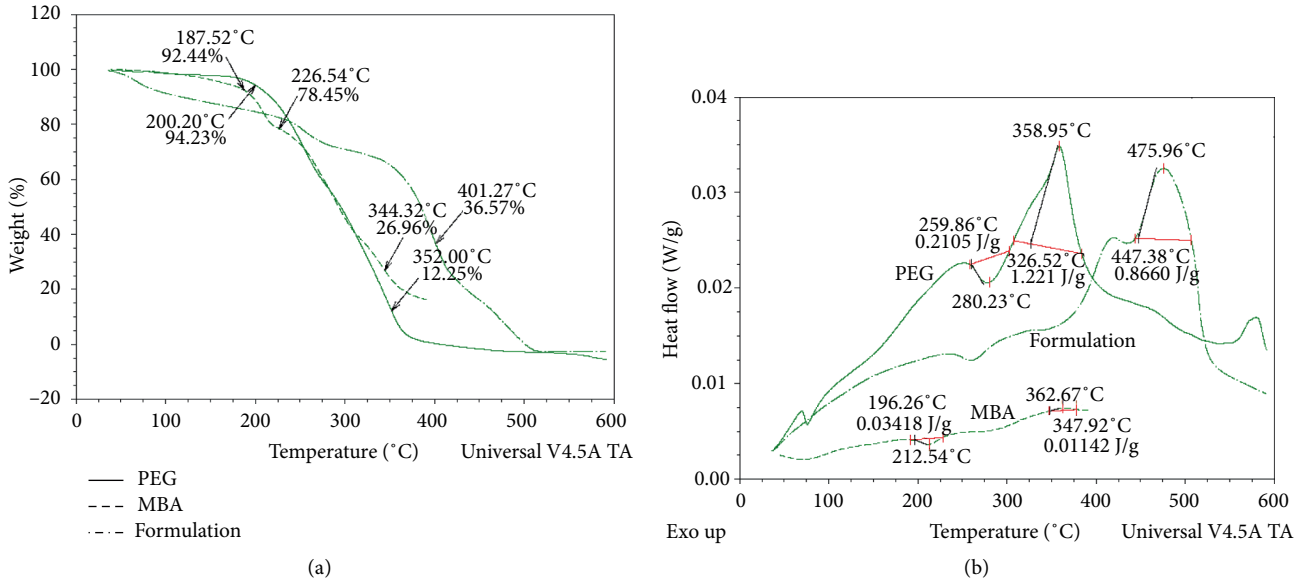

FIGURE 6: (a) TGA thermogram of PEG-6000, MBA, and PEG-g-poly (MAA) nanogels. (b) DSC thermogram of PEG-6000, MAA, and PEG-g-poly (MAA).

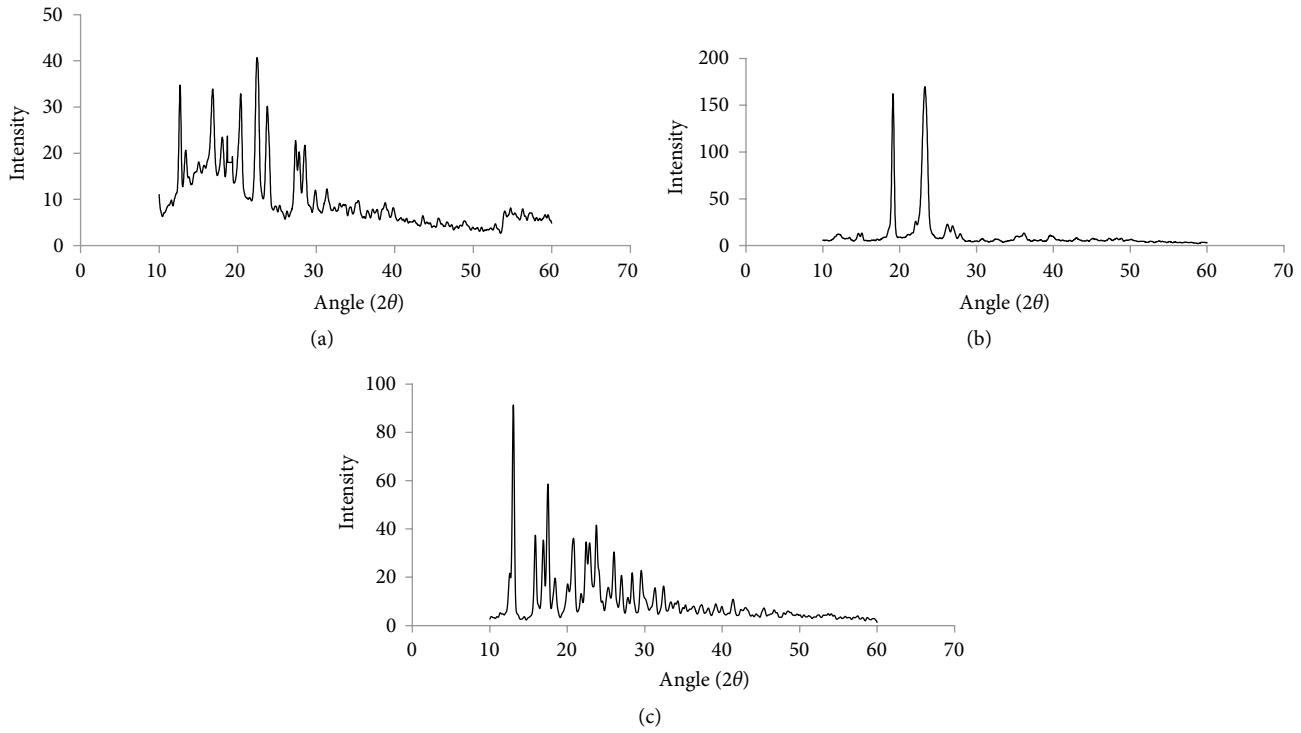

FIGURE 7: (a) XRD pattern of drug loaded PEG-g-poly (MAA) nanogels. (b) XRD pattern of PEG-6000. (c) XRD pattern of naproxen sodium.

degradation. While in DSC thermogram of nanogels formulations, endothermic peaks were present at 400°C followed by exothermic peaks at 475°C. This shifting of peaks toward higher temperature also confirmed the grafting and development of rigid copolymeric network systems. Similar result was reported in studies performed by Anwar et al. [50] where they prepared the alginate-PVA polymeric network systems and confirmed the grafting by indicating the shifting of exothermic peaks towards higher temperature. In another study performed by Jayaramudu et al. [51] improvement in thermal stability of PEG-6000 was reported when complexed with silver.

Thermal analysis of prepared formulation presented a better thermal stability as compared to individual ingredients that proposed a condensed structure for prepared nanogels. Such a condensed structure of prepared nanogels provided a better tool for targeted delivery of loaded drug.

Table 4: Models of *in-vitro* drug release kinetics of PEG-g-poly (MAA) nanogels formulations with varying concentration of polymer, PEG.

Model	Parameters	N1		N2		N3	
		pH 1.2	pH 6.8	pH 1.2	pH 6.8	pH 1.2	pH 6.8
Zero order	K_o	4.262	35.134	4.407	36.090	4.547	36.242
	R^2	0.6392	0.8944	0.5577	0.8602	0.4472	0.8848
First order	K_1	0.045	0.699	0.047	0.755	0.049	0.744
	R^2	0.6745	0.9714	0.5985	0.9705	0.4943	0.9606
Higuchi	K_H	6.473	52.002	6.724	53.646	6.975	53.691
	R^2	0.9707	0.9370	0.9526	0.9381	0.9195	0.9353
Korsmeyer Peppas	K_{Kp}	7.019	46.224	7.523	49.275	8.087	48.119
	R^2	0.9891	0.9598	0.9910	0.9510	0.9927	0.9551
	n	0.380	0.667	0.333	0.621	0.278	0.656

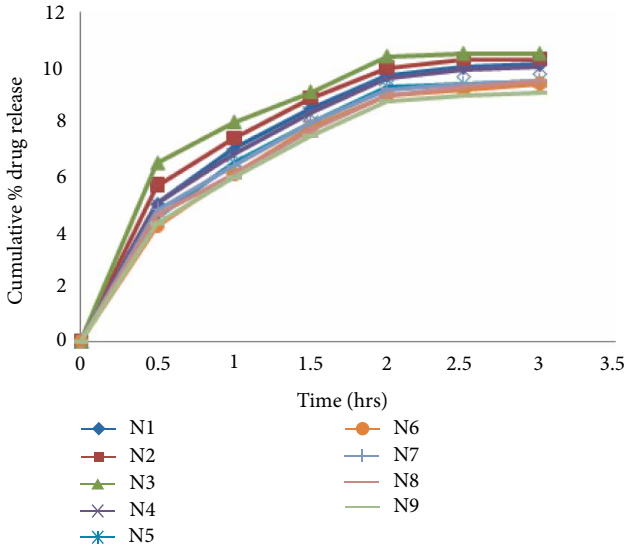

Figure 8: Cumulative percentage drug release from formulation (N1–N9) at pH 1.2.

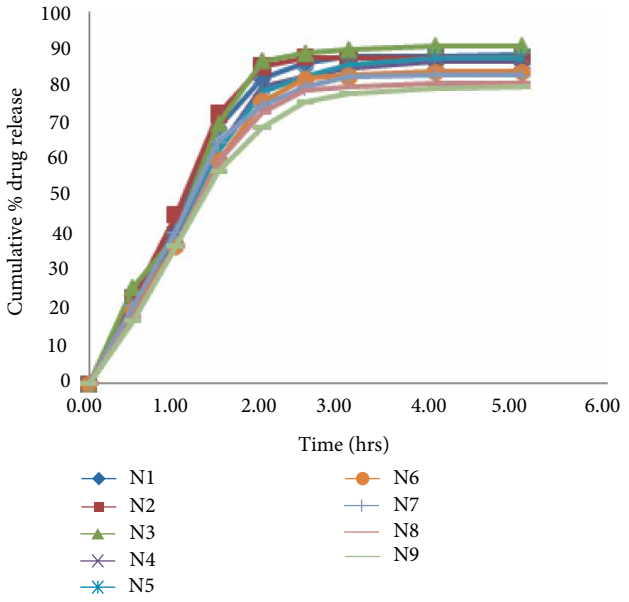

Figure 9: Cumulative percentage drug release from formulation (N1–N9) at pH 6.8.

4.9. Powder X-Rays Diffraction Studies. The diffractograms of pure drug presented the sharp peak at $2\theta = 13.04°$ and 17.5° while PEG-6000 at $2\theta = 19.1°$ that indicated the crystalline nature of these ingredients (Figures 7(a)–7(c)). There was no sharp peak in diffractograms of the nanogels copolymeric network that predicted the amorphous nature of these copolymeric network systems. Conversion of crystalline structure of polymers into amorphous form also confirmed the development of the grafted copolymeric networks. Similarly no sharp peaks were observed in diffraction patterns of the drug loaded nanogels that indicated the conversion of crystalline nature of naproxen sodium to amorphous nature. Conversion of crystalline nature of naproxen sodium into amorphous nature is also effective in the reduction of damaging effects of the drug to gastric mucosa as reported by Bodmeier and Chen [12].

4.10. In-Vitro Drug Release. A pH depended pattern of drug release was observed from prepared formulation as presented in Figures 8 and 9. Nanogels presented the drug release in the range of 8.2–10.5% at pH 1.2, while at higher pH i.e. 6.8, drug release is much high that is ranging from 80% to 91%. Maximum drug release was presented by formulation PM3 that was 91%. Such pH dependant release from these formulations was observed due to pH dependant swelling of these formulations. As at acidic pH, nanogels remain in collapse condition thus small amount of encapsulated drug was released but at pH 6.8, (intestinal pH) swelling of nanogels occurred that lead to higher release of drug. Such type of pH dependant pattern of drug release of this copolymeric network system made it a suitable candidate for gastro protective delivery of naproxen sodium as less drug was release in stomach pH and maximum drug was released at intestinal pH. Similar drug release was reported in studies performed by Peppas et al. [22] where they reported the gastro-protective delivery of insulin by using PMAA-g-EG nanogels carrier system. In another study performed by Sarfraz et al. [18], similar pH dependant release of rosuvastatin calcium was reported from β-cyclodextrin based hydrogel polymeric network system grafted with methacrylic acid.

Table 5: Models of *in-vitro* drug release kinetics of PEG-g-poly (MAA) nanogels formulations with varying concentration of MAA.

Model	Parameters	N4		N5		N6	
		pH 1.2	pH 6.8	pH 1.2	pH 6.8	pH 1.2	pH 6.8
Zero order	K_o	4.207	33.714	4.015	33.648	3.916	32.659
	R^2	0.6483	0.9085	0.6619	0.9220	0.7094	0.9237
First order	K_1	0.045	0.640	0.043	0.631	0.041	0.598
	R^2	0.6826	0.9736	0.6941	0.9693	0.7381	0.9756
Higuchi	K_H	6.386	49.800	6.090	49.572	5.922	48.145
	R^2	0.9731	0.9351	0.9711	0.9285	0.9792	0.9349
Korsmeyer Peppas	K_{Kp}	6.907	43.554	6.526	42.418	6.213	41.418
	R^2	0.9901	0.9634	0.9840	0.9648	0.9851	0.9691
	n	0.384	0.690	0.398	0.720	0.430	0.713

Table 6: Models of *in-vitro* drug release kinetics of PEG-g-poly (MAA) nanogels formulations with varying concentration of MBA.

Model	Parameters	N7		N8		N9	
		pH 1.2	pH 6.8	pH 1.2	pH 6.8	pH 1.2	pH 6.8
Zero order	K_o	4.009	32.813	3.943	31.626	3.815	30.462
	R^2	0.6420	0.8898	0.6917	0.9162	0.6872	0.9252
First order	K_1	0.042	0.619	0.042	0.567	0.040	0.529
	R^2	0.6749	0.9839	0.7214	0.9783	0.7163	0.9850
Higuchi	K_H	6.088	48.658	5.969	46.659	5.777	44.922
	R^2	0.9703	0.9486	0.9809	0.9335	0.9773	0.9393
Korsmeyer Peppas	K_{Kp}	6.595	43.932	6.341	40.401	6.134	38.761
	R^2	0.9881	0.9665	0.9905	0.9654	0.9867	0.9726
	n	0.382	0.646	0.411	0.704	0.412	0.708

Table 7: Comparison between swelling of all formulation at pH 1.2 and pH 6.8.

Code	Varying pH	Mean ± SEM	p-value	Sig. difference
N1	Degree of swelling at pH 1.2	2.36069 ± 0.15	0.0012	Yes
	Degree of swelling at pH 6.8	8.5308 ± 0.93		
N2	Degree of swelling at pH 1.2	2.41985 ± 0.15	0.0034	Yes
	Degree of swelling at pH 6.8	8.9151 ± 0.95		
N3	Degree of swelling at pH 1.2	2.50485 ± 0.15	0.0031	Yes
	Degree of swelling at pH 6.8	9.3701 ± 0. 93		
N4	Degree of swelling at pH 1.2	2.3103 ± 0. 15	0.0015	Yes
	Degree of swelling at pH 6.8	9.8958 ± 0.834		
N5	Degree of swelling at pH 1.2	2.2695 ± 0. 15	0.0012	Yes
	Degree of swelling at pH 6.8	10.389 ± 0. 93		
N6	Degree of swelling at pH 1.2	2.2109 ± 0. 15	0.0011	Yes
	Degree of swelling at pH 6.8	10.856 ± 0.829		
N7	Degree of swelling at pH 1.2	2.3993 ± 0. 15	0.0013	Yes
	Degree of swelling at pH 6.8	8.0408 ± 0. 96		
N8	Degree of swelling at pH 1.2	2.3023 ± 0. 15	0.0012	Yes
	Degree of swelling at pH 6.8	7.8608 ± 0. 94		
N9	Degree of swelling at pH 1.2	2.2230 ± 0. 15	0.0011	Yes
	Degree of swelling at pH 6.8	7.6408 ± 0.857		

4.11. Release Kinetics. Results for *in-vitro* drug release kinetics are presented in Tables 4–6. When dissolution data was evaluated with Higuchi model, results of drug release found the best fit model to regression line with values of R^2 more close to one. On the basis of these observations it was concluded that the best fit model for the mechanism of drug release from nanogels carrier systems was Higuchi model as value of R^2 was found more close to one at both pH values.

Table 8: Comparison between drug release of all formulation at pH 1.2 and pH 6.8.

Code	Varying pH	Mean ± SEM	p-value	Sig. difference
N1	Drug release at pH 1.2	6.7 ± 1.5	0.001	Yes
	Drug release at pH 6.8	62 ± 11		
N2	Drug release at pH 1.2	7.05 ± 1.6	0.001	Yes
	Drug release at pH 6.8	64.3 ± 11		
N3	Drug release at pH 1.2	7.42 ± 1.6	0.001	Yes
	Drug release at pH 6.8	64.9 ± 11		
N4	Drug release at pH 1.2	7.09 ± 1.4	0.001	Yes
	Drug release at pH 6.8	51.5 ± 9.2		
N5	Drug release at pH 1.2	6.74 ± 1.3	0.001	Yes
	Drug release at pH 6.8	51.1 ± 9.4		
N6	Drug release at pH 1.2	6.53 ± 1.3	0.001	Yes
	Drug release at pH 6.8	49.5 ± 8.9		
N7	Drug release at pH 1.2	6.76 ± 1.3	0.001	Yes
	Drug release at pH 6.8	50.6 ± 8.8		
N8	Drug release at pH 1.2	6.6 ± 1.3	0.001	Yes
	Drug release at pH 6.8	48.3 ± 8.7		
N9	Drug release at pH 1.2	6.39 ± 1.3	0.001	Yes
	Drug release at pH 6.8	46.5 ± 8.4		

On the basis of values of "n" it was concluded that all formulation follow anomalous i.e. dual mode of drug release (non-Fickian diffusion) as values of "n" lying between 0.45 and 0.89 for all formulations.

4.12. Statistical Analysis of Swelling Behaviour and Drug Release. Swelling data and drug release data was also analysed statistically by using Minitab software and results are presented in Tables 7 and 8.

From statistical analysis it was concluded that a significance difference in drug release was observed for all formulation at different pH values. These results also justified that prepared formulations are pH sensitive in nature.

5. Conclusion

In the current study copolymeric nanogels carrier systems were formulated for gastro-protective delivery of naproxen sodium. Polyethylene glycol was grafted with varying concentration of a monomer, methacrylic acid respectively through free radical polymerization technique. Nanogels carrier systems presented the pH dependent swelling behaviour with maximum swelling index at higher pH i.e. 6.8. PXRD studies of drug loaded formulation indicated the amorphous nature of carrier systems and loaded drug irrespective to the crystalline nature of individual ingredients that is effective in the improvement in the bioavailability as well as reduced irritant effect of the drug to the mucosal membrane of GIT. Nanogels carrier systems also presented the pH dependent drug release with maximum release at a higher pH i.e. 6.8 and less release at a lower pH i.e. 1.2 thus by-passed the acidic environment for drug release. On the basis of these investigation, it was concluded that these nanogels carrier systems proved to be an effective tool for the gastro-protective delivery of drug molecules that are gastric irritant like naproxen sodium. Further studies are required for the evaluation of *in-vivo* safety and efficacy of prepared nanogels carrier system in order to establish a safe, effective, and economic gastro-protective oral drug delivery system for gastric irritant drugs.

Data Availability

Data should be available openly.

Conflicts of Interest

The authors declare that they have no conflicts of interest.

References

[1] C. S. Sean and B. Paul, Ed., *Martindale, The Complete Drug Reference*, pp. 1693–1699, Pharmaceutical Press, London, 36th edition, 2009.

[2] B. K. Alldredge, R. L. Corelli, M. E. Ernst et al., *Koda-kimble and Young's Applied Therapeutics: The Clinical Use of Drugs*, pp. 661–667, Wolters Kluwer Health Adis (ESP), Alphen aan den Rijn, Netherlands, 10th edition, 2013.

[3] A. H. Soll, K. John, and J. E. McGuigan, "Ulcers, nonsteroidal antiinflammatory drugs, and related matters," *Gastroenterology*, vol. 96, no. 2, pp. 561–568, 1989.

[4] D. L. Earnest, "NSAID-induced gastric injury: its pathogenesis and management," *Seminars in Arthritis and Rheumatism*, vol. 19, no. 4 Suppl 2, pp. 6–10, 1990.

[5] G. G. Liversidge and P. Conzentino, "Drug particle size reduction for decreasing gastric irritancy and enhancing absorption of naproxen in rats," *International Journal of Pharmaceutics*, vol. 125, no. 2, pp. 309–313, 1995.

[6] A. Lanas and F. Sopeña, "Nonsteroidal anti-inflammatory drugs and lower gastrointestinal complications," *Gastroen-*

terology Clinics of North America, vol. 38, no. 2, pp. 333–352, 2009.

[7] V. R. Shanbhag, A. M. Crider, R. Gokhale, A. Harpalani, and M. D. Ronald, "Ester and amide prodrugs of ibuprofen and naproxen: synthesis, anti-inflammatory activity, and gastrointestinal toxicity," *Journal of Pharmaceutical Sciences*, vol. 81, no. 2, pp. 149–154, 1992.

[8] P. C. Sharma, S. Yadav, R. Pahwa, D. Kaushik, and S. Jain, "Synthesis and evaluation of novel prodrugs of naproxen," *Medicinal Chemistry Research*, vol. 20, no. 5, pp. 648–655, 2011.

[9] J. Sharma, A. K. Singla, and S. Dhawan, "Zinc–naproxen complex: synthesis, physicochemical and biological evaluation," *International Journal of Pharmaceutics*, vol. 260, no. 2, pp. 217–227, 2003.

[10] R. C. Mundargi, S. A. Patil, P. V. Kulkarni, N. N. Mallikarjuna, and T. M. Aminabhavi, "Sequential interpenetrating polymer network hydrogel microspheres of poly (methacrylic acid) and poly (vinyl alcohol) for oral controlled drug delivery to intestine," *Journal of Microencapsulation*, vol. 25, no. 4, pp. 228–240, 2008.

[11] I. Khalid, M. Ahmad, M. Usman Minhas, K. Barkat, and M. Sohail, "Cross-linked sodium alginate-g-poly (acrylic acid) structure: a potential hydrogel network for controlled delivery of loxoprofen sodium," *Advances in Polymer Technology*, vol. 37, no. 4, pp. 985–995, 2018.

[12] R. Bodmeier and H. Chen, "Preparation and characterization of microspheres containing the anti-inflammatory agents, indomethacin, ibuprofen, and ketoprofen," *Journal of Controlled Release*, vol. 10, no. 2, pp. 167–175, 1989.

[13] N. H. Stacey and C. Winder, "Toxicity of organic solvents," *Occupational Toxicology*, pp. 364–389, CRC Press, Boca Raton, FL, USA, 2004.

[14] L. Liu, W. D. Yao, Y. F. Rao, X. Y. Lu, and J. Q. Gao, "pH-responsive carriers for oral drug delivery: challenges and opportunities of current platforms," *Drug Delivery*, vol. 24, no. 1, pp. 569–581, 2017.

[15] A. V. Kabanov and S. V. Vinogradov, "Nanogels as pharmaceutical carriers: finite networks of infinite capabilities," *Angewandte Chemie International Edition*, vol. 48, no. 30, pp. 5418–5429, 2009.

[16] H. Q. Wu and C. C. Wang, "Biodegradable smart nanogels: a new platform for targeting drug delivery and biomedical diagnostics," *Langmuir*, vol. 32, no. 25, pp. 6211–6225, 2016.

[17] A. Mahmood, M. Ahmad, R. M. Sarfraz, and M. U. Minhas, "Development of acyclovir loaded β-cyclodextrin-g-poly methacrylic acid hydrogel microparticles: an *in vitro* characterization," *Advances in Polymer Technology*, vol. 37, no. 3, pp. 697–705, 2018.

[18] R. M. Sarfraz, M. Ahmad, A. Mahmood, and H. Ijaz, "Development, *in vitro* and *in vivo* evaluation of pH responsive β-CD-comethacrylic acid-crosslinked polymeric microparticulate system for solubility enhancement of rosuvastatin calcium," *Polymer-Plastics Technology and Engineering*, vol. 57, no. 12, pp. 1175–1187, 2018.

[19] J. P. K. Tan, A. Q. F. Zeng, C. C. Chang, and K. C. Tam, "Release kinetics of procaine hydrochloride (PrHy) from pH-responsive nanogels: theory and experiments," *International Journal of Pharmaceutics*, vol. 357, no. 1-2, pp. 305–313, 2008.

[20] I. Neamtu, A. G. Rusu, A. Diaconu, L. E. Nita, and A. P. Chiriac, "Basic concepts and recent advances in nanogels as carriers for medical applications," *Drug Delivery*, vol. 24, no. 1, pp. 539–557, 2017.

[21] C. W. Park, H. M. Yang, H. J. Lee, and J. D. Kim, "Core–shell nanogel of PEG–poly (aspartic acid) and its pH-responsive release of rh-insulin," *Soft Matter*, vol. 9, no. 6, pp. 1781–1788, 2013.

[22] N. A. Peppas, B. K. Kelley, T. L. Madeline, and A. M. Lowman, "Poly (ethylene glycol)-containing hydrogels in drug delivery," *Journal of Controlled Release*, vol. 62, no. 1-2, pp. 81–87, 1999.

[23] N. A. Peppas, "Devices based on intelligent biopolymers for oral protein delivery," *International Journal of Pharmaceutics*, vol. 277, no. 1-2, pp. 11–17, 2004.

[24] F. Zaaeri, M. Khoobi, M. Rouini, and H. A. Javar, "pH-responsive polymer in a core–shell magnetic structure as an efficient carrier for delivery of doxorubicin to tumor cells," *International Journal of Polymeric Materials and Polymeric Biomaterials*, vol. 67, no. 16, pp. 967–977, 2018.

[25] R. M. Sarfraz, M. Ahmad, A. Mahmood, M. U. Minhas, and A. Yaqoob, "Development and evaluation of rosuvastatin calcium based microparticles for solubility enhancement: an *in vitro* study," *Advances in Polymer Technology*, vol. 36, no. 4, pp. 433–441, 2017.

[26] A. M. Lowman, M. Morishita, M. Kajita, T. Nagai, and N. A. Peppas, "Oral delivery of insulin using pH-responsive complexation gels," *Journal of Pharmaceutical Sciences*, vol. 88, no. 9, pp. 933–937, 1999.

[27] S. Sajeesh and C. P. Sharma, "Interpolymer complex microparticles based on polymethacrylic acid-chitosan for oral insulin delivery," *Journal of Applied Polymer Science*, vol. 99, no. 2, pp. 506–512, 2006.

[28] B. K. Deka and T. K. Maji, "Effect of coupling agent and nanoclay on properties of HDPE, LDPE, PP, PVC blend and Phargamites karka nanocomposite," *Composites Science and Technology*, vol. 70, no. 12, pp. 1755–1761, 2010.

[29] M. Sohail, M. Ahmad, M. U. Minhas, L. Ali, I. Khalid, and H. Rashid, "Controlled delivery of valsartan by cross-linked polymeric matrices: synthesis, *in vitro* and *in vivo* evaluation," *International Journal of Pharmaceutics*, vol. 487, no. 1-2, pp. 110–119, 2015.

[30] A. Jalil, S. Khan, F. Naeem et al., "The structural, morphological and thermal properties of grafted pH-sensitive interpenetrating highly porous polymeric composites of sodium alginate/acrylic acid copolymers for controlled delivery of diclofenac potassium," *Designed Monomers and Polymers*, vol. 20, no. 1, pp. 308–324, 2017.

[31] A. Mahmood, M. Ahmad, R. M. Sarfraz, and M. U. Minhas, "β-CD based hydrogel microparticulate system to improve the solubility of acyclovir: optimization through *in-vitro, in-vivo* and toxicological evaluation," *Journal of Drug Delivery Science and Technology*, vol. 36, pp. 75–88, 2016.

[32] N. T. T. Huyen, N. H. Nhung, L. Thanh, P. D. Khanh, T. D. Lam, and H. A. Son, "Preparation and characterization of zerovalent iron nanoparticles," *Vietnam Journal of Chemistry*, vol. 56, no. 2, pp. 226–230, 2018.

[33] T. Di Francesco and G. Borchard, "A robust and easily reproducible protocol for the determination of size and size distribution of iron sucrose using dynamic light scattering," *Journal of Pharmaceutical and Biomedical Analysis*, vol. 152, pp. 89–93, 2018.

[34] K. Hafeezullah, A. Mahmood, S. Maheen et al., "Formulation and *in vitro* evaluation of novel antidiabetic orodispersible tablets using kyron-T134 and crosscaramellose sodium as superdisintegrants," *Lattin Aerican Journal of Pharmacy*, vol. 33, no. 4, pp. 631–639, 2014.

[35] R. M. Sarfraz, H. U. Khan, A. Mahmood, M. Ahmad, S. Maheen, and M. Sher, "Formulation and evaluation of mouth disintegrating tablets of atenolol and atorvastatin," *Indian Journal of Pharmaceutical Sciences*, vol. 77, no. 1, p. 83, 2015.

[36] S. Khan, M. Ahmad, G. Murtaza et al., "Formulation of nimesulide floating microparticles using low-viscosity hydroxypropyl methylcellulose," *Tropical Journal of Pharmaceutical Research*, vol. 9, no. 3, 2010.

[37] J. E. Elliott, M. Macdonald, J. Nie, and C. N. Bowman, "Structure and swelling of poly (acrylic acid) hydrogels: effect of pH, ionic strength, and dilution on the crosslinked polymer structure," *Polymer*, vol. 45, no. 5, pp. 1503–1510, 2004.

[38] H. Tu, Y. Yu, J. Chen et al., "Highly cost-effective and high-strength hydrogels as dye adsorbents from natural polymers: chitosan and cellulose," *Polymer Chemistry*, vol. 8, no. 19, pp. 2913–2921, 2017.

[39] H. Rashid, M. Ahmad, M. U. Minhas, M. Sohail, and M. F. Aamir, "Synthesis and characterization of poly (hydroxyethyl methacrylate-co-methacrylic acid) cross linked polymeric network for the delivery of analgesic agent," *Journal of the Chemical Society of Pakistan*, vol. 37, no. 5, pp. 999–1007, 2015.

[40] S. Huang, J. Wang, and Q. Shang, "Development and evaluation of a novel polymeric hydrogel of sucrose acrylate-co-polymethylacrylic acid for oral curcumin delivery," *Journal of Biomaterials Science, Polymer Edition*, vol. 28, no. 2, pp. 194–206, 2017.

[41] J. Li and D. J. Mooney, "Designing hydrogels for controlled drug delivery," *Nature Reviews Materials*, vol. 1, no. 12, p. 16071, 2016.

[42] S. K. Singh and A. A. Sameer, "Development and characterization of sublingual tablet of Lisinopril," *Asian Pacific Journal of Tropical Biomedicine*, vol. 2, no. 3, pp. S1711–S1719, 2012.

[43] M. U. Minhas, M. Ahmad, L. Ali, and M. Sohail, "Synthesis of chemically cross-linked polyvinyl alcohol-co-poly (methacrylic acid) hydrogels by copolymerization; a potential graft-polymeric carrier for oral delivery of 5-fluorouracil," *DARU Journal of Pharmaceutical Sciences*, vol. 21, no. 1, p. 44, 2013.

[44] M. Hamidi, A. Azadi, and P. Rafiei, "Hydrogel nanoparticles in drug delivery," *Advanced Drug Delivery Reviews*, vol. 60, no. 15, pp. 1638–1649, 2008.

[45] T. G. Van Thienen, J. Demeester, and S. C. De Smedt, "Screening poly (ethyleneglycol) micro-and nanogels for drug delivery purposes," *International Journal of Pharmaceutics*, vol. 351, no. 1-2, pp. 174–185, 2008.

[46] S. Tummala, M. N. S. Kumar, and A. Prakash, "Formulation and characterization of 5-Fluorouracil enteric coated nanoparticles for sustained and localized release in treating colorectal cancer," *Saudi Pharmaceutical Journal*, vol. 23, no. 3, pp. 308–314, 2015.

[47] D. L. Cruz, E. Francisco, Y. Zheng et al., "Zeta potential of modified multi-walled carbon nanotubes in presence of poly (vinyl alcohol) hydrogel," *International Journal of Electrochemical Sciences*, vol. 7, pp. 3577–3590, 2012.

[48] H. S. Mansur, R. L. Oréfice, and A. A. P. Mansur, "Characterization of poly (vinyl alcohol)/poly (ethylene glycol) hydrogels and PVA-derived hybrids by small-angle X-ray scattering and FTIR spectroscopy," *Polymer*, vol. 45, no. 21, pp. 7193–7202, 2004.

[49] C. Chang, Z. C. Wang, C. Y. Quan et al., "Fabrication of a novel pH-sensitive glutaraldehyde cross-linked pectin nanogel for drug delivery," *Journal of Biomaterials Science, Polymer Edition*, vol. 18, no. 12, pp. 1591–1599, 2007.

[50] H. Anwar, M. Ahmad, M. U. Minhas, and S. Rehmani, "Alginate-polyvinyl alcohol based interpenetrating polymer network for prolonged drug therapy, optimization and *in-vitro* characterization," *Carbohydrate polymers*, vol. 166, pp. 183–194, 2017.

[51] T. Jayaramudu, G. M. Raghavendra, K. Varaprasad et al., "Preparation and characterization of poly(ethylene glycol) stabilized nano silver particles by a mechanochemical assisted ball mill process," *Journal of Applied Polymer Science*, vol. 133, no. 7, 2016.

Hindawi
Advances in Polymer Technology
Volume 2019, Article ID 8625325, 10 pages
https://doi.org/10.1155/2019/8625325

Research Article

Crystallinity and Reinforcement in Poly-L-Lactic Acid Scaffold Induced by Carbon Nanotubes

Guoyong Wang,[1] Fangwei Qi,[1] Wenjing Yang,[1] Youwen Yang,[1] Chongxian He,[1] Shuping Peng ,[2,3] and Cijun Shuai [1,4]

[1]*Jiangxi University of Science and Technology, Ganzhou 341000, China*
[2]*NHC Key Laboratory of Carcinogenesis and The Key Laboratory of Carcinogenesis and Cancer Invasion of the Chinese Ministry of Education, Xiangya Hospital, Central South University, Changsha, Hunan, China*
[3]*Cancer Research Institute, School of Basic Medical Sciences, Central South University, Changsha, Hunan, China*
[4]*State Key Laboratory of High Performance Complex Manufacturing, Central South University, Changsha 410083, China*

Correspondence should be addressed to Shuping Peng; shuping@csu.edu.cn and Cijun Shuai; shuai@csu.edu.cn

Received 24 August 2019; Accepted 24 October 2019; Published 12 December 2019

Guest Editor: Yu Tao

Poly-L-Lactic Acid (PLLA) is a bioabsorbable implant material due to its favorable biocompatibility and inherent degradability, while the insufficient mechanical strength hinders its further bone repair application. In present work, carbon nanotubes (CNTs) were introduced into PLLA scaffolds fabricated via selective laser sintering. It was found that the crystallinity of PLLA increased considerably since CNTs could promote the orderly stacking of its molecular chains, thereby improving the mechanical strength of PLLA scaffold. Furthermore, the fracture surface analysis revealed that CNTs acted as a bridge across the cracks and hindered their further expansion. Moreover, CNTs pulled out from the matrix to consume a large amount of fracture energy, which enhanced the resistance to external forces. As a consequence, the compressive strength, Vickers hardness and tensile strength of the scaffold were enhanced by 22.7%, 58.8% and 17.6%, respectively. Besides, the cells exhibited good attachment, spreading and proliferation on the scaffold. This study demonstrated that PLLA/CNTs scaffold was a promising candidate as bone implant.

1. Introduction

Poly-L-Lactic Acid (PLLA) has been recognized as a promising bone repair material due to its good biocompatibility and desirable biodegradability [1–3]. It is able to degrade into lactic acid by hydrolysis, and then metabolize to water and carbon dioxide, which can be removed from the body via normal metabolic pathways [4, 5]. Given the attractive characteristic of PLLA, it has received the approval from the Food and Drug Administration for implant application [6]. Recently, numerous investigations have attempted to utilize PLLA as temporary bone implant [7, 8]. Nevertheless, these studies indicated that PLLA exhibited poor mechanical properties, especially for load bearing, which significantly hinder its further bone repair application [9].

Incorporation of reinforcement, such as nanoparticles [10, 11], nanowires [12], graphene nanoplatelets [13] and carbon nanotubes (CNTs) [14], is a workable approach to enhance the mechanical performance of polymer matrix. Among them, CNTs exhibited superior mechanical performance, including high strength, modules and hardness [15]. Meanwhile, CNTs have been proved to be of favorable biocompatibility and osteoprotective property [16]. Li et al. introduced CNTs into polycarbonate microfibrils, and enhanced the tensile strength and elastic modulus by 20%, 40%, respectively [17]. Wang et al. proved that CNTs as a nanofiller for PLLA could overcome the brittleness, with the elongation at break and the impact strength improved 205% and 30%, respectively [18]. Mesgar et al. used CNTs to reinforce the chitosan scaffolds, which enhanced the modulus to 11 times [19]. Luo et al. fabricated multi-walled carbon nanotubes polycaprolactone composite scaffolds using the solution evaporation technique [20]. *In vivo* results showed that the composite scaffolds had good bone bioactivity.

In present study, CNTs were incorporated into PLLA to enhance the mechanical properties. The PLLA/CNTs composite scaffold was prepared by selective laser sintering (SLS) process. Previous researchers have fabricated PLLA/CNTS scaffold via phase separation method [21], electrospinning technique [22], freeze-drying method [23], etc. Comparing

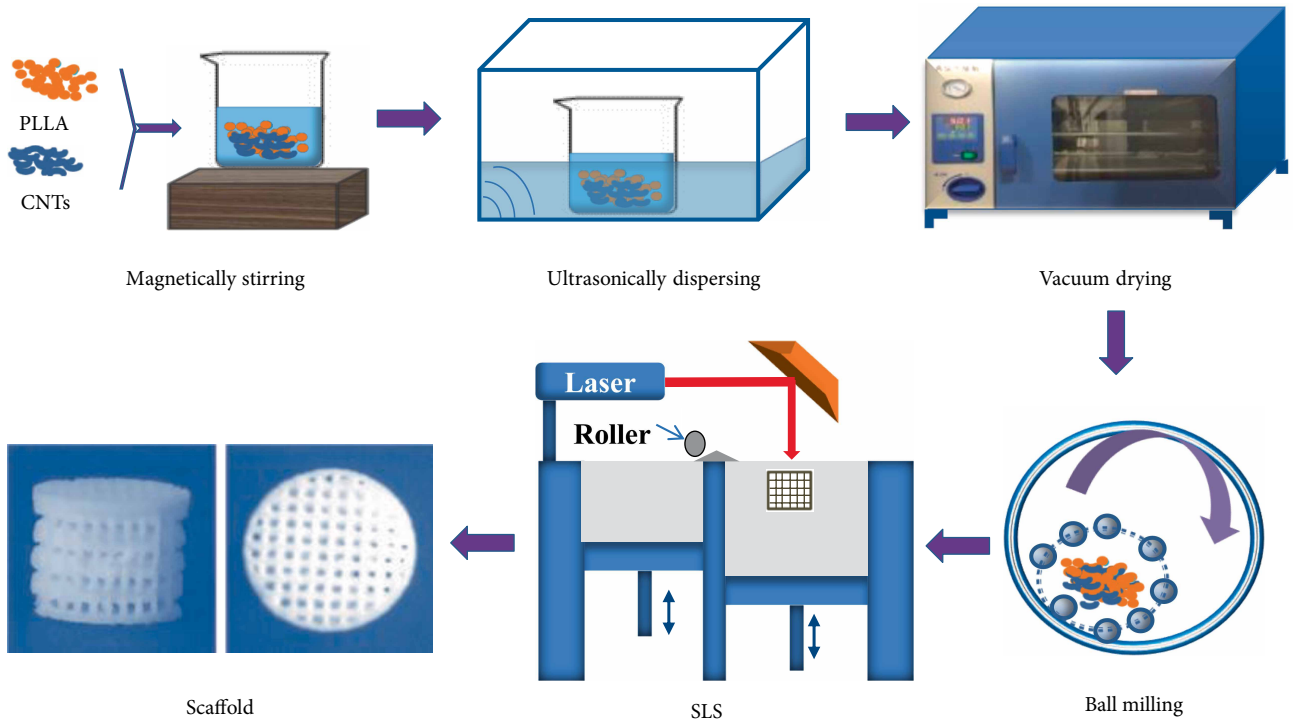

Figure 1: Schematic of the scaffold preparation process.

with previous methods, selective laser sintering exhibits great advantages including accurate control of the pore structure and strong ability to customize for specific defect sites [24–27]. The microstructure evolution and mechanical behavior of the composite scaffold were investigated. The effect of CNTs on the mechanical behavior was clarified in detail. In addition, the biocompatibility of the PLLA/CNTs scaffold was studied via *in vitro* cell experiments.

2. Materials and Methods

2.1. Materials. CNTs with the outside diameter ranging from 4 to 6 nm and the length ranging from 10 to 20 μm was provided from Chengdu Organic Chemicals Co. Ltd. The PLLA powder was purchased from Shenzhen Polymtek Biomaterial Co. Ltd. (Shenzhen, China) with average molecular weights 150 mol/g, purity more than 99%, and density 1.25 g/cm^3.

2.2. Preparation of PLLA/CNTs Composite Scaffold. The detailed fabrication process of PLLA/CNTs scaffold was depicted in Figure 1. Specifically, a certain quantity of CNTs was first added into anhydrous ethanol solution. The suspension was then magnetically stirred and ultrasonically dispersed for 6 h. Subsequently, the PLLA powder was added into the above CNTs suspension. Afterwards, the PLLA/CNTs suspension was magnetically stirred and ultrasonically dispersed for 12 h. The suspension was then dried in a vacuum oven at 45°C until the powder weight maintained stable. Finally, the PLLA/CNTs mixed powder was obtained after ball milling for 1 h.

The PLLA/CNTs composite scaffold was prepared using a self-developed SLS system. The detailed preparation process was described as follows: Firstly, the 3D model matching the bone scaffold was designed. The model was imported into the SLS system to create the slice file; secondly, the composite powder was spread on the workbench; thirdly, the composite powder was selectively sintered layer-by-layer according to the above slice file. The optimal process parameters of SLS process were determined by pilot experiments (laser power 2.5 W, scanning speed 120 mm/s, scanning distance 0.1 mm and layer thickness 0.1 mm). The obtained scaffolds with nominal CNTs of 0, 0.25, 0.5, and 1.0 wt.% were named as PLLA, PLLA/0.25CNTs, PLLA/0.5CNTs, and PLLA/1.0CNTs, respectively. The pore size and strut size of the sintered scaffolds were about 650 μm and 450 μm, respectively, as shown in Figure 1. In general, porous bone scaffolds was able to provide a favorable microenvironment for cell into-growth [28, 29].

2.3. Microstructural Characterization. The chemical characteristic of the samples was qualitatively evaluated by Fourier transform infrared spectroscopy (FTIR, Bruker Tensor 27). The samples and dried potassium bromide powder were mixed and grounded into fine powder. Then, they were pressed into discs in a mold. The FTIR spectra were obtained with a resolution of 2 cm^{-1} from 500 to 3000 cm^{-1} at room temperature. Subsequently, the intensity of transmittance and the characteristic peaks was measured. Raman spectroscopy was obtained using a Raman spectrometer (Renshaw, UK) with a laser excitation of 532 nm and scans range between 400 and 2500 cm^{-1}.

Polarized optical microscope (POM, Olympus Co., Japan) was used to investigate the crystalline morphology of PLLA/CNTs composites. The phase structure was investigated using an X-ray diffractometer (XRD, DMAX 2500, Japan Science Co., Japan) equipped with Cu Ka source. The data was recorded ranging from 10° to 50°.

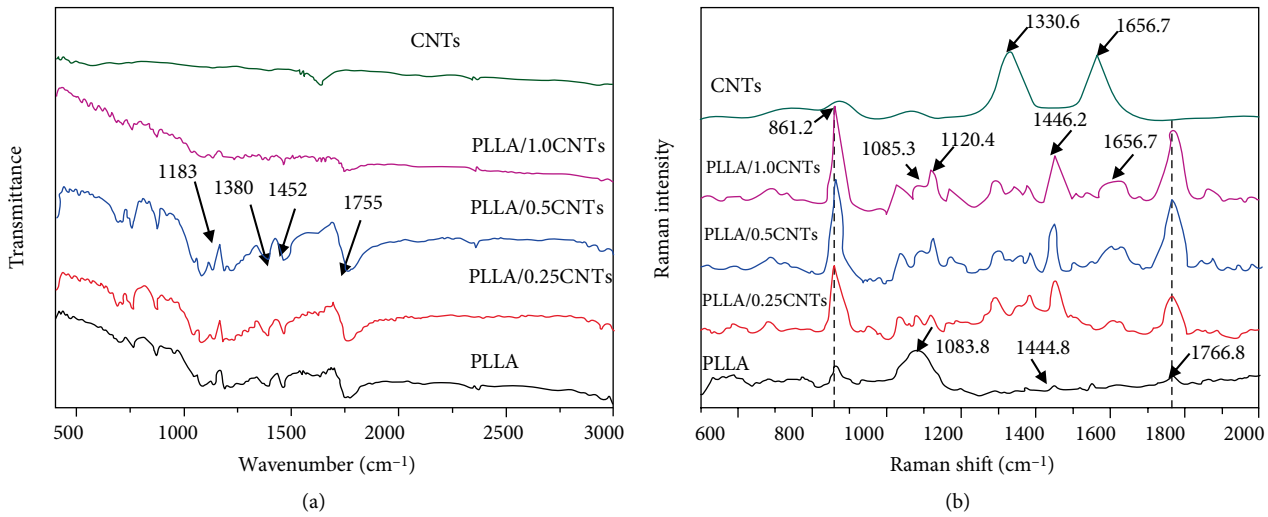

Figure 2: (a) FTIR and (b) Raman spectra of CNTs, neat PLLA, and PLLA/CNTs scaffolds.

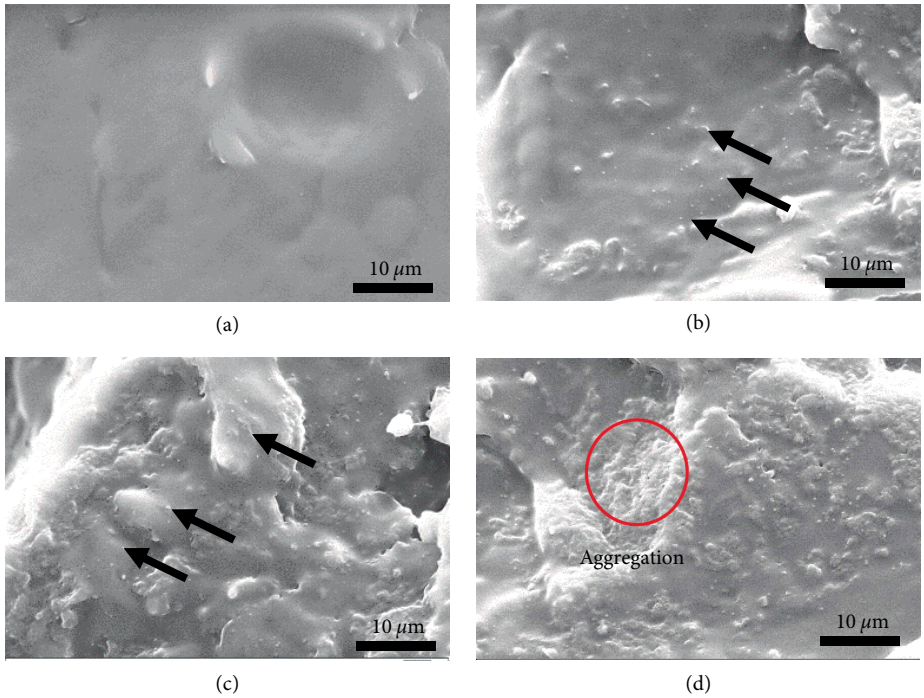

Figure 3: SEM showing the fracture surface of (a) PLLA, (b) PLLA/0.25CNTs, (c) PLLA/0.5CNTs, and (d) PLLA/1.0CNTs scaffolds.

2.4. Mechanical Tests. The Vickers hardness tester (TMVS-1, Beijing TIME High Technology Co. Ltd) was applied to measure the hardness. Three different measurements were carried out for each sample. A mechanical testing machine (WD-D1, LTD, China) was applied to perform the tensile and compressive tests. The tensile specimens (width 5 mm, length 20 mm) was subjected to tensile load until they were broken, and the compressive specimens with porous structure ($10 \times 10 \times 5$ mm^3) were subjected to compression load until they were crushed. The fracture surface morphologies of the scaffolds after tensile tests were observed using a scanning electron microscope (Phillips XL30, Eindhoven, Netherlands). Before SEM observation, the surface of samples was coated with gold for 2 min in a sputter coater.

2.5. Cell Experiments. MG63 cells were cultured in Dulbecco's Modified Eagle Medium supplemented with 10% fetal bovine serum and 1% (v/v) streptomycin/penicillin condition at 37°C (5% humid CO_2). The culture medium was changed every 2 days. Prior to cell seeding, the PLLA and PLLA/CNTs scaffold ($10 \times 10 \times 2$ mm^3) were sterilized under UV irradiation for 24 h. The incubate medium was renewed every day. The MG63 cells were seeded on the PLLA and PLLA/CNTs scaffolds with a density of 10^5 cells per well. After 1, 4 and 7 days, the specimens were rinsed three times using phosphate buffer solution (PBS) in order to remove nonadherent cells. The cell morphology on scaffolds with different culture time was observed by SEM.

The cell viability was assessed using live/dead staining after culture for 1, 4, 7 days. In brief, the cells were stained with

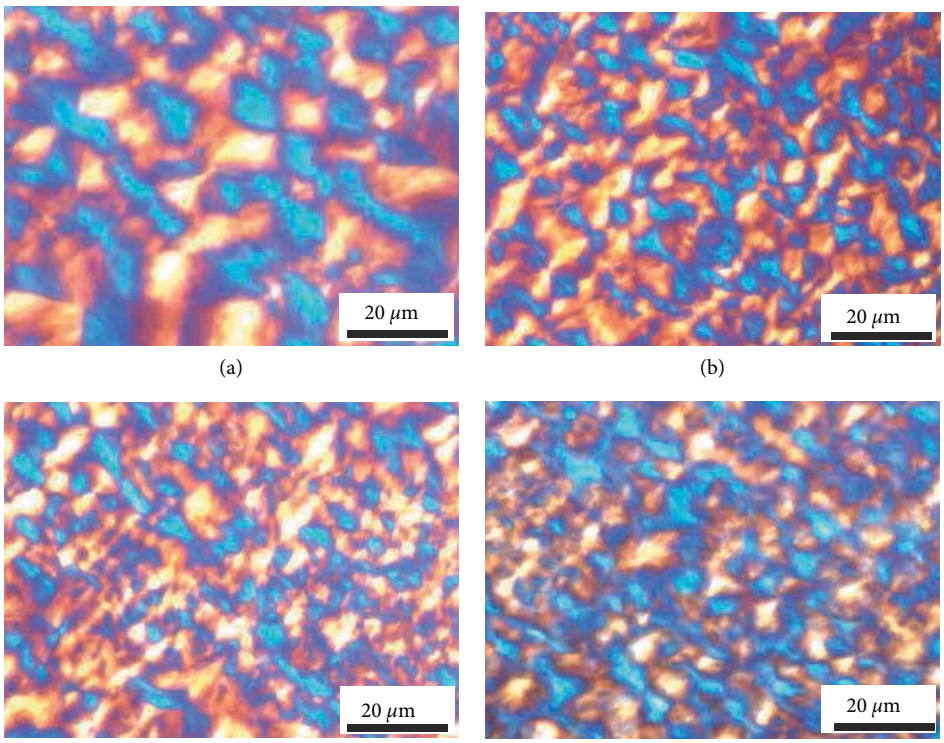

Figure 4: POM of (a) PLLA, (b) PLLA/0.25CNTs, (c) PLLA/0.5CNTs and (d) PLLA/1.0CNTs scaffolds.

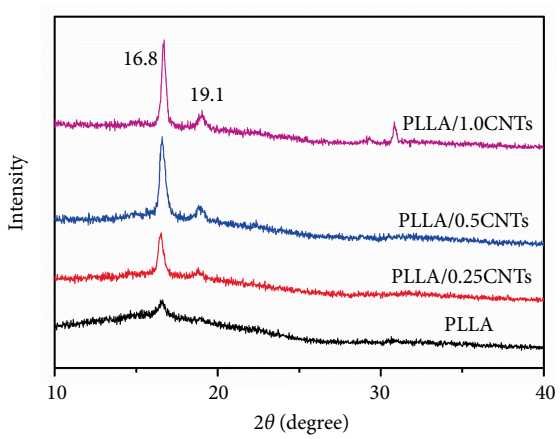

Figure 5: XRD patterns of CNTs, PLLA and PLLA/CNTs composite scaffolds.

2 μg/mL Calcein-AM and Ethidium homodimer-1 reagents for 20 min at 37°C. Then, the stained cells were refreshed with PBS and observed with fluorescence microscope (BX60, Olympus, Japan).

The proliferation of MG63 cells was further evaluated using cells counting kit-8 (CCK-8) assays. Cells were seeded on the scaffolds for 1, 4 and 7 days. Then, 40 μL of CCK-8 solution were added to every well and incubated for 4 h at 37°C. Then the optical density (OD) was measured at 450 nm by a spectrophotometric micro plate reader. Each sample testing was carried out for three times.

2.6. Statistical Analysis. All the experimental data were recorded using at least three separate operations, and expressed as means ± standard deviation. In all statistical analysis, it is considered to be significant with P value less than 0.05.

3. Results and Discussion

3.1. Characterization of the PLLA/CNTS Composite Scaffolds. The FTIR spectra of CNTs, PLLA and PLLA/CNTs scaffolds were displayed in Figure 2(a). As was expected, there was a peak presented at 1635 cm^{-1}, which was assigned to the stretching vibrations of C=C bonds in the CNTs. For PLLA, there were two obvious peaks at 1751 and 1452 cm^{-1}, which was ascribed to the C=O stretching vibrations of its carboxyl groups [30]. The peak located at 1380 cm^{-1} was assigned to the bending vibrations of $-CH_3$ groups [31]. There was a weak broad band appearing at 1183 cm^{-1} which was associated to C–O stretching vibration [32]. Compared with PLLA, there were no new peaks or peak shift in the FTIR spectra of PLLA/CNTs scaffolds.

The Raman measurements were used to further reveal the structural stability of the CNTs during the SLS process. The Raman spectra of CNTs, PLLA and PLLA/CNTs scaffolds were recorded, with results shown in Figure 2(b). It could be found that there were two distinct characteristic peaks observed at 1330.6 and 1656.7 cm^{-1}, which was ascribed to the D- and G-bands of CNTs, respectively. Generally, the D-band was related to the degree of disorder of CNTs, while the G- band was attributed to the in-plane motion of the sp^2 carbon atom

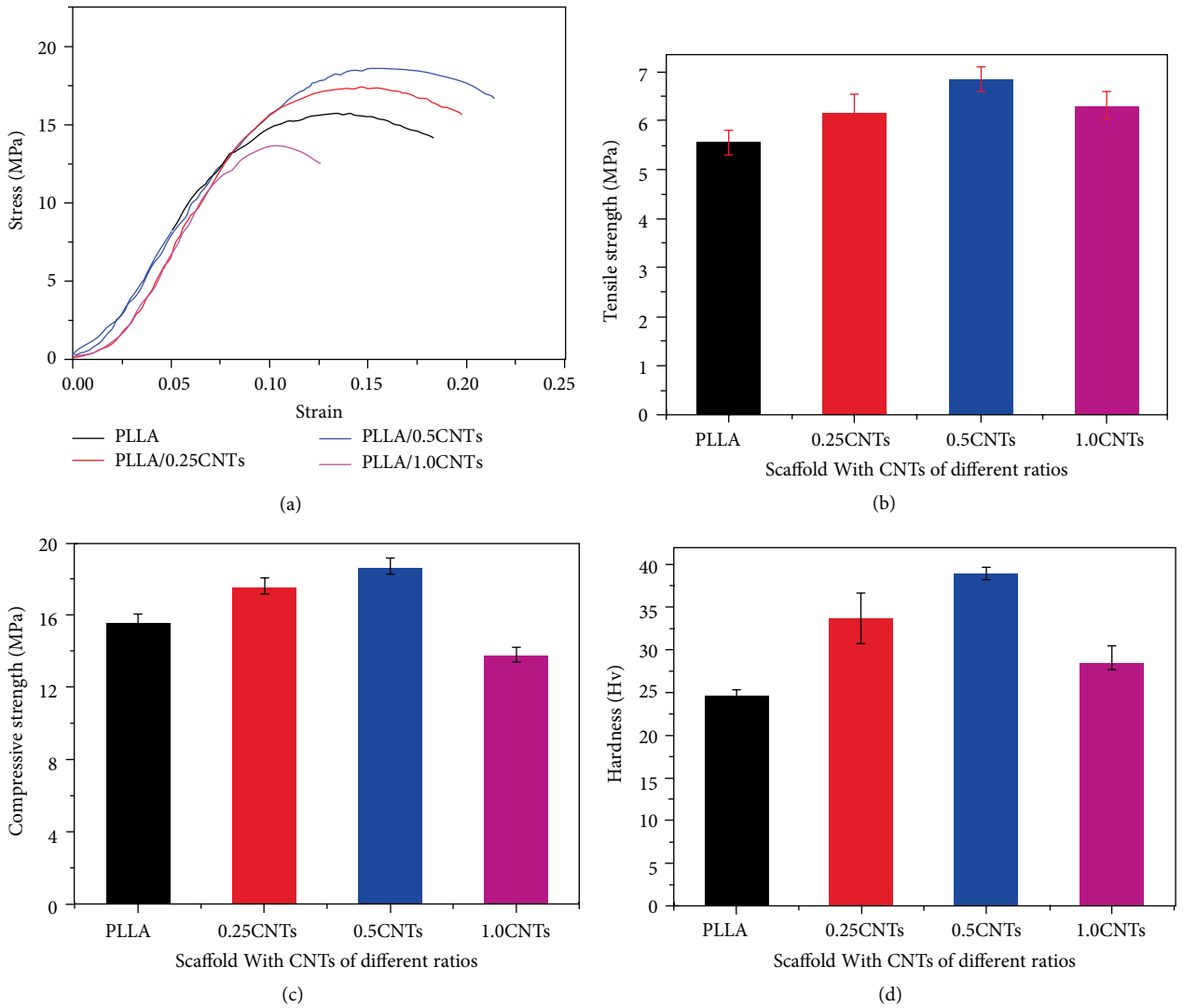

Figure 6: Tensile stress-strain curves (a), tensile strength (b), compressive strength (c), and hardness of PLLA and PLLA/CNTs composite scaffolds (d).

[4, 33]. PLLA exhibited three characteristic peaks at 859.6, 1083.8 and 1444.8 cm^{-1}, which were attributed to C–CH_3 stretching, –CH_3 rocking mode and –CH_3 asymmetric bending mode, respectively [34]. For the Raman spectrum of PLLA/CNTs scaffolds, they presented combined characteristic peaks of PLLA and CNTs. The D and G modes of the scaffolds exhibited no noticeable shifts as compared with the spectrum of CNTs. However, the PLLA resonances in the scaffolds included C–CH_3 stretching (861.2 cm^{-1}), –CH_3 rocking mode (1085.3 cm^{-1}), and –CH_3 asymmetric bending mode (1446.2 cm^{-1}) were red-shifted by 1.6, 1.5 and 1.4 cm^{-1}, respectively, as compared with the pure PLLA scaffold [4]. It might be due to the interaction between PLLA and CNTs during SLS.

The brittle fractured surfaces of PLLA/CNTs scaffolds were observed, as shown in Figure 3. PLLA exhibited an obvious brittle fracture with relative flat morphology. As a comparison, there were some micro-fibers on the fractured surface of the PLLA/0.5CNTs scaffold. The CNTs uniformly distributed in the PLLA matrix. The number of micro-fibers increased with the CNTs contents increasing to 0.5 wt.%. However, the agglomeration occurred with CNTs further increasing to 1.0 wt.%.

The crystalline morphology of PLLA/CNTs was investigated using POM, with results displayed in Figure 4. Clearly, PLLA exhibited large spherulites morphology with a typical maltese cross shape. As CNTs gradually increased to 0.5 wt.%, the size of the spherulites decreased considerably, accompanying with the significantly increased density. The results indicated that CNTs acted as heterogeneous nucleating agents and promoted the orderly arrangement, thus accelerating the crystallization of PLLA. Nevertheless, as the CNTs reached 1.0 wt.%, relatively coarsened spherulites were observed in the matrix, indicated the reduced nucleation ability of CNTs for composite matrix. Previous studies revealed that as nanoparticles exceeded a certain content, the ability to promote PLLA nucleation would decrease, which was believed to be related to their agglomeration in PLLA matrix [35].

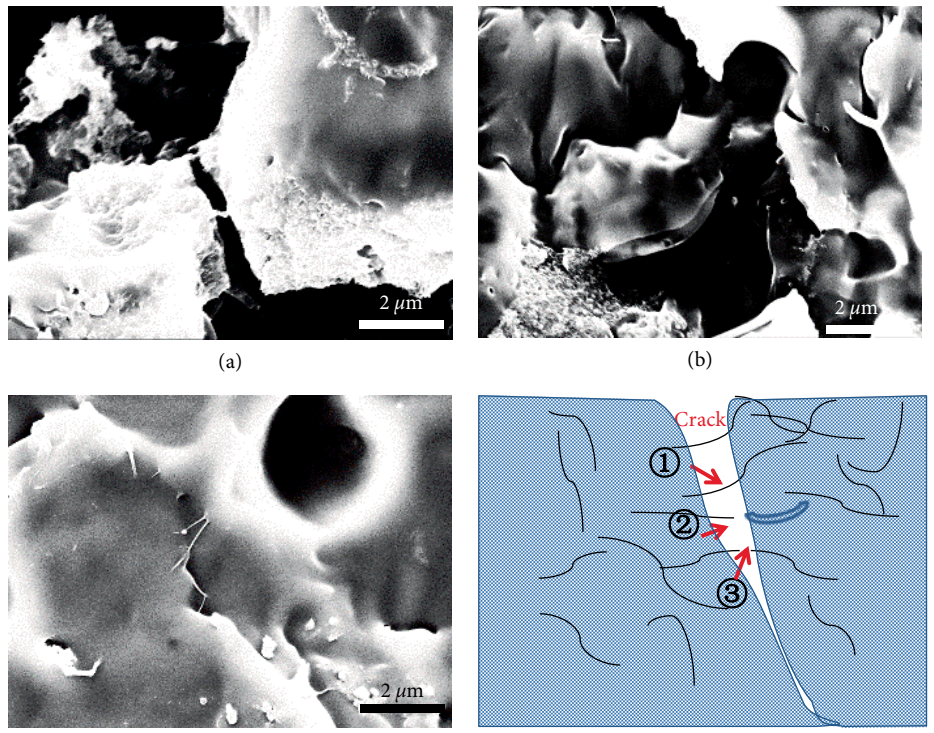

Figure 7: The introduced (a) bridging, (b) pulling out and (c) pinning effect of CNTs in PLLA scaffold. (d) Models of reinforcement mechanisms.

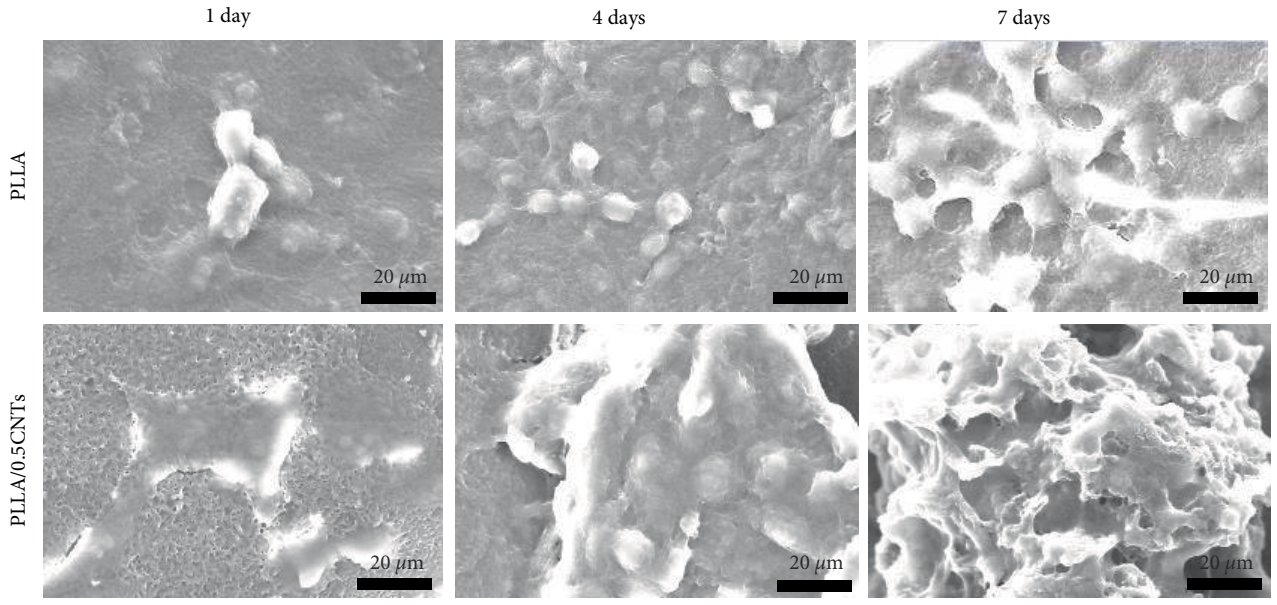

Figure 8: SEM images of the MG63 cells cultured on scaffolds for 1, 4 and 7 days.

The XRD patterns of PLLA and PLLA/CNTs were shown in Figure 5. Obviously, there were two strong diffraction peaks located at $2\theta = 16.8°$ and 19.1° [36], which indicated the occurrence of cold crystallization of PLLA [37]. The XRD patterns of the PLLA/CNTs scaffold still kept the characteristic peaks of PLLA, which indicated that the incorporation of CNTs did not exert a significant influence on the crystalline structure of PLLA. However, the intensity and sharpness of these peaks gradually increased with CNTs increasing, which indicated that the degree of crystallization of polymer composite was enhanced due to the heterogeneous nucleation of CNTs [30].

3.2. Mechanical Properties. Bone scaffolds require appropriate mechanical strength to provide structural support for

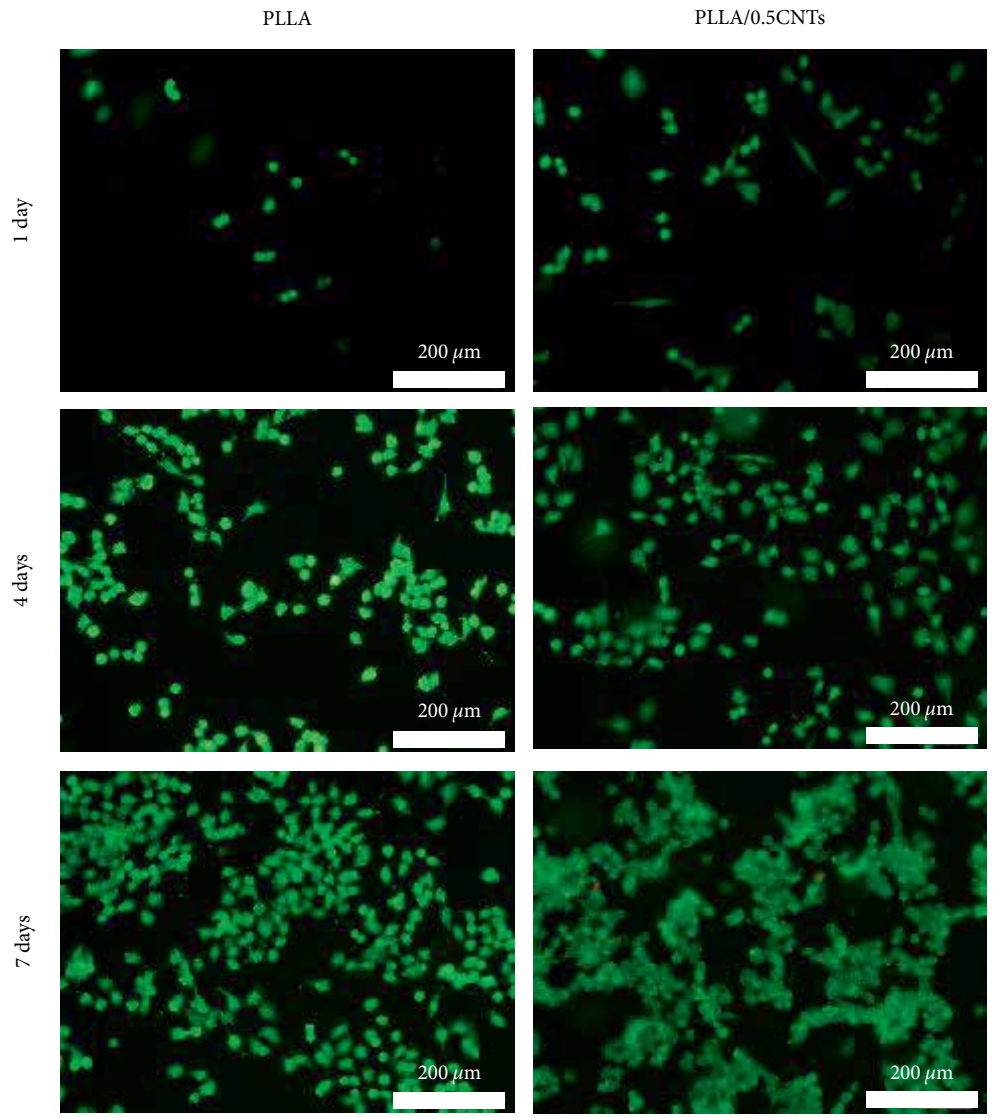

Figure 9: Representative fluorescence images of MG63 cells cultured on scaffolds for 1, 4 and 7 days.

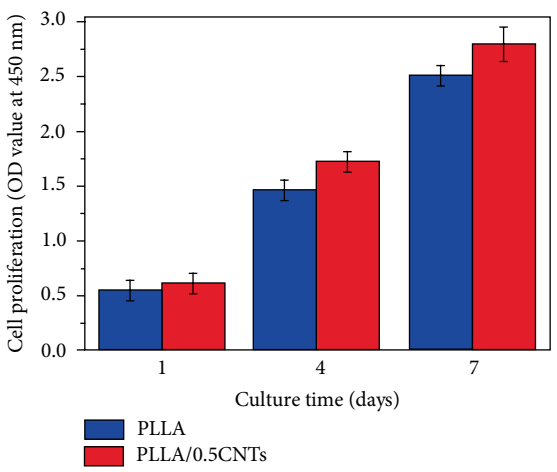

Figure 10: The obtained OD value using CCK-8 assays after 1, 4, 7 days' culture.

the newly formed tissue during bone repair [38, 39]. The mechanical properties of PLLA and PLLA/CNTs scaffolds were evaluated through compressive, hardness and tensile tests, with results shown in Figure 6. The typical compressive stress-strain curves were depicted in Figure 6(a). It could be found that all the samples exhibited the brittle characteristic. As the external force exceeded a certain degree during the compression, the scaffolds were directly fractured without yielding [40]. The compressive strengths derived from their compressive stress-strain curves were shown in Figure 6(b). The compressive strengths of PLLA/CNTs scaffolds increased by 22.7% (from 5.5 MPa to 6.82 MPa) with CNTs increasing to 0.50 wt.%. This could be ascribed to the fact that CNTs could act as a reinforced phase in the PLLA matrix [41]. However, there was a slight decrease in compressive strength with CNTs further increasing to 1.0 wt.%, which might be due to the aggregation of CNTs. It was well established that bone scaffolds should have sufficient mechanical strength to match

the surrounding connective bone. Usually, the compressive strength of the human cancellous bone and cortical bone were in the range of 2–12 MPa and 130–180 MPa, respectively [42]. In this work, the optimal compressive strength of PLLA/CNTs scaffolds was 6.8 MPa, which was in the range of cancellous bone and lower than cortical bone. Therefore, the PLLA/CNTs scaffolds have a potential application in bone repair.

The Vickers hardness and tensile strength of all specimens was shown in Figures 6(c) and 6(d), respectively. Similarly, the Vickers hardness and tensile strength of PLLA/0.5CNTs scaffolds increased to 38.9 Hv and 18.6 MPa, which was increased by 58.8% and 17.6%, respectively. Therefore, the addition of CNTs presented a positive role in enhancing the mechanical properties of PLLA scaffold.

In this work, the CNTs could act as a pinning action to hinder the crack propagation. This was due to the crack in the composite was difficult to deflect during the expansion process and could only continue in the original direction [43]. Thus, the CNTs immediately adjacent to the crack tip did not break, but created a bridging effect between the cracks [44, 45]. The typical crack bridge in the crack surface contact region was shown in Figure 7(a). This bridging effect would offset a part of the tensile stress, thereby hindering the further expansion of the crack. On the other hand, CNTs, as one dimensional material, exhibited significant fiber properties [46]. In this case, the CNTs were pulled out of the matrix during the tensile fracture of the composite scaffolds, thereby consuming a large amount of external energy [47]. As shown in Figure 7(b), some CNTs pulled out from the matrix, whose direction tended to align with the direction of the applied load. Besides, CNTs were embedded into PLLA matrix, which formed the pinning effects. The schematics of pulling out, bridging and crack deflection are shown in Figure 7(d). Furthermore, the increase in the crystallinity of PLLA also had a positive effect on their mechanical properties [48]. However, with the CNTs contents further increasing to 1.0 wt.%, they aggregated in the PLLA matrix, thus failing to enhance the mechanical properties of PLLA/CNTs scaffolds.

3.3. Cytocompatibility. Good biocompatibility was of great significance for the bone implants [49–51]. In present study, the PLLA/0.5CNTs scaffold with optimal mechanical properties was used to further evaluate the cytocompatibility, with the PLLA scaffold as control. The morphologies of cells adhered on scaffolds after cultivating for 1, 4, 7 days were observed by SEM, as shown in Figure 8. After 1 day' culture, cells began to spread on the PLLA/0.5CNTs scaffold with apparent cytoplasmic extensions, indicating a strong adhesion. As culture time increasing to 4, 7 days, the adhered cells on the PLLA/0.5CNTs scaffold increased significantly and overlapped with each other. Additionally, the cells on the PLLA/0.5CNTs scaffold presented much longer filopodia as compared with those on PLLA scaffold. It was indicated that PLLA/0.5CNTs scaffold was more beneficial for cell adhesion.

Stained fluorescent pictures of cells incubated on PLLA/0.5CNTs and PLLA scaffolds for various periods were exhibited in Figure 9. Herein, green represented live cells, whereas red represented dead cells. Clearly, nearly no dead cells were observed for all the samples during cell incubation. In particular, the cells exhibited typical fusiform shape after culture for 1 day, revealing that the cells growth normally on the scaffold. After further incubation for 4, 7 days, cells have expanded into filopodia, and formed numerous extracellular matrix. At the same time, live cells increased significantly with incubation time increasing, which indicated that both PLLA/0.5CNTs and PLLA scaffolds were favorable for cell proliferation. It should be noted that the PLLA/0.5CNTs scaffold exhibited a higher cell density than PLLA scaffold, indicating that it was more beneficial to cell growth.

The viability of cells incubated on PLLA/0.5CNTs and PLLA scaffolds was quantitatively assessed by CCK-8 assay, with results shown in Figure 10. It could be seen that the cell viability on PLLA/0.5CNTs and PLLA scaffolds increased with culture period extending from 1 to 7 days. In detail, the OD values increased from 0.6 to 2.8 for PLLA/0.5CNTs scaffold. Significantly, PLLA/0.5CNTs scaffolds presented enhanced OD values comparing with the PLLA scaffold at same time, which further proved that CNTs shown a positive effect on cell proliferation.

Basing on above cell experiments, it was indicated that PLLA/CNTs scaffold exhibited an enhanced cytocompatibility for cell adhesion and growth, as compared with PLLA scaffold. In general, cells were able to distinguish surfaces with different physical, chemistry and mechanical properties that directly affected cell behavior. As cells adhered to scaffold surface, they created a larger force at the adhesion site. It was believed that the PLLA/CNTs scaffold with stiffer matrix than PLLA scaffold could provide better cell adhesion. Secondly, the incorporation of CNTs into PLLA matrix resulted in the rough nano-scaled surface topography, which was more conducive for cell adhesion and growth [36]. In fact, rough surface was able to provide a variety of mechanical stimuli, thus promoting cell proliferation. Besides, the incorporated CNTs with excellent electrical properties could enhance the transmission of cell signals, thus promoting cell-cell communication and cellular activity [52].

4. Conclusions

In present study, CNTs were introduced into PLLA to improve the mechanical behavior. PLLA/CNTs scaffold was fabricated by SLS technique. CNTs enhanced the crystallinity of PLLA matrix due to its heterogeneous nucleation effect. More significantly, CNTs, as one-dimensional material, contributed to the crack bridging mechanism and pulling out effect. As a consequence, the obtained compressive strength, Vickers hardness and tensile strength of the scaffold were considerably enhanced from 5.6 to 6.8 MPa, 24.5 to 38.9 Hv, 15.5 to 18.6 MPa, respectively. Furthermore, PLLA/CNTs scaffold exhibited desirable biocompatibility. It was indicated that PLLA/CNTs scaffold was a promising candidate as bone implant.

Data Availability

The data used to support the findings of this study are available from the corresponding author upon request.

Conflicts of Interest

The authors declare that there are no conflicts of interest regarding the publication of this paper.

Authors' Contributions

Guoyong Wang and Fangwei Qi contributed equally in this work.

Acknowledgments

This study was supported by the following funds: (1) The Natural Science Foundation of China (51935014, 51905553, 81871494, 81871498, 51705540); (2) Hunan Provincial Natural Science Foundation of China (2019JJ50774, 2018JJ3671, 2019JJ50588); (3) JiangXi Provincial Natural Science Foundation of China (20192ACB20005); (4) Guangdong Province Higher Vocational Colleges & Schools Pearl River Scholar Funded Scheme (2018); (5) The Open Sharing Fund for the Large-scale Instruments and Equipments of Central South University; (6) The Project of Hunan Provincial Science and Technology Plan (2017RS3008); (7) The Natural Science Foundation of Jiangxi University Science and Technology (NSFJ2014-G29).

References

[1] P. Feng, J. He, S. Peng et al., "Characterizations and interfacial reinforcement mechanisms of multicomponent biopolymer based scaffold," *Materials Science and Engineering: C*, vol. 100, pp. 809–825, 2019.

[2] Z. Karimi, E. Seyedjafari, F. S. Mahdavi et al., "Baghdadite nanoparticle-coated Poly-L-Lactic Acid (PLLA) ceramics scaffold improved osteogenic differentiation of adipose tissue-derived mesenchymal stem cells," *Journal of Biomedical Materials Research Part A*, vol. 107, pp. 1284–1293, 2019.

[3] J. Feng, Z. Huang, and Y. Dong, "Effect of mixed solvents on the thermal properties of poly(L-lactic acid) (PLLA) solution and micromorphology of porous PLLA scaffolds," *Materials Research Express*, vol. 6, no. 1, p. 015314, 2018.

[4] D. Zhang, M. A. Kandadai, J. Cech, S. Roth, and S. A. Curran, "Poly (L-lactide)(PLLA)/multiwalled carbon nanotube (MWCNT) composite: characterization and biocompatibility evaluation," *The Journal of Physical Chemistry B*, vol. 110, no. 26, pp. 12910–12915, 2006.

[5] D. da Silva, M. Kaduri, M. Poley et al., "Biocompatibility, biodegradation and excretion of polylactic acid (PLA) in medical implants and theranostic systems," *Chemical Engineering Journal*, vol. 340, pp. 9–14, 2018.

[6] D. Vleggaar, R. Fitzgerald, Z. P. Lorenc et al., "Consensus recommendations on the use of injectable Poly-L-Lactic Acid for facial and nonfacial volumization," *Journal of Drugs in Dermatology*, vol. 13, no. 4, pp. s44–s51, 2014.

[7] D. J. Hickey, B. Ercan, L. Sun, and T. J. Webster, "Adding MgO nanoparticles to hydroxyapatite-PLLA nanocomposites for improved bone tissue engineering applications," *Acta Biomaterialia*, vol. 14, pp. 175–184, 2015.

[8] P. Feng, Y. Kong, L. Yu et al., "Molybdenum disulfide nanosheets embedded with nanodiamond particles: co-dispersion nanostructures as reinforcements for polymer scaffolds," *Applied Materials Today*, vol. 17, pp. 216–226, 2019.

[9] A. Pei, Q. Zhou, and L. A. Berglund, "Functionalized cellulose nanocrystals as biobased nucleation agents in poly(L-lactide) (PLLA): crystallization and mechanical property effects," *Composites Science and Technology*, vol. 70, no. 5, pp. 815–821, 2010.

[10] X. Hu, Y. Wang, L. Zhang, M. Xu, J. Zhang, and W. Dong, "Mechanical testing and reinforcing mechanisms of a magnetic field-sensitive hydrogel prepared by microwave-assisted polymerization," *Polymer Testing*, vol. 69, pp. 396–404, 2018.

[11] C. Shuai, J. Zan, F. Qi et al., "nMgO-incorporated PLLA bone scaffolds: Enhanced crystallinity and neutralized acidic products," *Materials & Design*, vol. 174, p. 107801, 2019.

[12] Y. Wang, X. Wang, Y. Xiang et al., "Hydroxyapatite-nanowires enhanced electrospun fiber via craze disperse stress for bone regeneration," *Nanoscience and Nanotechnology Letters*, vol. 10, no. 11, pp. 1498–1507, 2018.

[13] C. Gonçalves, A. Pinto, A. V. Machado, J. Moreira, I. C. Gonçalves, and F. Magalhães, "Biocompatible reinforcement of poly (lactic acid) with graphene nanoplatelets," *Polymer Composites*, vol. 39, pp. E308–E320, 2018.

[14] H.-B. Kim, D. K. Patel, Y.-R. Seo, and K.-T. Lim, "3D-printed scaffolds with reinforced poly (lactic acid)/carbon nanotube filaments based on melt extrusion," *Journal of Biosystems Engineering*, vol. 44, pp. 1–8, 2019.

[15] L. Valentini, S. B. Bon, M. Hernández, M. A. López-Manchado, and N. Pugno, "Nitrile butadiene rubber composites reinforced with reduced graphene oxide and carbon nanotubes show superior mechanical, electrical and icephobic properties," *Composites Science and Technology*, vol. 166, pp. 109–114, 2018.

[16] V. Amenta and K. Aschberger, "Carbon nanotubes: potential medical applications and safety concerns," *Wiley Interdisciplinary Reviews: Nanomedicine and Nanobiotechnology*, vol. 7, no. 3, pp. 371–386, 2015.

[17] Z.-M. Li, S.-N. Li, M.-B. Yang, and R. Huang, "A novel approach to preparing carbon nanotube reinforced thermoplastic polymer composites," *Carbon*, vol. 11, no. 43, pp. 2413–2416, 2005.

[18] X.-F. Wang, Z.-X. Zhang, J.-H. Yang, Y. Wang, and J.-H. Zhang, "{ZnO}@{ZnS} core/shell microrods with enhanced gas sensing properties," *RSC Advances*, vol. 5, no. 4, pp. 69522–69533, 2015.

[19] A. S. Mesgar, Z. Mohammadi, and S. Khosrovan, "Improvement of mechanical properties and in vitro bioactivity of freeze-dried gelatin/chitosan scaffolds by functionalized carbon nanotubes," *International Journal of Polymeric Materials and Polymeric Biomaterials*, vol. 67, no. 5, pp. 267–276, 2018.

[20] F. Luo, L. Pan, G. Hong et al., "In vitro and in vivo characterization of multi-walled carbon nanotubes/polycaprolactone composite scaffolds for bone tissue engineering applications," *Journal of Biomaterials and Tissue Engineering*, vol. 7, no. 9, pp. 787–797, 2017.

[21] Q. Cai, J. Mao, X. Li, and X. Yang, "Macroporous and nanofibrous {PLLA} scaffolds reinforced with calcium phosphate-coated multiwalled carbon nanotubes," *Materials Letters*, vol. 128, pp. 238–241, 2014.

[22] S. Ghorbani, H. Eyni, Z. Khosrowpour et al., "Spermatogenesis induction of spermatogonial stem cells using nanofibrous poly(L-lactic acid)/multi-walled carbon nanotube scaffolds and naringenin," *Polymers for Advanced Technologies*, 2019.

[23] Z. Fereshteh, *In Functional 3D Tissue Engineering Scaffolds*, pp. 151–174, Elsevier, Amsterdam, 2018.

[24] K. H. Tan, C. K. Chua, K. F. Leong et al., "Scaffold development using selective laser sintering of polyetheretherketone-hydroxyapatite biocomposite blends," *Biomaterials*, vol. 24, no. 18, pp. 3115–3123, 2003.

[25] C. Shuai, B. Wang, Y. Yang, S. Peng, and C. Gao, "3D honeycomb nanostructure-encapsulated magnesium alloys with superior corrosion resistance and mechanical properties," *Composites Part B: Engineering*, vol. 162, pp. 611–620, 2019.

[26] F. E. Wiria, C. K. Chua, K. F. Leong, Z. Y. Quah, M. Chandrasekaran, and M. W. Lee, "Improved biocomposite development of poly(vinyl alcohol) and hydroxyapatite for tissue engineering scaffold fabrication using selective laser sintering," *Journal of Materials Science: Materials in Medicine*, vol. 19, no. 3, pp. 989–996, 2008.

[27] H. Liang, Y. Yang, D. Xie et al., "Trabecular-like Ti-6Al-4V scaffolds for orthopedic: fabrication by selective laser melting and in vitro biocompatibility," *Journal of Materials Science & Technology*, vol. 35, no. 7, pp. 1284–1297, 2019.

[28] Y. Cao, T. Shi, C. Jiao et al., "Fabrication and properties of zirconia/hydroxyapatite composite scaffold based on digital light processing," *Ceramics International*, 2019.

[29] Y. Yang, F. Yuan, C. Gao et al., "A combined strategy to enhance the properties of Zn by laser rapid solidification and laser alloying," *Journal of the Mechanical Behavior of Biomedical Materials*, vol. 82, pp. 51–60, 2018.

[30] Y. Zhou, L. Lei, B. Yang, J. Li, and J. Ren, "Preparation and characterization of polylactic acid (PLA) carbon nanotube nanocomposites," *Polymer Testing*, vol. 68, pp. 34–38, 2018.

[31] C.-C. Chen, J.-Y. Chueh, H. Tseng, H.-M. Huang, and S.-Y. Lee, "Preparation and characterization of biodegradable PLA polymeric blends," *Biomaterials*, vol. 24, no. 7, pp. 1167–1173, 2003.

[32] S. Liu, G. Wu, and Y. Xiao, "Multi-interfaces investigation on the PLA composites toughened by modified MWCNTs," *Composite Interfaces*, vol. 24, no. 8, pp. 743–759, 2017.

[33] S. L. Rebelo, A. Guedes, M. E. Szefczyk, A. M. Pereira, J. P. Araújo, and C. Freire, "Progress in the Raman spectra analysis of covalently functionalized multiwalled carbon nanotubes: unraveling disorder in graphitic materials," *Physical Chemistry Chemical Physics*, vol. 18, no. 18, pp. 12784–12796, 2016.

[34] Z. Xu, Y. Niu, L. Yang et al., "Morphology, rheology and crystallization behavior of polylactide composites prepared through addition of five-armed star polylactide grafted multiwalled carbon nanotubes," *Polymer*, vol. 51, no. 3, pp. 730–737, 2010.

[35] C. Shuai, Y. Xu, P. Feng, G. Wang, S. Xiong, and S. Peng, "Antibacterial polymer scaffold based on mesoporous bioactive glass loaded with in situ grown silver," *Chemical Engineering Journal*, vol. 374, pp. 304–315, 2019.

[36] L. Pan, X. Pei, R. He, Q. Wan, and J. Wang, "Multiwall carbon nanotubes/polycaprolactone composites for bone tissue engineering application," *Colloids and Surfaces B: Biointerfaces*, vol. 93, pp. 226–234, 2012.

[37] T. Huang, J.-H. Yang, N. Zhang, J.-H. Zhang, and Y. Wang, "Highly efficient non-fullerene polymer solar cells enabled by novel non-conjugated small-molecule cathode interlayers," *Polymer Bulletin*, vol. 75, pp. 2641–2655, 2018.

[38] C. Shuai, Y. Cheng, Y. Yang, S. Peng, W. Yang, and F. Qi, "Laser additive manufacturing of Zn-2Al part for bone repair: formability, microstructure and properties," *Journal of Alloys and Compounds*, vol. 798, pp. 606–615, 2019.

[39] C. Gao, M. Yao, C. Shuai, S. Peng, and Y. Deng, "Nano-SiC reinforced Zn biocomposites prepared via laser melting: microstructure, mechanical properties and biodegradability," *Journal of Materials Science & Technology*, vol. 35, no. 11, pp. 2608–2617, 2019.

[40] S. Wong, R. A. Shanks, and A. Hodzic, "Mechanical behavior and fracture toughness of poly (L-lactic acid)-natural fiber composites modified with hyperbranched polymers," *Macromolecular Materials and Engineering*, vol. 289, no. 5, pp. 447–456, 2004.

[41] M. Xing, *Cardiac Regeneration and Repair*, pp. 3–16, Elsevier, Amsterdam, 2014.

[42] H. H. Bayraktar, E. F. Morgan, G. L. Niebur, G. E. Morris, E. K. Wong, and T. M. Keaveny, "Comparison of the elastic and yield properties of human femoral trabecular and cortical bone tissue," *Journal of Biomechanics*, vol. 37, no. 1, pp. 27–35, 2004.

[43] I. Srivastava and N. Koratkar, "Fatigue and fracture toughness of epoxy nanocomposites," *Journal of Management*, vol. 62, no. 2, pp. 50–57, 2010.

[44] S. H. Park and P. R. Bandaru, "Improved mechanical properties of carbon nanotube/polymer composites through the use of carboxyl-epoxide functional group linkages," *Polymer*, vol. 51, no. 22, pp. 5071–5077, 2010.

[45] V. Mirjalili and P. Hubert, "Modelling of the carbon nanotube bridging effect on the toughening of polymers and experimental verification," *Composites Science and Technology*, vol. 70, no. 10, pp. 1537–1543, 2010.

[46] Y. Liu and S. Kumar, "Polymer/carbon nanotube nano composite fibers–a review," *ACS Applied Materials & Interfaces*, vol. 6, no. 9, pp. 6069–6087, 2014.

[47] Z. Qi, Y. Tan, Z. Zhang, L. Gao, C. Zhang, and J. Tian, "Synergistic effect of functionalized graphene oxide and carbon nanotube hybrids on mechanical properties of epoxy composites," *RSC Advances*, vol. 8, no. 67, pp. 38689–38700, 2018.

[48] L. Aliotta, P. Cinelli, M. B. Coltelli, M. C. Righetti, M. Gazzano, and A. Lazzeri, "Effect of nucleating agents on crystallinity and properties of poly (lactic acid) (PLA)," *European Polymer Journal*, vol. 93, pp. 822–832, 2017.

[49] C. Gao, M. Yao, S. Li, P. Feng, S. Peng, and C. Shuai, "Highly biodegradable and bioactive Fe-Pd-bredigite biocomposites prepared by selective laser melting," *Journal of Advanced Research*, vol. 20, pp. 91–104, 2019.

[50] C. Shuai, S. Li, S. Peng, P. Feng, Y. Lai, and C. Gao, "Biodegradable metallic bone implants," *Materials Chemistry Frontiers*, vol. 3, pp. 544–562, 2019.

[51] Y. Yang, C. He, E. Dianyu et al., "Mg bone implant: features, developments and perspectives," *Materials & Design*, p. 108259, 2019.

[52] W. Wang, B. Huang, J. J. Byun, and P. Bartolo, "Assessment of PCL/carbon material scaffolds for bone regeneration," *Journal of the Mechanical Behavior of Biomedical Materials*, vol. 93, pp. 52–60, 2019.